REACTIONS OF (K-Rb)-FELDSPARS FROM RARE-ELEMENT GRANITIC PEGMATITES

by

David K. Teertstra

B.Sc (Queen's University)

M.Sc. (University of Manitoba)

A thesis presented to the

Faculty of Graduate Studies, University of Manitoba

in partial fulfillment of the requirements for the degree

Doctorate of Philosophy

Department of Geological Sciences

Winnipeg, Manitoba

THE UNIVERSITY OF MANITOBA

FACULTY OF GRADUATE STUDIES

*****

COPYRIGHT PERMISSION PAGE

REACTIONS OF (K-Rb)-FELDSPARS FROM RARE-ELEMENT GRANITIC PEGMATITES

BY

DAVID K. TEERTSTRA

A Thesis/Practicum submitted to the Faculty of Graduate Studies of The University of Manitoba in partial fulfillment of the requirements of the degree

of

DOCTOR OF PHILOSOPHY

ACKNOWLEDGEMENTS

This thesis is as much a product of my own efforts as it is of those who created an environment in which the work was possible. The continued professional and personal support and unbridled enthusiasm for an exploration of "things pegmatitic" provided by Petr Černý is foremost in this regard. Both my advisors, Petr Černý and Frank Hawthorne, by continually working for the acquisition and maintenance of top-notch instrumentation, have developed a centre of excellence for mineralogical research at the University of Manitoba. Although my research methods may also be considered unbridled and I have been accused of being artistic in these endeavors, I am grateful for the firm but light hands of my advisors at the editorial reins, and I think that the results speak well for themselves. To my accusers who note that I took two years to produce one decent analysis of K-feldspar, I ask that they send me one normal (*i.e.*, *non-pegmatite*) mineral.

Instant responses to queries and technical problems by technical support staff Ron Chapman, Neil Ball, Sergio Mejia and Wayne Blonski made day-to-day research as easy as it gets. The same can be said for the administrative support of Elizabeth Ross, Sharon Kirsch and Margo MacBride, whose help is appreciated.

At a time when thesis work ground to a halt due to problems with analytical standards, extensive scientific collaboration with Barbara Sherriff generated a necessary conceptual breakthrough. Also, without her initial and continued help with accommodation, I might not have remained in Winnipeg for this degree.

Among those not acknowledged in Appendix 1 for donation of specimens described in the thesis, I thank the following:

C.M.B. Henderson for the $Rb_2ZnSi_5O_{12}$ rubidium standard.

H. Wondratschek for the Volkesfeld, Eifel sanidine sample.

G. Müller for the Na-, H- and Li-exchanged Eifel sanidine samples.

Matt Taylor for the gemmy White Queen orthoclase sample.

Paul Tomascak for the N.W.T. P-rich feldspars.

Milan Novák for many feldspar and scapolite samples.

Peter Vanstone for sampling assistance at the Tanco pegmatite.

Mike Wise for sampling assistance of Maine pegmatites.

H.E. Belkin, J.M. Ferry, S.I. Lahti, D.J. Lieftink, A. Saal, M. Seyler, E.V. Sokolova, A.C. Turnock and A.A. Zolotarev for feldspar and scapolite samples.

Structural characterization of rubidium feldspar as new mineral species was made possible by the transmission electron microscopy work of Rod Ewing, Julie Pier and Lui-Min Wang at the University of New Mexico, Albuquerque.

This work was supported by a University of Manitoba Duff Roblin Fellowship to DKT (1993-1996), by NSERC Operating and Major Installation Grants to PČ, and by NSERC Operating, Equipment and Infrastructure Grants to FCH.

This work is dedicated to the loving memory of my grandmother, Wilma Bruinix (1908-1993), my grandfather, Gerritt Bruinix (1915-1997) and my father, Jack Teertstra (1947-1996). I have not known war or starvation but through them I have learned something of perseverance. I am grateful to my mother, Margaret, my brother, Jack, and my sisters, Angela and Susanne, who supported my work and prodded me to complete it. The cost of research is often high when it comes to personal relationships; I thank Margret Aaldyk, who in the face of difficult circumstance brought many good things to me. In a time of severe testing, I am grateful for the tough and sane advice of friends at the Meeting Place: Paul Wartman, Doug Jones, Jack Parker, Eva Harder and Murray Friesen.

Among friends during my stay here I have had the best, including in no particular order: (barfin') Paul Tomascak, Milan (Harry) Novák, Matt (kick-me) Taylor, Pamela Fulton, Xu Zhi, Ian Fieldm'house, Rivendell Bongard, Julie (tourmaline-queen) Selway, Jiangjie Liang, Mark Cooper, Janice Cramer, David Warrenchuck, Peter and Tammy Burns, Harvey (caveman) Buck, Michelle Davidson, Andy Stilling, Pavel Uher, Mike Wise, James Holland, Michael Schindler and many others. What can be said, except that I'll die rich!

ABSTRACT

This thesis describes the first minerals with Rb as an essential constituent, discovered during study of Rb- and Cs-rich-to-dominant feldspars and micas associated with pollucite from the interior zones of complex rare-element granitic pegmatites. Rubicline is the rubidium analog of triclinic microcline and rubidine is the proposed name for the rubidium analogue of monoclinic sanidine. The (K-Rb)-feldspars lie close to the join from $KAlSi_3O_8$ to $RbAlSi_3O_8$ and have up to 26.2 wt.% Rb_2O (91 mol.% Rbf) and 1.5 wt.% Cs_2O (3 mol.% Csf). EMP-measured compositions were constrained within 2% accuracy by characterizing a set of internally consistent standards with stoichiometry compatible with structural formulae, at a precision of less than 1% (4σ). Overlap of the EMP-analysed volume of feldspar with hematite and other micro-inclusions and with fluid-filled micropores can be recognized. Substitution of more than 1% of light-element *M*-cations, $(AlP)Si_{-2}$, and $\square Si_4O_8$ (not previously known in microcline) has been identified in pegmatite feldspar. As the $\square Si_4O_8$ substitution provides a mechanism for partial occupancy of the *M*-site by molecular H_2O, it is probable that the reconstructive monoclinic → triclinic (Al,Si)-ordering process in pegmatite K-feldspar goes to near-completion because it is internally catalysed by H_2O.

Three low-temperature processes generate Rb-enriched feldspars: (i) exsolution, (ii) subsolvus solution-reprecipitation, and (iii) direct subsolvus coprecipitation with K-feldspar. (i) Near-complete exsolution and phase separation of albite and (Rb,K)-feldspar is related to widespread substitution of $\square Si_4O_8$. Rb-rich microcline which does not have $\square Si_4O_8$ substitution is compositionally homogeneous, but Rb-feldspar exsolution is typical of (K,Rb)-feldspar with up to 5 mol.% $\square Si_4O_8$. (Rb,K)-feldspar coherent with host microcline is also (Al,Si)-

ordered and triclinic. Exsolution of the (Rb,K)-feldspar postdates that of albite because the rate of diffusion of Na is greater than that of Rb; however, migration of *M*-site vacancy allows for overall higher rates of diffusion than in non-vacant feldspar. (ii) Porous assemblages of adularian K-feldspar + (Rb,K)-feldspar are formed by solution-reprecipitation from Rb-bearing precursors under low-temperature hydrothermal conditions. (iii) Adularian (Rb,K)-feldspar also coprecipitates with end-member K-feldspar (± cookeite) due to reaction of hydrothermal fluid with early Rb-bearing feldspar at ~300-150°C. At low temperature, a broad solvus extends between K-feldspar (~Or_{100}) and Rb-feldspar (~Rbf_{80}), cresting at T<400°C. Feldspar zoned in K/Rb with compositions in the range Rbf_{50} to Rbf_{70} are common, but are probably metastable because of a slow rate of Rb-diffusion at low temperature. The adularian feldspars tend to be untwinned, monoclinic and disordered unless a nucleophilic catalyst such as OH, F or CO_3 was available for (Al,Si) surface-structural rearrangement. Rietveld refinement of X-ray powder-diffraction data gives accurate cell parameters for K-feldspars, and may be used to identify <3 vol.% of albite. The cell parameters *a* 8.591(1) Å, *b* 13.047(2)Å, *c* 7.170(1) Å, ß 115.97(1)° are closely representative of the structure of Or_{100} end-member high sanidine.

The occurrence of Rb- and Cs-rich-to-dominant micas and clay minerals, and a complex internal zoning of cesian analcime, indicate widespread activity of Rb and Cs under subsolidus conditions. Characteristic sequences of alteration of pollucite, petalite and spodumene, and sequences of crystallization in gem- and zeolite-bearing clay-filled pockets and in leaching cavities, indicate that hydrothermal wallrock-derived fluids have negligible influence on the internal evolution of late pegmatite fluid except at very low temperature.

CONTENTS

List of Figures **Page**

List of Tables

CHAPTER 1

INTRODUCTION

Feldspar-group minerals comprise a significant proportion of the crust of the Earth. They are framework aluminosilicates with the general formula MT_4O_8, where M = Na, K, NH_4, Ca, Ba or Sr, and T = Si, Al, Fe^{3+} or B. The most common minerals are solid solutions of the end-members potassium feldspar (Or) $KAlSi_3O_8$, albite (Ab) $NaAlSi_3O_8$ and anorthite (An) $CaAl_2Si_2O_8$; these and other minerals are described in Table 1.1. There has been much work on the feldspars, as variations of chemical composition and structure are a function of geologic environment (P, T, X), and are useful in unravelling the history of the Earth. In contrast, there has been little work on feldspars from granitic pegmatites.

During investigation of minerals associated with the cesium-aluminosilicate mineral pollucite from complex-type rare-element granitic pegmatites (Teertstra 1991), more than half of the 56 alkali-feldspar samples examined were enriched in Rb relative to K (locally with Rb > K). Multiple generations of (K-Rb)-feldspar coexist with, vein and later replace pollucite, indicating continued reaction and alkali-metal fractionation over the transition from magmatic to subsolidus conditions. Variable and complex textural and compositional relationships between K-feldspar and (Rb,K)-feldspar were revealed by back-scattered electron (BSE) imaging, a technique which is sensitive to variation in

Table 1.1: Feldspar species and composition.

Name, Formula, Symmetry, Notes and References

Albite, $NaAlSi_3O_8$, triclinic, our EMP standard is from a pegmatite in Amelia County, Virginia (Sinkankas 1968); Amelia albite has high degree of (Al,Si) order (Harlow & Brown 1980).

Reedmergnerite, $NaBSi_3O_8$, triclinic, has a high degree of (B,Si) order; known from a peralkaline pegmatite (Grew *et al.* 1993); type locality is Green River shale, Utah (Fleet 1992, Milton *et al.*1960).

Buddingtonite, $(NH_4)AlSi_3O_8$, monoclinic, high degree of (Al,Si) disorder (review by Voncken *et al.* 1993a).

Sanidine, $KAlSi_3O_8$, monoclinic, high degree of (Al,Si) disorder.

Orthoclase, $KAlSi_3O_8$, has long-range monoclinic symmetry with unit-cell-size (Al,Si)-ordered domains.

Microcline, $KAlSi_3O_8$, triclinic, high degree of (Al,Si) order.

Adularia, $KAlSi_3O_8$, varietal name for a morphologically-distinct form of K-feldspar occurring in low-temperature hydrothermal environments with solid solutions limited to near Or_{100} (Černý & Chapman 1984, 1986); the structure is usually monoclinic (sanidine) but may be (Al,Si)-ordered to orthoclase or microcline.

Anorthite, $CaAl_2Si_2O_8$, triclinic, high degree of (Al,Si) order.

Celsian, $BaAl_2Si_2O_8$, monoclinic, dimorphous with monoclinic paracelsian.

Polymorphs and non-IMA-approved names:

unnamed, $K(Fe,Al)Si_3O_8$, monoclinic (Linthout & Lustenhouwer 1993).

Hyalophane, $(K,Ba)Al(Al,Si)_3O_8$, monoclinic, intermediate in $KAlSi_3O_8$ - $BaAl_2Si_2O_8$ series.

Banalcite, $Ba_{0.5}Na_2Al_2Si_2O_8$, orthorhombic.

Stronalcite, $Sr_{0.5}Na_2Al_2Si_2O_8$, orthorhombic.

Slawsonite, $(Sr,Ca)Al_2Si_2O_8$, monoclinic.

mean atomic number. This thesis examines the subsolidus reactions of (K,Rb)-feldspar which generate (Rb,K)-feldspar (and associated Rb- and Cs-rich minerals) and describes the compositional, textural and paragenetic relationships of the (K-Rb)-feldspar series. Associations of (Rb,K)-feldspar with the reaction products of early, blocky K-feldspar and with late low-temperature adularia of variable (Al,Si)-order indicate widely variable conditions of crystallization.

The feldspars richest in Rb have been found so far only in rare-element granitic pegmatites of the complex type (*cf.* classification by Černý 1991), although K-rich alkali feldspars with elevated levels of Rb are known in some volcanic environments. The process of Rb-enrichment of primary (K,Na)-feldspar associated with pollucite is generally understood, even though specific details remain to be elucidated. To a degree, the fate of Rb in magmatic differentiation is similar to that of Cs. Cesium has the largest metal radius, the smallest ionization enthalpy and the smallest hydrated radius of the Group IA cations. It is volatile at high temperature and is the most electropositive of the natural elements. Relatively incompatible and excluded from the structures of most minerals, Cs accumulates in late silicious residues of granitic magmas to form primary pollucite. Along with Cs, Rb is also fractionated during pegmatite crystallization, but due to its smaller size, Rb has a much stronger tendency to disperse among the K-rich aluminosilicate minerals (Černý 1982, Icenhower & London 1996). Thus, even though elevated levels of Rb are characteristic of

LCT (Li-, Cs- and Ta-enriched) pegmatites of the rare-element class, it is rather surprising to discover a feldspar with atomic proportions of Rb > K. This may be considered the most chemically evolved feldspar, with extreme fractionation of the alkali metals.

Preliminary analytical results indicate that the rubidium analogue of potassium feldspar must be introduced as a new mineral species into the feldspar group. This is the first known mineral with Rb as an essential constituent. Ideally forming a series with K-feldspar, the predicted end-member is $RbAlSi_3O_8$. Methods of accurate analysis need to be developed and suitable electron-microprobe standards are required to verify the chemical composition. Variations in its structural state are probably analogous to those of sanidine, orthoclase and microcline, but are not yet established.

The feldspar structure is composed of corner-sharing AlO_4 and SiO_4 tetrahedra forming 4-membered rings cross-linked in an infinite three-dimensional array. There are two symmetrically non-equivalent tetrahedral sites in monoclinic alkali feldspar, designated T_1o and T_2o. In fully-disordered monoclinic high-sanidine, Al and Si are equally distributed among the *T*-sites (Ferguson *et al.* 1991). A highly ordered (Al,Si)-distribution is found in orthoclase, but adjacent ordered and antiordered domains are only a few unit cells in size (Eggleton & Buseck 1980) and the long-range symmetry is monoclinic. The triclinic alkali feldspars

have four non-equivalent tetrahedral sites, designated T_1o, T_2o, T_1m and T_2m. Trivalent cations (including Al, Fe^{3+} and B) preferentially order at T_1o (Ribbe 1994). In general, disordered structures are likely to have equilibrated at high temperature than ordered structures, but rates of crystallization, and P_{H2O} also strongly influence the (Al,Si) ordering process. The structure of adularia, formed at rather low temperature, covers the full range of (Al,Si)-order from low microcline to high sanidine but tends to be monoclinic (Martin 1974, Černý & Chapman 1986, Ferguson *et al.* 1991).

Sequences of crystallization of internal units of rare-element pegmatites may be traced by the evolving chemical composition of tourmaline (*e.g.*, Jolliff *et al.* 1986), Nb-Ta oxides (*e.g.*, Mulja *et al.* 1996) and micas (*e.g.*, Černý *et al.* 1995). The K/Rb ratio and Cs (ppm) content of K-feldspar have found general use as indicators of progressive fractionation in granites and pegmatites, and among cogenetic suites of pegmatites, and has been used to indicate sequences of crystallization of internal units of complex zoned pegmatites. For example, at the Tin Mountain pegmatite, South Dakota, the highest concentrations of Rb occur in the first- and second-intermediate zones, rather than in the later-crystallizing third-intermediate zone (Walker *et al.* 1989b). The highest concentration of Rb_2O generally occurs in K-feldspar from the pollucite-bearing zones. A complicating factor (disturbing primary compositions) is extensive recrystallization of K-feldspar due to the sanidine → microcline monoclinic → triclinic transformation

which generates pseudomorphism of the primary phase (Martin 1988).

Systematic study of the petrogenesis of pegmatite feldspars must deal with three areas of concern: (1) the primary subsolvus feldspars exhibit distinct spatial and temporal separation in zoned complex-type pegmatites, rendering estimates of modal proportions and original melt composition problematic; (2) the sanidine → microcline, monoclinic → triclinic phase transformation and the Ab-Or exsolution processes go to (near) completion in the water-rich environment of granitic pegmatites, and the structure and composition of the original phase is largely obliterated; (3) extensive subsolidus-reaction processes are operative to near-ambient conditions, often leading to widespread replacement of early-formed feldspar and producing late low-temperature generations.

Normally, the various reactions of K-feldspar are obscure in outcrop, hand specimen and even in thin section unless there is a marked change in colour or texture of the feldspar (*e.g.*, Černý & Macek 1972, 1974). If the feldspar has significant Rb_2O, many of the reactions, including low-temperature compositional disturbance, may be observed using BSE (back-scattered electron) imaging. In a review of the evolution of feldspars in granitic pegmatites, Černý (1994) commented that "the rock-forming feldspars are a Cinderella of pegmatite research". The present study will begin to remedy this situation for the alkali feldspars.

CHAPTER 2

PREVIOUS WORK

A review of the reactions of feldspars in igneous rocks has been given by Brown & Parsons (1994), and the structures of feldspars were reviewed by Ribbe (1994). A review of Rb in pegmatite K-feldspar was given by Černý *et al.* (1985). An overview of the evolution of feldspars from granitic pegmatites was given by Černý (1994). Models of the genesis and internal evolution of complex rare-element pegmatites are given by London (1990) and Černý (1991). The role of H_2O in the orthoclase → microcline monoclinic → triclinic transformation and in the generation of turbidity, microporosity and permeability is discussed by Waldron *et al.* (1993) and Walker *et al.* (1995), respectively.

2.1 *Chemical composition*

In the literature, there are no electron-microprobe (EMP) studies of natural Rb-rich feldspar, in part because only a few laboratories have suitable reference standards for Rb, and because Rb has been considered a minor-to-trace element. The only data available are on bulk samples with less than a few wt. % Rb_2O; the compositional data are based on wet-chemical analysis and X-ray powder diffraction. Previous to this thesis work, the highest known Rb content of any feldspar was in microcline from the pollucite-bearing Red Cross Lake (RCL)

pegmatites, NE Manitoba. Bulk chemical analysis gave up to 5.9 wt.% Rb_2O (Černý *et al.* 1985). Other Rb-bearing feldspars recorded in the literature include samples from Tanco and lower Tanco at Bernic Lake, Manitoba, the Varuträsk pegmatite in Sweden, and pegmatites in the Kola Peninsula, Russia, all of which typically have <3 wt.% Rb_2O (*c.f.* Černý *et al.* 1985).

As far as synthetic feldspar is concerned, a wide variety of compositions have been produced, with M^+ = H, Li, Na, K, Rb, Tl and NH_4, M^{2+} = Ca, Fe, Sr, Pb, Ba, Eu and La, and T = B, Al, Si, P, Fe^{3+}, Mg, Ga and Ge (Table 2.1). Synthetic (Al,Si)-ordered Rb-feldspar has been produced only by cation-exchange (McMillan *et al.* 1980, Pentinghaus & Henderson 1979, Wietze & Viswanathan 1971). Hydrothermal synthesis generates disordered to partly-ordered Rb-feldspar (Voncken *et al.* 1993b, Gasperin 1971, Bruno & Pentinghaus 1974, Ghelis & Gasperin 1970). Dry, high-temperature synthesis generates Rb-leucite rather than disordered Rb-feldspar (the phase relations are given in Bambauer *et al.* 1974).

Experimental measurement of the feldspar/melt partition coefficients of Rb allows interpretation of the conditions of Rb-feldspar formation. At high temperature, values for partition coefficients between feldspar and peraluminous melt are high (*e.g.*, 1.0, Icenhower & London 1996; 0.8, Congdon & Nash 1991). At low temperature, values for partition coefficients between feldspar and aqueous solution are lower (*e.g.*, 0.28 at 180°C/1kbar, Pauwels *et al.* 1989; 0.26 at

Table 2.1: Selected synthetic feldspars: formulae, notes and references.

$RbAlSi_3O_8$: monoclinic, from hydrothermal synthesis (Voncken *et al.* 1993b, Borutskaya 1975, Bruno & Pentinghaus 1974, Ghelis & Gasperin 1970, Barrer & McCallum 1953). Structure refined by Gasperin (1971).

$RbAlSi_3O_8$: triclinic, prepared by cation exchange (McMillan *et al.* 1980, Pentinghaus & Henderson 1979, Weitze & Viswanathan 1971). Thermal expansion was studied (Henderson 1978).

$KFeSi_3O_8$: may be monoclinic and triclinic (Wones & Appleman 1963, Faust 1936, Hautefeuille & Perry 1888). Solid solution with $KAlSi_3O_8$ prepared by Lindqvist (1966).

$KBSi_3O_8$: forms a series with $KAlSi_3O_8$ (Martin 1971).

$HAlSi_3O_8$: prepared by cation exchange of Na-exchanged sanidine in H_2SO_4 (Müller 1988). Structure refined by Paulus & Müller (1988).

$LiAlSi_3O_8$: prepared by cation exchange (Müller 1988), Deubener *et al.* 1991).

$NH_4AlSi_3O_8$: prepared under anhydrous conditions(Voncken *et al.* 1993a), earlier work by Barker (1964) and Hallum & Eugster (1976).

$NaBSi_3O_8$: hydrothermal synthesis using H_3BO_3 (structure refined, Fleet 1992), earlier work was by Kimata (1977), Bruno & Pentinghaus (1974), Eugster & McIver (1959). Morphology was studied by Mason (1980a, 1980b).

$LaAl_3SiO_8$: containing trivalent non-tetrahedral cations (Kneip & Liebau 1994)

400°C/1kbar, Volfinger 1976). Factors that influence partitioning include variation in melt composition or melt structure, temperature and pressure, and the composition and structure of the mineral. Partition coefficients for Rb in alkali feldspar increase with Or content according to $D(Rb)^{Fsp/glass} = 0.03 + (0.01)Or$; the literature data are summarized by Icenhower & London (1996). The intercept (0.03) corresponds to average distribution coefficients determined for albitic plagioclase compositions. The intercept with Or_{100} gives a value near 1.0, and although some measurements of $D(Rb)^{Fsp/glass}$ exceed 1.0, most are less than this and Rb typically behaves as a marginally incompatible element in primary (K,Na)-feldspar. It might be expected, by analogy to the results of Rb-feldspar synthesis, that the disordered monoclinic *C*2/*m* sanidine structure accepts Rb more readily than the ordered triclinic $C\bar{1}$ microcline structure, but both can accommodate Rb.

2.2 *Crystal structure*

The highest symmetry observed for alkali feldspars is monoclinic (space group *C2/m*), but triclinic symmetry (*C*$\bar{1}$) occurs with increased (Al,Si) order, replacement of K by Na, and decreasing temperature of equilibration (Ribbe 1994). The transition temperature of the displacive phase transition (framework shearing) decreases rapidly with increasing K content. However, the transition temperature for (Al,Si)-ordering does not change drastically with substitution of Na by K. For alkali feldspar with Or>25 mol.%, the (Al,Si)-ordering transition occurs at higher temperature than the displacive phase transition (Brown & Parsons 1989).

The strain-controlled tweed microtexture of orthoclase, consisting of adjacent ordered and anti-ordered domains with dimensions of several unit-cells, is typically recrystallized in plutonic rocks to a coarse mosaic of subgrains. The driving force for the reactivity of orthoclase in typical plutonic rocks with low-temperature fluid is the relatively large elastic-strain energy of coherent cryptoperthite and of the tweed texture (Waldron *et al.* 1993). TEM studies show that individual crystals may be an intimate mixture of tweed orthoclase and tartan microcline (*e.g.*, White & Barnett 1990, Bambauer *et al.* 1989). Increased turbidity and microporosity invariably accompanies the transformation to microcline, and underlines the importance of fluids in the transformation (Walker

et al. 1995, Lee *et al.* 1995). (Al,Si)-ordered low microcline is normally characterized optically by the irregular tartan microtexture of intersecting albite and pericline twins.

For K-rich feldspar, the following nomenclature is commonly used: (1) high sanidine (HS) for highly disordered monoclinic feldspar; (2) orthoclase for ordered monoclinic feldspar; (3) intermediate microcline for disordered triclinic feldspar; (4) low or maximum microcline (MM) for highly ordered triclinic feldspar. These may be distinguished by optical microscopy and by X-ray methods (Bambauer *et al.* 1989). In this thesis, feldspar which appears fully ordered or disordered by optical and X-ray methods is referred to by the prefix "end-member".

An extensive review of the changes in the feldspar structure with Rb (and other) substitution was given by Brown *et al.* (1984), and few new data have been added until now. The changes in cell parameters are not as large across the (K-Rb)-feldspar series as in the (K-Na)-feldspar series. With increasing Rb along the join from K-feldspar to Rb-feldspar, the cell parameters a, c and β increase regularly, but b is relatively constant (McMillan *et al.* 1980). The most significant feature of Rb substitution is increased cell volume of ~3.2% (Fig. 2.1B). In going from pure ordered $KAlSi_3O_8$ to pure ordered $RbAlSi_3O_8$ an expansion of ~0.0% and ~0.4% occurs in b and c, respectively, and ~2.2% in a. From pure $NaAlSi_3O_8$

to pure $KAlSi_3O_8$, expansions of -1.3% and -0.9% occur in *b* and *c*, respectively, and -5.4% in *a*. Albite exsolution with lattice coherency generates elastic strain at the phase boundary by an expansion of *a* in the K-rich phase and a contraction of *a* in the Na-rich phase. Incorporation of Rb also increases *a*, and by analogy with albite, potential coherent exsolution-lamellae of Rb-rich feldspar are expected to be parallel to Ab lamellae, with elastic lattice strain being incorporated by the K-rich feldspar. By analogy with the synthetic methods of Rb-feldspar generation, it may be predicted that natural ordered Rb-feldspar may be generated by alkali-cation diffusion (exsolution) within an ordered framework of increased cell dimensions, and that disordered Rb-feldspar may be generated by direct precipitation, likely associated with a disordered host K-feldspar.

Details of structural characterization of end-member feldspars are summarized by Blasi & Blasi De Pol (1994). Uncertainties exist concerning the cell parameters of end-member high-sanidine. Direct synthesis and dry annealing of partly ordered feldspar both produce material with minor long-range (Al,Si) order. However, crystal-structure refinement of Or_{100} sanidine from Buck Claim, SE Manitoba, gave values of $<T_1\text{-}O>$ and $<T_2\text{-}O>$ equal within standard deviations, and the cell parameters are indicative of complete long-range (Al,Si) disorder (Ferguson *et al.* 1991). In this thesis, the data of Ferguson *et al.* (1991) are used as reference points for end-member high-sanidine (HS), and the data of Kroll & Ribbe (1987) are used for end-member maximum-microcline (MM).

The relations between cell parameters, (Al,Si)-order and the composition of (K,Rb)-feldspar were summarized by Černý *et al.* (1985). Cell parameters increase with substitution of Rb for K and also with increasing (Al,Si) disorder. Cell parameters for the (Al,Si)-ordered (K-Rb)-feldspar series, prepared by cation exchange of albite, were determined by Pentinghaus & Henderson (1979), by McMillan *et al.* (1980) and by Weitze & Viswanathan (1971). The reference point for Rbf_{100} rubidian maximum microcline (RbMM) is taken from Pentinghaus & Henderson (1979). The cell parameters agree closely with those of McMillan *et al.* (1980) determined for Rbf_{93} RbMM.

Because the cell volume of RbMM is larger than that of RbHS, Pentinghaus & Henderson (1979) suggested that the RbMM structural state is metastable. However, because complete disorder may not have been attained for synthetic RbHS, the cell parameters for end-member RbHS are uncertain. As with high sanidine, there may be experimental difficulties in the synthesis of fully disordered rubidian high-sanidine. RbHS must be synthesized by hydrothermal methods, because high-temperature dry synthesis, otherwise conducive to generating disordered feldspar, produces rubidian leucite (Bambauer *et al.* 1974, Martin & Lagache 1970). Plots of *c vs. b* and *V vs. b* for rubidian sanidine show a range of cell parameters that might result from slight but variable degrees of (Al,Si) order, or from poor accuracy (Fig. 2.1A, B). Structure refinement of synthetic rubidian sanidine gave values of $<T_1\text{-}O> = 1.635$ (3) Å and $<T_2\text{-}O>$

= 1.632 (4) Å, indicative of complete (Al,Si) disorder (Gasperin 1971). However, the cell parameters of Gasperin (1971) derived from single-crystal methods lie within the field of (Na,K)-feldspars (Fig. 2.1A), and are probably less accurate than those derived from powder XRD using an internal standard (Table 2.2). Further work is required for accurate characterization of end-member rubidian high-sanidine.

In the substitutional series from LA to MM and from HA to HS, the cell parameter trends are parallel to one another due to near-identical mechanisms of substitution. In the order-disorder series from MM to HS and LA to HA, cell parameter trends are also parallel one-another, due to near-identical mechanisms of (Al,Si)-disorder (Stewart & Ribbe 1969; Fig. 4.1). Trends for the substitutional series from MM to RbMM and from HS to RbHS, and for the (Al,Si) order-disorder series from MM to HS and from RbMM to RbHS might also be expected to parallel one-another. The series most well-characterized is from MM to RbMM, in which V increases at constant b. If accurate values for HS and RbHS are determined, plots of V *vs.* b or c *vs.* b should form a parallelogram with MM, RbMM, HS and RbHS at the corners. This is not observed for the present values of HS and RbHS (Fig. 2.1). Either these values are inaccurate or a structural explanation different from that of Stewart & Ribbe (1969) is required for the difference in substitution of Rb in MM *vs.* Rb in HS, and for the difference in (Al,Si) disorder from MM to HS *vs.* RbMM to RbHS.

Table 2.2: Cell parameters of (K-Rb)-feldspar end-members.

	phase	*a* (Å)	*b* (Å)	*c* (Å)	$\alpha°$	$\beta°$	$\gamma°$	*V* (Å^3)
1.	RbHS	8.820	12.992	7.161	90	116.24	90	736.0
		0.002	0.003	0.002		0.02		0.2
2.	RbHS	8.839	13.034	7.182	90	116.29	90	741.8
		0.001	0.001	0.001		0.01		0.2
3.	RbHS	8.837	13.035	7.187	90	116.27	90	742.4
		0.005	0.007	0.004		0.01		0.4
4.	RbHS	8.834	13.042	7.195	90	116.42	90	742.4
		0.004	0.005	0.003		0.03		0.1
5.	RbHS	8.843	13.044	7.191	90	116.30	90	743.7
		0.003	0.004	0.003		0.02		0.3
6.	RbHS	8.846	13.048	7.193	90	116.30	90	744.3
		0.001	0.002	0.001		0.01		0.2
7.	MM	8.592	12.963	7.222	90.62	115.95	87.67	722.7
		0.004	0.007	0.003	0.08	0.08	0.08	0.4
8.	HS	8.603	13.036	7.174	90	116.03	90	722.9
		0.002	0.004	0.002		0.02		0.3
9.	RbMM	8.840	12.962	7.252	90.52	116.16	88.01	745.3
		0.001	0.001	0.001	0.01	0.01	0.01	0.2
10.	RbMM	8.843	12.961	7.256	90.53	116.20	88.01	745.7
		0.002	0.002	0.002	0.01	0.01	0.01	0.4
11.	RbMM	8.844	12.964	7.250	90.51	116.14	88.05	745.8
		0.002	0.002	0.002	0.05	0.05	0.05	0.5

Phase: Rubidian high sanidine (RbHS), maximum microcline (MM), high sanidine (HS) and rubidian maximum microcline (RbMM).
References: 1. Gasperin (1971), 2. Bruno & Pentinghaus (1974), 3. Voncken *et al.* (1993b), 4. Ghelis & Gasperin (1970), 5. Henderson (1978), 6. and 9. Pentinghaus & Henderson (1979), 7. Kroll & Ribbe (1987), 8. Ferguson *et al.* (1991), 10. McMillan *et al.*(1980), 11. Wietze & Viswanathan (1971).

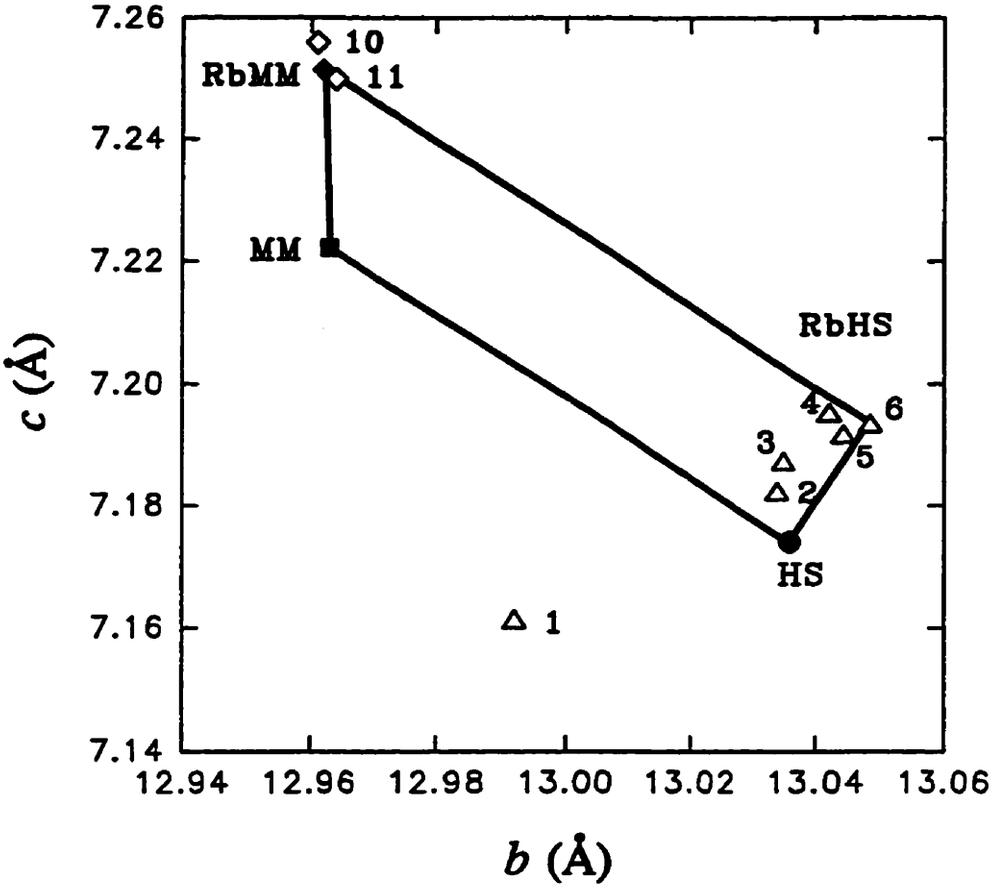

Fig. 2.1. (A) Cell dimensions *c* (Å) *vs. b* (Å) of maximum microcline (MM, ■), high sanidine (HS,•), rubidian maximum microcline (RbMM, ●, ◇) and rubidian high sanidine (RbHS, ▵). Values for end members are marked using filled symbols, see text and Table 2.2 for details.

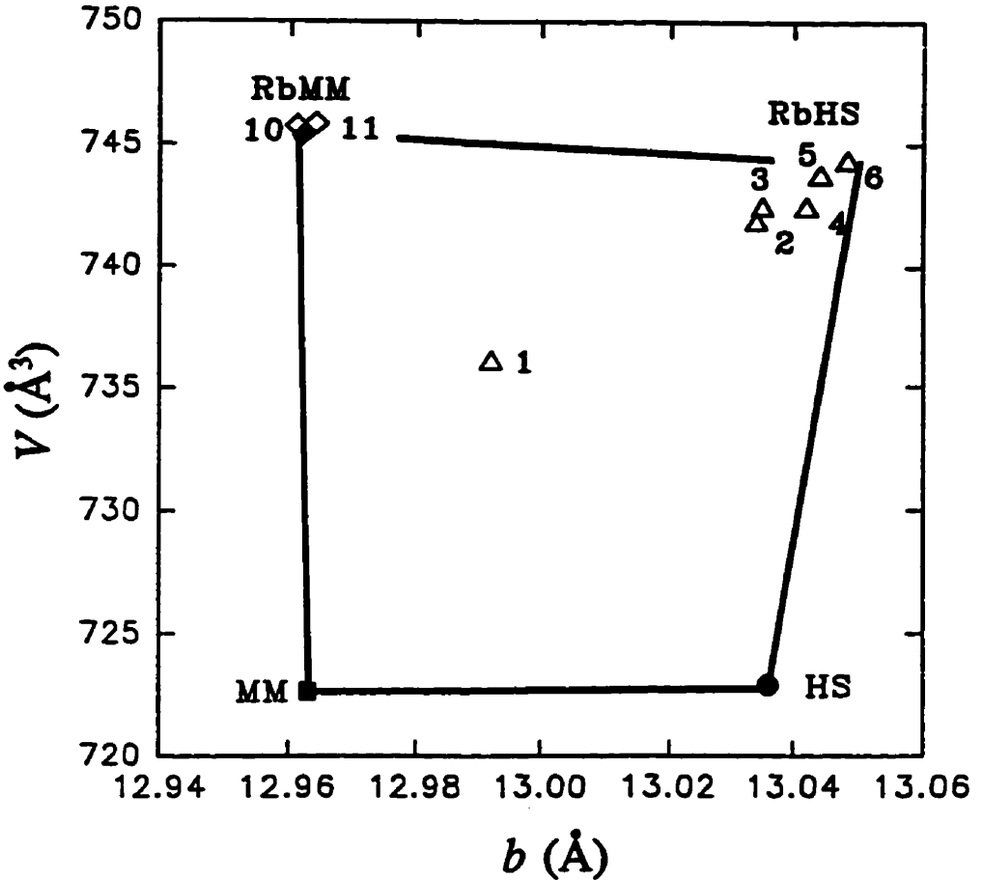

Fig. 2.1. (B) Cell dimensions V (Å^3) *vs.* b (Å) of maximum microcline (MM, ■), high sanidine (HS,•), rubidian maximum microcline (RbMM, ◆, ◇) and rubidian high sanidine (RbHS, △). Values for end-members are marked using filled symbols, see text and Table 2.2 for details.

2.3 *Petrogenesis*

The conditions of crystallization of highly fractionated peraluminous melts of granitic composition are estimated to be as low as 650-450°C at 4-2 kbar (London 1986, Chakoumakos & Lumpkin 1990). In this temperature range, microcline-forming phase transformations (at T<500°C) and intracrystalline exsolution textures probably develop soon after pegmatite consolidation (Brown & Parsons 1989, 1994). In granitic pegmatites, microcline is by far the most abundant K-feldspar, although occurrences of orthoclase are not particularly rare (Martin 1982, Abad-Ortega *et al.* 1993). Twin-domain coarsening is enhanced by an order of magnitude in the fluid-rich environment of granitic pegmatites; microcline "subgrains" may be several cm in size (Černý & Macek 1974, Černý & Simpson 1978). Crystallization of K-feldspar may continue to very low temperature, constituting Ginsburg's (1960) "second K-stage" of pegmatite evolution. In late adularia, a disordered (Al,Si)-distribution and fine grain size are suggested to result from high rates of nucleation and growth (Černý & Chapman 1984, 1986). Compositions are similar to those of diagenetic feldspar (Or_{100} in association with Ab_{100}) and are indicative of crystallization at T < 300-200°C (Worden & Rushton 1992).

A general comparison of plutonic K-feldspar to pegmatite K-feldspar is in order, to illustrate the unique character of the latter. The equigranular texture of granitic

rocks is formed by near-equilibrium crystallization of discrete grains of quartz and feldspar, with a typical grain-size of 0.5 mm but ranging up to ~15 mm. In contrast, pegmatite K-feldspar may occur as large individual club-shaped crystals up to 6 m long, or as crystallographically-oriented comb agggregates, widening from the wall zone inward to the core-margin and core. Large crystals of K-feldspar often occur in graphic intergrowth with quartz (as do plagioclase, tourmaline and other pegmatite minerals). Albite is not all necessarily coarse-grained in pegmatites, but may form essentially monomineralic fine-grained masses (late saccharoidal albite units) or "line-rock" (layered albitic aplite). Many of the typical zonal and textural features of granitic pegmatites may be classified as oscillatory type, and these features are typical of systems crystallizing far from equilibrium (Fowler 1990).

In an open system, zonation in rocks and minerals may be attributed to loss of components or to influxed changes in composition (*e.g.*,hydrothermal alteration). However, in a closed system, oscillatory textural and chemical features are characteristic of systems driven far from equilibrium, and indicate the operation of self-organized feedback mechanisms (Fowler 1990, Pearce 1994). Oscillatory behaviour is controlled by the rate-limiting component of a reaction. A common example in granitic pegmatites is the generation of graphic texture, in which the growth rate of quartz in a granitic melt is limited by diffusion of Si. As Si is consumed, the growth rate decreases and a euhedral surface develops. A second

mineral becomes stable in the rejected solute near the crystal/fluid boundary layer and grows until the adjacent melt is supersaturated in Si. Quartz again begins rapid crystallization, but the growth rate continually decreases as nearby Si is consumed. It is the repetition of these cycles which generates the oscillatory-type textures (Lentz & Fowler 1992).

Various other lines of evidence suggest that, in contrast to plutonic granites, pegmatite crystallization approaches but does not attain equilibrium. The small size of pegmatites and their intrusion into relatively cool host-rocks require rapid magmatic crystallization. Even conservative rates of heat transfer suggest solidification in less than 1000 years (Chakoumakos & Lumpkin 1990, London 1992a). Experimentally, such a large degree of undercooling has been shown to enhance supersaturation and inhibit nucleation (London 1990); these conditions favour the growth of large individual crystals (Swanson & Fenn 1992). Silicate-melt depolymerization by network modifiers such as H_2O, Li, B and F, measurably increases element diffusivity in volatile-rich granitic melts (Scarfe 1986, Dingwell 1989). Historically, many of the textural features of pegmatites have been attributed to various influences of H_2O, although it is now recognized that supersaturation is probably not requisite for the development of most textures in granitic pegmatites (London 1990). Pegmatite-like zoning and textures were closely simulated in H_2O-undersaturated but very (H_2O + B, F, P)-rich experimental charges (London *et al.* 1989). Different (but high) rates of diffusion

of Na and K (relative to H_2O-poor granite) may also enhance phase separation and favour the development of internal zonation. Textural and other evidence for the disequilibrium character of primary crystallization of granitic pegmatites is summarized in London (1990). Many of the reactions of (K,Rb)-feldspar might be the result of post-crystallization attempts to attain equilibrium as a function of decreasing temperature.

The classification of certain pegmatite units as primary or secondary has been the topic of much debate. Arguments suggesting that pollucite and lepidolite units are primary were summarized by Černý & Simpson (1978). If these units are secondary, the source of the additional highly fractionated magma is questionable. External introduction of late pulses of fluid requires much more complicated models regarding the source, material transfer and generation of emplacement space than does single-pulse emplacement (Černý 1991). Such a mechanism is supported neither by observations on natural pegmatites nor by experimental work.

During the course of pegmatite consolidation, residual fluids become silica-depleted and rich in Na and incompatible elements. Fluid-inclusion evidence indicates that these late fluids are sodic, alkaline "solution-melts" (London & Burt 1982). Removal of the fluxing components Li, B and P, due to crystallization of spodumene, tourmaline and phosphate minerals, leads to rapid crystallization of

units of fine-grained albite and mica (London 1990). In particular, mica units show metasomatic contacts with early zones, and were traditionally considered to be entirely of replacement origin.

Correlations between the internal evolution of pegmatite units and sequences of exomorphic alteration were made by Morgan & London (1987). Li- and B-rich fluids infiltrated wall-rock on destabilization of late sodic borosilicate melts ("boron-quench") at near-solidus temperature (less than 500°C). These were followed by F-rich fluids which also reacted with K-feldspar. At Tanco, unmixing of hydrous + carbonic fluids took place at less than 420°C and 2.6 kbar (London 1990). These fluids caused internal alteration, generated exomorphic alteration haloes, and were possibly involved in the formation of miarolitic cavities. Miarolitic and leaching cavities, lined with late-stage minerals including cookeite, calcite, adularia, cesian analcime and other zeolites, and various phosphate minerals (*e.g.*, Černý 1972), represent Ginsburg's (1960) "alpine-vein" stage of pegmatite evolution. Chakoumakos & Lumpkin (1990) gathered evidence to suggest that subsolidus hydrothermal replacement and reequilibration, including eucryptite replacement after spodumene at 200-100°C, continues for several million years after pegmatite consolidation.

Postmagmatic sequences of evolution of K-feldspar, including subsolidus transformations, deuteric reactions, and hydrothermal alteration, have not been

correlated with specific stages in the late-fluid evolution of granitic pegmatites. Examination of the reactions of (K,Rb)-feldspar and associated Rb- and Cs-rich minerals may provide insight into late-magmatic and subsolidus evolutionary processes in granitic pegmatites and the geochemical behaviour of Rb and Cs. Previous to this study, recognition of the largely isochemical reactions in K-feldspar were restricted to cases in which late generations had a colour distinct from that of the original phase, or where there was an obvious change in texture either in hand specimen or thin section (*e.g.*, Černý & Macek 1972, 1974). Otherwise, replacement of primary feldspar by later generations of feldspar is largely inconspicuous, but locally comprises a significant proportion of the alkali budget of pegmatite bodies (Černý 1994). Development of a microporous structure has recently been shown to be an important textural indicator of deuteric alteration (Walker *et al.* 1995). This thesis shows that multiple generations of K-feldspar may be recognized by BSE imaging if the original phase contains significant Rb. The relative timing of alkali-feldspar reaction events may then be correlated with the well-established sequence of alteration of pollucite (Teertstra *et al.* 1993, Teertstra & Černý 1995), and bracketed between the pegmatite solidus and the latest low-temperature hydrothermal fluids precipitating adularia.

CHAPTER 3

ACCURACY AND PRECISION IN THE CHARACTERIZATION OF ELECTRON-MICROPROBE REFERENCE STANDARDS

This work was initiated in 1992 as an electron-microprobe survey of compositionally heterogeneous Rb-rich K-feldspars. The emphasis was on obtaining accurate concentrations of Rb in unknown feldspars using a slightly inhomogeneous rubidian microcline standard from Red Cross Lake (RCL). The RCL microcline was characterized by bulk-chemical methods (Černý *et al.* 1985), and analysis of Rb contents of unknown (K,Rb)-feldspar samples relied exclusively on this standard. In the analytical procedure, the major elements K, Al and Si were measured using an orthoclase standard (2ORTHO). I found that both of these standards gave poor results and thus required re-examination.

3.1 *Collection and treatment of data*

Feldspar compositions were determined using wavelength-dispersive (WDS) X-ray analysis on a CAMECA SX-50 electron microprobe (EMP) operating at 15 kV and 20 nA with a beam diameter of 5 μm. Each element was analysed using the standards listed in Table 3.1. Na and Ca were collected first in order to minimize the effects of diffusion of elements out of (or into) the analysed volume. The "PAP" (phi-rho-Z) data-reduction procedure of Pouchou & Pichoir (1985) was applied. In order to minimize potential error arising from matrix effects, feldspar standards (RCL and 2ORTHO) were used to analyse unknown feldspars.

Table 3.1: Collection of initial feldspar electron-microprobe data.

Standard	Element, line		Time (s)	Detection limit (wt.%)	
orthoclase	K	*Kα*	20	K_2O	0.036
(2ORTHO)	Al	*Kα*	20	Al_2O_3	0.045
	Si	*Kα*	20	SiO_2	0.060
Amelia albite	Na	*Kα*	20	Na_2O	0.049
anorthite	Ca	*Kα*	20	CaO	0.025
RCL microcline	Rb	*Lα*	20	Rb_2O	0.087
almandine	Fe	*Kα*	60	Fe_2O_3	0.086
pollucite	Cs	*Lα*	60	Cs_2O	0.032
$SrTiO_3$	Sr	*Lα*	60	SrO	0.059
	Ti	*Kα*	60	TiO_2	0.057
riebeckite	F	*Kα*	120	F	0.069
VP_2O_7	P	*Kα*	60	P_2O_5	0.073
sanidine	Ba	*Lβ*	60	BaO	0.087
pyrope	Mg	*Kα*	60	MgO	0.010
$GdGaO_3$	Ga	*Kα*	60	Ga_2O_3	0.031
spessartine	Mn	*Kα*	120	MnO	0.025
PbTe	Pb	*Mα*	60	PbO	0.041

Notes: Limits of detection were calculated using L.D. = $[3(\text{wt.\% oxide})(R_b/t_b)^{1/2}]/(R_p-R_b)$ where R_b = background count rate (counts/s), t_b = background count time (s), R_p = peak count rate.

The quality of analytical results can be assessed before calculation of the formula using the following criteria:

(1) Σ wt.% oxides = 100 ($\pm$ x). A survey of the literature suggested that all the known major and minor substituent elements in feldspars were part of the analytical program of Table 3.1. Feldspars are essentially anhydrous with H_2O contents of less than 0.1 wt.% (Beran 1986). Light-element substitutions, despite being known in certain species of feldspar, occur in restricted environments and are not reported to be widespread. Their presence may be indicated by anomalies in charge balance more so than by deviations from 100 in the wt.% oxide totals. Charge build-up affects both the standards and unknowns to varying degree, and may be due to inadequate carbon-coating. This is recognized by instability in BSE or SE images, low specimen current, and by low counts for each element analysed. Oxide totals are low in these cases, but formulae are stoichiometric. If anomalous results are due to poor conduction, this may be tested by re-coating of the sample, followed by re-analysis.

(2) **Electroneutrality.** The negative charge generated by the feldspar framework (TO_2^-) is ideally balanced by the positive charge of the non-framework alkali cations (M^+). Most formula calculations of Fe-bearing feldspar indicate that Fe is trivalent and substitutes into the framework. This is the case for the 2ORTHO orthoclase standard, simplified as $(Na_{0.1}K_{0.9})(Fe_{0.1}Al_{0.9}Si_3)O_8$, in which the sum of the M-cation charges (M^+ = Na+K) per formula unit equals the sum of the charges generated by the framework (TO_2^- = Al+Fe^{3+}).

3) Si/Al ratio. If the framework contains only Al, Si and O, and monovalent alkali cations fill the *M* site ($\Sigma M = 1.0$), the maximum Si/Al ratio is 3.0. Minor trivalent Fe may be included with Al so that Si/(Al+Fe^{3+}) equals 3.0 for Or_{100} ($An_{0.0}$). The plagioclase solid-solution from $NaAlSi_3O_8$ to $CaAl_2Si_2O_8$ has a coupled substitution $Ca^{2+} + Al^{3+} = Na^{+} + Si^{4+}$ such that Si/Al ratios vary from 3 in albite to 1 in anorthite. A plagioclase-like substitution is one in which divalent *M*-cations plus trivalent *T*-cations substitute for monovalent *M*-cations plus tetravalent *T*-cations. The only exceptions to this are feldspars from high-temperature environments which may have excess Si along with *M*-site vacancy (*e.g.*, Linthout & Lustenhouwer 1993, Kuehner & Joswiak 1996). Synthetic feldspar has been prepared with non-tetrahedral trivalent cations, but this substitution is not known in natural feldspar (Kneip & Liebau 1994).

In the present study, BSE imaging and EMP analysis indicate that many K-feldspars of rare-element granitic pegmatites, particularly those associated with pollucite, have unusual compositions compared to typical granitic K-feldspars. A reconnaissance survey, involving analysis of several hundred samples (using the 2ORTHO and RCL standards), indicated a wide range of composition. If the quality of an individual analysis is assessed using the criteria given above, most of the results would be classified as "good". The data examined as a whole showed oxide totals near 100 (±2) wt.%. The charge of the *M* cations was typically balanced by Al (most have negligible Fe), but a systematic trend of low Si/Al ratio was noticed in a large proportion of the results. Formula calculations gave poor stoichiometry. Therefore, the reference standards required careful re-examination for accuracy. The analytical precision also needed to be established.

The calculation of a stoichiometric chemical formula from wt.% oxides is based upon the stoichiometry indicated by the crystal structure. In the feldspar structure, *T* cations are in tetrahedral coordination with oxygen atoms, and each oxygen is shared by two tetrahedra to form a framework with *M* cations in the interstices. The general formula conforming to this structure is MT_4O_8. After atomic proportions are calculated from wt.% oxides, the cations are assigned a valence, oxygen is calculated by charge balance, and the formula is normalized on the basis of 8 atoms of oxygen per formula unit. The formula may also be normalized on the basis of 4 *T* cations. The results are then compared to the stoichiometric requirements of maximum site occupancy, and balance of the (+) charge of *M*-cations with the (-) charge of the framework. Any particular analytical result is judged poor if it does not conform to the model formula within error of measurement. If a statistically anomalous result is not caused by experimental difficulties, it may represent a real variation in chemical composition (Dollase & Newman 1984).

3.2 *Errors in accuracy of the standards*

The supplied compositions (hereafter the "book value") of the reference standards 2ORTHO, 2ALBITE and RCL microcline are given in Table 3.2. The quoted analytical precision (1 standard deviation in brackets) was measured from (N) duplicate analyses distributed over the entire exposed surface. The formula calculations show that, in 2ORTHO, even though both the *M* and *T* sites are fully occupied, values of Si > 3.0 apfu and (Al + Fe) < 1.0 *apfu* (atoms per formula unit) indicate poor stoichiometry (Table 3.2). In comparison, the 2ALBITE

Table 3.2: Supplied compositions, analytical precision and formulae of EMP standards.

orthoclase - 2ORTHO (N=12)

oxide (wt.%)		formula (apfu)			
SiO_2	64.80 (31)	Si	3.010 (6)	ΣM	0.998 (5)
Al_2O_3	16.72 (6)	Al	0.916 (5)	M^+	0.999 (5)
Fe_2O_3	2.08 (7)	Fe	0.070 (3)	TO_2^-	0.986 (6)
Na_2O	0.91 (2)	Na	0.081 (2)	ΣT	3.996 (1)
K_2O	15.48 (7)	K	0.917 (4)	Si/Al	3.05 (3)
sum	100.00	O	8		

Amelia albite - 2ALBITE (N=17)

oxide (wt.%)		formula (apfu)			
SiO_2	68.16 (31)	Si	2.981 (8)	ΣM	1.003 (19)
Al_2O_3	19.76 (1)	Al	1.019 (7)	M^+	1.020 (19)
Na_2O	11.46 (11)	Na	0.972 (11)	TO_2^-	1.019 (7)
K_2O	0.22 (3)	K	0.013 (19)	ΣT	4.000 (5)
CaO	0.22 (9)	Ca	0.018 (4)	Si/Al	2.93 (2)
sum	100.00	O	8		

RCL microcline* - 3RBMICRO (N=10)

oxide (wt.%)		formula (apfu)			
SiO_2	63.87 (33)	Si	2.763 (6)	ΣM	0.912 (6)
Al_2O_3	17.53 (8)	Al	0.904 (6)	M^+	0.912 (6)
Fe_2O_3	0.09 (3)	Fe	0.003 (1)	TO_2^-	0.907 (6)
Li_2O	0.11	Li	0.019	ΣT	3.669 (1)
Na_2O	0.40 (4)	Na	0.034 (3)	Si/Al	3.047 (19)
K_2O	10.19 (19)	K	0.685 (11)		
Rb_2O	5.87 (38)	Rb	0.165 (12)	%Rbf	16.5
Cs_2O	0.48 (38)	Cs	0.009 (1)		
sum	100.00	O	8		

* RC-10B of Černý *et al.* (1985)

(Amelia albite) formula is closer to ideal. The RCL microcline formula has equal values of M^+ and TO_2^-, but with (Al + Fe) < 1.0 *apfu* and a ΣT value considerably less than 4.0.

Any compositional inaccuracy of a reference standard is transferred to the unknowns. The scope of the analytical problems, qualitatively noted in the reconnaissance survey, is demonstrated by quantitative analysis of the well-characterized gem-sanidine megacrysts from the Volkesfeld area in the Eifel region (Behrens & Müller 1995, Hovis 1988, Beran 1986, Bernotat-Wulf *et al.* 1988 and references therein) and microcline perthite (Royal Ontario Museum samples; Sherriff & Hartman 1985). The samples were analysed using K, Al and Si from 2ORTHO, Na from 2ALBITE, and Rb from RCL microcline (Table 3.1). The ROM microclines are perthitic but otherwise inclusion-free, semi-translucent and colourless. They are end-member alkali-feldspars in that they contain only minor-to-trace quantities of divalent cations; elements sought but not detected are Ca, Fe, Cs, Sr, Ti, F, P, Mg, Mn and Pb. The ROM feldspars have a distinct range of Na/K contents, so the analytical results were not averaged. In contrast, the inclusion-free Eifel sanidine is compositionally homogeneous and a meaningful average can be reported. The formula is complicated with respect to an ideal end-member alkali feldspar in that it contains Fe and Ba.

Several systematic trends are noted in the analytical results presented in Table 3.3. The oxide sums tend to exceed 100 wt.%. The formulae have $M^+ < TO_2^-$, with a mean (Al+Fe) value of 1.031 *apfu*. The mean ΣM value is 1.004, and the mean ΣT value is 4.005 *apfu*. Even taking into account correction for decreased

Table 3.3: Results of analysis (wt.%) and formula calculations (*apfu*) of ROM and Eifel feldspars using the analytical conditions of Table 3.1 and the reference standards of Table 3.2.

oxide	M36144	M36145	M36146	M36148	M36150	Eifel
SiO_2	65.20	65.29	65.71	64.94	65.02	64.70
Al_2O_3	19.13	18.97	19.14	19.23	19.02	19.40
Fe_2O_3	0.00	0.03	0.04	0.08	0.03	0.18
Na_2O	0.82	0.71	0.67	0.94	0.80	2.87
K_2O	15.84	16.13	15.69	15.69	16.13	12.44
Rb_2O	0.00	0.00	0.19	0.00	0.03	0.00
SrO	0.04	0.00	0.00	0.05	0.00	0.13
BaO	0.16	0.10	0.00	0.22	0.00	1.25
sum	101.26	101.40	101.92	101.25	101.04	100.97
Si	2.977	2.982	2.981	2.971	2.977	2.955
Al	1.030	1.021	1.023	1.037	1.026	1.044
Fe	0.000	0.000	0.000	0.000	0.000	0.006
Na	0.073	0.063	0.059	0.083	0.071	0.254
K	0.923	0.940	0.943	0.916	0.942	0.724
Rb	0.000	0.000	0.006	0.000	0.001	0.000
Sr	0.000	0.000	0.000	0.000	0.000	0.003
Ba	0.003	0.002	0.000	0.004	0.000	0.022
ΣM	0.999	1.005	1.008	0.993	1.014	1.004
M^+	1.002	1.007	1.008	0.997	1.014	1.030
ΣT	4.007	4.003	4.004	4.008	4.003	4.005
Si/Al	2.89	2.92	2.91	2.86	2.90	2.95

ROM microcline perthite localities:
M36144 Conger Twp., Parry Sound, Ontario
M36145 Hungry Lake Mine, Chapton Twp., Parry Sound
M36146 Brignal Mine, Conger Twp., Parry Sound
M36148 Ryerson Twp., Parry Sound
M36150 Lount Twp., Parry Sound

Si/Al ratio due to slightly increased An content (according to $CaAl(NaSi)_{-1}$ substitution), the measured Si contents are less than expected. In contrast, the 2ORTHO book value shows an anomalous composition with Si > 3.0 *apfu* and Si/Al ratio > 3.0 (Table 3.2). Discrepancies concerning 2ORTHO are also shown if it is analysed using Al and Si from 2ALBITE: the 2ORTHO totals are usually lower, only about 99.5 wt.%. As the high Si/Al ratio of 2ORTHO generates a low Si/Al ratio for the ROM feldspars, it was not clear how to model the composition of 2ORTHO without generating systematic deviations from the ideal formula.

The above results exemplify some analytical problems of the present standards:
(1) Al and Fe values do not generally agree in cross-analysis of standards, be they of similar or very different matrix;
(2) Si values do not tend to agree on cross-analysis of standards of different matrix (*e.g.*, Si in fayalite *vs.* Si in albite);
(3) for some elements significant to feldspars (K, Na, Rb, Cs, Sr, Ba), only one standard is available and accuracy cannot be assessed by cross-analysis.

3.3 *Characterization of standards*

The main requirement for an EMP standard is chemical homogeneity. This is more important than knowledge of the true chemical composition, because this can always be improved, whereas inhomogeneity cannot. All the major elements in the standard must be restricted to a small wt.% range. For example, in the compound $(X,Y)SiO_4$ if X and Y have different atomic weights, then variation in

X/Y ratio will change the wt.% SiO_2.

The most easily-defined and trustworthy standards are those with fixed stoichiometry and a limited range of solid solution. End-members of series are useful because a reduced number of components simplifies the formula. Gem materials are preferred because optical clarity generally ensures freedom from inclusions and from fine-scale alteration. EMP methods have improved accuracy over bulk-chemical methods, in part because inclusions larger than about 1 μm may be avoided. The intent of this work is to produce stoichiometric standards which give a consistent data-set on cross-analysis with other standards. Results from EMP analysis should agree with results from other chemical-analytical methods and from crystal-structure refinement.

3.3a *Scapolite*

The general formula of scapolite is $M_4T_{12}O_{24}A$ where M = Na, Ca and K, T = Al and Si and A = Cl, CO_3 and SO_4. A continuous solid-solution extends between the end-members marialite $Na_4Al_3Si_9O_{24}Cl$ and meionite $Ca_4Al_6Si_6O_{24}CO_3$ (Teertstra & Sherriff 1996). Compositions of 20 samples were measured using a CAMECA SX-50 electron microprobe (EMP) operating at 15 kV and 20 nA with a beam diameter of 10 μm. A summary of the analytical conditions is given in Table 3.4. The principal reference standards are a gem-quality meionite from Brazil (USNM R6600-1, Dunn *et al.* 1978, Jarosewich *et al.* 1979), albite from the Amelia pegmatite, Virginia (Harlow & Brown 1980 and references therein),

Table 3.4: Collection of scapolite electron-microprobe data.

Standard	Element, line		Time (s)	Detection limit (wt.%)	
Amelia albite	Na	*Kα*	20	Na_2O	0.049
	Si	*Kα*	20	SiO_2	0.060
scapolite	Al	*Kα*	20	Al_2O_3	0.045
anorthite	Ca	*Kα*	20	CaO	0.025
orthoclase	K	*Kα*	20	K_2O	0.036
tugtupite	Cl	*Kα*	20	Cl	0.014
anhydrite	S	*Kα*	20	SO_3	0.050
almandine	Fe	*Kα*	60	Fe_2O_3	0.086
$SrTiO_3$	Sr	*Lα*	60	SrO	0.059
	Ti	*Kα*	80	TiO_2	0.057
riebeckite	F	*Kα*	120	F	0.069
VP_2O_7	P	*Kα*	60	P_2O_5	0.073
sanidine	Ba	*Lβ*	80	BaO	0.087
pyrope	Mg	*Kα*	80	MgO	0.010
spessartine	Mn	*Kα*	120	MnO	0.025
PbTe	Pb	*Mα*	60	PbO	0.041

Notes: Limits of detection were calculated using L.D. = $[3(\text{wt.\% oxide})(R_b/t_b)^{1/2}]/(R_p-R_b)$ where R_b = background count rate (counts/s), t_b = background count time (s), R_p = peak count rate.

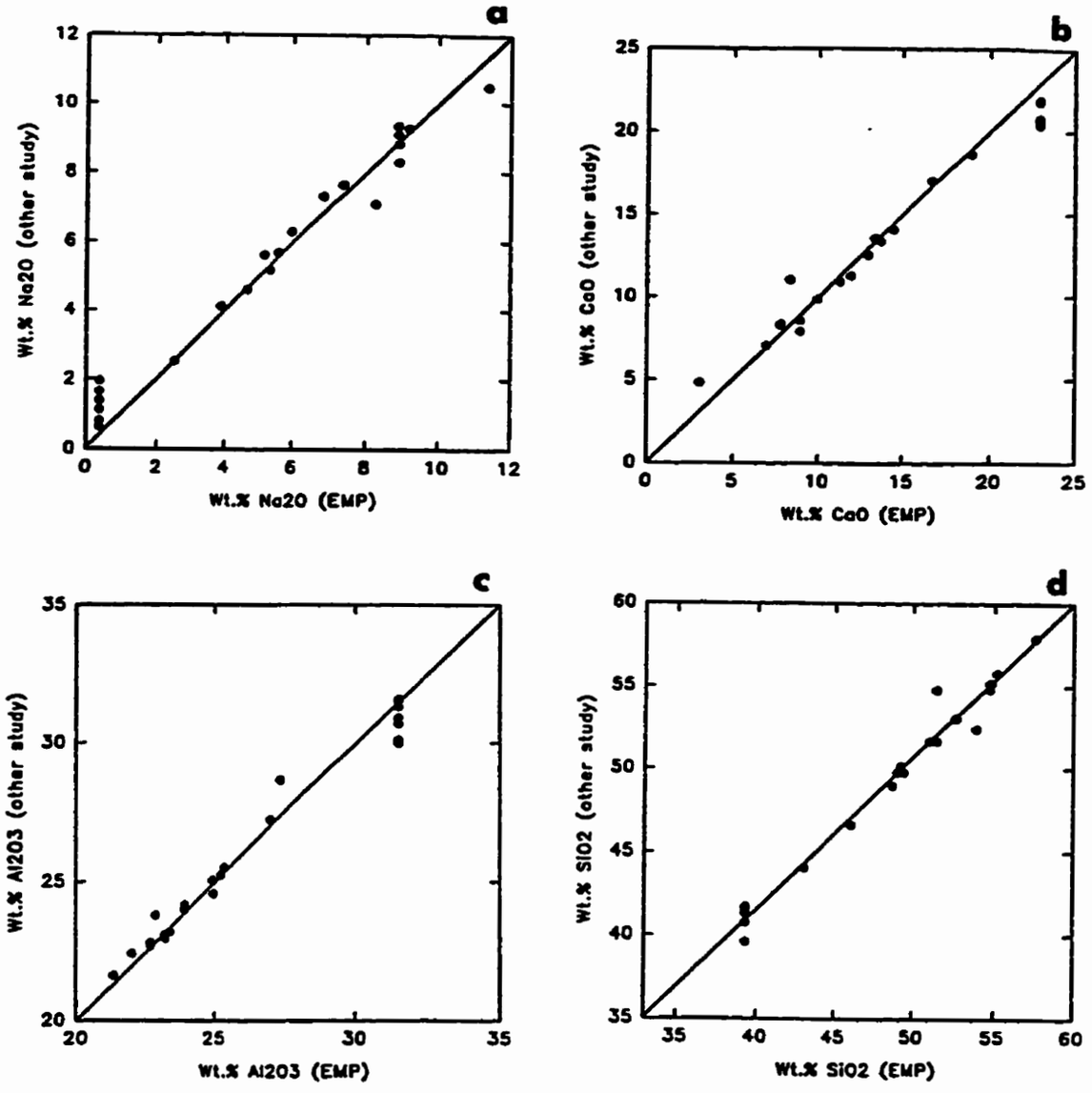

Fig. 3.1. (a to d): wt.% oxide measurements from the literature *vs.* EMP measurements (this study) on the same samples of scapolite. The lines represent exact agreement between the two measurements.

anorthite from Great Sitkin Island (USNM 137041, Jarosewich *et al.* 1979) and tugtupite from the type locality, South Greenland (ROM # M32790, Danø 1966). The stoichiometry of the standards, as determined by chemical analysis, is rather close to that expected from the ideal formulae.

Analytical accuracy was assessed by comparison of my EMP results with the results of bulk analysis on the same 20 scapolite samples, as published in the literature. The purpose is to demonstrate a lack of systematic error for the major elements and to provide an estimate of the analytical accuracy. All but one of the samples are compositionally homogeneous (the sample richest in Ca is inhomogeneous). Two of the samples have numerous inclusions of feldspar and analcime, generating inaccurate bulk compositions. Sample descriptions and analytical results are reported elsewhere (Teertstra & Sherriff 1997). Across the series from marialite to meionite (with a compositional range similar to that of the albite-anorthite series), Na, Ca, Al and Si values from this study agree well with the compositions determined by wet-chemical analysis. Compared to a line representing perfect agreement between the two measurements, 90% of the data fall within $\pm$ 0.7% (absolute) for Na_2O, $\pm$ 1.2% for CaO, $\pm$ 0.7% for Al_2O_3, and $\pm$ 1.4% for SiO_2 (Fig. 3.1).

3.3b *Tugtupite*

Analysis of tugtupite from the type locality, South Greenland (ROM # M32790, Danø 1966) using the Table 3.4 program, shows a composition that is close to that expected by the ideal formula $Na_8Al_2Be_2Si_8O_{24}Cl_2$ (Table 3.5). Analysis and

Table 3.5: Results of analysis (wt.%) of tugtupite using the Table 3.4 reference standards.

standard-block 1 tugtupite			
oxide	ideal	meas.(N=10)	deviation
SiO_2	51.38	52.72 (44)	+2.6% from 2ALBITE
Al_2O_3	10.90	11.17 (7)	+2.5% from SCAPOL
Na_2O	26.50	25.89 (16)	-2.3% from 2ALBITE
Cl	7.58	7.66 (9)	+1.1% from 4TUGTUP
BeO	5.35	----	
sum	101.71		
O=Cl	1.71		
	100.00		

standard-block 4 tugtupite			
oxide	ideal	meas.(N=6)	deviation
SiO_2	51.38	51.80 (26)	+0.8% from 2ALBITE
Al_2O_3	10.90	11.12 (8)	+2.0% from SCAPOL
Na_2O	26.50	25.89 (26)	-2.3% from 2ALBITE
Cl	7.58	7.68 (6)	+1.1% from 4TUGTUP
BeO	5.35	----	
sum	101.71		
O=Cl	1.71		
	100.00		

Table 3.6: Collection of electron-microprobe data using ideal-formula tugtupite as the main standard.

Standard	Element, line		Time (s)	Detection limit (wt.%)	
tugtupite	Na	*Kα*	20	Na_2O	0.049
	Al	*Kα*	20	Al_2O_3	0.045
	Si	*Kα*	20	SiO_2	0.060
	Cl	*Kα*	20	Cl	0.014
anorthite	Ca	*Kα*	20	CaO	0.025
orthoclase	K	*Kα*	20	K_2O	0.036
almandine	Fe	*Kα*	60	Fe_2O_3	0.086
$SrTiO_3$	Sr	*Lα*	60	SrO	0.059
	Ti	*Kα*	80	TiO_2	0.057
riebeckite	F	*Kα*	120	F	0.069
VP_2O_7	P	*Kα*	60	P_2O_5	0.073
sanidine	Ba	*Lβ*	80	BaO	0.087
pyrope	Mg	*Kα*	80	MgO	0.010
spessartine	Mn	*Kα*	120	MnO	0.025
PbTe	Pb	*Mα*	60	PbO	0.041

Notes: Limits of detection were calculated using L.D. = $[3(\text{wt.\% oxide})(R_b/t_b)^{1/2}]/(R_p-R_b)$ where R_b = background count rate (counts/s), t_b = background count time (s), R_p = peak count rate.

wavelength scans showed no additional minor elements. Cross-analysis with 4TUGTUP shows that it is compositionally identical to 1TUGTUP within experimental error. Crystal-structure refinement (Hassan & Grundy 1991) and NMR spectroscopy (Xu & Sherriff 1994) show that this sample is extremely well-ordered. Because of the crystallographic constraints on the compositional range, this may be our most accurately known standard.

The formula was fixed at ideal stoichiometry and 1TUGTUP was used as a standard (Table 3.6) for the analysis of Na, Al, Si and Cl in Amelia albite, orthoclase, Sitkin anorthite, Vesuvius leucite, jadeite and Eifel sanidine. The results are summarized in Tables 3.7a and 3.7b.

Analysis of Amelia albite reproduces the book values within experimental error and gives a well-balanced formula. The *M* site-occupancy is 1.005, suggesting that absolute content of Na in albite is correct.

Analysis of orthoclase (2ORTHO) also confirms the book values (Table 3.2), suggesting good accuracy for the wt.% oxide values of the major elements, but confirming aspects of the poor stoichiometry. Formula calculations indicate low values of (Al+Fe), with values for both Si *apfu* and Si/(Al+Fe) being greater than 3.0. Values of TO_2^- = (Al+Fe) of 0.960 *pfu* do not correspond well with the *M*-cation charge (M^+) of 0.992 *pfu*; however, K was not measured using an independent standard. 2ORTHO might have $\square Si_4O_8$ substitution (Ch. 3.7).

Analysis of Sitkin anorthite gives a well-balanced stoichiometric formula, despite

Table 3.7a: Results of analysis (wt.%) and formula calculation using the Table 3.6 reference standards.

Amelia albite (2ALBITE)

oxide	book	meas.(N=3)	formula (*apfu*)			
SiO_2	68.16	67.97 (31)	Si	2.976	ΣM	1.005
Al_2O_3	19.76	19.85 (1)	Al	1.024	M^+	1.024
Na_2O	11.46	11.51 (11)	Na	0.972	TO_2^-	1.019
K_2O	0.22	0.15 (3)	K	0.013	ΣT	4.000
CaO	0.22	0.38 (9)	Ca	0.018	Si/Al	2.91
sum	100.00	99.86	O	8		

orthoclase (2ORTHO)

oxide	book	meas.(N=3)	formula (*apfu*)			
SiO_2	64.80	64.95 (31)	Si	3.032	ΣM	0.992
Al_2O_3	16.72	16.31 (6)	Al	0.897	M^+	0.992
Fe_2O_3	2.08	1.86 (7)	Fe	0.063	TO_2^-	0.960
Na_2O	0.91	0.93 (2)	Na	0.084	ΣT	3.992
K_2O	15.48	15.24 (7)	K	0.908	Si/Al	3.158
sum	100.00	99.29	O	8		

Sitkin anorthite (15ANORTH)

oxide	book	meas.(N=3)	formula (*apfu*)			
SiO_2	43.84	43.64 (42)	Si	2.051	ΣM	1.000
Al_2O_3	35.90	34.88 (9)	Al	1.932	M^+	1.951
Fe_2O_3	0.72	0.49 (2)	Fe	0.017	TO_2^-	1.949
Na_2O	0.53	0.53 (1)	Na	0.048	ΣT	4.000
CaO	19.02	18.91 (3)	Ca	0.952	Si/Al	1.052
sum	100.00	98.45	O	8		

Table 3.7b: Results of analysis (wt.%) and formula calculation using the Table 3.6 reference standards.

Vesuvius leucite (1LEUC)

oxide	ideal	meas.(N=12)	formula (*apfu*)			
SiO_2	55.37	55.52 (32)	Si	2.016	ΣM	0.996
Al_2O_3	23.37	22.67 (6)	Al	0.970	TO_2^-	0.977
Fe_2O_3	0.19	0.26 (14)	Fe	0.007	Si	2.016
K_2O	19.85	19.69 (16)	K	0.912	ΣT	3.040
Na_2O	1.22	1.19 (16)	Na	0.084	Si/Al	2.06
sum	100.00	99.53	O	6		

jadeite (1JADE)

oxide	ideal	meas.(N=10)	formula (*apfu*)			
SiO_2	59.39	60.40 (23)	Si	2.002	M^+	0.998
Al_2O_3	25.02	25.33 (25)	Al	0.990	TO_2^-	0.997
Fe_2O_3	0.28	0.29 (17)	Fe	0.007	ΣT	2.999
Na_2O	15.31	15.53 (13)	Na	0.998	Si/Al	2.007
sum	100.00	101.55	O	6		

Eifel sanidine

oxide	meas.(N=12)	formula (*apfu*)				
SiO_2	64.48 (17)	Si	2.976 (5)	ΣM	1.009 (4)	
Al_2O_3	18.67 (3)	Al	1.015 (6)	M^+	1.035 (6)	
Fe_2O_3	0.17 (17)	Fe	0.006 (1)	TO_2^-	1.021 (6)	
Na_2O	2.88 (7)	Na	0.258 (5)	ΣT	3.997 (2)	
K_2O	12.33 (7)	K	0.726 (4)	An	2.6 (3)	
BaO	1.15 (13)	Ba	0.020 (2)	Si/Al	2.915 (23)	
SrO	0.15 (4)	Sr	0.004 (1)			
sum	99.84	O	8			

low wt.% values for Al_2O_3 compared to the book values (Table 3.7a). It is possible that the measured Al_2O_3 contents are slightly inaccurate because of the considerable extrapolation from the low-Al content of tugtupite to the high-Al content of anorthite, but this is not indicated by the formula.

3.3c *Leucite, jadeite and kyanite*

Analysis of Vesuvius leucite ($KAlSi_2O_6$) using K from 2ORTHO (the Table 3.6 program) gives an (Na+K) value close to that of (Al+Fe) (Table 3.7b). This indicates a close approach to an ideal formula in which the *M* site is filled (ΣM = 0.996 *apfu*), and suggests that the measured K value is accurate. Si/Al ratios slightly exceed 2.0, but these are known to vary in natural specimens (this may be related to a high degree of (Al,Si)-disorder of leucite; Phillips & Kirkpatrick 1994, Teertstra *et al.* 1994). In order to use this leucite as a standard, it was necessary to adjust the composition to closer agreement with the ideal formula. To accomplish this, determinations of Na were assumed accurate and K was calculated as (1 - Na) *apfu*, thus increasing the content of K by 0.004 *apfu* (*i.e.*, the ideal value is extremely close to the measured value, so the difference is assumed due to minor analytical error). The measured Fe content (0.007 *apfu*) was assumed to be accurate and Al was calculated as (1 - Fe) *apfu*. The ideal formula of this sample is therefore $(Na_{0.085}K_{0.915})(Fe_{0.007}Al_{0.993})Si_2O_6$.

Analysis of jadeite gives an Na content of 0.998 *apfu*, perfectly balanced with measurements of (Al+Fe). Si/Al ratios of 2.007 are in close agreement with the ideal formula $NaAlSi_2O_6$. The site filling suggests that accurate values were

obtained for all major components. The best formula for this sample is $Na(Fe_{0.007}Al_{0.993})Si_2O_6$.

Analysis of kyanite (11KYAN) gave 62.47 Al_2O_3, 0.12 Fe_2O_3 and 37.35 SiO_2, sum 100.06 wt.%, and an (Al+Fe)/Si ratio of 1.97, in close agreement with the ideal formula Al_2SiO_5.

3.3d *Eifel sanidine and (K,Rb)-feldspar*

Analysis of Eifel sanidine using the tugtupite standard (Table 3.6) produced a near-stoichiometric formula (Table 3.7b). Amelia albite and tugtupite have stoichiometrically ideal formulae and cross-analyse within error; when used as standards to characterize leucite and jadeite, they give near-ideal formulae for the latter. Hence, the K, Na, Al and Si contents of any of these standards may be used to characterize the Eifel sanidine. The principal standards chosen were tugtupite (Na, Si), leucite (K, Al) and barite (Ba). In order to analyse Rb-bearing feldspars (including the RCL microcline), a Rb-rich standard was required. A rubidium-zinc-silicate glass, prepared for synthesis of analogues of leucite composition $Rb_2ZnSi_5O_{12}$ with 30.06 wt.% Rb was used (Kohn *et al.* 1994). A beam-size of 20-25 μm (at 15 kV, 20 nA) was sufficient to give stable Rb $L\alpha$ X-ray counts over exposure times of up to 5 minutes. Cross-analysis with Rb_2ZnPO_3 glass with 30.95 wt.% Rb gave a low value of 29.60 wt.% Rb. However, loss of Rb counts seems to be a problem with this phosphate glass, even using a large beam diameter.

Analytical results for Eifel sanidine, the RCL microcline and a Rb-rich microcline vein in pollucite (from a rare-element granitic pegmatite in Kola Peninsula, Ch. 4.7) are given in Table 3.8. The RCL formula, including a Li value from bulk analysis, is greatly improved over that given in Table 3.2. The Kola formula also has reasonable stoichiometry, and the ΣM value (including 0.267 Rb *apfu*) of 1.010 *apfu* suggests that Rb measurements are reasonably accurate. In conclusion, the three compositions all have relatively good stoichiometric features, although in each the oxide, *M*, and *T* sums are slightly high.

3.4 *Analysis using the 1EIFEL standard*

Assuming all the elements present have been analysed, the Eifel sanidine may be designated as a standard, with minor modifications. K was reduced slightly by calculating the amount as K = 1-(Na+Ba+Sr) = 0.715 *apfu*, giving an M^+ charge of 1.027 *pfu*. Al was reduced slightly to Al = (M^+-Fe^{3+})= 1.021 *apfu*, with an increase in Si to correspond with full site-occupancy (ΣM =1 *apfu* and ΣT = 4 *apfu*). These minor adjustments from the measured values give a neutral formula of $(Na_{0.258}K_{0.715}Ba_{0.023}Sr_{0.004})(Fe_{0.006}Al_{1.021}Si_{2.973})O_8$.

If the adjustments to the Eifel sanidine composition are correct, analysis using this mineral as a standard should reproduce the book values and ideal formulae of the other standards (generating an internally-consistent set of alkali aluminosilicate mineral standards). This check is actually redundant, as the 1EIFEL composition was measured using these standards. A better control is analysis of the other feldspars using the adjusted 1EIFEL composition as a standard for K, Al and Si

Table 3.8: Composition (wt.%) and formulae (*apfu*) of feldspars using tugtupite (Na, Si), leucite (K, Al) and $Rb_2ZnSi_5O_{12}$ (Rb) as standards.

Eifel sanidine - 1EIFEL (N=7)

oxide (wt.%)			formula (*apfu*)				
SiO_2	64.62	(23)	Si	2.958	(5)	ΣM	1.013
Al_2O_3	19.21	(11)	Al	1.037	(6)	M^+	1.040
Fe_2O_3	0.18	(3)	Fe	0.006	(1)	TO_2^-	1.043
Na_2O	2.90	(3)	Na	0.258	(3)	ΣT	4.001
K_2O	12.48	(4)	K	0.729	(4)	Si/Al	2.84
BaO	1.27	(12)	Ba	0.023	(2)	An	2.7
SrO	0.15	(2)	Sr	0.004	(1)		
sum	100.81		O	8			

Kola rubidian microcline (N=4)

oxide (wt.%)			formula (*apfu*)				
SiO_2	60.77	(37)	Si	2.937	(4)	ΣM	1.010
Al_2O_3	18.30	(8)	Al	1.042	(5)	M^+	1.014
P_2O_5	0.53	(3)	P	0.022	(1)	TO_2^-	1.021
Na_2O	0.30	(11)	Na	0.029	(4)	ΣT	4.002
K_2O	11.27	(21)	K	0.695	(11)	%Rbf	26.7
Rb_2O	8.60	(27)	Rb	0.267	(9)	Si/Al	2.93
Cs_2O	0.73	(5)	Cs	0.015	(1)		
SrO	0.11	(5)	Sr	0.003	(1)		
sum	100.31		O	8			

RCL microcline - 3RBMICRO (N=10)

oxide (wt.%)			formula (*apfu*)				
SiO_2	62.29	(33)	Si	2.955	(6)	ΣM	1.003
Al_2O_3	18.51	(8)	Al	1.035	(6)	M+Li	1.022
P_2O_5	0.35	(3)	P	0.014	(1)	TO_2^-	1.021
Li_2O	0.11		Li	0.019		ΣT	4.005
Na_2O	0.25	(4)	Na	0.023	(3)	An	0.0
K_2O	13.57	(19)	K	0.821	(11)	%Rbf	15.1
Rb_2O	4.96	(38)	Rb	0.151	(12)		
Cs_2O	0.38	(38)	Cs	0.008	(1)		
sum	100.17		O	8			

(Table 3.9 shows the analytical program).

The results of analysis of the ROM feldspars (Table 3.10) show great improvement over results using the 2ORTHO standard (compare Table 3.3) The oxide sums average 100.1 ± 0.3 wt.%. Si contents *pfu* seem slightly low and Al may be slightly high: this results in Si/Al ratios less than 3.0, even in samples free from divalent cations. The mean ΣM value of 0.985 *apfu* is less than the ideal 1.0, and the mean M^+ value of 0.990 is slightly less than the mean Al content of 1.007 *apfu*.

The composition of 1EIFEL was again slightly modified. To start, K was increased by 0.01 *apfu* to give a ΣM value of 0.995 *apfu* and returning it closer to the composition measured relative to leucite (Table 3.8). Na was calculated as 1 - (K+Ba+Sr), Al as (M^+ - Fe^{3+}), and Si as 4 - (Al+Fe) [equivalent to (4 - M^+) *apfu*]. This gives the formula $(Na_{0.249}K_{0.725}Ba_{0.023}Sr_{0.003})(Fe_{0.006}Al_{1.020}Si_{2.974})O_8$. Repeat analyses of the ROM feldspars and fine-tuning of the 1EIFEL formula were iterated to agreement in three cycles (*i.e.*, optimized within the stoichiometric constraints of electroneutrality and maximum site-occupancy). The final results are given in Table 3.11. Subsequent analysis of unknown samples should be accurate within the constraints of the standards matrix. Analysis of a large number of feldspar samples should provide a test of the accuracy of 1EIFEL sanidine standard.

Table 3.9: Collection of feldspar EMP data.

Standard	Element, line		Time (s)	Detection limit (wt.%)	
Eifel sanidine	K	*Kα*	20	K_2O	0.036
	Al	*Kα*	20	Al_2O_3	0.045
	Si	*Kα*	20	SiO_2	0.060
anorthite	Ca	*Kα*	20	CaO	0.025
Amelia albite	Na	*Kα*	20	Na_2O	0.049
$Rb_2ZnSi_5O_{12}$	Rb	*Lα*	20	Rb_2O	0.014
almandine	Fe	*Kα*	60	Fe_2O_3	0.086
	Mg	*Kα*	60	MgO	0.010
pollucite	Cs	*Lα*	60	Cs_2O	0.032
$SrTiO_3$	Sr	*Lα*	60	SrO	0.059
	Ti	*Kα*	80	TiO_2	0.057
riebeckite	F	*Kα*	120	F	0.069
VP_2O_7	P	*Kα*	60	P_2O_5	0.073
barite	Ba	*Lβ*	60	BaO	0.087
spessartine	Mn	*Kα*	120	MnO	0.025
$GdGaO_3$	Ga	*Kα*	60	Ga_2O_3	0.031
PbTe	Pb	*Mα*	60	PbO	0.041

Notes: Limits of detection were calculated using L.D. = $[3(\text{wt.\% oxide})(R_b/t_b)^{1/2}]/(R_p-R_b)$ where R_b = background count rate (counts/s), t_b = background count time (s), R_p = peak count rate.

Table 3.10: Results of analysis (wt.%) and formula calculations (*apfu*) of ROM feldspars using the Table 3.9 reference standards.

oxide	M36144	M36145	M36146	M36148	M36150
SiO_2	65.16	65.04	64.83	64.76	65.08
Al_2O_3	18.49	18.45	18.48	18.59	18.51
Fe_2O_3	0.09	0.00	0.01	0.00	0.02
Na_2O	0.61	0.63	0.60	0.71	0.83
K_2O	15.54	15.84	15.72	15.61	15.56
Rb_2O	0.00	0.00	0.00	0.00	0.00
SrO	0.00	0.04	0.00	0.05	0.10
BaO	0.00	0.26	0.13	0.50	0.00
sum	99.92	100.28	99.78	100.25	100.12
Si	3.003	2.998	2.997	2.989	2.997
Al	1.004	1.002	1.007	1.012	1.005
Fe	0.003	0.000	0.000	0.000	0.000
Na	0.055	0.056	0.054	0.064	0.074
K	0.913	0.931	0.927	0.919	0.915
Rb	0.000	0.000	0.000	0.000	0.000
Sr	0.000	0.000	0.000	0.000	0.002
Ba	0.003	0.005	0.001	0.009	0.000
ΣM	0.968	0.993	0.983	0.992	0.989
M^+	0.968	0.999	0.985	1.004	0.994
ΣT	4.010	4.000	4.005	4.002	4.003
Si/Al	2.98	2.99	2.98	2.96	2.98

Table 3.11: Final lEIFEL composition (wt.%) and formula (*apfu*) giving optimized ROM feldspar results using the Table 3.9 reference standards.

oxide	M36144	M36145	M36146	M36148	M36150	EIFEL
SiO_2	64.56	64.16	64.39	63.99	64.76	64.63
Al_2O_3	18.31	18.46	18.30	18.43	18.33	18.78
Fe_2O_3	0.05	0.00	0.00	0.05	0.04	0.18
Na_2O	0.63	0.58	0.64	0.80	0.88	2.84
K_2O	15.89	15.83	15.85	15.52	15.58	12.30
SrO	0.03	0.04	0.04	0.09	0.03	0.15
BaO	0.00	0.10	0.11	0.29	0.06	1.11
sum	99.63	99.23	99.57	99.21	99.79	100
Si	2.997	2.990	2.996	2.986	2.998	2.975
Al	1.002	1.014	1.004	1.013	1.000	1.019
Fe	0.002	0.000	0.000	0.002	0.001	0.006
Na	0.057	0.053	0.058	0.073	0.079	0.254
K	0.941	0.941	0.941	0.924	0.920	0.722
Sr	0.001	0.001	0.001	0.002	0.001	0.004
Ba	0.000	0.002	0.002	0.005	0.001	0.020
ΣM	0.999	0.996	1.002	1.004	1.001	1
M^+	1.000	0.999	1.005	1.012	1.004	1.024
TO_2^-	1.003	1.014	1.004	1.015	1.001	1.025
ΣT	4.001	4.004	4.000	4.001	3.999	4
Si/Al	2.99	2.95	2.98	2.94	3.00	2.92

3.5 *Limitations of the analytical method*

The method of cross-analysis followed by adjustment of composition to the ideal formula with the purpose of improving the accuracy of standards ($\leq \pm 2\%$) has been limited so far to minerals with major elements of $Z<20$. An outstanding problem is attainment of high accuracy for standards of dissimilar matrix. The problem is exemplified by analysis of minerals in the garnet group. The general formula is $X_3Y_2Z_3O_{12}$ where X is typically Ca, Mg, Mn, Fe^{2+}, Y is Al, Fe^{3+}, Ti, Cr, V, and Z is dominantly Si. Pure end-members are rare and zoning with extensive solid solution is common. I attempted to "solve" the problem of disagreement between the compositions of garnet standards.

Trial and error has shown that the best results for analysis of unknown garnets involves using a mix of standards (*e.g.*, Si from pyrope, Al from almandine, Mn from spessartine). One would think that to analyse spessartine, a single spessartine standard could be used for all the major elements. The stored compositions of six garnet standards are given in Table 3.12. There is significant variation in values for ΣX, ΣY, and ΣZ among the standards. An analytical program was prepared to cover all the significant $Z > 8$ substitutions in garnet (Table 3.13). The choice of standards is not critical for the minor elements Na, Y, F, Sc, Zn, V, P, Sr, Zr, Cr and Sn, provided the standard has a major quantity of that element. 6GARRV752 has a good stoichiometry and was chosen as a standard for Al (1.996 *apfu*) and Si (3.000 *apfu*).

Cross-analysis of the garnets using this program gives results which disagree with

Table 3.12: Stored composition (wt.%) and formulae (*apfu*) of garnet reference standards.

oxide	2PYROPE	2SPESS	4PYROPE	4ALMANGAR	6GARRV752	6GARRV375
SiO_2	42.16	36.41	43.11	39.19	40.07	39.41
Al_2O_3	21.46	20.60	22.01	22.05	22.65	22.24
V_2O_3	0.04	----	----	----	----	----
Cr_2O_3	1.87	----	2.22	----	----	----
TiO_2	0.50	0.11	----	----	0.35	0.38
Fe_2O_3	1.14	0.00	0.00	0.00	0.00	0.00
FeO	7.32	2.47	8.17	23.27	11.30	16.21
Na_2O	0.07	----	----	----	----	----
SnO	----	0.06	----	----	----	----
MgO	20.36	----	19.11	10.70	7.15	6.53
CaO	4.44	0.06	5.07	4.20	18.08	14.36
MnO	0.35	40.31	0.32	0.59	0.19	0.59
total	99.99	100.02	100.00	100.00	99.79	99.72
Si	3.001	2.998	3.065	2.981	2.999	3.000
Al	1.800	1.999	1.844	1.977	1.998	1.996
V	0.002	-----	-----	-----	-----	-----
Cr	0.105	-----	0.125	-----	-----	-----
Ti	0.027	0.007	-----	-----	0.020	0.022
Fe^{3+}	0.061	0.000	0.000	0.000	0.000	0.000
Fe^{2+}	0.436	0.170	0.486	1.480	0.707	1.032
Na	0.010	-----	-----	-----	-----	-----
Sn	-----	0.002	-----	-----	-----	-----
Mg	2.189	-----	2.025	1.213	0.798	0.721
Ca	0.339	0.005	0.402	0.342	1.450	1.171
Mn	0.021	2.182	0.019	0.038	0.012	0.038
X	2.995	2.987	2.932	3.073	2.987	2.984
Y	1.995	2.008	1.969	1.977	1.998	1.996
Z	3.001	2.998	3.065	2.981	2.999	3.000

Table 3.13: Collection of garnet EMP data.

Standard	Element, line		Time (s)	Detection limit (wt.%)	
grossular	Si	*Kα*	20	SiO_2	0.078
(6GARRV7S2)	Al	*Kα*	20	Al_2O_3	0.030
anorthite	Ca	*Kα*	20	CaO	0.034
spessartine	Mn	*Kα*	20	MnO	0.099
Amelia albite	Na	*Kα*	20	Na_2O	0.034
fayalite	Fe	*Kα*	60	Fe_2O_3	0.092
pyrope	Mg	*Kα*	60	MgO	0.028
$SrTiO_3$	Sr	*Lα*	60	SrO	0.015
	Ti	*Kα*	80	TiO_2	0.016
riebeckite	F	*Kα*	80	F	0.12
VP_2O_7	P	*Kα*	20	P_2O_5	0.089
	V	*Kα*	20	V_2O_3	0.12
Y-Al-garnet	Y	*Kα*	20	Y_2O_3	0.087
Na-Sc-silicate	Sc	*Kα*	40	Sc_2O_3	0.099
chromite	Cr	*Kα*	20	Cr_2O_3	0.074
gahnite	Zn	*Kα*	20	ZnO	0.21
zircon	Zr	*Lα*	20	ZrO_2	0.16
cassiterite	Sn	*Lα*	20	SnO_2	0.081

Notes: Limits of detection were calculated using L.D. = $[3(\text{wt.\% oxide})(R_b/t_b)^{1/2}]/(R_p-R_b)$ where R_b = background count rate (counts/s), t_b = background count time (s), R_p = peak count rate.

the stored compositions (Table 3.14), perhaps due to one or more errors in composition. In some cases (*e.g.*, 4ALMANGAR) the analysis gave improved stoichiometry, but in other cases (*e.g.*, 2PYROPE) the stoichiometry was apparently worsened.

The program was then used to analyse minerals with simple composition (*e.g.*, albite, anorthite, diopside, fayalite), but except for Mg and Al, systematic errors still remain (Table 3.15).

The analysis was repeated, but using 2SPESS as a standard for Mn, Al and Si. For cross-analysis of garnets, the results were similar to those found above. Analysis of albite, anorthite, diopside and fayalite indicates systematically high Si values (Table 3.16).

In order to constrain the problem, rhodonite ($Mn_2Si_2O_6$) was analysed (Table 3.17). Measured Si values are higher, and Mn values lower, than the book values, but there is close agreement for the minor elements Ca, Fe and Mg. Fe was assumed to be divalent and there are no monovalent cations present. Mn was calculated by 2-(Ca+Fe+Mg) and Si was fixed at 2 *apfu*. This moves the Mn content closer to the values measured using 2SPESS. The ideal formula for this sample is $(Mn_{1.609}Ca_{0.189}Mg_{0.116}Fe_{0.092})Si_2O_6$ (Table 3.17), and this composition of rhodonite was stored for use of rhodonite as a Mn and Si standard. Analysis of garnet using the idealized-composition rhodonite did not improve the analytical results. The overall accuracy could not be improved to less than about 4-5%. In conclusion, I suspect that the analytical problems of cross-analysis of

Table 3.14: Results of analysis of garnet standards (wt.%) and formula calculations (*apfu*) using the Table 3.13 analytical program.

oxide	2PYROPE	4PYROPE	4ALMANGAR	2SPESS (N = 9)
SiO_2	42.34	42.57	39.83	36.73 (.30)
Al_2O_3	21.12	21.31	22.49	20.46 (.14)
V_2O_3	0.00	0.00	0.02	0.00
Cr_2O_3	1.89	3.88	0.00	0.00
TiO_2	0.37	0.11	0.09	0.10 (.06)
FeO	8.48	7.61	23.35	2.23 (.07)
Na_2O	0.05	0.01	0.00	0.00
SnO	0.00	0.02	0.02	0.00
MgO	20.67	20.13	10.23	0.00
CaO	4.34	4.83	4.01	0.08 (.06)
MnO	0.33	0.43	0.57	40.17 (.23)
total	99.59	100.90	100.61	99.53 (.60)
Si	3.006	2.985	3.016	3.001(9)
Al	2.004	1.993	1.781	1.992(8)
V	0.002	0.000	0.000	0.000
Cr	0.110	0.002	0.210	0.000
Ti	0.016	0.009	0.003	0.007(3)
Fe^{2+}	0.696	0.167	0.452	0.154(5)
Na	0.013	0.000	0.003	0.000
Mg	0.804	0.000	2.136	0.000
Ca	1.439	0.005	0.369	0.005(1)
Mn	0.006	2.846	0.018	2.825(56)
X	2.976	3.020	2.981	2.985(16)
Y	2.116	1.995	1.991	1.992(8)
Z	3.006	2.985	3.016	3.001(9)

Note: 2SPESS also contains 0.10 wt.% Y_2O_3 (0.002 Y apfu), 0.14 wt.% P_2O_5 (0.010 P apfu) and 0.05 SnO_2 (0.002 Sn apfu).

Table 3.15: Results of analysis (wt.%) of standards using the Table 3.13 analytical program.

2ALBITE

oxide	book	meas.	deviation
SiO_2	68.16	69.65	+2.2% from 6GARRV752
Al_2O_3	19.76	19.84	+0.4% from 6GARRV752
Na_2O	11.46	11.40	2ALBITE standard
K_2O	0.22	----	not in program
CaO	0.22	0.36	
sum	100.00	101.25	

1ANORTH

oxide	book	meas.	deviation
SiO_2	43.84	44.43	+1.3% from 6GARRV752
Al_2O_3	35.90	35.52	-1.1% from 6GARRV752
Fe_2O_3	0.72	0.62	
Na_2O	0.53	0.56	
CaO	19.02	19.00	1ANORTH standard
sum	100.00	100.13	

4DIOPSIDE

oxide	book	meas.	deviation
SiO_2	55.37	56.70	+2.4% from 6GARRV752
Al_2O_3	0.19	0.05	-1.1% from 6GARRV752
MgO	18.62	18.19	-2.3% from 2PYROPE
CaO	25.73	25.99	+1.0% from 1ANORTH
TiO_2	0.08	0.11	
MnO	0.05	0.01	
FeO	0.05	0.07	
sum	100.09	101.12	

1FAYREF

oxide	book	meas.	deviation
SiO_2	29.48	29.43	+0.2% from 6GARRV752
FeO	70.24	69.91	1FAYREF standard
MnO	0.26	0.12	
sum	99.98	99.46	

Table 3.16: Results of analysis (wt.%) of standards with 2SPESS in place of 6GARRV752 in Table 3.13 analytical program.

2ALBITE

oxide	book	meas.	deviation
SiO_2	68.16	69.59	+2.1% from 2SPESS
Al_2O_3	19.76	19.78	+0.1% from 2SPESS
Na_2O	11.46	11.46	2ALBITE standard
K_2O	0.22	----	not in program
CaO	0.22	0.26	
sum	100.00	101.09	

1ANORTH

oxide	book	meas.	deviation
SiO_2	43.84	44.92	+2.5% from 2SPESS
Al_2O_3	35.90	35.63	-0.8% from 2SPESS
Fe_2O_3	0.72	0.52	
Na_2O	0.53	0.51	
CaO	19.02	18.78	1ANORTH standard
sum	100.00	100.36	

4DIOPSIDE

oxide	book	meas.	deviation
SiO_2	55.37	57.09	+3.1% from 2SPESS
Al_2O_3	0.19	0.05	
MgO	18.62	18.30	-1.7% from 2PYROPE
CaO	25.73	25.65	-0.3% from 1ANORTH
TiO_2	0.08	0.08	
MnO	0.05	0.01	
FeO	0.05	0.02	
sum	100.09	101.20	

1FAYREF

oxide	book	meas.	deviation
SiO_2	29.48	29.84	+1.2% from 2SPESS
FeO	70.24	70.15	1FAYREF standard
MnO	0.26	0.20	
sum	99.98	100.19	

Table 3.17: Recharacterization of rhodonite (4RHODON) Mn, Si standard.

oxide	book wt.%		formula apfu		
SiO_2	46.06	Si	1.981	ΣT	1.981
MnO	46.23	Mn	1.684	ΣM	2.038
CaO	4.00	Ca	0.184		
FeO	2.44	Fe	0.088		
MgO	1.28	Mg	0.082		
sum	100.01	O	6		

oxide	meas.(N=4)		formula		
SiO_2	47.68	Si	2.013	ΣT	2.013
MnO	44.12	Mn	1.577	ΣM	1.974
CaO	4.18	Ca	0.189		
FeO	2.60	Fe	0.092		
MgO	1.85	Mg	0.116		
sum	100.43	O	6		

oxide	ideal		formula		
SiO_2	46.98	Si	2	ΣT	2
MnO	44.45	Mn	1.603	ΣM	2
CaO	4.14	Ca	0.189		
FeO	2.59	Fe	0.092		
MgO	1.82	Mg	0.116		
sum	99.98	O	6		

aluminosilicate minerals containing major elements with $Z \geq 25$ (Mn) are due to inaccurate values for the matrix-correction procedure.

3.6 *Precision of measurement of the 1EIFEL standard*

In order to study the measurement variation of a typical analytical run, the Eifel sanidine was analysed 32 consecutive times. The average measured values should equal those of the stored composition; the average values, standard deviations and compositional ranges are given in Table 3.18. The measured BaO content is somewhat variable, whereas Al_2O_3 and K_2O have a very restricted range. Variations in oxide totals of $\pm$ 0.76 wt.% are mainly due to variations in SiO_2 of $\pm$ 0.63 wt.%. In measurement of unknown feldspars, oxide totals which lie outside the range 99.24 to 100.76 are considered suspect. For the purposes of identifying anomalous results, the range of measured values may be used as the 4σ level of confidence which includes 99% of the data in a normal distribution. For SiO_2, the per-cent error calculated as 100[(65.26-64.01)/2]/64.63 is $\pm$ 0.97 wt.%, close to the 4σ value of 1.16. The precision expected in SiO_2 analysis of unknowns is approximately 1 wt.%.

In chemically-heterogeneous minerals exhibiting a range of solid solution, coupled substitutions are indicated by linear correlations between elements. Lack of such correlations is an indication of homogeneity. For the 1EIFEL standard, plots of Si *apfu vs. M* monovalent cations, and of (Al+Fe) *apfu vs. M*-cation charge, show no such trend (Fig. 3.2). This indicates that the measured variations are due to counting statistics. These variations provide a good estimate of the precision

expected in measurement of unknown feldspar.

The measured Si values have a range of 0.017 *apfu*; the precision is ± 0. 008 *apfu* (4σ). Values for ΣM and for Al *apfu* have a similar range and precision (~ ±0.01 *apfu*). Values of ΣT outside the range 3.997-4.003 may be considered anomalous, as are values of ΣM outside the range 0.99-1.01 *apfu*. In other words, substitution of more than 1 mol.% of a component such as $LiAlSi_3O_8$ may be recognized. The data of Ch. 4 represent the test of the accuracy of the standards.

Table 3.18: Results of statistical analysis of N = 32 measurements of the lEIFEL standard.

oxide	wt.% (1σ)	range (wt.%)	% error*
SiO_2	64.63 (0.29)	64.01-65.26	0.97
Al_2O_3	18.78 (0.07)	18.63-18.93	0.80
Fe_2O_3	0.18 (0.02)	0.13-0.23	28
Na_2O	2.84 (0.04)	2.76-2.93	3.0
K_2O	12.30 (0.07)	12.12-12.48	1.5
SrO	0.15 (0.04)	0.08-0.22	47
BaO	1.11 (0.14)	0.81-1.41	27
sum	99.99 (0.35)	99.24-100.76	0.76
	atoms per formula unit		
Si	2.975 (0.004)	2.967-2.984	0.29
Al	1.019 (0.004)	1.008-1.030	1.1
Fe	0.006 (0.001)	0.004-0.008	33
Na	0.254 (0.004)	0.246-0.262	3.2
K	0.722 (0.004)	0.708-0.736	1.9
Sr	0.004 (0.001)	0.002-0.006	50
Ba	0.020 (0.003)	0.014-0.026	30
O	8		
ΣM	1.000 (0.005)	0.991-1.009	0.90
M^+	1.024 (0.006)	1.012-1.038	1.3
TO_2^-	1.025 (0.005)	1.014-1.036	1.1
ΣT	4.000 (0.002)	3.997-4.003	0.08
Si/Al	2.92 (0.02)	2.88-2.96	1.4

* at the 4σ level of confidence including 99% of data.

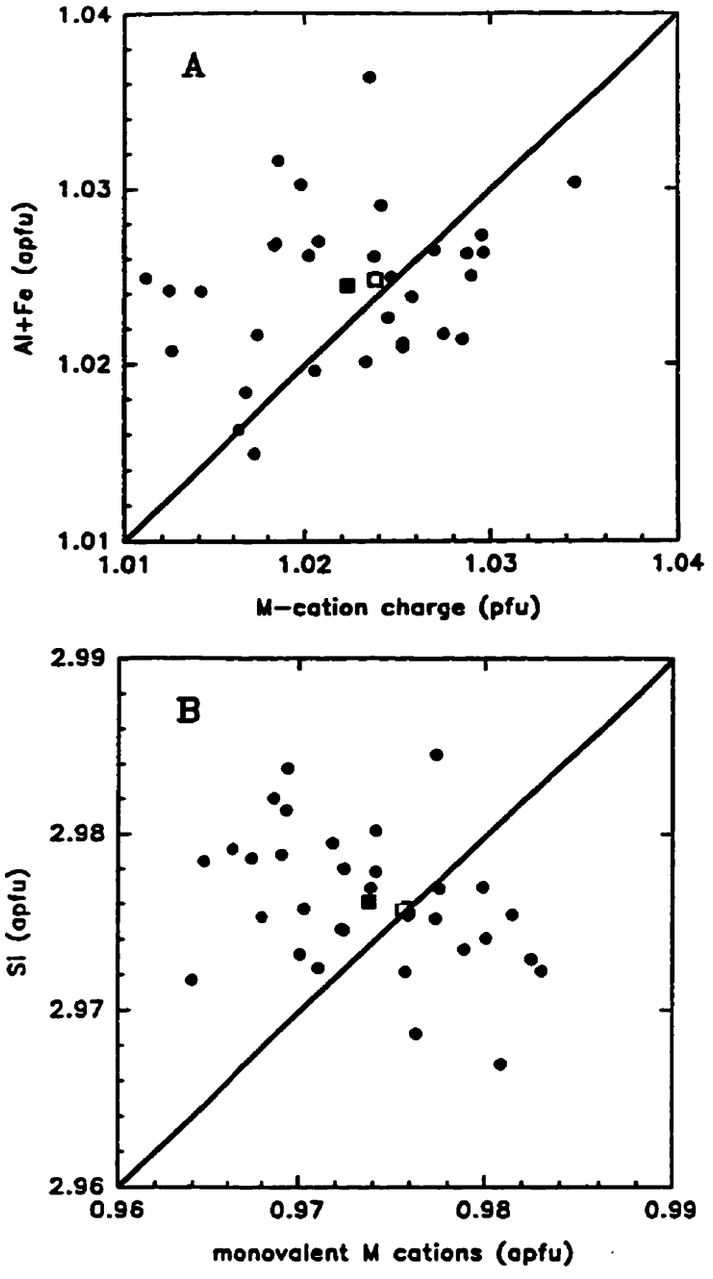

Fig. 3.2. Measurement variations for analysis of Eifel sanidine: (A) (Al+Fe) *vs.* *M*-cation charge, with a diagonal line indicating identical values of both; (B) Si *vs.* monovalent *M* cations, with a diagonal line for a plagioclase-like substitution. Symbols: measurements (•); mean value (■); and 1EIFEL ideal composition (□).

3.7 *Compositional trends for the berlinite,* $\square Si_4O_8$ *and plagioclase-type substitutions*

If the standard minerals are accurately characterized, then analysis of the compositional variations of unknown minerals should reveal the important substitution mechanisms. The analytical method must also be precise: the compositional variation which results from substitution must significantly exceed the scatter of values which result from analytical variability. In feldspar, compliance of the data with the stoichiometric constraints can be tested by a plot of the framework charge (*i.e.*, Al+Fe, or Al+Fe-P) against the *M*-cation charge (*i.e.*, Na + 2Ca). Plagioclase-like substitutions are revealed in plots of Si against the sum of the monovalent cations. If the $\square Si_4O_8$ substitution is important, it will appear as a compositional trend perpendicular to the $CaAl(NaSi)_{-1}$ vector.

An outstanding problem has been verification of the mechanism of P incorporation in alkali feldspars. Simpson (1977) synthesized $NaAl_2PSiO_8$ and KAl_2PSiO_8 with the feldspar structure and suggested that the likely charge-balance mechanism of phosphorus substitution in aluminosilicates is $(AlP)Si_{-2}$. London (1992b) suggested that there may be deviation from the berlinite ($AlPO_4$) substitution because values of P/(Al-1) (at.) deviate significantly from unity for relatively P-rich compositions. The deviations may be due to poor analytical accuracy or precision, or to operation of a substitutional mechanism other than $(AlP)Si_{-2}$ (*e.g.*, substitution of $\square Si_4O_8$). Phosphorus may participate in a variety of substitutions such as $Ca^{2+} + Si^{4+} \rightleftarrows P^{5+} + Na^+$, or the vacancy-generating substitution $Na^+ + Si^{4+} \rightleftarrows P^{5+} + \square$, both of which are related to the plagioclase substitution $Ca^{2+} + Al^{3+} \rightleftarrows Si^{4+} + Na^+$.

The data trend for one suite of P-rich granitic K-feldspars analysed by Frýda & Breiter (1995) indicate close correspondence with the berlinite substitution; however, data trends for two other suites (the Homolka and Podlesí granites) show a systematic "excess" of Si. Although complete analytical results were not presented, the accuracy of measurement was not assessed, and they did not examine correlations with *M*-cations, I interpret their data as indicating 1-2 mol.% $\square Si_4O_8$ substitution. The data of Kontak *et al.* (1996) closely follow the berlinite substitution; however, their analytical results have significantly low sums of alkali-cation charge.

The feldspars I analysed are Ca- and Fe-free, with Sr or Ba present in minor-to-negligible quantities in some of the specimens. If only monovalent cations are present, compositional trends are constrained to the origin of the plagioclase substitution. Samples analysed from the study of Pan (1988) are as follows:

(1) HAG-1 and HAG-2 intermediate-microcline perthite from the Hagendorf pegmatite, Bavaria, West Germany;

(2) PRL-1 and PRL-14 microcline perthite from the Peerless pegmatite, Black Hills, South Dakota;

(3) TM-2 microcline perthite from the Tin Mountain pegmatite, Black Hills, South Dakota.

Microcline-perthite samples analysed from the study of Tomascak (1991) are:

(1) MACRO pegmatite series- dike 10 (sample 3) from the Aylmer Lake area, Northwest Territories;

(2) GHIT pegmatite series - dike 12 (sample 1) and dike 9 (sample 5), Aylmer Lake area NWT;

(3) THON pegmatite group - dike 92 (sample 1), Thonokied Lake area, NWT.

In addition, I analysed P-rich brown microcline perthite from Cross Lake (London *et al.* 1990), and glassy overgrowths of non-perthitic orthoclase described by Jahns & Wright (1951) from the pocket zone of the White Queen Mine, Pala District, San Diego County, California. The orthoclase was also analysed by Rietveld refinement (Ch. 5.3). Similar material from the nearby Himalaya Mine, Mesa Grande district, was studied by Horsky & Martin (1977) and Prince *et al.* (1973).

The distribution of P in the K-feldspar is slightly variable on a scale of $\sim 20\ \mu m$. The range of P content is greater in areas which show well-developed microporosity. Thin lamellae of albite have equal or lower contents of P than adjacent K-feldspar, but P contents are considerably lower in coarse lath or patch albite. Small grains of apatite are common near albite (or muscovite) and in microporous areas. Representative compositions of the P-richest K-feldspar from each locality are given in Table 3.19. Average results are reported for the compositionally homogeneous White Queen orthoclase.

On average, the Al *vs.* P data closely follow a line representing 1:1 substitution (Fig. 3.3A); in detail, some of the data appear slightly Al-rich. The Si *vs.* P data closely follow a 2:1 substitution, or lie slightly above it for "excess"-Si compositions (Fig. 3.3B). On a formula basis, ΣT values including P are near 4.00 *apfu* within error. In order to clarify other compositional trends, data were then adjusted for the berlinite substitution using $TO_2^{\cdot} = (Al\text{-}P)$ and $Si_{adjusted} = (Si_{measured} - 2P)$, where 2P indicates (P + P-equivalent-to-Al). Plots of (Al-P) *vs.* *M*-cation charge and (Si+2P) *vs.* the monovalent *M* cations indicate a minor but widespread deficiency of *M*-cations required for charge balance with the

framework (Fig. 3.3C, D). A plot of P *vs.* the *M*-cation charge (Fig. 3.3E) indicates that P substitution is independent of *M*-cation substitution. Multiple analysis of the White Queen orthoclase indicates an average of 2 mol.% $\square Si_4O_8$ substitution, homogeneously distributed throughout the sample. The P-free feldspars from Tin Mountain have 0-2 mol.% $\square Si_4O_8$ and lie along trend 2 in Figure 3.3D, but $\square Si_4O_8$ is not widespread in the P-rich feldspars examined.

Average values for the P-rich feldspars (excluding only the orthoclase data) indicate close adherence to the feldspar formula: (Si+2P) = 3.002(8); TO_2 [= (Al-P)] = 1.000(9); ΣT = 4.002(2); ΣM = 0.989(8) and M^+ = 0.991(7). The variation in individual values of M^+ from 1.00 to as low as 0.98 *apfu* suggests up to 2% substitution of light-element *M* cations, with a variable distribution on a local scale. It is possible that 1-2 at.% Li^+ or H^+ is incorporated for local charge balance with the underbonded oxygen atom which has a double bond with P.

In all the samples I investigated (including the data of Ch. 4), the mechanism of P incorporation is restricted to the berlinite substitution. The non-stoichiometry reported in the literature for P-rich feldspar is probably due to a few percent of $\square Si_4O_8$ substitution, and to light-element *M*-cation substitution. $\square Si_4O_8$ is not widespread in the P-rich samples reported here; however, if the data of Frýda & Breiter (1995) are accurate, then 1-2 mol.% $\square Si_4O_8$ is widespread in K-feldspar from some granitic suites. The main chemical anomaly in P-rich samples is insufficient *M*-cation charge, a feature which is not observed in the majority of P-free alkali feldspars.The possibility of substitution of light elements associated with substitution of P remains to be investigated by direct analysis.

Table 3.19: Representative compositions of P-rich feldspar.

oxide	1	2	3	4	5	6 mean (1σ)	range
SiO_2	63.42	63.18	64.83	63.20	61.52	65.44(25)	64.88-65.92
Al_2O_3	18.75	18.93	17.92	18.97	19.68	18.47(12)	18.25-18.74
P_2O_5	0.68	0.76	0.08	0.88	2.08	0.20(3)	0.12-0.24
Na_2O	0.16	0.64	0.39	0.14	0.37	0.88(9)	0.63-1.01
K_2O	16.42	15.87	15.66	16.25	15.92	15.39(20)	15.09-15.83
Rb_2O	0.00	0.00	0.68	0.18	0.17	0.05(5)	0.00-0.22
Cs_2O	0.01	0.05	0.12	0.18	0.22	0.01(2)	0.00-0.05
SrO	0.02	0.03	0.06	0.02	0.01	0.03(3)	0.00-0.09
BaO	0.00	0.00	0.08	0.03	0.18	0.05(6)	0.00-0.19
sum	99.58	99.48	99.97	99.89	100.27	100.53(34)	99.35-100.38
	atomic contents based on 8 atoms of oxygen						
Si	2.948	2.935	3.012	2.933	2.846	2.997(5)	2.988-3.007
Al	1.027	1.036	0.981	1.035	1.073	0.997(6)	0.985-1.011
P	0.027	0.030	0.003	0.035	0.081	0.008(1)	0.005-0.009
Na	0.014	0.058	0.035	0.013	0.034	0.078(8)	0.056-0.089
K	0.974	0.940	0.928	0.962	0.939	0.899(9)	0.877-0.926
Rb	0.000	0.000	0.020	0.005	0.005	0.001(1)	0.000-0.006
Cs	0.000	0.001	0.002	0.004	0.004	0.000	0.000-0.005
Sr	0.000	0.001	0.001	0.001	0.000	0.001(1)	0.000-0.002
Ba	0.000	0.000	0.002	0.001	0.003	0.001(1)	0.000-0.003
ΣM	0.988	0.999	0.989	0.987	0.986	0.980(6)	0.970-0.989
M^+	0.988	1.000	0.993	0.989	0.990	0.981(6)	0.970-0.991
TO_2^-	1.002	1.007	0.978	1.000	0.992	0.990(6)	0.977-1.003
ΣT	4.003	4.002	3.996	4.003	4.001	4.002(2)	3.999-4.006

1. HAG-1 microcline, Hagendorf pegmatite.
2. PRL-1 microcline, Peerless pegmatite.
3. TM-2 microcline, Tin Mountain, South Dakota.
4. Typical P of Cross Lake microcline.
5. Highest P of Cross Lake microcline.
6. Mean (N=28) and range of orthoclase, White Queen Mine.

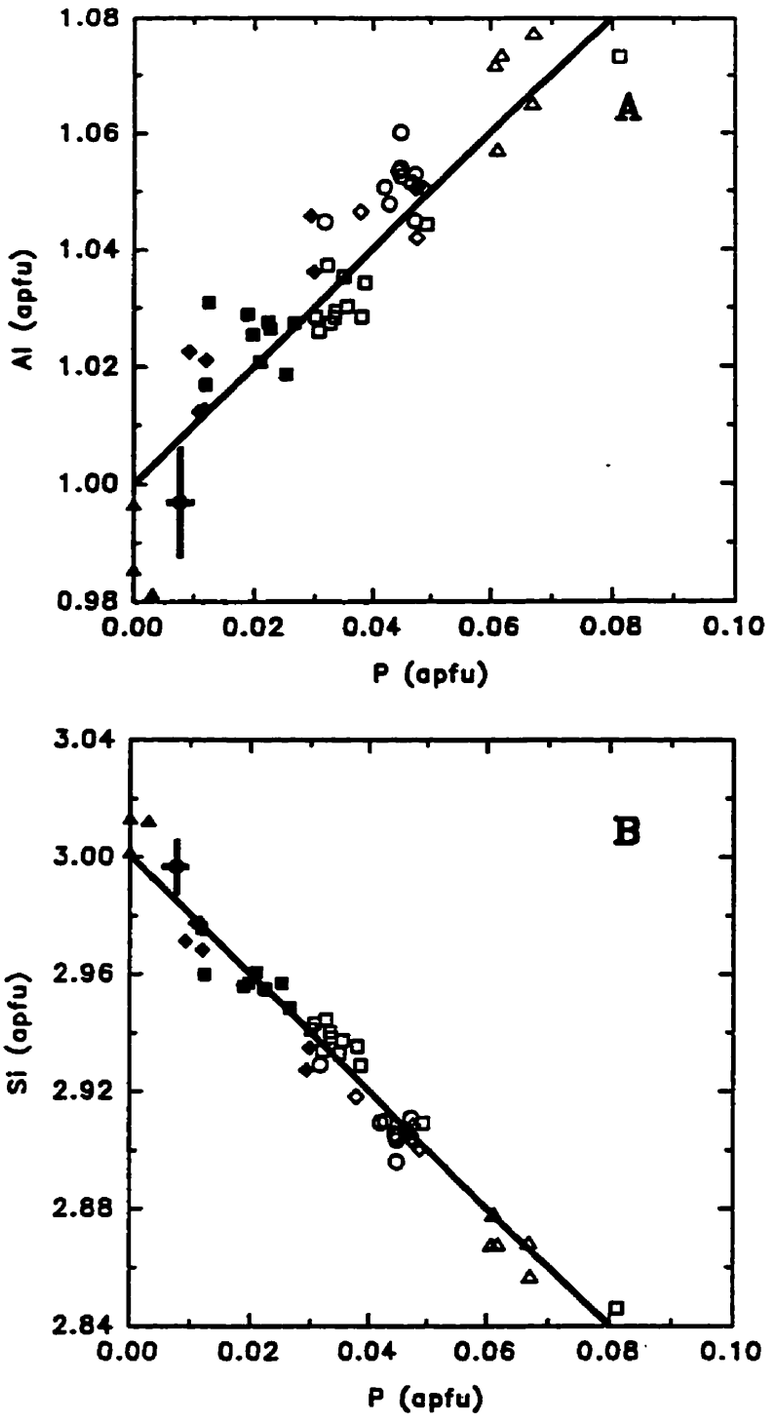

Fig. 3.3. Element variations for P-rich feldspar: (A) Al *vs.* P; (B) Si *vs.* P: lines indicate the $AlPSi_2$ substitution. Symbols for localities: Tin Mountain (▲); Peerless (◆); Hagendorf (■); Cross Lake (□); GHIT (○); THON (◇); and MACRO (△). Error bars (4σ) were determined by multiple analysis of White Queen orthoclase (•).

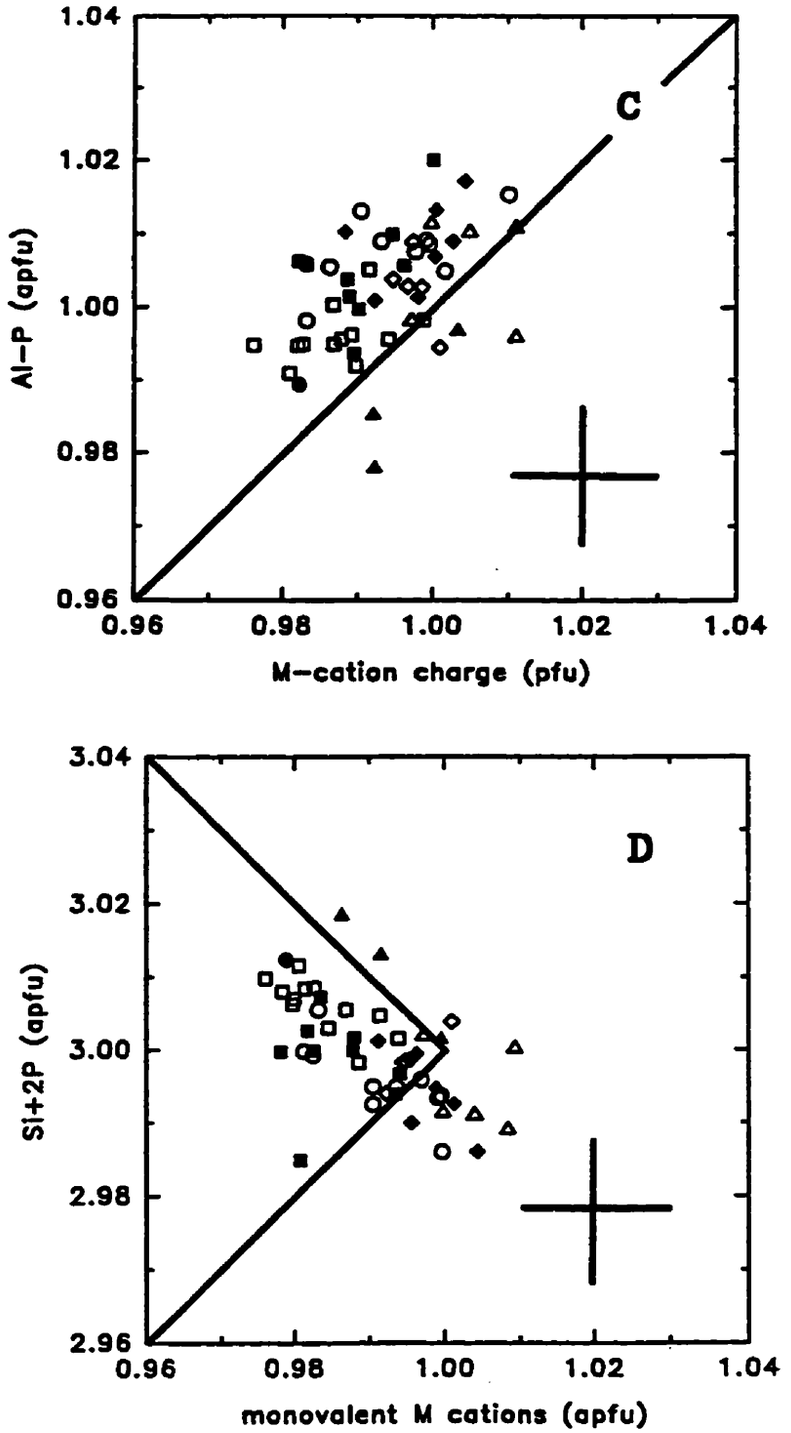

Fig. 3.3. Element variations for P-rich feldspar: (C) (Al-P) *vs.* *M*-cation charge with a line indicating equal values of each; (D) (Si+2P) *vs.* monovalent *M* cations with lines for (1) the plagioclase and (2) the $\square Si_4O_8$ substitutions. Error bars (4σ) were determined by multiple analysis of Eifel sanidine.

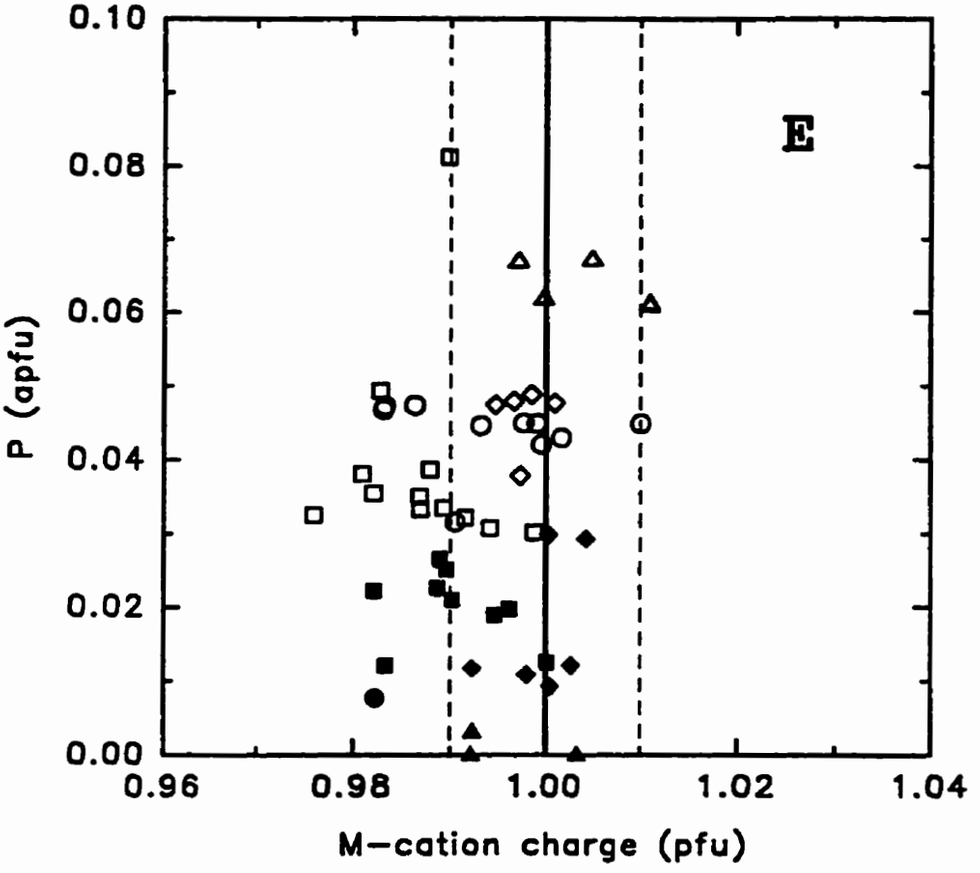

Fig. 3.3. Element variations for P-rich feldspar: (E) P *vs.* *M*-cation charge. Data for feldspar free of divalent and light-element *M*-cations should vary about $M^{+} = 1.00$ (solid line) within $\pm$ 0.01 *apfu* (4σ) (dashed lines).

CHAPTER 4

COMPOSITIONAL AND TEXTURAL FEATURES OF THE (K,Rb)-FELDSPAR SERIES

The composition of the Eifel sanidine standard has been constrained to ~2% error for the major elements by measurement against a set of well-characterized alkali-aluminosilicate minerals. By adjusting the composition to close agreement with the ideal formula MT_4O_8, the accuracy is increased to less than 2%, giving excellent stoichiometry for most feldspar analyses. The precision of measurement is less than 1% for the oxide, *M*, and *T* sums, potentially allowing identification of feldspar which has anomalous composition. This chapter provides a detailed investigation of the compositional features of the (K-Rb)-feldspar series, and emphasizes the textural features of the reactions of (K,Rb)-feldspar. Due to variable availability of material, and wide variation in the distribution of interesting features, a systematic locality-by-locality description cannot be given. The organization of this chapter results from emphasizing features specific to a single locality, or from the grouping of similar features found at more than one locality. In order to provide a context into which the complex sequences of crystallization and reaction of the various generations of (K-Rb)-feldspar could be placed, it was necessary to the emphasize relations to the alteration sequence of pollucite. The reactions of (K-Rb)-feldspar do not occur independently; associated Rb- and Cs-rich minerals also are examined insofar as they document the geochemical behaviour of Rb and Cs in granitic pegmatites.

Analysis of the (K-Rb)-feldspar series begins with a study of adularia, the low-

temperature euhedral form of K-feldspar with a Na-free composition closely approaching Or_{100} (Ch. 4.1). Anhedral end-member K-feldspar is a common low-temperature product of alteration of microcline (this thesis), but by virtue of its compositional, structural and paragenetic similarity to adularia, it may be called "adularian". Analysis of adularian K-feldspar replacing pollucite at Morrua and Tin Mountain indicates significant Rb substitution (Ch. 4.2). Higher-temperature reactions which generate Rb-rich to Rb-dominant feldspar in early K-feldspar are examined at the pollucite-bearing Rubellite pegmatite (Ch. 4.3). Intermediate-temperature reactions in (K,Rb)-feldspar veining pollucite at two localities (Luolamäki and Elba) are very similar in terms of texture and compositional range (Ch. 4.4). The full range of reaction of (K-Rb)-feldspar, from high to low temperature, is represented at Tanco (Ch. 4.5) and also at High Grade Dyke (Ch. 4.6). Extreme Rb-enrichment of feldspar and associated mica occurs at two localities, Kola Peninsula and Red Cross Lake (Ch. 4.7). Relations between (K,Rb)-feldspar composition and the alteration sequence of pollucite are then documented for a variety of localities at which simple compositional features were found, and at localities for which insufficient material was available for detailed examination (Ch. 4.8). Evidence for widespread subsolidus activity of Rb and Cs, as indicated by the compositional features of cesian analcime, Rb- and Cs-rich micas and clay minerals, is summarized for several localities (Ch. 4.9).

4.1 *End-member $KAlSi_3O_8$ adularia: normal and anomalous compositional trends*

Adularia is defined as a morphologically distinct variety of end-member K-feldspar, characteristic of low-temperature hydrothermal or diagenetic paragenesis (*cf.* discussion Ch. 6.4). In epithermal-vein deposits, fine grain-size and rhombic-to-tabular morphology of adularia has been related to Au mineralization because a high rate of feldspar crystallization from boiling aqueous fluids also precipitates Au (Dong & Morrison 1995). A disordered (Al,Si) distribution was suggested to result from high rates of nucleation and crystallization for adularia in late hydrothermal assemblages from granitic pegmatites and in hydrothermal veins (Černý & Chapman 1984, 1986). Adularia from the Buck Claim pegmatite is the most-disordered K-feldspar yet examined by single-crystal X-ray methods, and represents end-member high-sanidine (Ferguson *et al.* 1991). Some of the highly disordered samples examined by Černý & Chapman (1986) have unusual cell-parameters which plot significantly beyond the high-sanidine corner of the *b-c* quadrilateral (Fig. 4.1). The cell parameters cannot be influenced by strain because adularia is Na-free and non-perthitic. The composition of adularia does not vary from that of near end-member $KAlSi_3O_8$ except in chemically specialized environments (*e.g.*, the concentration of significant ammonium in diagenetic K-feldspar from organic-rich sediments). The compositional measurements of Černý & Chapman (1984) required an albite standard (2ALBITE) because poor results were obtained using a K-feldspar standard (2ORTHO). Sanidine is known to have a few per cent *M*-site vacancy coupled with a high Si/Al ratio (Linthout & Lustenhouwer 1993, Kuehner & Joswiak 1996) and this might be observed in

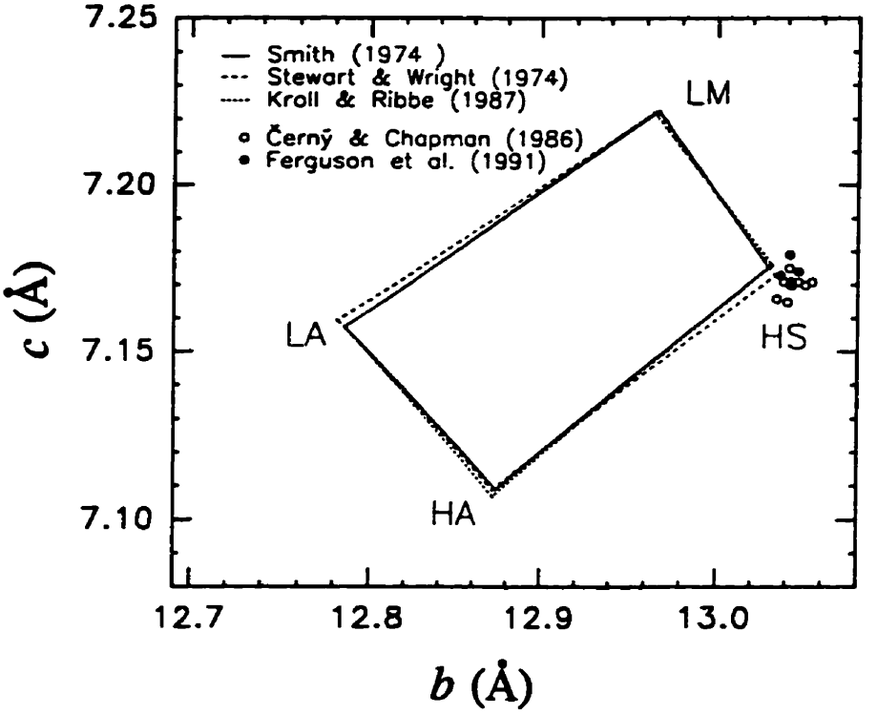

Fig. 4.1. Plot of *c* (Å) *vs. b* (Å) for alkali feldspars showing the relationships between low microcline (LM), high sanidine (HS), low albite (LA) and high albite (HA). Data which lie outside the quadrilateral are plotted.

disordered adularia. Accurate compositional measurements must be made in order to provide accurate correlation with cell parameters (Ch. 5.2).

The following samples have been previously described by Černý & Chapman (1986); I have added the data concerning inclusions and minor-element chemistry.

Disordered adularia from the St. Andreasberg district, Germany is of Cretaceous age and occurs in epithermal Ag-ore deposits (Mertz *et al.* 1989). No inclusions were noted in our sample; it is compositionally homogeneous with BaO<0.12 wt.%.

Disordered but structurally heterogeneous adularia from the Guanajuato epithermal ore deposits, Mexico (USNM #120408) occurs as small grains within quartz and also as overgrowths on quartz. Our sample is compositionally homogeneous with BaO < 0.12 wt.%.

No minor elements were detected in disordered adularia from the copper deposits of the Upper Michigan Peninsula (Harvard Museum specimens from Copper Falls #84720, # 84721 and #84722, Superior Mine at Ontonagon # 115103, and Phoenix Mine #88628).

No minor elements were detected in pink (University of Manitoba Mineralogical museum M5945) and white (M59460) turbid ordered adularia from the Xihuashan tungsten deposit, China.

Adularia with intermediate order from the **Hot Springs** deposits of rock crystal, Arkansas (Harvard #122797), has a patchy distribution of Ba (zones >50 μm) with 0.54-2.94 wt.% BaO.

Variable Ba was found in adularia from the **Puklice**, Czech Republic, pegmatite (0-0.85 wt.% BaO), whereas adularia from the **Nová Ves u Českého Krumlova** pegmatite is homogeneous with negligible Ba. Adularia from **Věžná** locally contains stringers (<1 μm wide) of albite, but is otherwise Na- and Ba-free.

The following samples have been previously described by Černý & Chapman (1984).

Adularia with intermediate order from the **Etta** pegmatite, near Keystone, South Dakota, has variable Ba, from 0-0.56 wt.% BaO.

Our sample of adularia from **Wausau**, Wisconsin, is ordered with no detectable minor elements.

Adularia from the **Buck Claim** pegmatite, SE Manitoba, is disordered (end-member high sanidine) with no minor elements detected, but contains small (<5 μm) blebs of Fe-oxides. Analytical overlap with these inclusions gives a poor stoichiometry for the feldspar, particularly for ΣT.

Adularia from the **Brown Derby** No.1 pegmatite, Colorado, has intermediate order, contains variable BaO (0.09-1.15 wt.%) and is partly altered by late

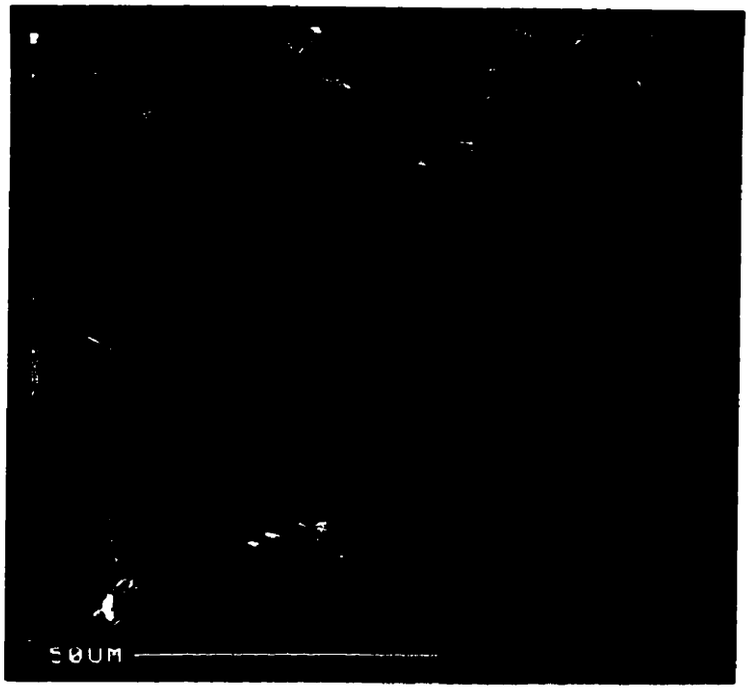

(A)

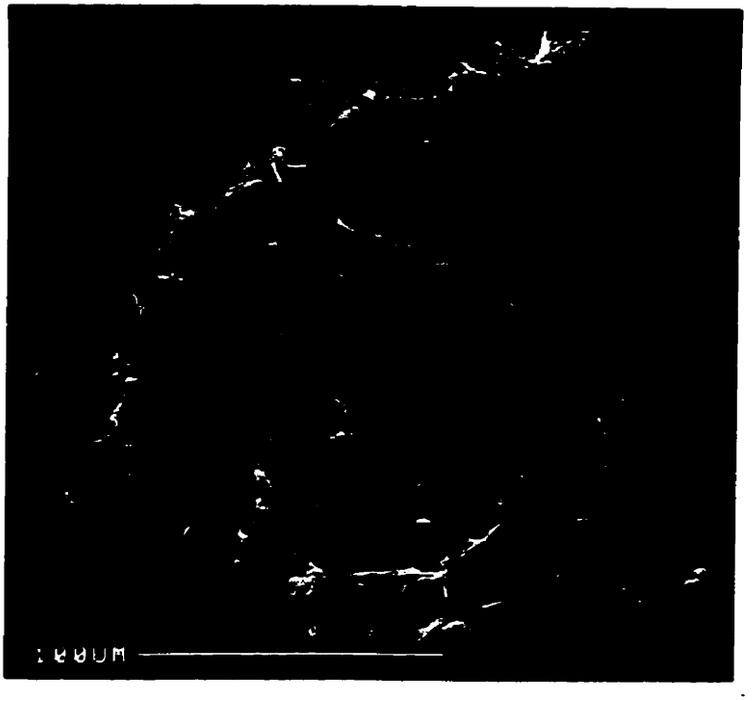

(B)

Fig. 4.2. SEM images of overgrowths of a fibrous mineral on adularia from Brown Derby No.1, Colorado, showing a gradation from (A) a platy, elongated morphology to (B) a fibrous morphology.

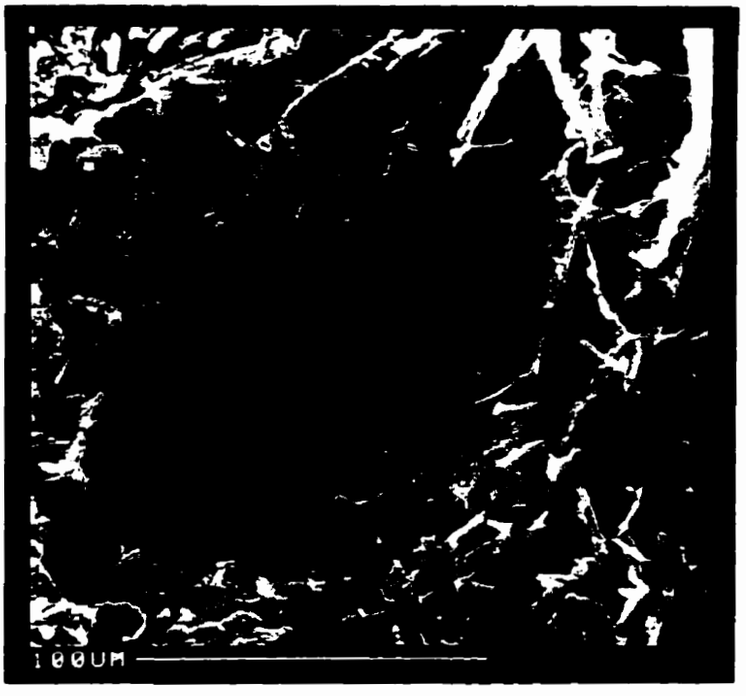

(C)

Fig. 4.2. SEM images of overgrowths of a fibrous mineral on adularia from Brown Derby No.1, Colorado, (C) showing fibres with capillary form.

muscovite and apatite. The feldspar forms fine-grained masses which seem to be of metasomatic origin but with no relics of the replaced phase (it may be blocky K-feldspar; adularia also replaces pollucite: Ch. 4.8). Hand specimens show small cavities in which adularia is overgrown by cobwebs of a late fibrous mineral (Fig. 4.2A, B). The smallest of the fibres have a capillary form (Fig. 4.2C). The feldspar seems to grade from a finely crystalline aggregate to elongate surface crystals, and through to distinctly fibrous material (1-10 μm in width and up to 500 μm in length). EDS analysis using an SEM shows that all of the fibres have the same composition as the massive fine-grained adularia.

Adularia (with 0.15 wt.% BaO and with a high-temperature habit) from **Baveno**, Italy, is intergrown (in 50-50 vol.% proportions) with end-member albite.

Adularia grains (1-2 mm in size) on the surface of rock crystal (containing black acicular toumaline) from the **Minas Gerais** district, Brazil, have BaO contents of 0.03-0.26 wt.% and 0.07-0.17 wt.% Fe_2O_3.

At the **Tanco** pegmatite, Bernic Lake, Manitoba, adularia occurs in low-temperature hydrothermal cavities in the spodumene-rich zones (Černý 1972). Alteration of spodumene (+ quartz) generated leaching cavities with secondary quartz and spodumene, beryl, albite, adularia, cesian analcime, illite-montmorillonite, cookeite, phosphates and carbonates. Found *in situ*, vugs contain a hydrous white "slime" which dries to a white clay-like powder, locally with reddish staining. In some samples, the anhedral bases of analcime, albite and adularia crystals rest in this material, and the adularia grains have a layer of red

Fe-oxide inclusions near the base. Outer, euhedral parts of the adularia crystals are clear. Analysis of the white clay-like material found at the base of euhedral crystals of adularia gave 55.04-57.00 SiO_2, 20.89-21.27 Al_2O_3, 1.24-1.35 Fe_2O_3, 5.63-5.84 MgO, 0.11-0.15 Na_2O, 8.55-8.71 K_2O, 0.14-0.67 CaO, 0.00-0.19 BaO, and 0.00-0.39 F, sum 93.5-94.0 wt.%. This material has the compositional characteristics which could make it a precurser for crystallization of K-feldspar. It is slightly birefringent and XRD shows diffraction peaks of a chlorite-group mineral. XRD data for the feldspar is given in Ch. 5.

Representative analytical results for adularia are given in Tables 4.1a and 4.1b. Elements sought but not detected in any of the samples are P, Sr, Ca, Cs, Rb, Mg, F, Ga, Ti, Mn and Pb. Minor elements found in some of the samples were $Na_2O < 0.46$ wt.%, $BaO < 2.94$ wt.% and $Fe_2O_3 < 0.17$ wt.%. Atomic contents of Fe do not exceed 0.002 *apfu*. Most of the samples have equal values of Al and *M*-cation charge, near 1.00 ($\pm$0.01) (Fig. 4.3A), in agreement with the Si values near 3.00 ($\pm$0.02) *apfu* and ΣM values of 1.00 ($\pm$0.01) *apfu* (Fig. 4.3B). The compositions are within the ranges of accuracy and precision expected for the 1EIFEL standard. There are, however, significant deviations from trends expected for a plagioclase-like substitution (along which the Ba-substituted samples lie: Fig. 4.3, line 1), and some data follow the trend expected for the $\square Si_4O_8$ substitution (Fig. 4.3, line 2). Samples with distinctly high Si (defined as Si>3.02 *apfu*) and with compositional trends indicative of the $\square Si_4O_8$ substitution include: Věžná, Czech Republic; Hot Springs, Arkansas; Copper Falls, Michigan; Tanco, Manitoba; Guanajuato, Mexico. The data also indicate that a few samples have insufficient *M*-cation charge and low ΣM *apfu* in

Table 4.1a: Representative compositions of adularia, analysed using the Table 3.9 reference standards.

oxide	1	2	3	4	5	6	7	8
SiO_2	65.05	64.73	64.53	64.89	64.09	64.81	65.46	64.20
Al_2O_3	18.00	18.16	18.20	17.97	18.27	18.24	18.24	18.37
Fe_2O_3	0.06	0.00	0.00	0.00	0.00	0.07	0.02	0.17
Na_2O	0.23	0.11	0.09	0.02	0.11	0.04	0.07	0.05
K_2O	16.48	16.55	16.20	16.84	16.49	16.95	16.83	16.79
SrO	0.02	0.02	0.06	0.01	0.02	0.03	0.00	0.02
BaO	0.00	0.00	0.56	0.07	0.46	0.05	0.13	0.26
sum	99.87	99.64	99.65	99.92	99.51	100.26	100.85	99.96
	Atomic contents based on 8 atoms of oxygen							
Si	3.013	3.006	3.003	3.012	2.993	3.000	3.008	3.007
Al	0.982	0.994	0.998	0.983	1.006	0.995	0.988	0.988
Fe	0.002	0.000	0.000	0.000	0.000	0.002	0.001	0.002
Na	0.021	0.010	0.008	0.002	0.010	0.004	0.006	0.007
K	0.974	0.980	0.962	0.997	0.982	1.001	0.987	0.991
Sr	0.001	0.001	0.002	0.000	0.001	0.001	0.000	0.000
Ba	0.000	0.000	0.010	0.001	0.008	0.001	0.002	0.001
ΣM	0.995	0.991	0.982	1.000	1.002	1.006	0.995	0.999
M^+	0.996	0.992	0.993	1.002	1.011	1.008	0.997	1.000
TO_2^-	0.985	0.994	0.998	0.983	1.006	0.996	0.988	0.990
ΣT	3.997	4.001	4.001	3.995	3.999	3.997	3.998	3.998
Si/Al	3.06	3.02	3.01	3.07	2.98	3.01	3.04	3.04

1. Wausau, Wisconsin; red.
2. Xihuashan, Jianxi Province, China; pink.
3. Etta, near Keystone, Pennington County, South Dakota; Ba-rich area.
4. Nová Ves, near Český Krumlov, southern Bohemia, Czech Republic.
5. Puklice, near Jihlava, western Moravia, Czech Republic; slightly Ba-rich area.
6. Věžná, western Moravia, Czech Republic.
7. Brown Derby, Colorado.
8. Brazil, Minas Gerais district; on rock crystal.

Table 4.1b: Representative compositions of adularia, analysed using the Table 3.9 reference standards.

oxide	1	2	3	4	5	6	7	8
SiO_2	65.40	65.65	64.41	62.30	65.22	64.80	65.18	65.23
Al_2O_3	18.13	17.75	18.22	18.72	18.26	18.11	18.29	18.26
Fe_2O_3	0.01	0.01	0.03	0.00	0.05	0.01	0.06	0.00
Na_2O	0.03	0.16	0.18	0.11	0.00	0.00	0.03	0.00
K_2O	16.90	16.46	16.60	15.32	16.72	16.92	17.04	17.10
SrO	0.00	0.00	0.02	0.04	0.00	0.00	0.00	0.01
BaO	0.09	0.00	0.16	2.94	0.10	0.00	0.13	0.00
sum	100.62	100.05	99.66	99.47	100.52	99.91	100.84	100.63
	Atomic contents based on 8 atoms of oxygen							
Si	3.014	3.029	2.997	2.953	3.006	3.008	3.001	3.005
Al	0.981	0.966	0.999	1.046	0.992	0.989	0.992	0.992
Fe	0.000	0.000	0.001	0.000	0.002	0.000	0.002	0.000
Na	0.005	0.014	0.016	0.012	0.000	0.000	0.003	0.000
K	0.987	0.969	0.985	0.927	0.983	1.000	1.001	1.005
Sr	0.002	0.000	0.000	0.001	0.000	0.000	0.000	0.000
Ba	0.002	0.000	0.003	0.055	0.002	0.000	0.002	0.000
ΣM	0.995	0.983	1.005	0.994	0.985	1.000	1.006	1.005
M^+	0.999	0.983	1.008	1.050	0.987	1.000	1.008	1.005
TO_2^-	0.981	0.966	1.000	1.046	0.994	0.989	0.994	0.992
ΣT	3.995	3.996	3.998	3.999	4.001	3.997	3.996	3.996
Si/Al	3.07	3.14	3.00	2.82	3.03	3.04	3.02	3.00

1. St. Andreasberg, FRG.
2. Guanajuato epithermal deposit, Mexico.
3. Baveno, Italy.
4. Hot Springs, Arkansas; Ba-rich grain (Harvard #122797).
5. Buck Claim, SE Manitoba.
6. Phoenix Mine, Michigan (Harvard #88628).
7. Superior Mine, Michigan (Harvard #115103).
8. Copper Falls Mine, Michigan (Harvard #84720).

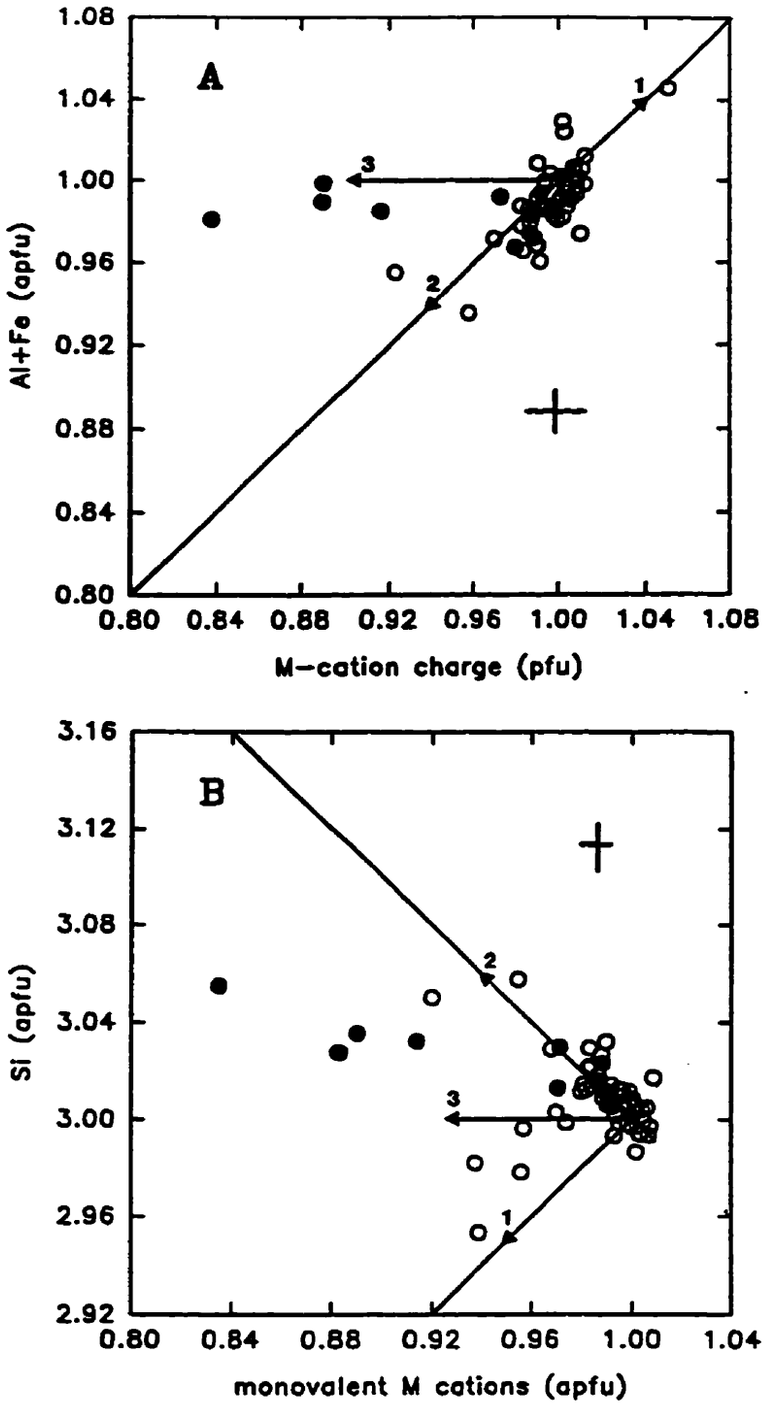

Fig. 4.3. Chemical trends of adularia: (A) Al *vs.* *M*-cation charge with a line indicating equal values of each; (B) Si *vs.* monovalent *M* cations. The analytical precision (4σ, 99% confidence) is indicated by crosses. The arrows mark trends for (1) the plagioclase-like substitution; (2) the $\square Si_4O_8$ substitution, and (3) decreasing *M*-cation charge at constant Al or Si. Tanco samples are indicated by filled symbols.

comparison to the charge generated by the framework (Fig. 4.3, line 3). This latter feature suggests light-element *M*-cation substitution.

Deviations from the ideal feldspar formula were investigated in detail for several of the samples of Tanco adularia. This adularia also has anomalous cell parameters. There are three features which may generate anomalous composition:

(1) BSE imaging of adularia, which is red at its base, showed blebby clusters of Fe-rich material (Fig. 4.4A). Analysis indicates a feldspar-like composition with a few wt.% Fe_2O_3 and oxide totals near 100 wt.%; however, calculation of the formula gives ΣT values up to 4.1 *apfu*. The red material is probably hematite, finely dispersed in the adularia. It is significant that overlap of the analysing volume of the electron beam can be recognized even at small volumes of the contaminating phase. Inclusions less than 1 μm in size are not visible by BSE imaging but must contribute to analytical error in finely altered samples.

(2) Evidence for $\square Si_4O_8$ substitution is provided by some of the analytical results of Tanco adularia. In single crystals of Tanco adularia (as well as in the other high-Si samples investigated), a systematic core-to-rim variation is not observed, but the high-Si areas have a patchy distribution in zones less than 20 μm in size. Values of *M*-cation charge (essentially only K) and framework Al are equal, but both are less than 1 *apfu*. Si values exceed 3 *apfu* by a few percent, and Si/Al ratios extend to 3.2 (no. 6 in Table 4.2).

Back-scattered electron imaging of rims of the Tanco adularia reveals lower grey

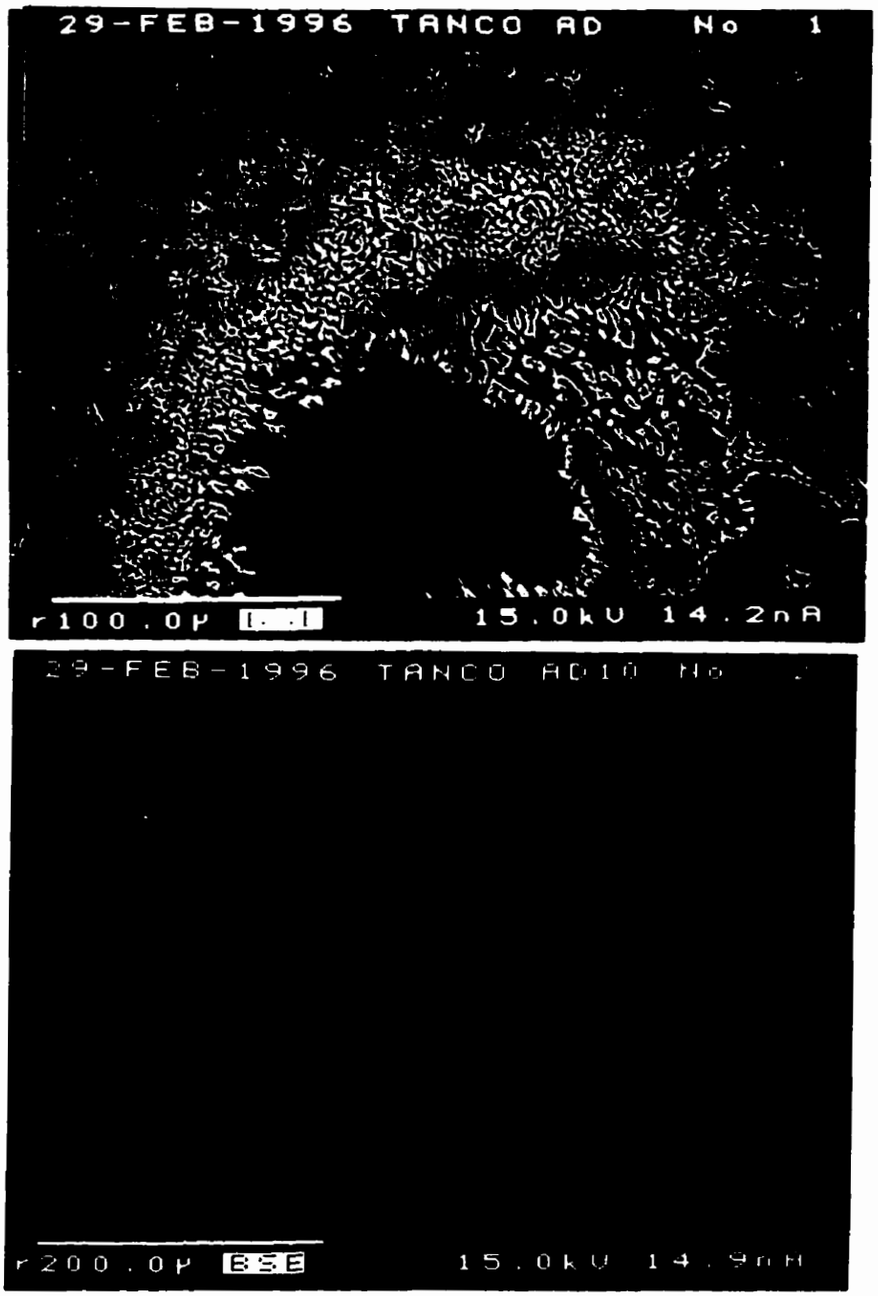

(A)

(B)

Fig. 4.4. BSE images of AD-10 adularia from Tanco, Manitoba: (A) Overgrowth of adularia on semi-amorphous gel-like material (dark grey). The adularia contains small clusters of Fe-oxide (light blebs); (B) Euhedral crystal with normal-composition core and dark rims corresponding to K-feldspar with a lower mean atomic number.

Table 4.2: Representative compositions of adularia from Tanco, Manitoba (sample AD-10, Fig 4.4).

oxide	1	2	3	4	5	6
SiO_2	64.85	65.66	65.96	66.23	65.95	66.95
Al_2O_3	17.85	18.01	17.99	18.32	17.97	17.09
Na_2O	0.07	0.01	0.03	0.01	0.01	0.01
K_2O	16.50	16.71	16.84	15.20	14.09	15.80
SrO	0.00	0.00	0.00	0.00	0.05	0.06
sum	99.34	100.52	100.92	99.84	98.17	100.13
	Atomic contents *per formula unit*					
Si	3.018	3.021	3.023	3.017	3.027	3.043
Al	0.979	0.977	0.972	0.984	0.973	0.954
Na	0.006	0.001	0.003	0.001	0.001	0.001
K	0.980	0.981	0.985	0.888	0.825	0.916
Sr	0.000	0.000	0.000	0.000	0.001	0.002
M^*	0.008	0.006	0.016	-0.101	-0.134	-0.033
ΣM	0.986	0.983	0.988	0.990	0.961	0.922
M^+	0.986	0.983	0.988	0.889	0.828	0.921
TO_2^-	0.979	0.977	0.972	0.984	0.972	0.954
ΣT	3.998	3.999	3.996	4	4	4
Si/Al	3.08	3.09	3.11	3.07	3.12	3.19

1-3. Core; formulae normalized to 8 O *apfu*.
4-6. Rim; formulae normalized to (Al+Si) = 4 *apfu*.
M^* calculated as ($M^+ - TO_2^-$) *pfu*.

levels than the core, indicative of a lower mean atomic number. The rim is <20 μm wide, is parallel to the face of the crystal, and has a sharp internal boundary (Fig. 4.4B). Analysis of the rims gives slightly high Si/Al ratios, but a distinct deficiency of *M* cations, and a low (wt.%) oxide sum (no. 5 in Table 4.2), whereas analysis of the core gives a well-balanced formula. This suggests a light-element *M*-cation substitution; this remains to be verified by microbeam analysis of light elements. The "light-element" rims are retained from fresh (clear) to altered (opaque green) samples.

In order to assess the accuracy of measurement of "missing" elements in EMP analysis, Na-, H-, and Li-exchanged feldspar was examined. The samples had been previously characterized by EMP analysis, bulk-sample H_2O determination, infrared spectroscopy and crystal-structure refinement (Behrens & Müller 1995, Deubener *et al.* 1991, Paulus & Müller 1988 and Müller 1988). The wide range of composition noted by Behrens & Müller (1995) was not verified by our analysis. Crystals were rather homogeneous and showed no zoning by BSE imaging. As the formula calculated from the Na-exchanged feldspar has *T*-sums very near 4.00 (which implies no significant reaction of the aluminosilicate framework with the cation-exchanging medium), the formulae of the H- and Li-feldspars were calculated by normalization to $(Al+Fe^{3+}+Si) = 4$ *apfu* (Table 4.3). Light-element contents (M^*) were calculated by charge-balance using $M^* = [(Na+K) + 2(Sr+Ba) - (Al+Fe^{3+})]$ and indicated good accuracy by virtue of a fully-occupied *M*-site. It is probable that light-element substitution of more than 1 at.% in feldspar can be recognized by EMP analysis and that calculated light-element contents might be accurate to within a few percent. The absolute

accuracy remains to be verified by direct analysis of light elements.

In summary, analysis of adularia has established that the majority of samples of adularia have compositions corresponding to ideal end-member K-feldspar, indicating that the adjusted Eifel sanidine composition used for calibration gives accurate results. The principal deviation from stoichiometry is due to $\square Si_4O_8$ and light-element *M*-cation substitutions.

Table 4.3: Average compositions of Na-, H- and Li-exchanged Eifel sanidine.

oxide	1	2	3
SiO_2	66.97	72.79	72.65
Al_2O_3	19.68	21.12	20.96
Fe_2O_3	0.19	0.21	0.21
Na_2O	11.11	0.33	0.04
K_2O	0.35	0.18	0.14
SrO	0.21	0.20	0.22
BaO	0.86	0.91	0.91
sum	99.37	95.73	95.13
	atomic contents *pfu*		
Si	2.970	2.976	2.982
Al	1.028	1.018	1.012
Fe	0.006	0.007	0.006
Na	0.955	0.026	0.003
K	0.020	0.009	0.007
Sr	0.005	0.005	0.005
Ba	0.015	0.015	0.015
M^*	-0.018	-0.950	-0.968
ΣM	0.996	1.005	1.000
M^+	1.016	0.075	0.053
TO_2^-	1.034	1.025	1.018
ΣT	4.004	4	4

1. Na-exchanged (sample 43-1).
2. Li-exchanged (sample 43-3).
3. H-exchanged (sample 43-2).

M^* calculated as ($M^+ - TO_2^-$).
Average of 6 analyses per sample.

4.2 *Adularian (K-Rb)-feldspar from Morrua, Mozambique, and Tin Mountain, South Dakota*

The Morrua Mine exploits a highly fractionated zoned spodumene-subtype pegmatite in the Alto Ligonha area, Mozambique (Correia Neves 1981). The pegmatite contains a large body of pollucite (P. Vanstone, pers. comm. 1996, Quadrado 1963). Bulk compositions of blocky microcline perthite have 14400-27500 ppm Rb and K/Rb ratios of 3.8-7.4 (Correia Neves 1981).

The late feldspar examined here occurs as part of a sequence of minerals formed by alteration of pollucite (Fig. 4.5). In hand specimen, pollucite is white to colourless, and is penetrated by 2-3 mm-wide veins of coarse-grained mauve lepidolite (± quartz, apatite and spodumene). Later veins of fine-grained mica are partly replaced by fine-grained spodumene. Granular aggregates of feldspar, less than 1 mm in size, replace pollucite at its contact with the mica veins and also form spherical aggregates along fractures within the pollucite (Figs. 4.6A, B). Microscopic leaching channels (less than 10 μm wide) extend into the pollucite from the surfaces of the feldspar and also from fractures. Late analcimization is associated with the formation of these channels in the pollucite. Fractures in pollucite are filled locally with a buff-to-white clay mineral, and surfaces are stained with black and red Mn- and Fe-bearing oxides.

Three main stages can be observed in the feldspar that replaces pollucite (Fig. 4.7). Stage-(1) feldspar is heterogeneous with patchy and variable Rb contents, and is associated with cookeite and apatite. From core to rim, K/Rb decreases as

does the abundance of cookeite inclusions. Late local reequilibration resulted in 10 μm wide veins of Rb-rich feldspar crossing the early feldspar. Stage-(1) feldspar is locally veined, replaced and overgrown by a 100 μm-thick layer of non-porous Stage-(2) end-member K-feldspar and a final layer of porous Stage-(3) end-member K-feldspar. This latest stage was closely related to leaching and cation exchange of the adjacent pollucite.

Optical data are not readily determined on the feldspars because of abundant inclusions and the very small grain size of the feldspars. The Stage-(1) feldspar has a sweeping extinction but appears untwinned. The Stage-(2) and Stage-(3) feldspar overgrowths appear twinned, however, the potential twin planes radiate from the core of the feldspar assemblage and may represent subparallel growth.

The Stage-(1) feldspar that replaces pollucite is almost pure (K-Rb)$AlSi_3O_8$, with up to 66 mol.% Rbf. Compositions of the Stage-(2) and Stage-(3) feldspars correspond to almost end-member K-feldspar. Representative compositions are given in Table 4.4. Within error, values of Al are equal to values of the *M*-cation charge (Fig. 4.8A). There is a trend of increasing Si with the sum of the monovalent *M* cations, evident in the Stage-(1), -(2) and -(3) feldspars (Fig. 4.8B). As no divalent cations were detected in analysis, this trend probably represents substitution of up to 4 mol.% $\square Si_4O_8$. Mean values of M^+ = 0.994(15), TO_2 = 0.993(13), Si = 3.007(13) and ΣT = 4.000(2) *apfu* indicate good stoichiometry if substitution of $\square Si_4O_8$ is taken into account. A plot of K *vs.* Rb shows substitution along a line from 1 K to 1 Rb *apfu* (Fig. 4.8C). Substitution of Cs increases with Rb but is less than 0.02 *apfu* (Fig. 4.8D).

The close association of K-feldspar with end-member pollucite at other localities suggests an approximate temperature of co-precipitation of 300-200°C, with subsequent analcimization at 200-100°C (Teertstra & Černý 1995; Ch. 4.8). Because the Morrua feldspar is associated with analcime (formed by cation exchange of pollucite) rather than with reprecipitated end-member pollucite, the temperature of precipitation may be in the range 250-150°C. This estimate is supported by association of the feldspar with cookeite (Vidal & Goffé 1991), by the lack of Rb or K diffusion which is restricted at low temperature, and by the end-member compositions of Stage-(2) and Stage-(3) feldspar, which are as expected by low-temperature extrapolation of the Or-Ab solvus. The equilibrium Rb/K distribution-coefficient between K-feldspar and aqueous fluid at 180°C is 0.28 (Pauwels *et al.* 1989). This indicates that the parent fluids for the Morrua feldspars were considerably enriched in Rb. The sequence of alteration of pollucite and the progressive stages of (K,Rb)-feldspar crystallization indicate that the late-stage pegmatitic fluids at this locality had the following sequence of activities: Rb < Li < K < Na.

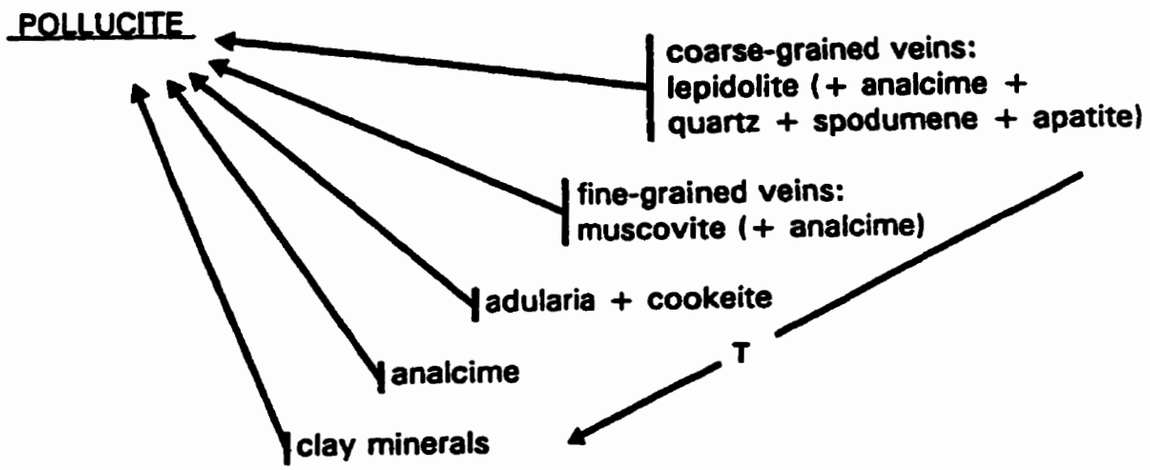

Fig. 4.5. Schematic sequence of alteration products of pollucite from the Morrua Mine, Mozambique. The arrow (T) indicates later products appearing at decreasing temperature.

(A)

(B)

Fig. 4.6. Associations of Morrua feldspar: (A) Granular aggregate of (K,Rb)-feldspar with a cookeite-rich core (black). The feldspar is located between wide veins of lepidolite (black) and thin veins of muscovite (black) and replaces pollucite (white); (B) Feldspar showing three stages of growth (dark core including cookeite + apatite; inclusion-free K-feldspar (white), and outer layer of porous K-feldspar) overgrowing both sides of a thin vein of fine-grained mica. The vertical edge of both photo-micrographs (plane-polarized light) is 0.5 mm.

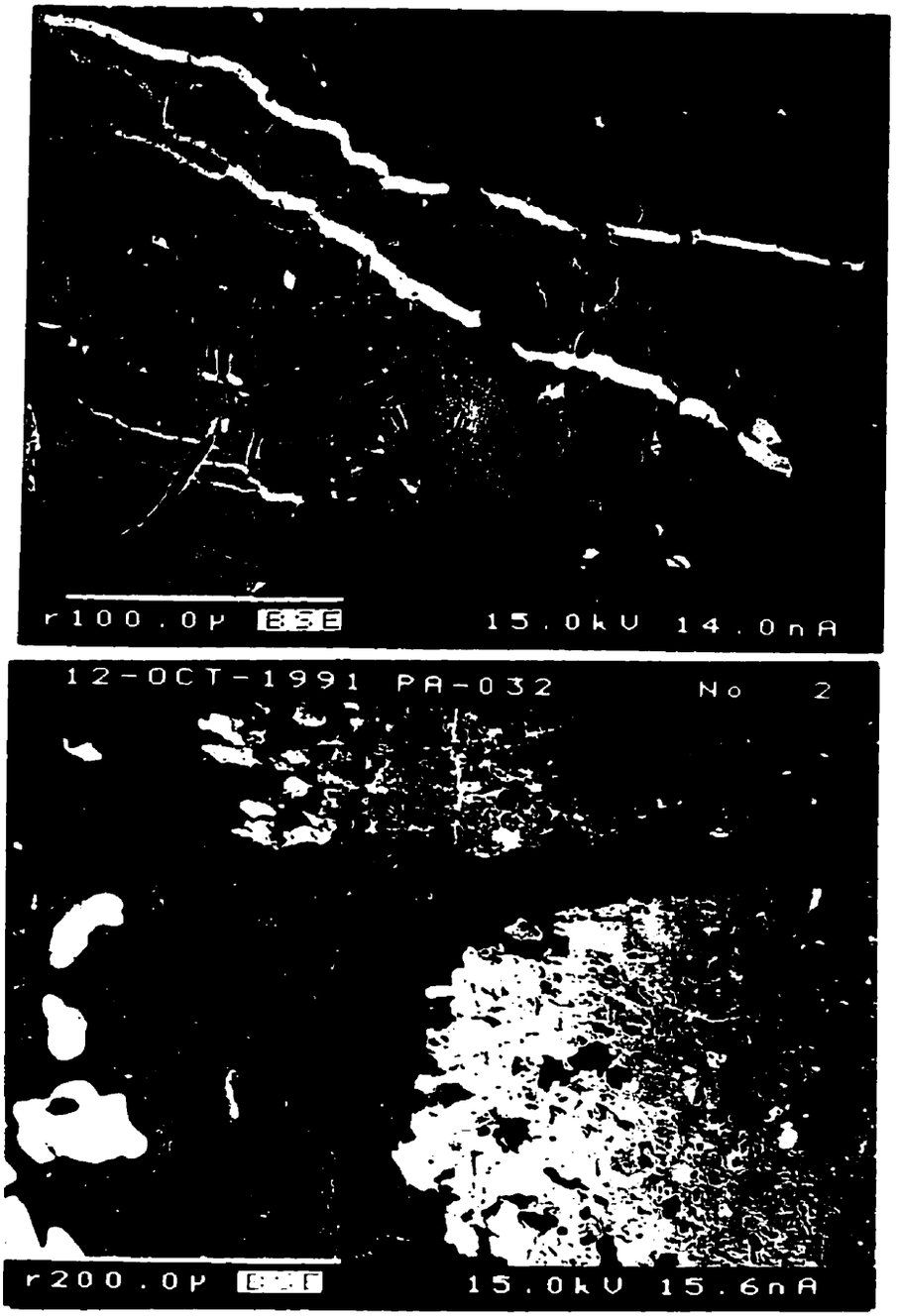

(A)

(B)

Fig. 4.7. BSE images of Morrua feldspar: (A) (K-Rb)-feldspar (variable grey), containing cookeite (black), cut by late veinlets of Rb-rich feldspar (white) and overgrown and cut by K-feldspar (dark grey); (B) Stage 1 (K-Rb)-feldspar (grey to white), with cookeite (black) overgrowing a thin vein of fine-grained mica. Stages of non-porous and porous feldspar follow (grey, centre to left), the latter associated with analcimization of the pollucite (black grading to white, lower left).

Table 4.4: Representative compositions of (K-Rb)-feldspar from Morrua, Mozambique.

	Stage-1						Stage2	Stage3
oxide	1	2	3	4	5	6	7	8
SiO_2	63.12	63.26	61.18	59.69	57.20	59.77	65.06	65.57
Al_2O_3	17.73	17.34	17.09	16.99	16.69	16.32	18.24	17.56
Na_2O	0.02	0.01	0.02	0.01	0.00	0.00	0.02	0.00
K_2O	14.62	12.71	9.22	8.30	5.07	6.45	16.89	16.31
Rb_2O	3.09	6.22	12.37	14.37	19.81	16.62	0.00	0.00
Cs_2O	0.00	0.29	0.29	0.38	0.59	0.39	0.00	0.00
SrO	0.06	0.01	0.08	0.03	0.08	0.19	0.04	0.01
BaO	0.17	0.07	0.03	0.04	0.12	0.00	0.00	0.03
sum	99.28	100.03	100.32	99.90	99.65	99.84	100.40	99.68
	Atomic contents based on 8 atoms of oxygen							
Si	3.005	3.023	3.010	2.993	2.976	3.024	3.006	3.039
Al	0.995	0.977	0.991	1.004	1.024	0.973	0.993	0.959
Na	0.002	0.001	0.002	0.001	0.000	0.000	0.002	0.000
K	0.888	0.775	0.579	0.531	0.337	0.416	0.995	0.964
Rb	0.095	0.191	0.391	0.463	0.663	0.540	0.000	0.000
Cs	0.000	0.006	0.006	0.008	0.013	0.005	0.000	0.000
Sr	0.002	0.000	0.002	0.001	0.003	0.005	0.001	0.000
Ba	0.003	0.001	0.001	0.001	0.002	0.000	0.000	0.001
ΣM	0.989	0.975	0.981	1.005	1.018	0.970	0.998	0.965
M^+	0.994	0.977	0.984	1.007	1.024	0.970	0.999	0.966
TO_2^-	0.995	0.977	0.991	1.006	1.024	0.973	0.993	0.960
ΣT	4.000	4.000	4.002	4.000	4.000	3.999	3.999	3.999

1-2. Main area of stage-1 (K-Rb)-feldspar.
3-5. Outer Rb-rich margins of Stage-1 feldspar.
6. (Rb,K)-feldspar vein cutting Stage-1.
7. Stage-2 non-porous K-feldspar.
8. Stage-3 porous K-feldspar.

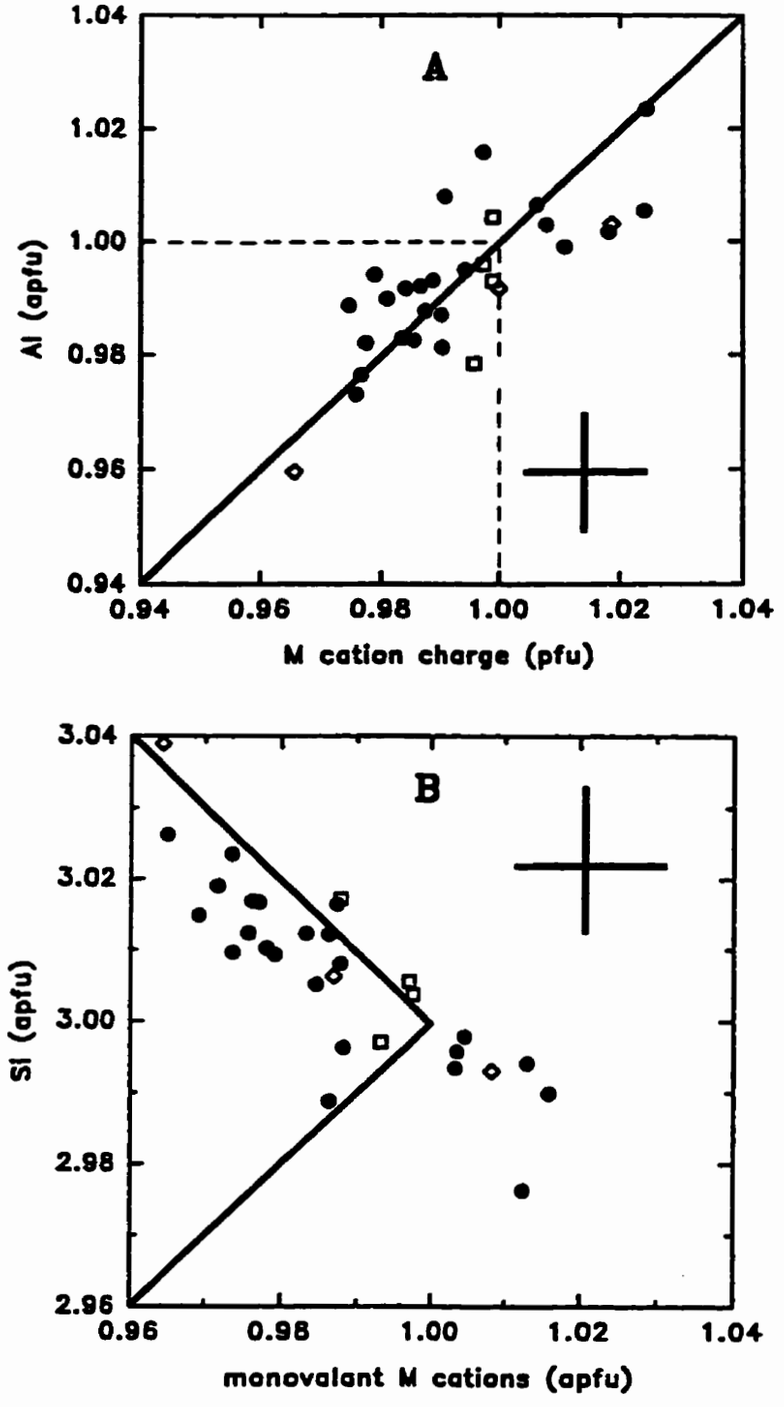

Fig. 4.8. Element variation in (K-Rb)-feldspar from the Morrua pegmatite: (A) Al *vs.* *M*-cation charge; (B) Si *vs.* monovalent *M* cations. Symbols: Stage 1 (•), Stage 2 (□) and Stage 3 (◇) feldspars. Error bars and substitutional lines as in Figure 4.3.

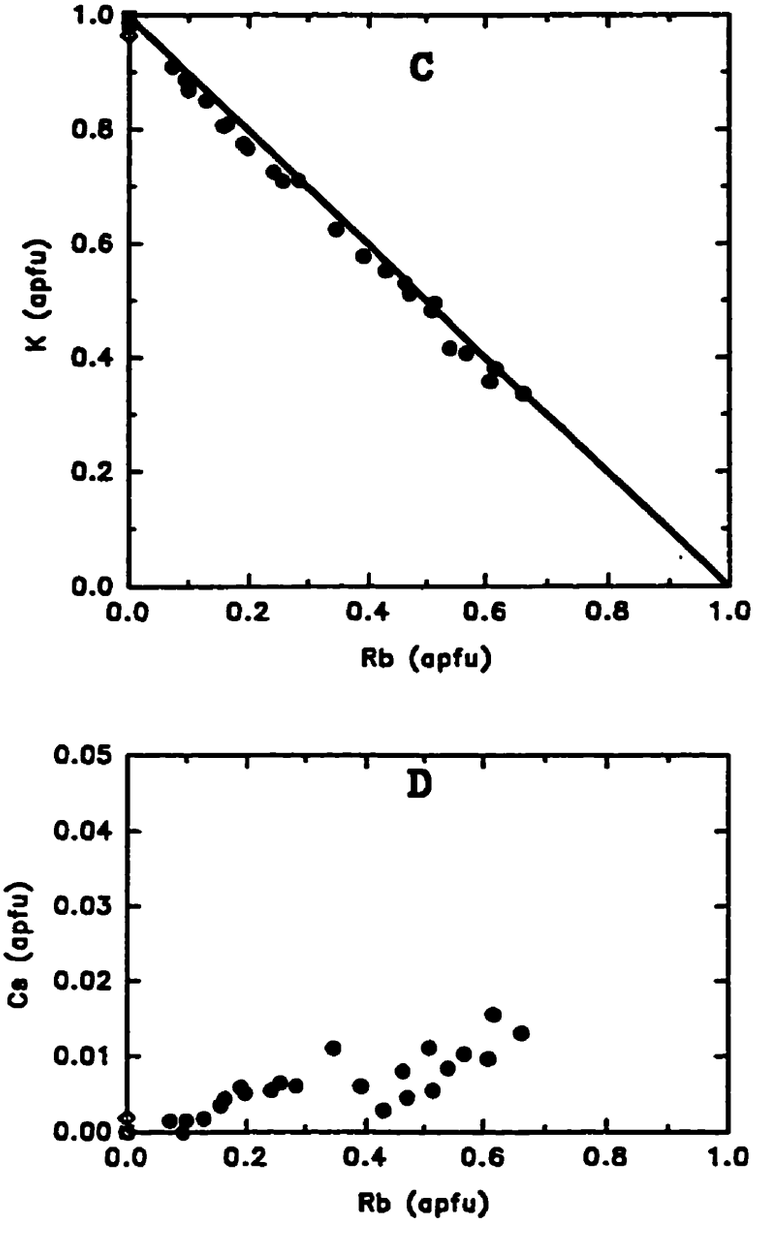

Fig. 4.8. Element variation in (K-Rb)-feldspar from the Morrua pegmatite: (C) K *vs.* Rb, with a line indicating $\Sigma M = 1$; (D) Cs *vs.* Rb.

The Tin Mountain spodumene-subtype complex-type pegmatite is located in the pegmatite field surrounding the Harney Peak granite in the southern Black Hills, Custer County, South Dakota. The 200 m long, 20 m wide and 30 m thick L-shaped pegmatite consists of five major textural/mineralogical zones, each of which comprises ~20% of the volume of the pegmatite (Walker *et al.* 1989b). At least 45000 kg of pollucite was mined from 4 separate masses located near the pegmatite core (composed of quartz, spodumene and mica with minor albite, beryl and amblygonite), and adjacent to the second intermediate zone (composed largely of microcline perthite with minor quartz, albite and muscovite). The highest concentrations of Rb occur in feldspar of the first- and second-intermediate zones, rather than in the third-intermediate zone which crystallized later. The Rb-Sr and other radiogenic isotope systems investigated so far were disturbed by primary consolidation and subsolidus processes (Walker *et al.* 1989a).

I studied one sample of microcline perthite from the second-intermediate zone, and several samples of pollucite and altered material from the margins of pollucite bodies. Most of my observations concerning Rb-rich feldspar come from one small grain of altered material closely associated with pollucite; insufficient material is available for the separation of Rb-rich feldspar from its host K-feldspar. However, in the search for additional Rb-rich feldspar, a total of 27 thin sections were examined (without success) from 8 samples of pollucite and 12 samples of altered pollucite.

The sequence of alteration of the pollucite from Tin Mountain is given in Figure

4.9. Veins of coarse-grained lepidolite (+ quartz) cross-cut the pollucite, as well as thin veins of fine-grained muscovite and spodumene. Adularia overgrowths occur on the surfaces of both types of veins. Margins of pollucite bodies are replaced by a massive green rock, forming pseudomorphs which preserve the early mica veining but with no remnants of pollucite. Pseudomorphs are composed of fine-grained quartz, muscovite, cookeite and untwinned K-feldspar, with minor calcite, apatite, albite and Fe-oxide minerals. The analcimization of pollucite and this late metasomatic alteration are responsible for reduced ore grades of the pollucite from an average of 32 wt. % Cs_2O in fresh material to only 1 wt. % Cs_2O in the altered material (Kennedy 1938).

Microcline perthite from the second-intermediate zone has 1.2 wt. % Rb_2O, 0.42 wt. % Na_2O, 0.11 wt. % Cs_2O and 0.44 wt. % P_2O_5 (Table 4.8). BSE imaging indicates that Rb redistribution is negligible. P_2O_5 is not found in any of the later generations of feldspar. The adularia overgrowths in pollucite have a slightly variable composition, with the bulk of the material showing 1.79-2.06 wt. % Rb_2O and 0.02-0.08 wt. % Cs_2O. Locally, the adularia is Rb-poor, with minor Ba (0.16-0.23 wt. % BaO and 0.00-0.72 wt. % Rb_2O).

The K-feldspar in the altered margins of pollucite bodies comprises 5-20 vol. % of the rock. Most has near-Or_{100} composition with 0.2-0.5 wt. % BaO, but BaO shows local increases to 1.8 wt. %. Areas of Rb-enrichment are very rare and volumetrically insignificant; the Rb-enriched feldspars contain no Ba but have up to 5.8 wt. % Rb_2O. Rare clusters of Rb-rich feldspar, with 50-60 mol. % $RbAlSi_3O_8$ (up to 19 wt. % Rb_2O and 1.2 wt. % Cs_2O; Table 4.5), are found in

porous Or_{100} adularia + cookeite (Fig. 4.10A) closely associated with pollucite. Intermediate compositions of (K,Rb)-feldspar are rare (Fig. 4.10B), and are locally crossed by veins of Rb-rich feldspar; both are replaced by Or_{100} adularia (Fig. 4.10C). (K,Rb)-feldspar of intermediate composition is found locally with a complex internal zonation with variable K/Rb ratio (Fig. 4.10D).

The microcline perthite has near-ideal stoichiometric features (Table 4.5); however, most of the later generations of feldspar have a distinct *M*-cation deficiency (Fig. 4.11A). Although the average value of (Al-P) is 0.996 *apfu*, the average *M*-cation charge is 0.985 *pfu* (Fig. 4.11A). The average (Si+2P) value is 3.007, but individual values from 3.00 to 3.02 *apfu* suggest less than 2 mol.% $\square Si_4O_8$ (Fig. 4.11B). A plot of K *vs.* Rb indicates that clusters of Rb-rich feldspar have ~40-60 mol.% Rbf (Fig. 4.11C). The Rb-richest feldspar has 64 mol.% Rb-f and 2.7 mol.% of a hypothetical Cs-feldspar component (Fig. 4.11D).

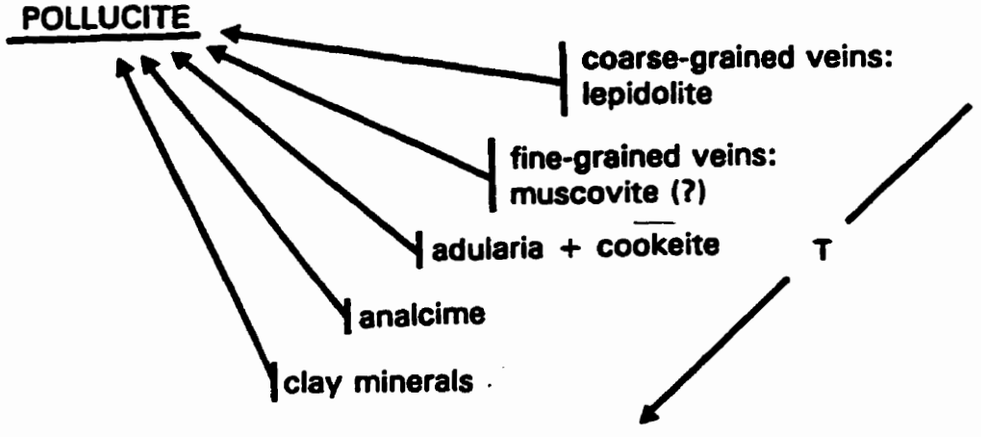

Fig. 4.9. Schematic sequence of alteration products after pollucite from Tin Mountain, South Dakota. The arrow (T) indicates later products appearing at decreasing temperature (see Figure 4.30 for T estimates).

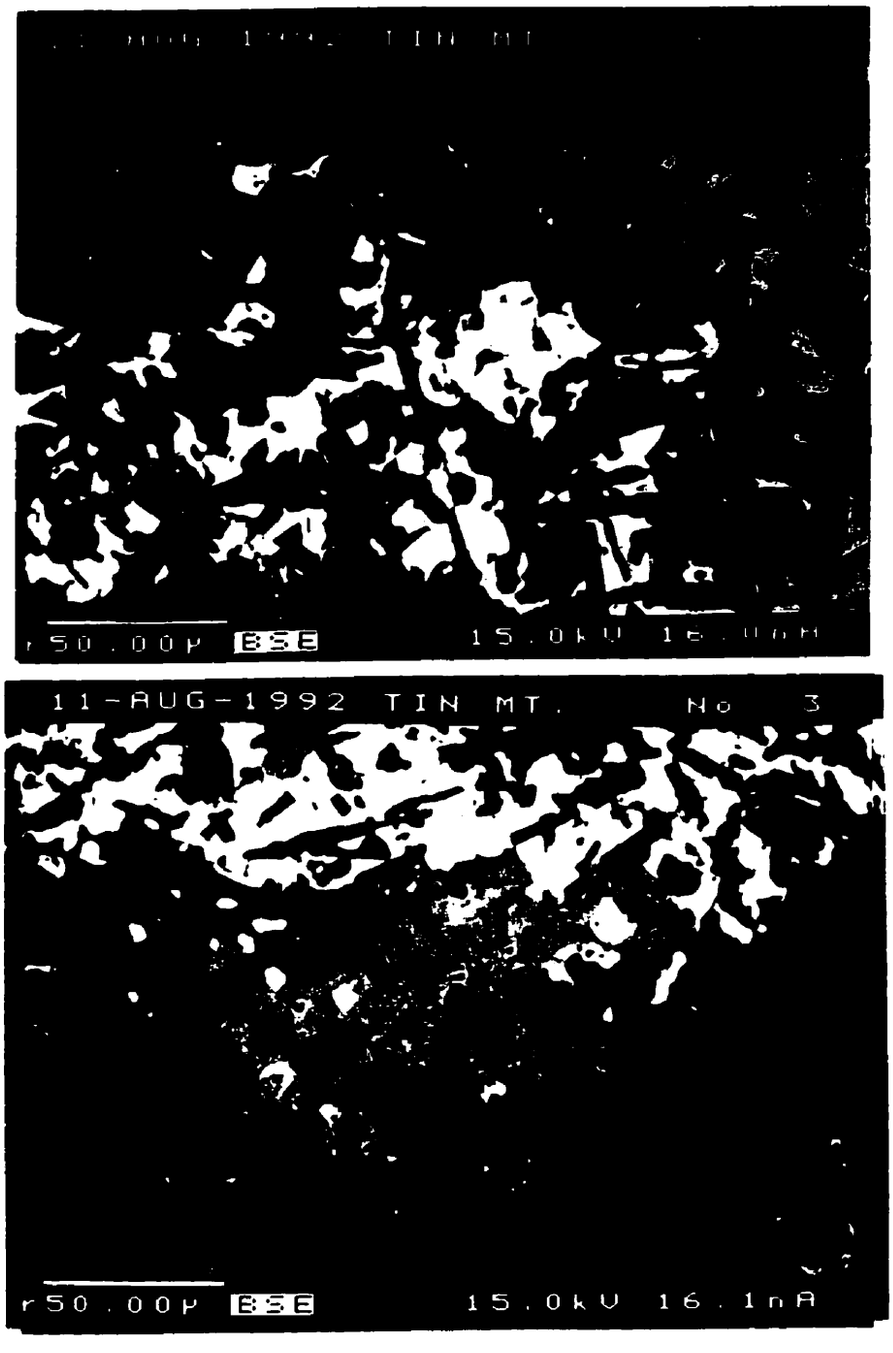

(A)

(B)

Fig. 4.10. BSE images of feldspar from Tin Mountain: (A) and (B) Rb-rich (white) and variable-Rb feldspar (grey to white) assocociated with cookeite (black laths) in Rb-free adularia host (dark grey, porous).

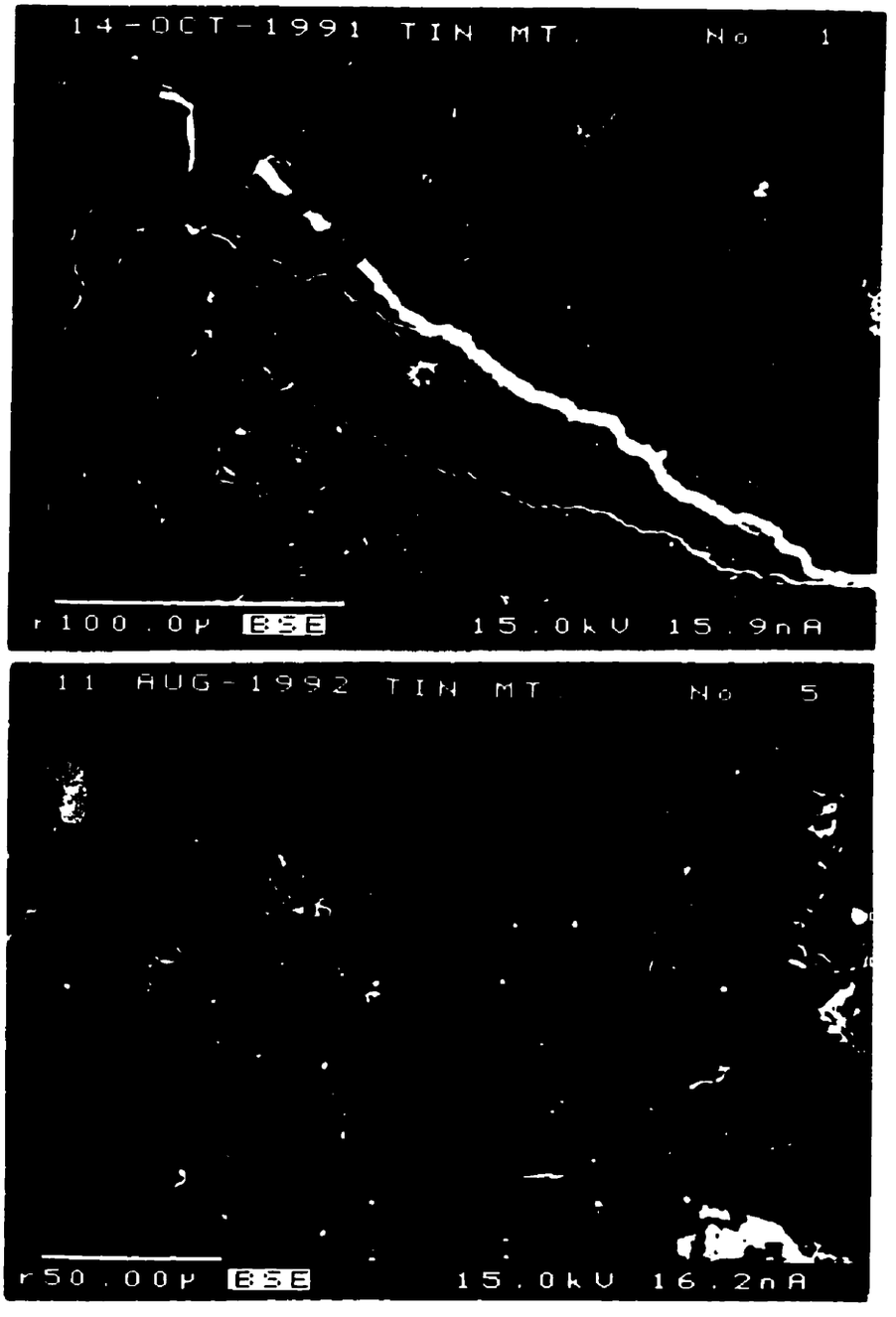

(C)

(D)

Fig. 4.10. BSE images of feldspar from Tin, Mountain: (C) Variable-Rb feldspar (variable grey) containing cookeite (black), cut by a vein of Rb-rich feldspar (white) and replaced by Rb-free adularia (dark grey) and quartz (grey); (D) Complex zoning in (K,Rb)-feldspar (variable grey), hosted by adularia (dark grey).

Table 4.5: Representative compositions of (K-Rb)-feldspar from Tin Mountain, South Dakota.

oxide	1	2	3	4	5	6	7	8
SiO_2	63.73	64.66	62.84	63.68	60.31	59.15	58.37	58.10
Al_2O_3	18.61	18.32	18.67	17.67	17.04	16.30	16.62	16.31
P_2O_5	0.44	0.01	0.00	0.00	0.00	0.00	0.00	0.02
Na_2O	0.42	0.01	0.22	0.00	0.00	0.00	0.00	0.00
K_2O	15.41	16.95	15.41	13.72	9.09	5.64	5.79	4.51
Rb_2O	1.22	0.00	0.00	4.88	13.21	17.49	18.32	19.24
Cs_2O	0.16	0.00	0.02	0.11	0.23	0.90	0.51	1.21
SrO	0.00	0.10	0.18	0.00	0.14	0.13	0.02	0.11
BaO	0.00	0.00	1.77	0.00	0.05	0.06	0.07	0.00
sum	100.08	100.06	99.28	100.10	100.16	99.74	99.84	99.51
	Atomic contents based on 8 atoms of oxygen							
Si	2.965	2.997	2.965	3.016	2.998	3.021	2.996	3.009
Al	1.020	1.001	1.038	0.986	0.998	0.981	1.005	0.996
P	0.017	0.000	0.000	0.000	0.000	0.000	0.000	0.001
Na	0.038	0.001	0.020	0.000	0.000	0.000	0.000	0.000
K	0.915	1.002	0.928	0.829	0.577	0.367	0.379	0.298
Rb	0.036	0.000	0.000	0.148	0.422	0.574	0.604	0.641
Cs	0.003	0.000	0.000	0.002	0.005	0.020	0.011	0.027
Sr	0.000	0.003	0.005	0.000	0.004	0.004	0.001	0.003
Ba	0.000	0.000	0.033	0.000	0.001	0.001	0.001	0.000
ΣM	0.992	1.006	0.986	0.980	1.009	0.966	0.996	0.968
M^+	0.992	1.009	1.024	0.980	1.014	0.971	0.999	0.971
TO_2^-	1.003	1.000	1.039	0.986	0.998	0.981	1.006	0.995
ΣT	4.003	3.998	4.004	4.002	3.996	4.003	4.002	4.006
Si/Al	2.99	3.00	2.85	3.06	3.00	3.08	2.98	3.03

1. K-phase of microcline perthite, second-intermediate zone.
2. Adularia replacing margins of pollucite bodies.
3. Ba-rich adularia, from margin of pollucite bodies.
4. Main area of zoned (Rb,K)-feldspar in pollucite (Fig. 4.10D).
5. Rb-rich tip of zoned (Rb,K)-feldspar adularia (Fig. 4.10D).
7, 8 and 9. Clusters of Rb-rich feldspar hosted by the Or_{100} adularia of Fig. 4.10 A,B.

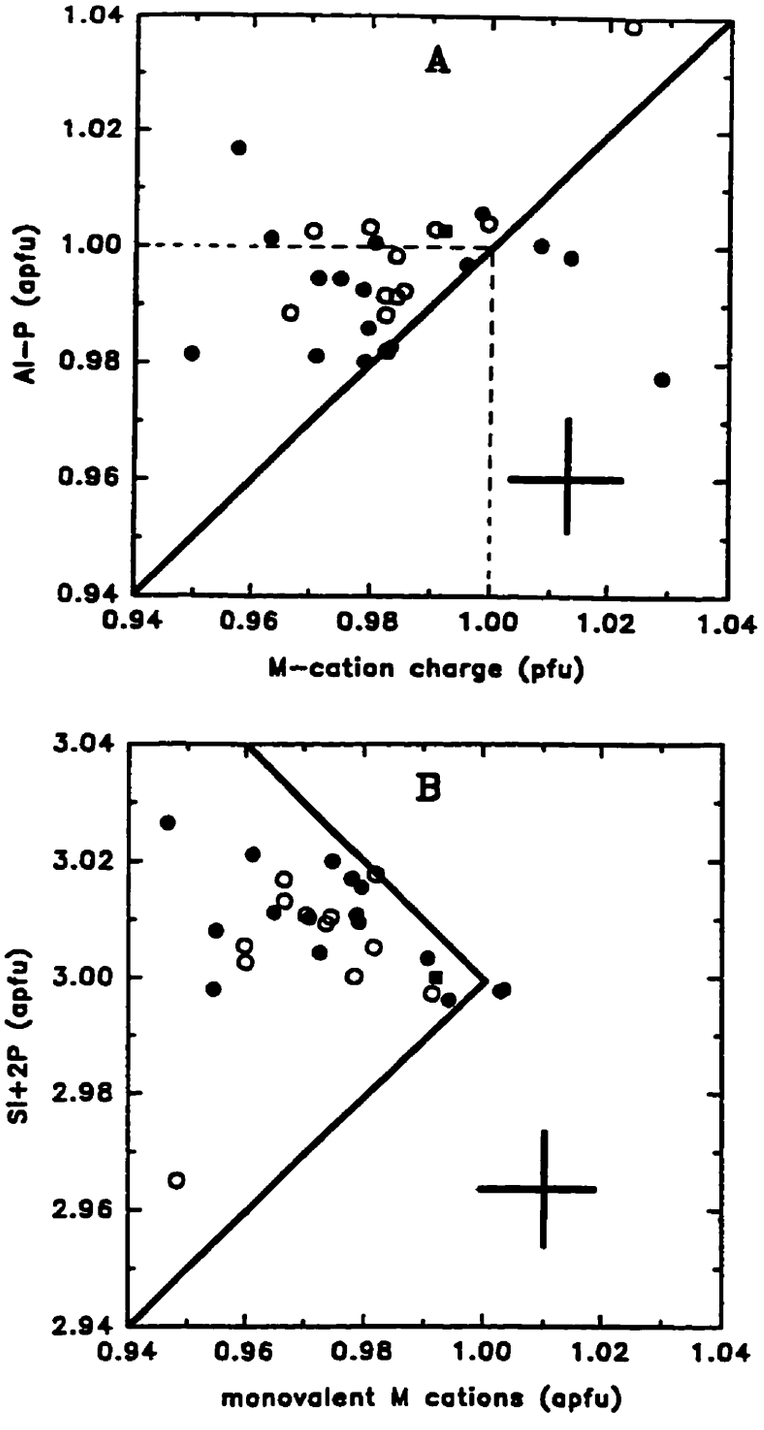

Fig. 4.11. Element variation in (K-Rb)-feldspar from the Tin Mountain pegmatite: (A) (Al-P) *vs.* *M*-cation charge; (B) (Si+2P) *vs.* monovalent *M* cations. Symbols: K-phase of microcline-perthite (■); (K-Rb)-feldspar replacing pollucite (•); (K,Rb)-feldspar replacing margins of pollucite body (○). Error bars and substitutional lines as in Figure 4.3.

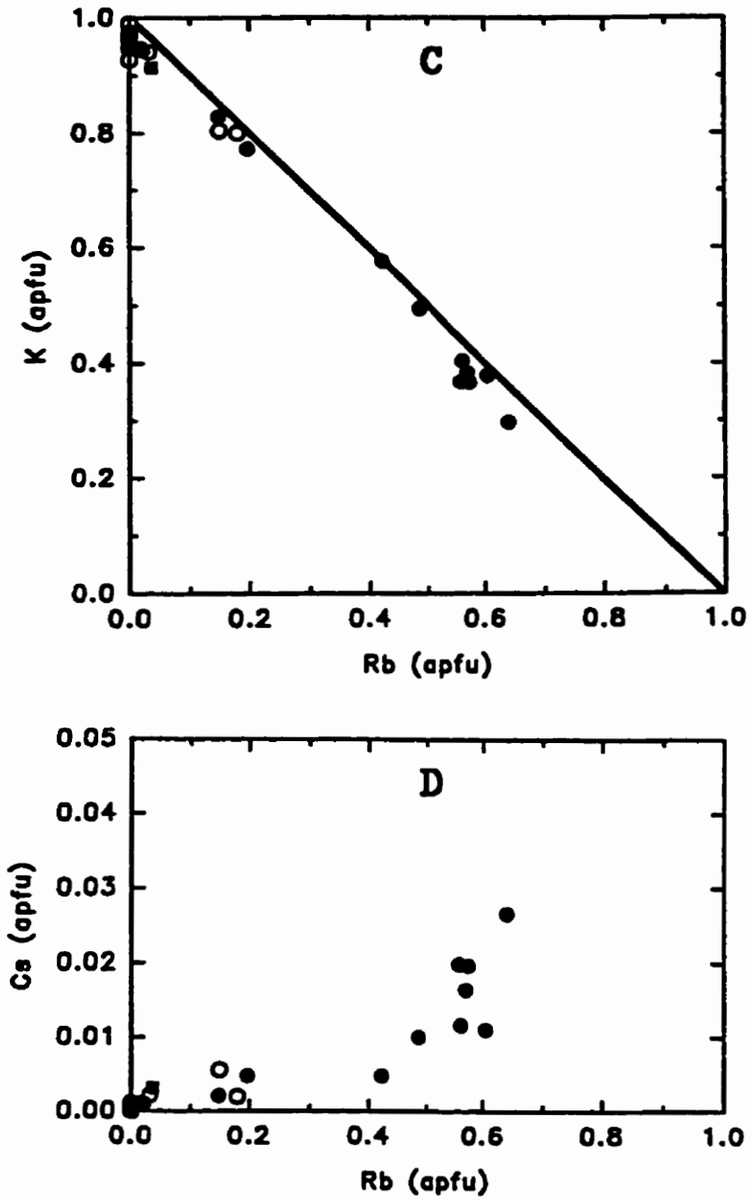

Fig. 4.11. Element variation in (K-Rb)-feldspar from the Tin Mountain pegmatite: (C) K *vs.* Rb, with a line indicating $\Sigma M = 1$; (D) Cs *vs.* Rb.

4.3 *Multiple generations of feldspar from the Rubellite pegmatite, NW Ontario*

The spodumene-subtype complex-type Rubellite pegmatite lies 15 km W-NW of Fort Hope, near Lilypad Lakes, NW Ontario (Wallace 1978), and belongs to the most fractionated of the pollucite-bearing pegmatites in the Fort Hope field. The pegmatite is rather isolated, but about 50 hand specimens were collected by Mark Cooper on two visits by helicopter. Additional samples were collected by Petr Černý. The pegmatite is poorly zoned; the dominant mineral assemblage includes semi-transparent black to dark grey microcline, quartz, spodumene and coarse-grained albite. One of the latest primary phases is pollucite, in association with beryl and rubellite. Spodumene grains near pollucite have a myrmekitic intergrowth with quartz, and are rimmed by pollucite with end-member composition (Teertstra & Černý 1995). Fine-grained albite + quartz (± microlite) and lepidolite typically fills interstices between large primary crystals; and vein and partly replace K-feldspar and pollucite. Late muscovite is also present locally. Late-hydrothermal minerals include calcite, phosphates and bavenite. Significant proportions of the black K-feldspar are replaced by porous, opaque salmon-coloured K-feldspar + purple fluorite ± calcite. A total of 25 polished thin-sections were prepared from the hand specimens and examined by optical microscopy and BSE imaging.

Pollucite forms monomineralic segregations up to 10 cm in size and interstitial to primary K-feldspar, spodumene and albite. Fine-grained albite (+ quartz) and lepidolite occur along contacts between these minerals; although albite and lepidolite may have crystallized from residual intergranular fluid, there is evidence for local veining and replacement of primary phases. Segregations of

pollucite also are crosscut by 1-2 cm-wide veins of quartz and coarse-grained lepidolite, followed by 1-2 mm-wide veinlets of fine-grained muscovite and spodumene. Both types of veins are locally overgrown by small single grains (< 0.5 mm) of untwinned K-feldspar; these also occur fully embedded in the pollucite, but are not abundant.

Late Rb-rich feldspars are associated with reconstitution of blocky black microcline and with adularia in pollucite, whereas the salmon-coloured K-feldspar is virtually Rb-free.

The black, tartan-twinned, slightly disordered microcline is largely non-perthitic but contains abundant scattered grains of albite. SEM examination shows that microporosity in the black microcline (Fig. 4.12A) is developed mainly in areas which are turbid in thin section. Black feldspar closest to the pollucite has extreme coarsening of microcline twin domains (up to 1 cm), and contains the smallest amounts of albite. Coarse albite lamellae up to 2 mm wide are rare and are mainly replaced by K-feldspar; lamellae which are partly replaced have a fragmented texture. Areas adjacent to lamellae or former lamellae show evidence of extensive interaction with fluid: these are microporous, turbid in thin section, and are associated with abundant apatite < 0.5 μm in size. BSE imaging shows that the black K-feldspar has a patchy composition, particularly near areas in which microporosity is well developed. Rb_2O values for the black feldspar closely associated with pollucite vary from 2.7-4.9 wt.% (8.3-15.3 mol.% Rbf), Na_2O varies from 0.16-0.63 wt.% (1.5-5.6 mol.% Ab) and P_2O_5 distribution is patchy but reaches 0.56 wt.%. Microcline is Rb-depleted in areas adjacent to irregular partly replaced albite lamellae (Fig. 4.13A). Diffuse veinlets of Rb-rich feldspar

show a distinct relationship (parallel or perpendicular) to cleavage planes of the host (Fig. 4.13A, B, C). Some veinlets consist of a mixture of Rb-rich (up to 13.4 wt.% Rb_2O) and Rb-poor feldspar (Fig. 4.13B), both of which are Na- and P-poor.

The late salmon-coloured K-feldspar is extremely porous, with pores to 1 mm in size (Fig. 4.12B, and left side of 4.12A). Except for local enrichment in Ba, the bulk of the salmon K-feldspar has Or_{100} composition. In association with albite and abundant fluorite ($\pm$ calcite), salmon-coloured K-feldspar forms pseudomorphs after black microcline, preserving its cleavage and textural features such as albite-lepidolite veining. In the initial stages of replacement, the salmon K-feldspar preferentially replaces one set of the microcline twins. In later stages, the rest of the microcline is replaced until all traces of twinning are destroyed. Rb is dispersed in the process (Fig. 4.12D). The salmon-coloured K-feldspar is extremely fine-grained, to the extent of being almost opaque in thin section. Except for some of the larger grains (< 0.5 mm) which seem to be untwinned, optical characteristics could not be determined. XRD analysis indicates a structure corresponding to end-member maximum microcline.

In terms of high Rb content, the small grains of adularia which replace pollucite are the most interesting (Table 4.6). Individual grains are homogeneous in BSE imaging, but Rb_2O varies between grains from 6-12 wt.%. Margins of the grains are irregular in shape; small (< 5-15 μm) outliers in the pollucite are richer in Rb than the main parts and have up to 22 wt.% Rb_2O (74 mol.% Rbf) and 0.9 wt.% Cs_2O (2 mol.% Csf). Representative compositions are given in Table 4.6.

Mean values for (Al-P) of 1.001(18) and *M*-cation charge of 0.991(20) *pfu* suggest minor light-element substitution (Fig. 4.14A). The Al-rich data belong to the late salmon-coloured K-feldspar with local substitution of Ba. Data are scattered about (Si+2P) = 3.002(17) *apfu* and an average of 0.984(15) monovalent *M* cations (Fig. 4.14B), indicating less than 2 mol.% $\square Si_4O_8$ substitution. A mean ΣT of 4.003(4) *apfu* indicates relatively close agreement with the ideal formula. A plot of K *vs.* Rb shows that compositions lie close to the K-feldspar - Rb-feldspar join (Fig. 4.14C), with minor deviations of $\Sigma M < 1$ due to substitution of □, Na, Ba and Cs. The small outlying grains in pollucite have atomic proportions of Rb > K and these also have the highest Cs values (Fig. 4.14D).

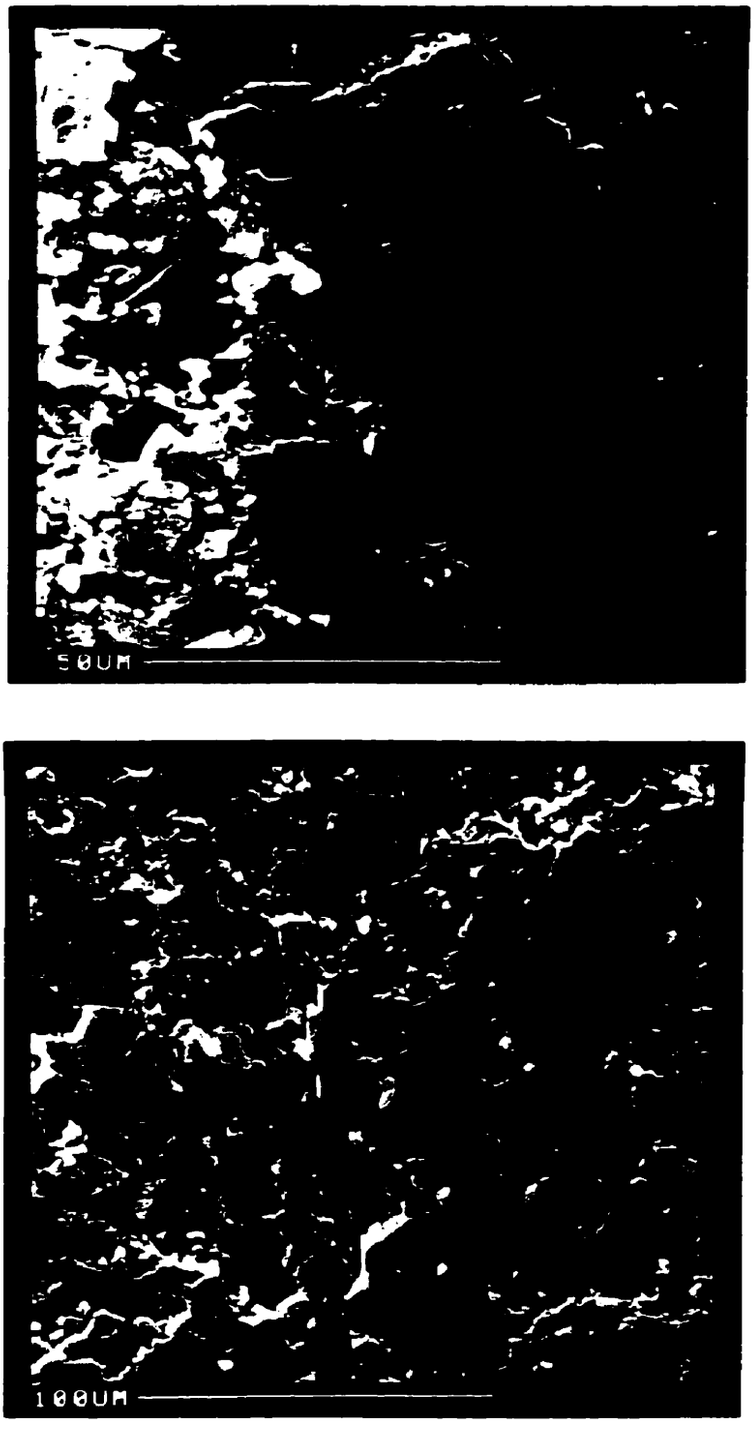

(A)

(B)

Fig. 4.12. SEM images of cleaved fragments of feldspar from the Rubellite pegmatite: (A) Black microcline with minimal porosity, replaced by salmon-coloured microcline with high porosity from the left; (B) the late salmon-coloured microcline has extreme porosity.

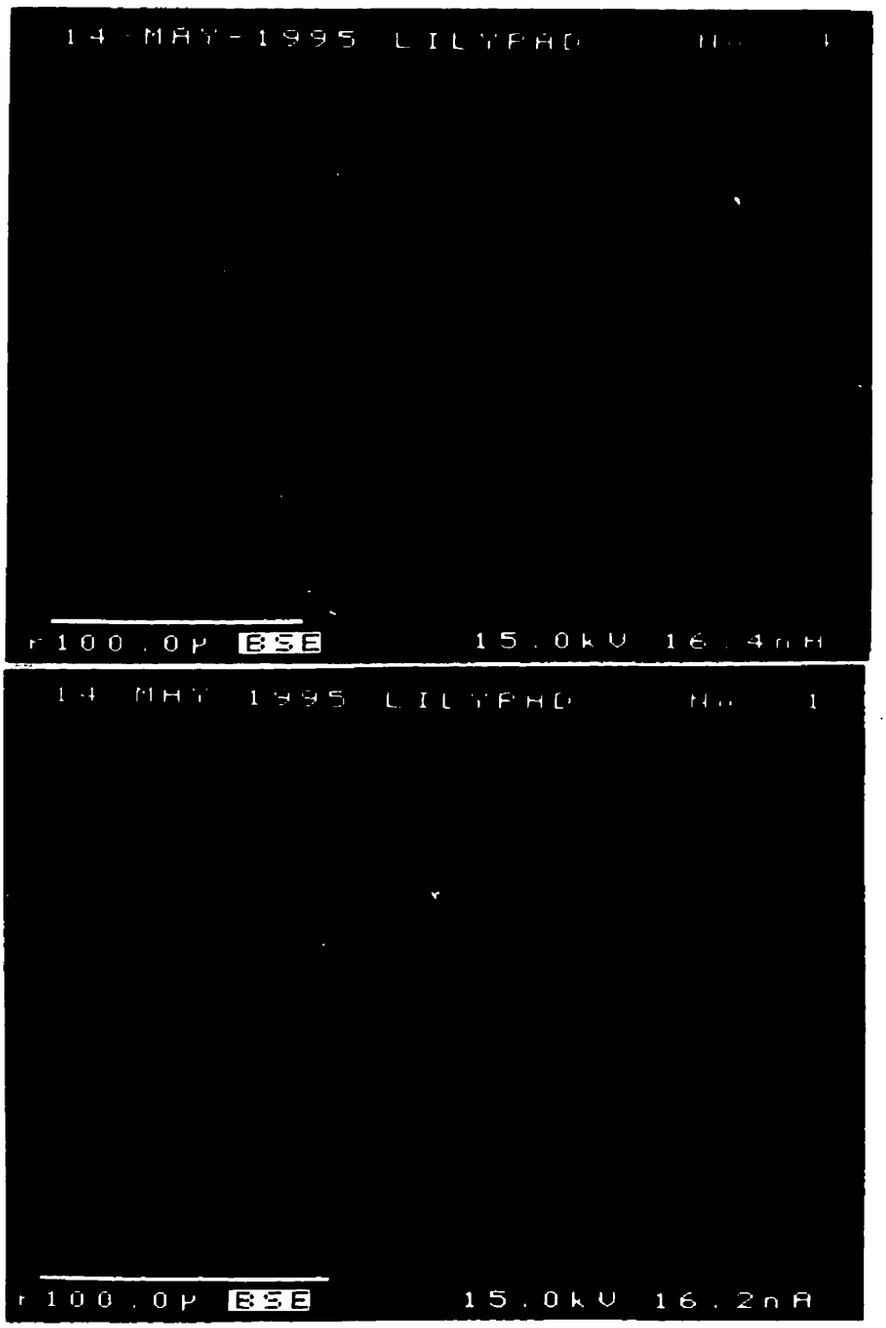

(A)

(B)

Fig. 4.13. BSE images of feldspar from the Rubellite pegmatite: (A) Porous Rb-bearing microcline (grey) with Rb-depleted microcline (dark grey) adjacent to albite (black) and veinlets of Rb-rich feldspar (pale grey); (B) Veinlets of porous (K,Rb)-feldspar (pale grey) with albite (black) running nearly perpendicular to the cleavage of blocky microcline, and crosscut by late adularia (dark grey, highly porous or plucked).

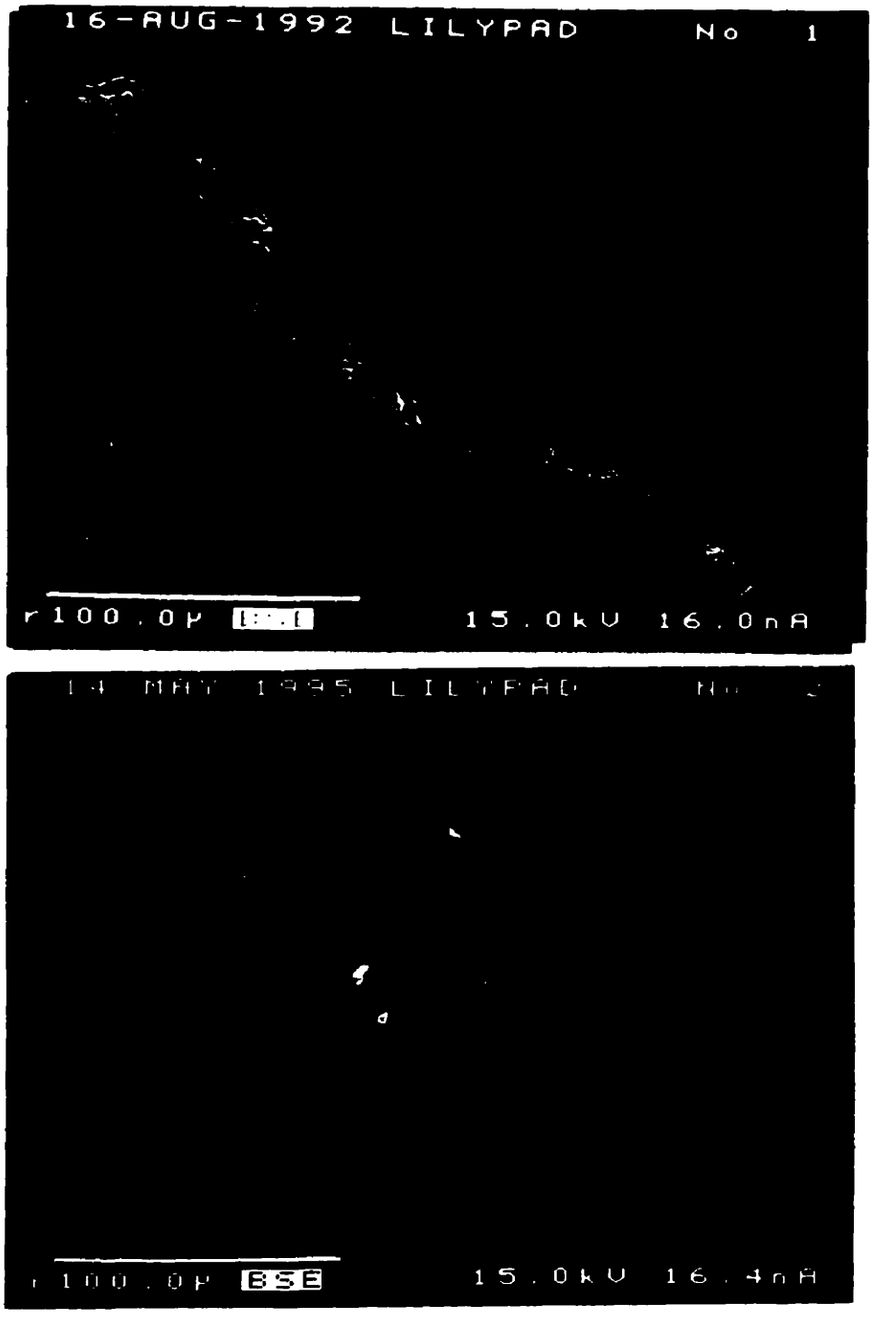

(C)

(D)

Fig. 4.13. BSE images of feldspar from the Rubellite pegmatite: (C) veinlet of Rb-enriched feldspar (light grey), parallel to the cleavage of the variable-composition host microcline; (D) Remnant blocks of Rb-bearing microcline (light grey) replaced by porous K-feldspar (dark grey) and albite (black) (±apatite, white).

Table 4.6: Representative compositions of (K-Rb)-feldspar from the Rubellite pegmatite, NW Ontario.

oxide	1	2	3	4	5	6	7	8
SiO_2	62.74	63.16	61.80	60.04	61.54	64.15	61.41	57.82
Al_2O_3	17.97	18.18	17.75	17.02	19.09	18.12	17.18	16.13
P_2O_5	0.38	0.32	0.07	0.00	0.00	0.00	0.00	0.00
Na_2O	0.32	0.17	0.10	0.01	0.31	0.14	0.00	0.00
K_2O	13.79	14.03	13.02	8.28	14.50	16.25	10.67	3.72
Rb_2O	2.96	3.42	4.92	13.44	0.00	0.00	9.77	22.00
Cs_2O	0.43	0.35	0.20	0.83	0.08	0.03	0.38	0.92
SrO	0.00	0.09	0.15	0.17	0.33	0.00	0.15	0.05
BaO	0.13	0.00	0.03	0.00	3.44	0.53	0.04	0.17
sum	98.73	99.73	98.12	99.80	99.37	99.24	99.66	100.82
	Atomic contents based on 8 atoms of oxygen							
Si	2.985	2.984	2.990	3.002	2.993	3.002	3.010	3.007
Al	1.005	1.010	1.012	1.001	1.070	0.997	0.990	0.986
P	0.015	0.013	0.003	0.000	0.000	0.000	0.000	0.000
Na	0.029	0.015	0.010	0.001	0.029	0.013	0.000	0.000
K	0.833	0.841	0.804	0.526	0.877	0.965	0.664	0.246
Rb	0.091	0.104	0.153	0.432	0.000	0.000	0.308	0.736
Cs	0.009	0.007	0.004	0.018	0.002	0.001	0.008	0.020
Sr	0.000	0.003	0.004	0.005	0.009	0.000	0.004	0.002
Ba	0.002	0.000	0.000	0.000	0.064	0.010	0.001	0.003
ΣM	0.964	0.970	0.986	0.982	0.981	0.989	0.985	1.007
M^+	0.966	0.973	0.990	0.987	1.055	0.999	0.989	1.012
TO_2^-	0.990	0.997	1.009	1.001	1.071	0.997	0.990	0.986
ΣT	4.006	4.006	4.005	4.004	4.004	4.000	4.000	3.994
Si/Al	3.05	3.02	2.96	3.00	2.74	3.01	3.04	3.05

1-3. Black microcline associated with pollucite.
4. Rb-rich vein in black microcline.
5-6. Late salmon-coloured K-feldspar.
7. Main area of untwinned K-feldspar replacing pollucite.
8. Outlying grain of K-feldspar in pollucite.

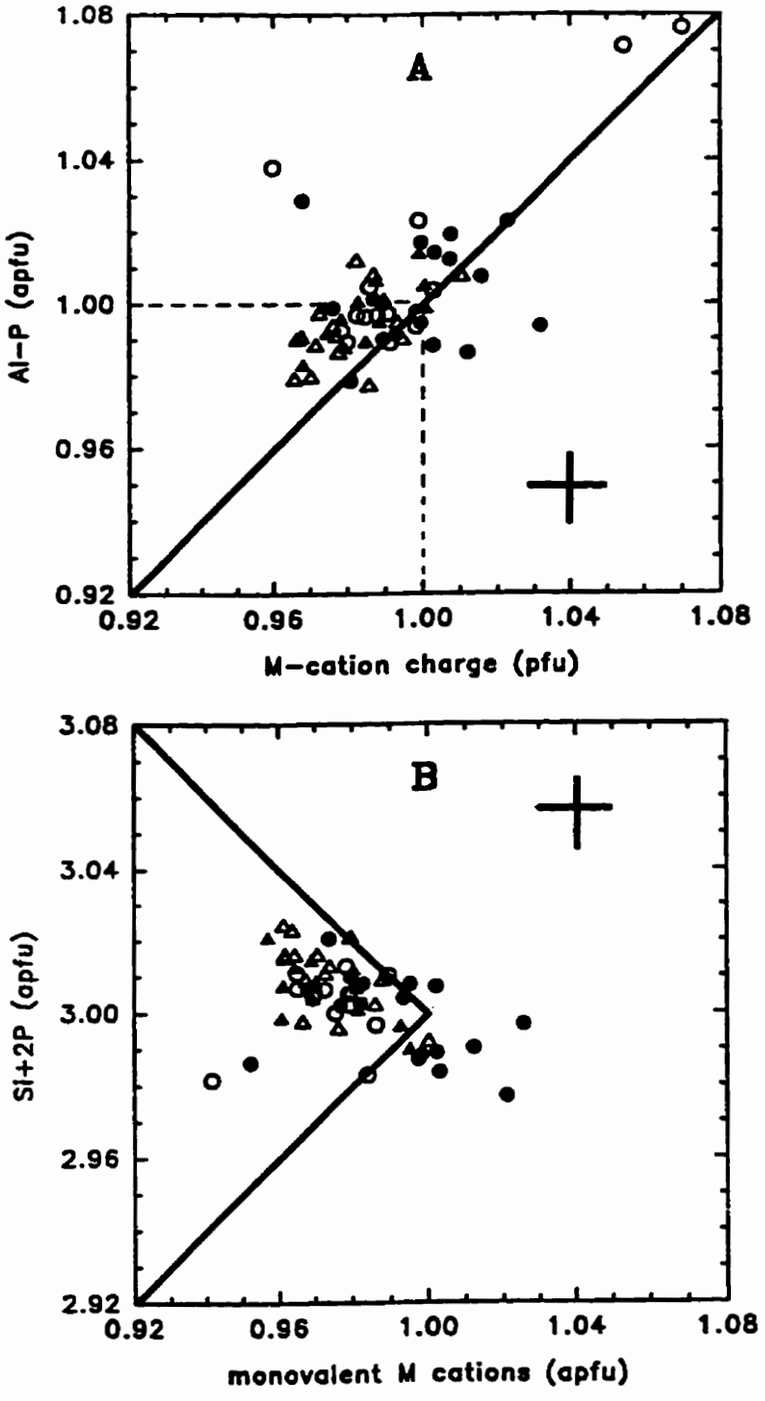

Fig. 4.14. Element variation in (K-Rb)-feldspar from the Rubellite pegmatite: (A) (Al-P) *vs.* *M*-cation charge; (B) (Si+2P) *vs.* monovalent $\dot{M}$ cations. Symbols: black microcline (△) with Rb-rich or Rb-poor veins (▲), salmon-coloured microcline (○) and adularia replacing pollucite (●). Error bars and substitutional lines as in Figure 4.3.

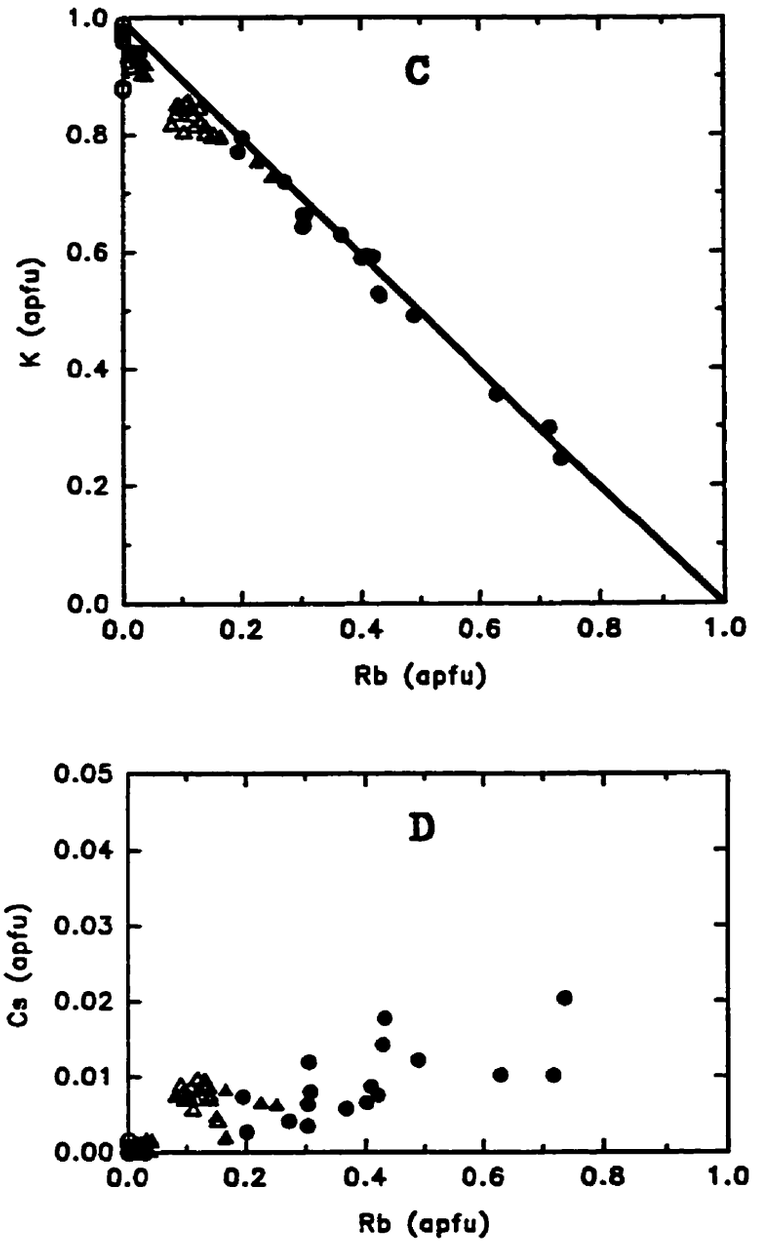

Fig. 4.14. Element variation in (K-Rb)-feldspar from the Rubellite pegmatite: (C) K *vs.* Rb, with a line indicating $\Sigma M = 1$; (D) Cs *vs.* Rb.

4.4 *Feldspar veins in pollucite from Luolamäki, Finland, and Elba, Italy*

The Luolamäki pegmatite is a member of the Somero-Tammela pegmatite field, located about 100 km northwest of Helsinki, SW Finland. Sixty four of the more than 100 pegmatites in the field are known to contain rare-element minerals. The petalite-subtype Luolamäki pegmatite is among the largest of these, and has a well-developed asymmetric internal structure. The hanging-wall contact is bordered by albite-quartz aplite and the footwall contact by fine-grained mica (+ chlorite, sillimanite, schorl). The upper half of the pegmatite is albite-rich and the lower half is K-feldspar-rich: bulk compositions of this microcline-perthite have 1.51 wt.% Rb_2O (Neuvonen & Vesasalo 1960). Large quartz bodies and cleavelanditic units occur near the core. Petalite, quartz and pollucite occur in the core and are cut by veins of cleavelandite, quartz, schorl and muscovite. The pegmatite has negligible contents of lithian micas and no primary spodumene. Accessory minerals include lepidolite, elbaite, beryl, cassiterite, Nb,Ta-minerals, alluaudite, cesian analcime and spodumene.

Pollucite pods contain scattered grains of quartz, apatite and K-feldspar. The sequence of alteration of pollucite, given in Figure 4.15, begins with wide (0.5-2 cm) veins of coarse-grained albite, petalite, non-perthitic microcline (+ lepidolite) and lepidolite (+ quartz) which crosscut the pollucite. Later veins of mica + quartz + apatite (1-2 mm wide) are followed by thinner veins (< 1 mm) of fine-

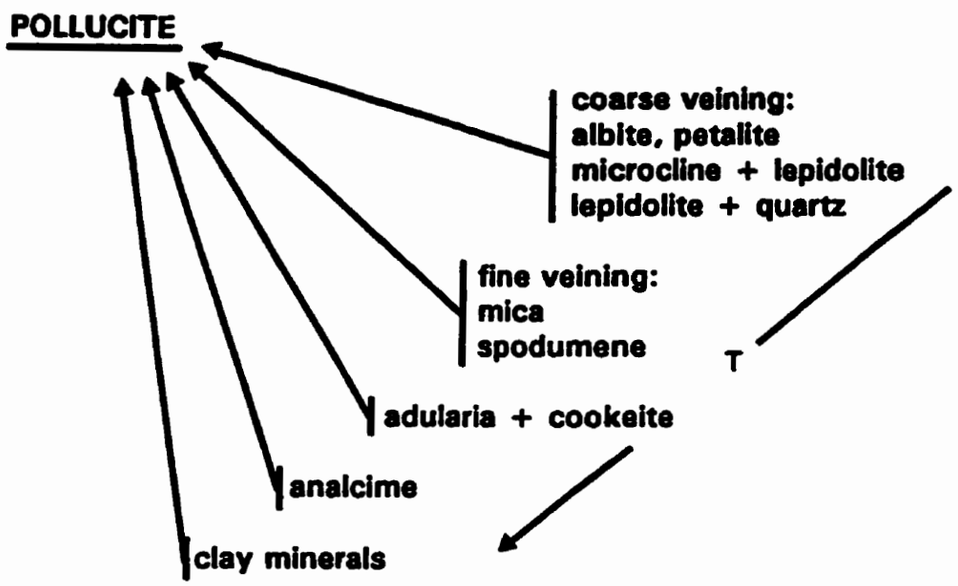

Fig. 4.15. Schematic sequence of alteration products of pollucite from the Luolamäki pegmatite, Finland. The arrow (T) indicates products appearing at decreasing temperature.

grained mica + spodumene. Aggregates of fine-grained K-feldspar (termed "nodules" by Neuvonen & Vesasalo 1960, and "adularia" in Fig. 4.15 and in text below) overgrow many of the veins, replacing both pollucite and vein microcline. Bulk compositions of this K-feldspar from the altered margins of pollucite bodies are non-perthitic and have 2.98 wt.% Rb_2O. Cation-exchange and leaching of pollucite is followed by replacement by clay minerals. Further details on the pegmatite and the products of alteration of pollucite are given in Teertstra *et al.* (1993).

Eight polished thin-sections were prepared, emphasizing microcline veins in pollucite and late adularia. The elements Mg, F, Ga, Fe, Ti, Mn, Ca, Sr, Ba, and Pb were sought by EMP analysis, but except for trace Sr or Ba in late generations, were not detected. P was found only in the microcline.

The vein microcline is tartan-twinned and forms a vein network with uniform optical orientation throughout sizeable volumes of pollucite. The microcline has a patchy compositional distribution, particularly in microporous areas, with wt.% ranges 1.32-5.64 Rb_2O, 0.09-0.29 Na_2O, 0.12-0.32 Cs_2O, and 0.13-0.62 P_2O_5. The variation in Rb_2O corresponds to 4-17 mol.% Rbf. Areas of non-porous microcline tend to have higher contents of Rb, Na and P and a more homogeneous composition than areas which are porous (Fig. 4.16B, 4.16C, 4.16E). (Rb,K)-feldspar is associated with irregular veins of patch albite which

lie roughly parallel to planes of cleavage, and are crosscut by thin veinlets of (Rb,K)-feldspar (Fig. 4.16C). Adularia locally overgrows microcline in parallel orientation, indicating that the microcline substrate provided a surface for easy epitaxial nucleation and growth. (Rb,K)-feldspar adjacent to grains of lepidolite commonly shows a gradation of K/Rb from the host microcline (Fig. 4.16A). Small round blebs of (Rb,K)-feldspar also occur fully embedded in the microcline which is otherwise commonly replaced by end-member K-feldspar (Fig. 4.16B). The assemblage (Rb,K)-feldspar + quartz occurs within some of the irregular and narrow veins of microcline in pollucite (Fig. 4.16D). Compositions of the (Rb,K)-feldspar in microcline do not vary according to association with albite or lepidolite, but range up to a limit of approximately 20.9 wt. % Rb_2O (69 mol. % Rbf) and 1.3 wt. % Cs_2O (3 mol. % Csf). The Rb-richest feldspar (89 mol. % Rbf; Table 4.7) occurs as a small grain between grains of lepidolite and isolated from the microcline.

Adularian (K,Rb)-feldspar replacing pollucite contains 2.98 wt. % Rb_2O in its bulk composition (Neuvonen & Vesasalo 1960) . However, it is actually zoned with variable K/Rb and contains abundant inclusions of cookeite, with minor apatite and small (<1 μm diameter) grains of pollucite (Fig. 4.16F). Late overgrowths of adularia tend to be extremely porous and are associated with leaching and analcimization of pollucite. The bulk of the adularia has end-member $KAlSi_3O_8$ composition, but local gradations to (Rb,K)-feldspar are relatively common. The

adularian (Rb-K)-feldspar has a similar compositional range and upper compositional limit as the (Rb-K)-feldspar in microcline, with up to 20.95 wt.% Rb_2O (70 mol.% Rbf). Representative compositions are given in Table 4.7.

Mean values for (Al-P) of 0.995(15) atoms per formula unit (*apfu*) and *M*-cation charge of 0.987(16) *pfu* suggest on average 1 at.% light-element substitution, with individual values up to 4 at.% (Fig. 4.17A). Compositional trends indicate widespread substitution of $\square Si_4O_8$, with individual values attaining 4 mol.% $\square Si_4O_8$ substitution (Fig. 4.17B). Mean values for (Si+2P) of 3.007(14) and mean values of ΣT of 4.002(4) indicate good overall agreement with the feldspar formula, taking into account the $\square Si_4O_8$ and berlinite substitutions. Sums of (K+Rb) are slightly lower than the ideal 1.0 *apfu* line because of minor □, Na and Cs (Fig. 4.17C) and the mean ΣM value is 0.984(15) *apfu*. Substitution of Cs increases irregularly with Rb to a maximum of approximately 0.03 *apfu* (3 mol.% Csf), corresponding to 1.5 wt.% Cs_2O (Fig. 4.17D).

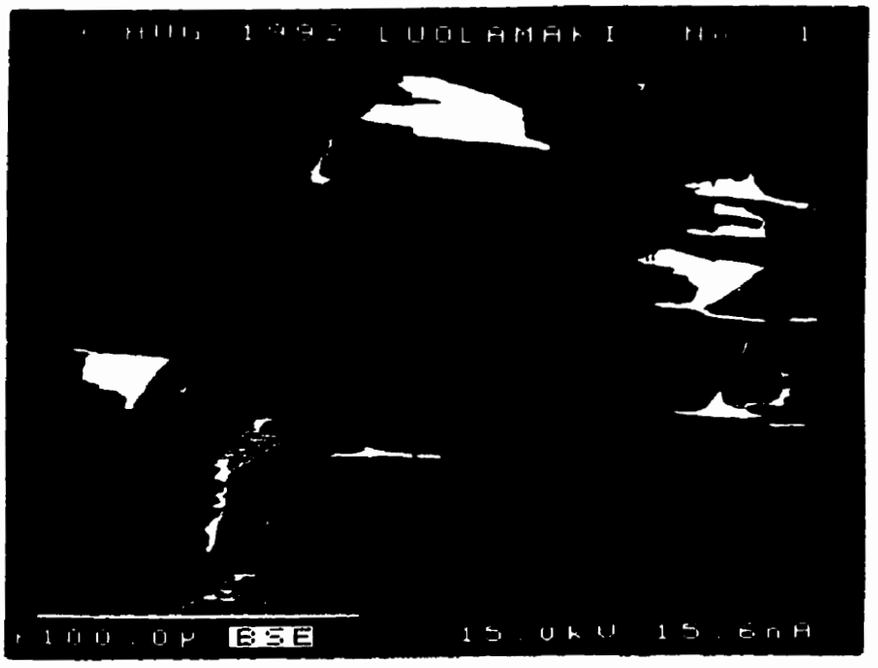

(A)

(B)

Fig. 4.16. BSE images of feldspar from Luolamäki: (A) (Rb,K)-feldspar (white) between grains of lepidolite (black), showing a compositional gradient from microcline (grey) ; (B) laths of lepidolite (interlayer apatite - white) in microcline (grey) associated with Rb-rich feldspar (white) and surrounded by Rb-poor K-feldspar (dark grey).

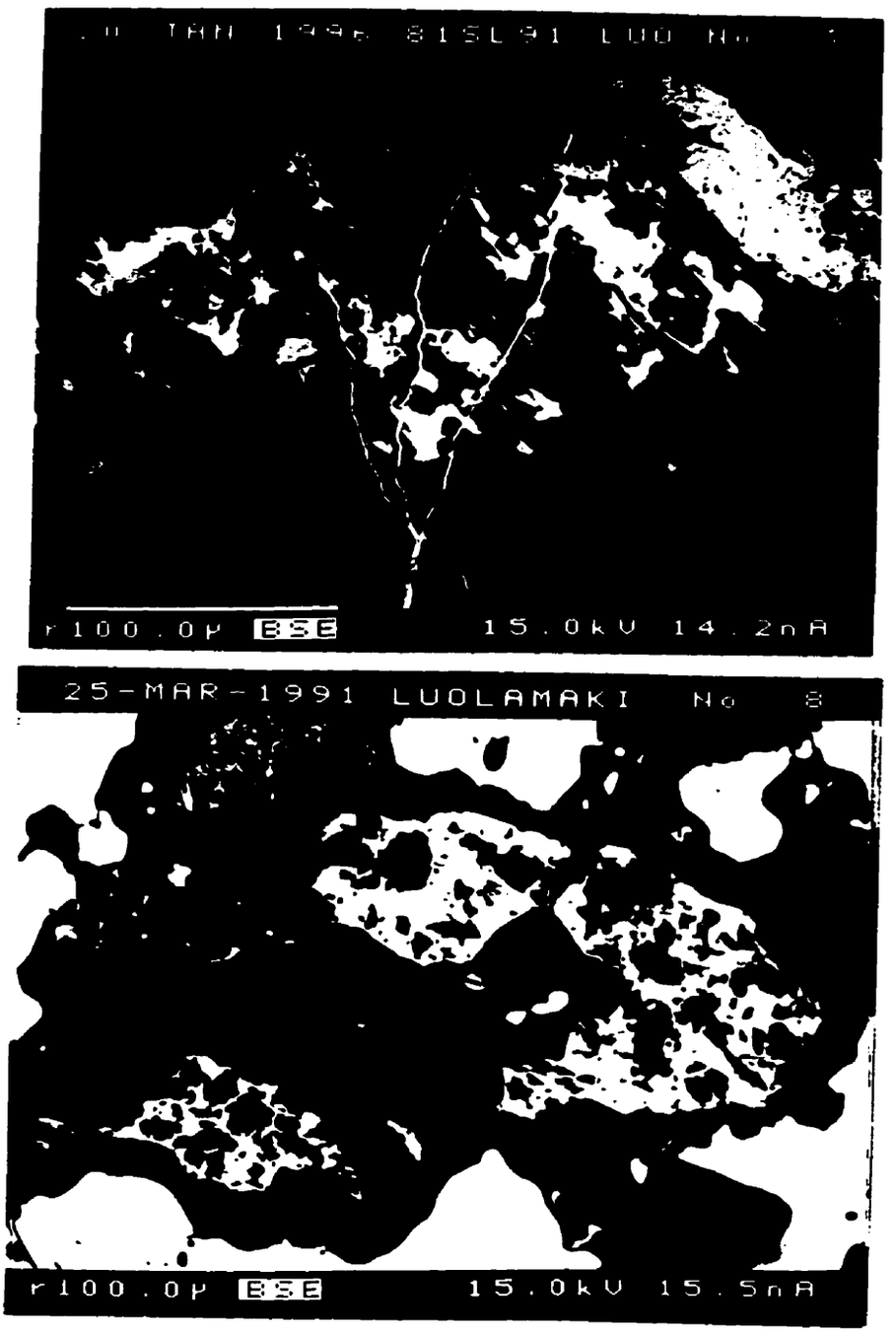

(C)

(D)

Fig. 4.16. BSE images of feldspar from Luolamäki: (C) microporous microcline with a patchy distribution of Rb (grey) contains aggregates of albite (black) + (Rb,K)-feldspar (white), cut by veinlets of (Rb,K)-feldspar; (D) blebs of (Rb,K)-feldspar (white) + quartz (black) in Rb-bearing K-feldspar (grey), surrounded by pollucite (white).

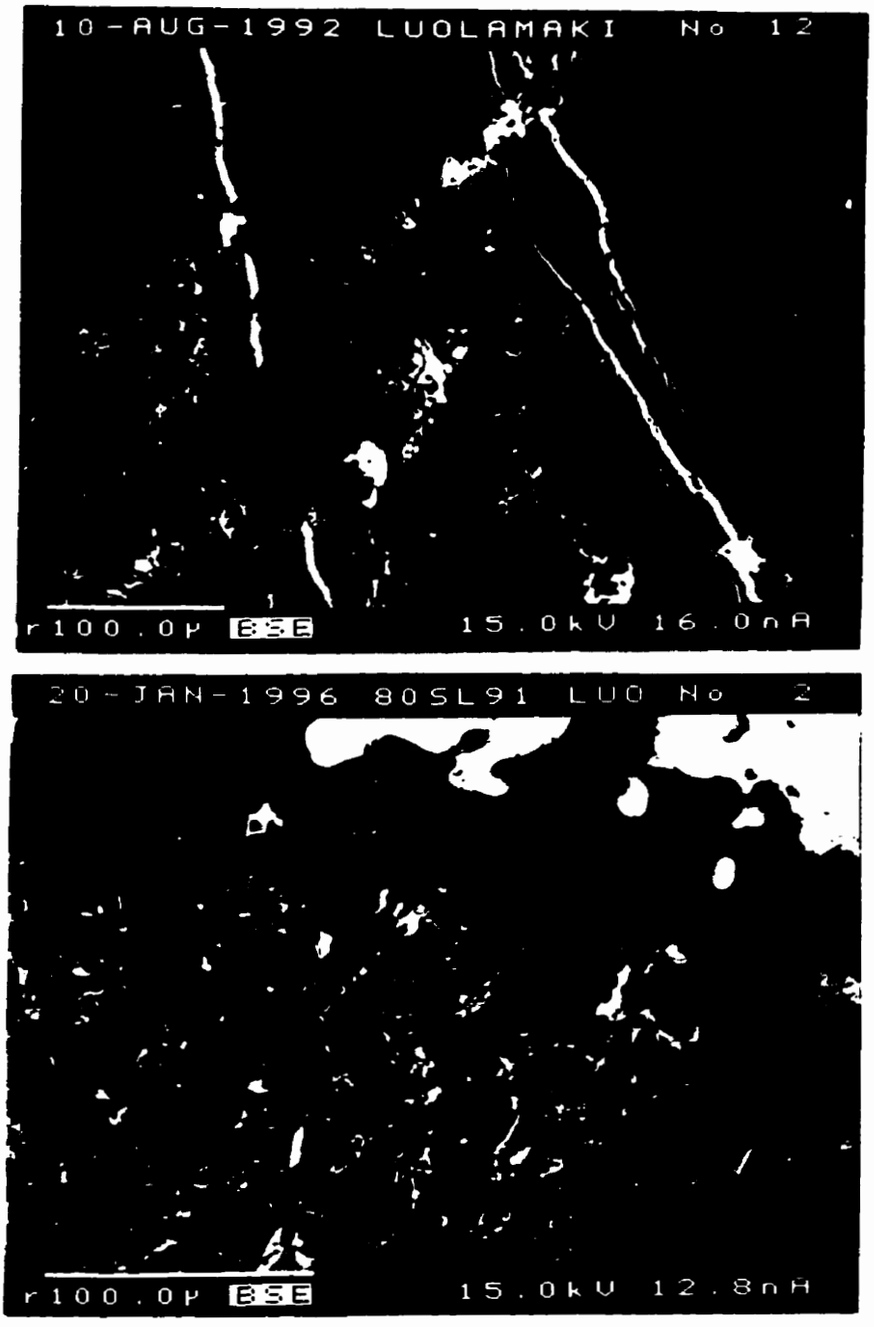

(E)

(F)

Fig. 4.16. BSE images of feldspar from Luolamäki: (E) Microporous Rb-variable microcline, cut by veinlets of (Rb,K)-feldspar (white) and replaced by porous late K-feldspar (dark grey); (F) late adularian (K-Rb)-feldspar with cookeite (black) and a rim of K-feldspar (dark grey) which is closely associated with analcimization of pollucite (upper right, grey to white).

Table 4.7: Representative compositions of (K-Rb)-feldspar from Luolamäki, Finland.

oxide	1	2	3	4	5	6	7	8
SiO_2	63.66	58.06	63.46	58.05	60.85	55.98	63.98	58.05
Al_2O_3	18.13	16.42	17.68	16.02	17.03	16.10	18.64	15.97
P_2O_5	0.20	0.02	0.00	0.00	0.00	0.06	0.05	0.19
Na_2O	0.09	0.00	0.03	0.00	0.02	0.00	0.08	0.00
K_2O	14.84	5.10	13.43	3.92	8.94	1.64	16.27	4.84
Rb_2O	2.77	19.55	4.53	20.55	12.43	26.02	0.00	18.25
Cs_2O	0.23	0.66	0.08	1.05	0.49	0.60	0.02	1.26
SrO	0.05	0.09	0.00	0.05	0.09	0.06	0.00	0.11
BaO	0.00	0.14	0.10	0.08	0.05	0.06	0.31	0.01
sum	100.01	100.12	99.40	99.79	99.94	100.61	99.51	99.01
	Atomic contents based on 8 atoms of oxygen							
Si	2.991	2.997	3.017	3.019	3.010	2.982	2.982	3.009
Al	1.004	0.999	0.990	0.982	0.993	1.011	1.024	0.976
P	0.008	0.001	0.000	0.000	0.000	0.003	0.002	0.009
Na	0.008	0.000	0.003	0.000	0.002	0.000	0.007	0.000
K	0.889	0.336	0.814	0.260	0.564	0.112	0.967	0.320
Rb	0.084	0.649	0.138	0.687	0.395	0.891	0.000	0.608
Cs	0.005	0.014	0.002	0.023	0.010	0.014	0.000	0.028
Sr	0.001	0.003	0.000	0.002	0.003	0.002	0.000	0.003
Ba	0.000	0.003	0.002	0.002	0.001	0.001	0.006	0.000
ΣM	0.987	1.004	0.959	0.974	0.975	1.019	0.981	0.974
M^+	0.989	1.010	0.961	0.977	0.979	1.022	0.987	0.993
TO_2^-	0.996	0.999	0.990	0.982	0.993	1.010	1.023	0.968
ΣT	4.002	3.997	4.007	4.001	4.004	3.997	4.009	3.994
Si/Al	3.02	3.00	3.05	3.08	3.03	2.96	2.92	3.13

1 and 2. Microcline vein in pollucite and coexisting exsolved bleb of (Rb,K)-feldspar, respectively.
3 and 4. A second microcline - (Rb,K)-feldspar pair.
5. Rb-rich feldspar associated with late albite.
6. (Rb,K)-feldspar associated with lepidolite.
7 and 8. Adularia - (Rb,K)-feldspar pair.

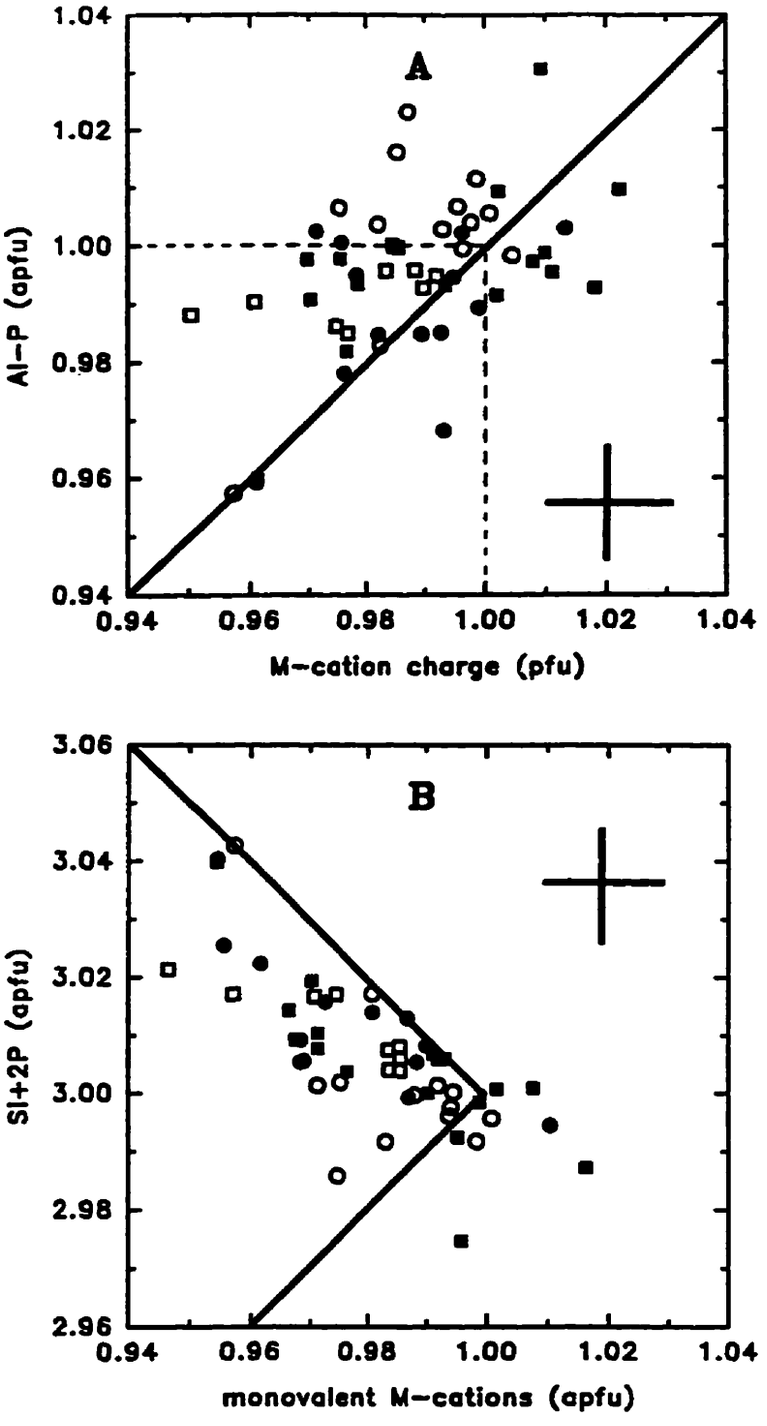

Fig. 4.17. Element variation in (K-Rb)-feldspar from the Luolamäki pegmatite: (A) (Al-P) *vs.* *M*-cation charge; (B) (Si+2P) *vs.* the sum of monovalent *M* cations. Symbols: vein microcline in pollucite (□) and associated (Rb,K)-feldspar (■), late adularia (○) and associated (Rb,K)-feldspar (•). Error bars and substitutional lines as in Figure 4.3.

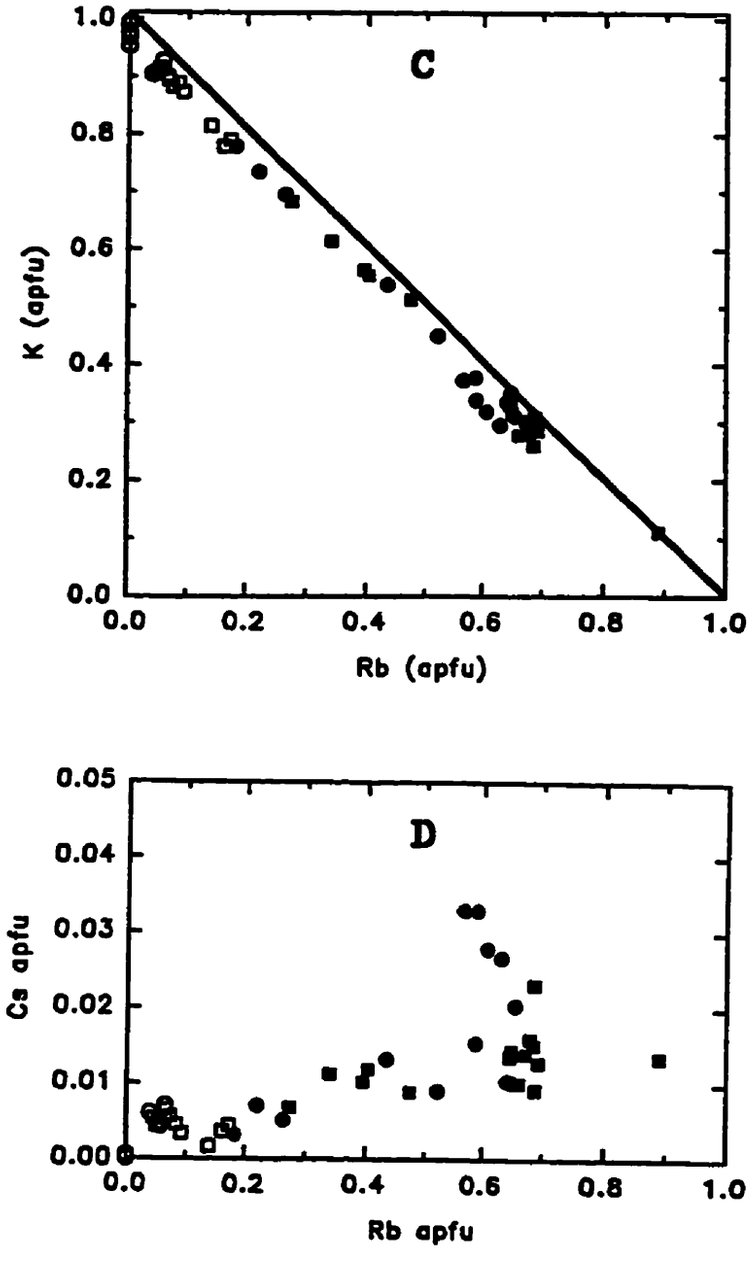

Fig. 4.17. Element variation in (K-Rb)-feldspar from the Luolamäki pegmatite: (C) K *vs.* Rb, with a line indicating $\Sigma M = 1$; (D) Cs *vs.* Rb.

The Monte Capanne monzogranitic pluton is well-exposed at the western end of the Island of Elba in the Tyrrhenian Sea, Italy. Numerous rare-element pegmatites occur along its eastern margin, but pollucite is known only from the pegmatite veins near San Piero in Campo, Elba, including La Speranza, Fonte del Prete, Filone della Speranza and Masso Foresi (Orlandi & Scortecci 1985). Pollucite and petalite were first described from Elba (Briethaupt 1846). The sample investigated here (Ecole des Mines, Paris) is probably from the La Speranza dyke. Fifty m SW of this locality lies the Filone-Rosina aplite-pegmatite dyke, in which foitite was recently discovered (Pezzotta *et al.* 1996). Pollucite is found in miarolitic cavities in association with primary microcline, albite, lepidolite, elbaite, quartz, and overgrown by late mica and zeolite minerals.

Abundant (Rb,K)-feldspar occurs in 1-2 cm-wide veins of twinned microcline (+ muscovite, albite, quartz, apatite) which crosscut pollucite. Minor (Rb,K)-feldspar is associated with metasomatic untwinned adularia (+ cookeite) which replaces microcline and pollucite along grain boundaries and which overgrows microcline. The microcline has patchy distributions of 0.11-0.35 wt. % Na_2O, 0.90-3.39 Rb_2O and 0.10-0.31 Cs_2O; most is P-free, but local concentrations extend to 0.35 wt. % P_2O_5. The bulk of the microcline has approximately 5 mol. % Rbf. All later generations of feldspar are Na- and P-free with $BaO \leq 0.16$ wt. % and $SrO \leq 0.16$ wt. %. Small (<20-50 μm) grains of (Rb,K)-feldspar + quartz occur throughout the microcline in association with muscovite (1.4-1.7 wt. % Rb_2O), albite (Ab_{100})

and minor apatite (4.1 wt.% MnO) (Fig. 4.18A-D). The (Rb,K)-feldspar has 5.10-21.55 wt.% Rb_2O and 0.15-1.37 Cs_2O. Clusters of grains have similar composition (Fig. 4.18A). Individual grains have a slight compositional heterogeneity (Fig. 4.18B). Most grains of (Rb,K)-feldspar occur with quartz at the core (Fig. 4.18C,D). Microcline is partly replaced and overgrown by untwinned adularian K-feldspar (Fig. 4.18D). Small blebs and veinlets of (Rb,K)-feldspar also occur in association with albite (Fig. 4.18E). Small round blebs of Rb-rich feldspar occur in association with the Or_{100} adularia replacing microcline (Fig. 4.18F). The adularian (Rb,K)-feldspar is largely Na-free with 8.45-18.86 wt.% Rb_2O and 0.17-1.69 wt.% Cs_2O.

The (Rb-K)-feldspar was analysed using four different sets of standards. Initial analysis of the Rb-rich feldspar in microcline using RCL microcline (Rb) and 2ORTHO (K, Al, Si) gave poor stoichiometry but indicated more than 20 wt.% Rb_2O. To improve the results, several grains of Rb-rich feldspar from a locality in the Kola Peninsula, Russia (Ch. 4.7), with a total exposed area of 50 μm and a relatively homogeneous composition, were then analysed for use as a standard (1RBAD). Curves for wt.% variations in Al_2O_3, SiO_2, Rb_2O and K_2O across the series $KAlSi_3O_8$ - $RbAlSi_3O_8$ were prepared, and using the assumption that measurements of K from 2ORTHO were accurate, values for Si, Al and Rb were taken from the curves. The value for Rb_2O from the curve was corrected for minor Cs_2O (0.56 wt.%). No other minor elements were detected on analysis.

This gave 2.29 K_2O, 24.44 Rb_2O, 0.56 Cs_2O, 16.00 Al_2O_3, 56.70 SiO_2, sum 100 wt.% for this particular cluster of grains. The standards 1RBAD (Rb, Al, Si) and 2ORTHO (K) were used to analyse the Elba (Rb-K)-feldspar. The vein of microcline from Kola Peninsula was also used as a standard (1RBKOLA) for K, Al and Si. Later analysis were done using the finalized 1EIFEL (K, Al, Si) composition and the $Rb_2ZnSi_5O_{12}$ (Rb) standard. The latter three sets of analyses gave closely comparable results, with mean values (N=59) for ΣT of 4.002(4) *apfu*, ΣM (= M^+) of 0.993(15) *pfu*, (Si+2P) = 3.001(15) *apfu* and TO_2^- = 1.001(17) *pfu*, indicating close agreement with ideal feldspar stoichiometry. The data reported below, in Figure 4.19 and Table 4.8 were determined using the 1EIFEL standard.

Individual values for *M*-cation charge tend to be slightly lower (by <1 at.%) than values of (Al-P) (Fig. 4.19A). Values of (Si+2P) cluster near 3.0 *apfu* for microcline, adularia and adularian (K-Rb)-feldspar, but lie along the trend for the $\square Si_4O_8$ substitution for the (K-Rb)-feldspar occurring in microcline (Fig. 4.19B). High Si/Al ratios correspond to low *M*-cation sums and equally low (Al-P); an extreme value with ~3% $\square Si_4O_8$ has Si = 3.032 (or 3.000 + 0.032) *apfu*, Al = 0.969 *apfu*, M^+ = 0.966 (or 1 - 0.034) *pfu* and ΣT = 4.001 *apfu* (No. 5 in Table 4.8). Extreme values for Rb_2O in the microcline-associated (Rb,K)-feldspar correspond to 72.7 mol.% $RbAlSi_3O_8$ (Fig. 4.19C), and in the Rb-rich samples, substitution of Cs extends to 0.04 *apfu* (Fig. 4.19D).

(A)

(B)

Fig. 4.18. BSE images of (K-Rb)-feldspar from Elba, Italy: (A) (Rb,K)-feldspar (white) + quartz (black) occurs in microcline (grey) associated with albite (black) and muscovite (mottled grey-black); (B) the cleavage of microcline (dark grey) is continuous through (Rb,K)-feldspar (white) + quartz (black).

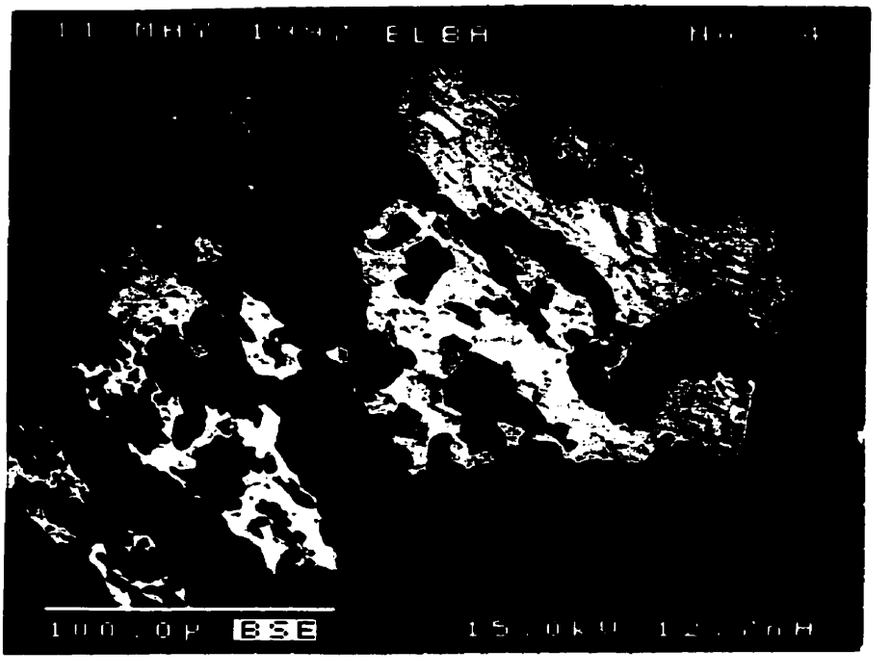

(C)

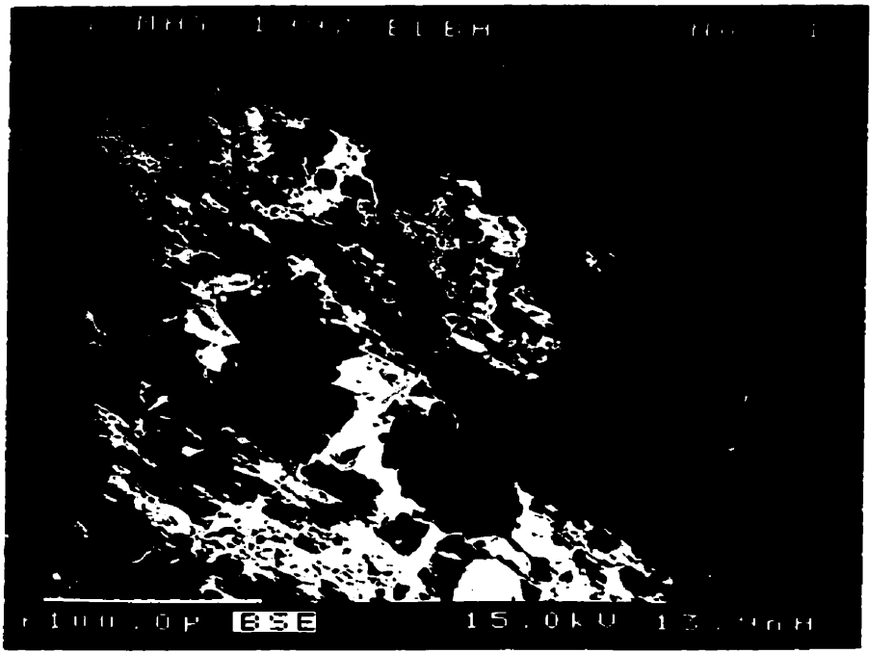

(D)

Fig. 4.18. BSE images of (K-Rb)-feldspar from Elba, Italy: (D) (Rb,K)-feldspar (white) + quartz (black) in microcline (grey) associated with albite (black) and muscovite (mottled grey-black); (E) (Rb,K)-feldspar (white) + quartz (black) in a thin vein of microcline (light grey) surrounded by porous adularia (dark grey) ± cookeite (black).

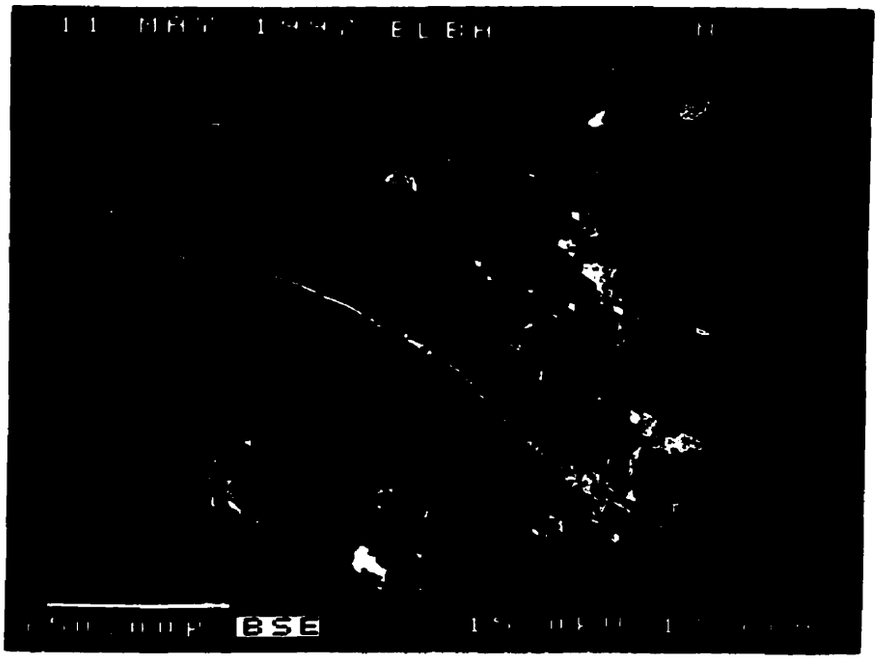

(E)

(F)

Fig. 4.18. BSE images of (K-Rb)-feldspar from Elba, Italy: (E) veinlet of (Rb,K)-feldspar (white) in microcline (grey) associated with albite (black) + fine-grained (Rb,K)-feldspar (white). (F) fine-grained (Rb,K)-feldspar (white) + quartz (black) associated with adularia (dark grey) which replaces microcline (light grey).

Table 4.8: Representative compositions of (K-Rb)-feldspar from Elba, Italy.

oxide	1	2	3	4	5	6	7	8
SiO_2	63.34	64.00	63.72	60.77	58.42	56.96	64.80	57.89
Al_2O_3	18.25	18.12	18.34	17.27	15.84	16.32	18.24	16.65
P_2O_5	0.25	0.00	0.00	0.00	0.00	0.00	0.01	0.00
Na_2O	0.30	0.14	0.11	0.02	0.00	0.00	0.00	0.00
K_2O	15.60	15.51	14.52	10.35	4.16	3.75	16.56	5.08
Rb_2O	0.90	1.66	3.39	10.90	19.61	21.55	0.00	18.86
Cs_2O	0.25	0.22	0.10	0.38	1.37	1.10	0.02	0.78
SrO	0.00	0.00	0.08	0.03	0.09	0.08	0.02	0.07
BaO	0.00	0.09	0.03	0.00	0.00	0.00	0.00	0.00
sum	98.97	99.84	99.98	99.79	99.59	99.83	99.75	99.44
	Atomic contents based on 8 atoms of oxygen							
Si	2.980	2.999	2.991	2.996	3.032	2.990	3.006	2.991
Al	1.012	1.001	1.014	1.003	0.969	1.010	0.997	1.014
P	0.010	0.000	0.000	0.000	0.000	0.000	0.000	0.000
Na	0.027	0.013	0.010	0.002	0.000	0.000	0.000	0.000
K	0.936	0.927	0.870	0.651	0.276	0.251	0.980	0.335
Rb	0.027	0.050	0.102	0.345	0.654	0.727	0.000	0.626
Cs	0.005	0.004	0.002	0.008	0.030	0.025	0.000	0.017
Sr	0.000	0.000	0.002	0.001	0.003	0.002	0.000	0.002
Ba	0.000	0.002	0.001	0.000	0.000	0.000	0.000	0.000
ΣM	0.996	0.996	0.987	1.007	0.963	1.006	0.981	0.981
M^+	0.996	0.998	0.989	1.008	0.966	1.010	0.982	0.984
TO_2^-	1.002	1.002	1.015	1.003	0.969	1.010	0.997	1.014
ΣT	4.002	4.001	4.007	3.999	4.001	4.000	4.004	4.008
Si/Al	2.99	3.00	2.95	2.99	3.13	2.96	3.02	2.94

1-3. Microcline veins in pollucite.
4. (Rb,K)-feldspar associated with albite in microcline.
5 and 6. (Rb,K)-feldspar in microcline.
7. Adularia replacing pollucite.
8. (Rb,K)-feldspar in adularia.

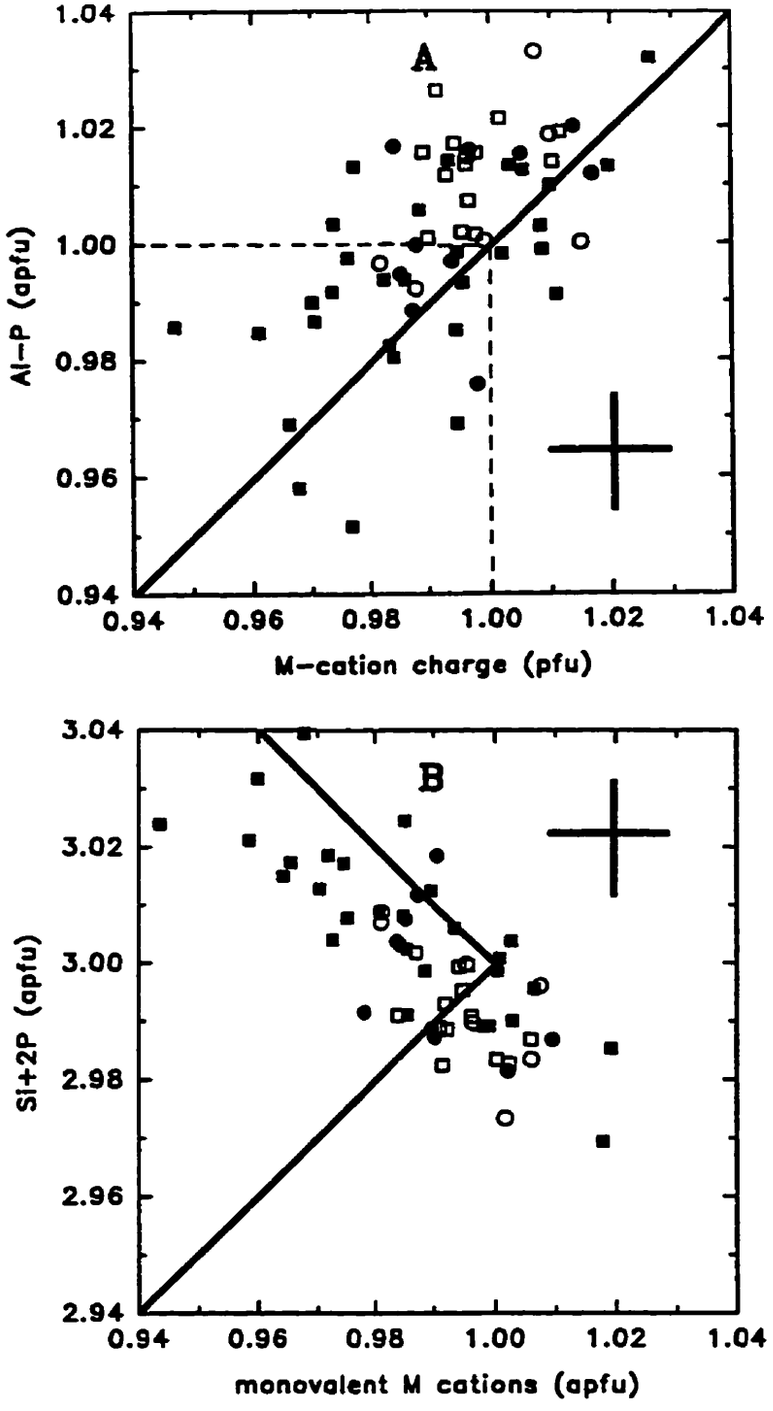

Fig. 4.19. Element variation in (K-Rb)-feldspar from the Elba pegmatite: (A) (Al-P) *vs.* *M*-cation charge; (B) (Si+2P) *vs.* monovalent *M* cations. Symbols: microcline (□) and associated (Rb,K)-feldspar (■), adularia (○) and associated (Rb,K)-feldspar (•). Error bars and substitutional lines as in Figure 4.3.

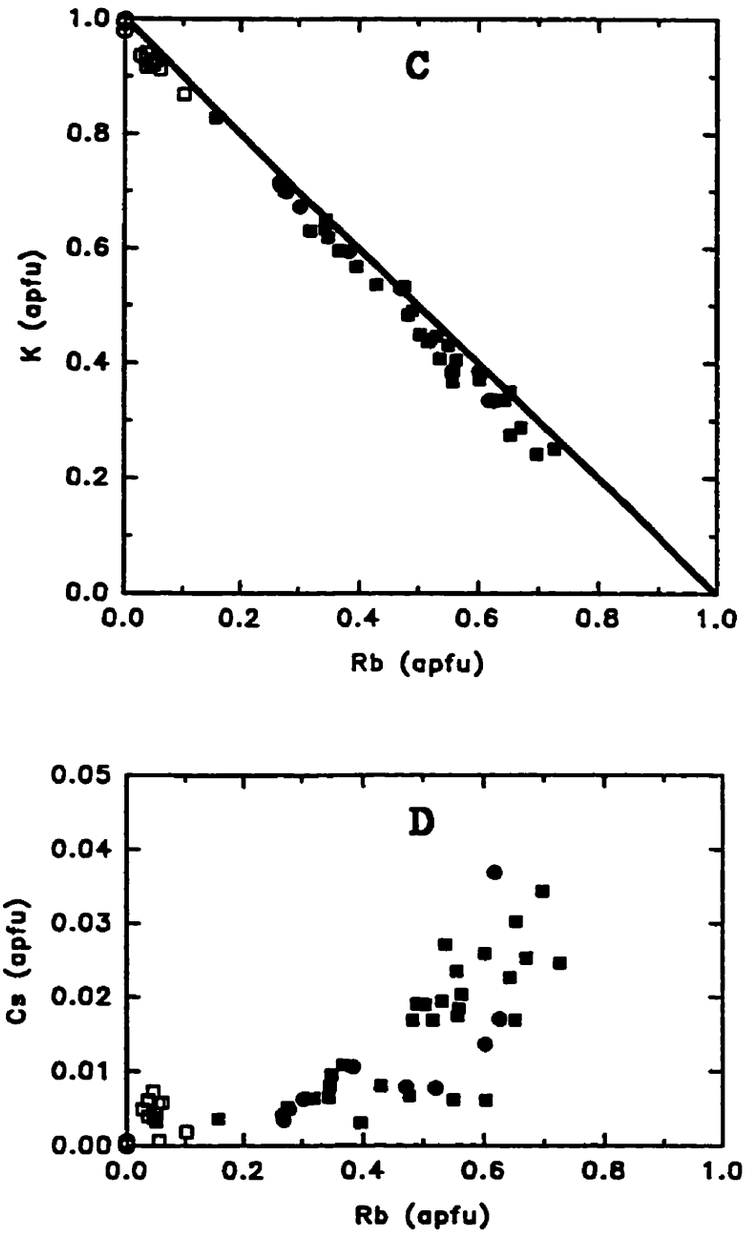

Fig. 4.19. Element variation in (K-Rb)-feldspar from the Elba pegmatite: (C) K *vs.* Rb, with a line indicating $\Sigma M = 1$; (D) Cs *vs.* Rb.

4.5 *(K-Rb)-feldspar from the Tanco rare-element pegmatite, SE Manitoba*

The highly fractionated Tanco pegmatite is located about 180 km E-NE of Winnipeg at Bernic Lake, SE Manitoba. It occurs in the southernmost-exposed part of the Bird River Greenstone Belt of the Superior Province, and is hosted by greenschist-to-lower-amphibolite facies metavolcanics and related metasediments. The pegmatite forms a bilobate sheet 1600 m long, 820 m wide and up to 110 m thick, shallowly north-dipping and doubly plunging (E and W). There is a series of related pegmatites below and adjacent to the main body. Nine zones may be distinguished on the basis of differing mineralogy, texture and location, as well as a zone of contact exomorphism. The ~5-30 cm-thick border zone (1) consists of fine-grained albite and quartz along the pegmatite-wallrock contacts. The wall zone (2) is up to 35 m thick and contains columnar microcline-perthite up to 3 m in size in a matrix of quartz, albite and muscovite. The Nb-Ta-bearing albite aplite (+ quartz) zone (3) forms 16 m-thick sheets and smaller lens-like bodies in the eastern lobe of the pegmatite. The lower intermediate zone (4) forms bodies up to 25 m thick, mainly in the lower part of the pegmatite, and consists of large crystals of microcline-perthite, spodumene-quartz pseudomorphs after petalite, albite, quartz, mica and amblygonite-montebrasite. The upper intermediate zone (5) grades upward from zone (4) but is gradually depleted in albite and mica. In zone (5), crystals of microcline-perthite, petalite and amblygonite reach several metres in size. Miarolitic cavities form in the spodumene-rich portions of this zone. The central intermediate zone (6) is up to 60 m thick and consists of microcline-perthite, albite, muscovite, quartz, beryl and Nb,Ta-oxide minerals. Zone (7) consists almost entirely of quartz. Zone (8) is located in the eastern lobe of the pegmatite and consists mainly of pollucite (and its alteration products). There is also a substantial body of pollucite in the western orebody, and several small (<2 m) blocks of pollucite are located near

the large bodies. Zone (9) consists largely of lepidolite, with minor quartz and microcline-perthite. A detailed description of the local and regional geology, internal structure and mineralogy of the Tanco pegmatite may be found in Černý *et al.* (1996).

Pale-gray to beige microcline-perthite is a major component of zones (2), (4), (5), (6) and (9), a minor component of zones (1) and (8), and is virtually absent in zones (3) and (7). I examined several samples of feldspar from various locations within the pegmatite. BSE imaging shows that most of the feldspar is compositionally homogeneous or has a slight patchy heterogeneity on a microscopic scale. EMP-determined Rb_2O contents generally agree with those previously determined by bulk methods for each of the zones (Černý *et al.* 1996).

Giant crystals in zone (5) have a striped grey-and-white pattern in their interior and pink-rusty margins, and show increasing degrees of (Al,Si) order from grey to white to rusty feldspar. The most-ordered and triclinic material tends to be untwinned and nonperthitic (Černý & Macek 1972). One of the largest K-feldspar crystals at Tanco, over 5 m long, occurs in the "lunch room" of zone (5). BSE imaging of a 2 cm chunk from the core of the crystal, the colour of which varies from grey to white over about 1 cm, indicated a rather homogeneous composition. Analysis gave a similar composition for the grey and white material, with $Rb_2O \sim 1.5$ wt.%, $Na_2O \sim 0.4$ wt.%, and $Cs_2O \sim 0.2$ wt.% and negligible Mg, F, Ga, Ba, Ti, Mn, Fe, Ca, Sr or Pb. Rb_2O values are variable by up to 0.5 wt.% over a scale of mm. The principal compositional difference between the grey and white K-feldspar is a tendency for loss of Cs and a decrease in P_2O_5 from 0.43 wt.% (grey) to 0.03 wt.% (white). This suggests a loss of framework P with increasing (Al,Si) order from the grey to white feldspar.

Rb_2O (and P_2O_5) increase from zone (2) to zones (4), (5) and (6), but the Rb-richest feldspar occurs as non-perthitic untwinned inclusions and veins of microcline in the pollucite bodies. Veins of microcline, albite and quartz are 0.5 to 2 mm wide and are most abundant toward the margins of pollucite bodies, but lepidolite veins form a polygonal network throughout the pollucite. Thin (< 0.5 mm) subparallel veins of fine-grained mica and spodumene are abundant in all samples of pollucite. Both the coarse and the fine veins are locally overgrown by small (<1 mm) grains of untwinned (Al,Si)-disordered adularia, but these are not abundant. Adularia metasomatically replaces microcline as well as pollucite. Minor local analcimization preceded late alteration by clay minerals (illite, montmorillonite and kaolinite).

A total of 35 thin sections were examined which emphasized microcline veining in the larger pollucite bodies. BSE imaging shows that the bulk of the vein feldspar is compositionally homogeneous on this scale. The variation of Rb_2O (2-4 wt.%) is greater along a single vein than between separate veins of a pollucite body. There are no obvious compositional differences in the vein microcline between the interior or margins of pollucite bodies, or which could be correlated with the mine location of the pollucite body. Veins of feldspar occurring in small bodies of highly altered white pollucite in the western lobe are homogeneous in composition and show minimal evidence of subsolidus reaction; Rb-rich phases are rare. In contrast, veins of feldspar in the larger of the western bodies and in the giant pollucite body in the eastern lobe both show local reactions. The intensity of reaction is not related to the proximity of the vein to the margins of the pollucite body.

EMP analysis shows that the vein microcline has 2-4 wt.% Rb_2O, 0.2-0.4 wt.% P_2O_5, and less than 0.30 wt.% Na_2O. The distribution of Rb tends to be patchy

in the microcline, and varies by up to 1 wt.% Rb_2O over <50 μm. Wispy veinlets of Rb-enriched feldspar grading to veinlets of Rb-feldspar are commonly associated with alteration of pollucite (Fig. 4.20A). Aggregates of (Rb,K)-feldspar form in association with grains of albite (Fig. 4.20A, B). Inclusion-filled porous Rb-rich feldspar is also associated with grains of mica (Fig. 4.20C). Porous Rb-rich feldspar grading to Rb-feldspar often contains inclusions of cookeite (Fig. 4.20E). The (Rb,K)-feldspar associated with vein microcline has 10-24.8 wt.% Rb_2O and up to 1.4 wt.% Cs_2O. Breakdown of microcline to Rb-free adularia + (Rb,K)-feldspar (with up to 23.8 wt.% Rb_2O, 81 mol.% Rbf) occurs locally (Fig. 4.20F). Adularia replacing pollucite is largely Rb-, Na- and P-free with near-Or_{100} to Or_{100} composition. All generations of feldspar are Fe-free and also have negligible Mg, F, Ga, Ba, Ti, Mn, Ca, Sr and Pb. Representative compositions are given in Table 4.9.

Most individual values of (Al-P) and *M*-cation charge are equal within error (Fig. 4.21A) as are mean values are $TO_2^- = 0.993(8)$ *apfu* and $M^+ = 0.995(9)$ *apfu*. Average values for the sum of divalent cations of 0.003 *apfu* are due to minor-to-trace substitution of Sr or Ba. A plot of (Si+2P) *vs.* the sum of monovalent cations shows a cluster of data along the $\square Si_4O_8$ trend, indicating that up to 2 mol.% $\square Si_4O_8$ substitution is widespread among all generations of feldspar at Tanco (Fig. 4.21B). The average (Si+2P) value of 3.007(7) and the mean ΣT value of 4.000(3) indicate that Tanco feldspar compositions correspond closely to the ideal formula when taking into account the berlinite and $\square Si_4O_8$ substitutions. A plot of K *vs.* Rb shows that compositions lie close to the join from K-feldspar to Rb-feldspar, with minor deviations due to minor Na and $\square$ (Fig. 4.21C). A large proportion of the (Rb,K)-feldspar has 60-80 mol.% Rbf; the Rb-richest sample has 84.6 mol.% Rbf and 3.2 mol.% Csf (Fig. 4.21D).

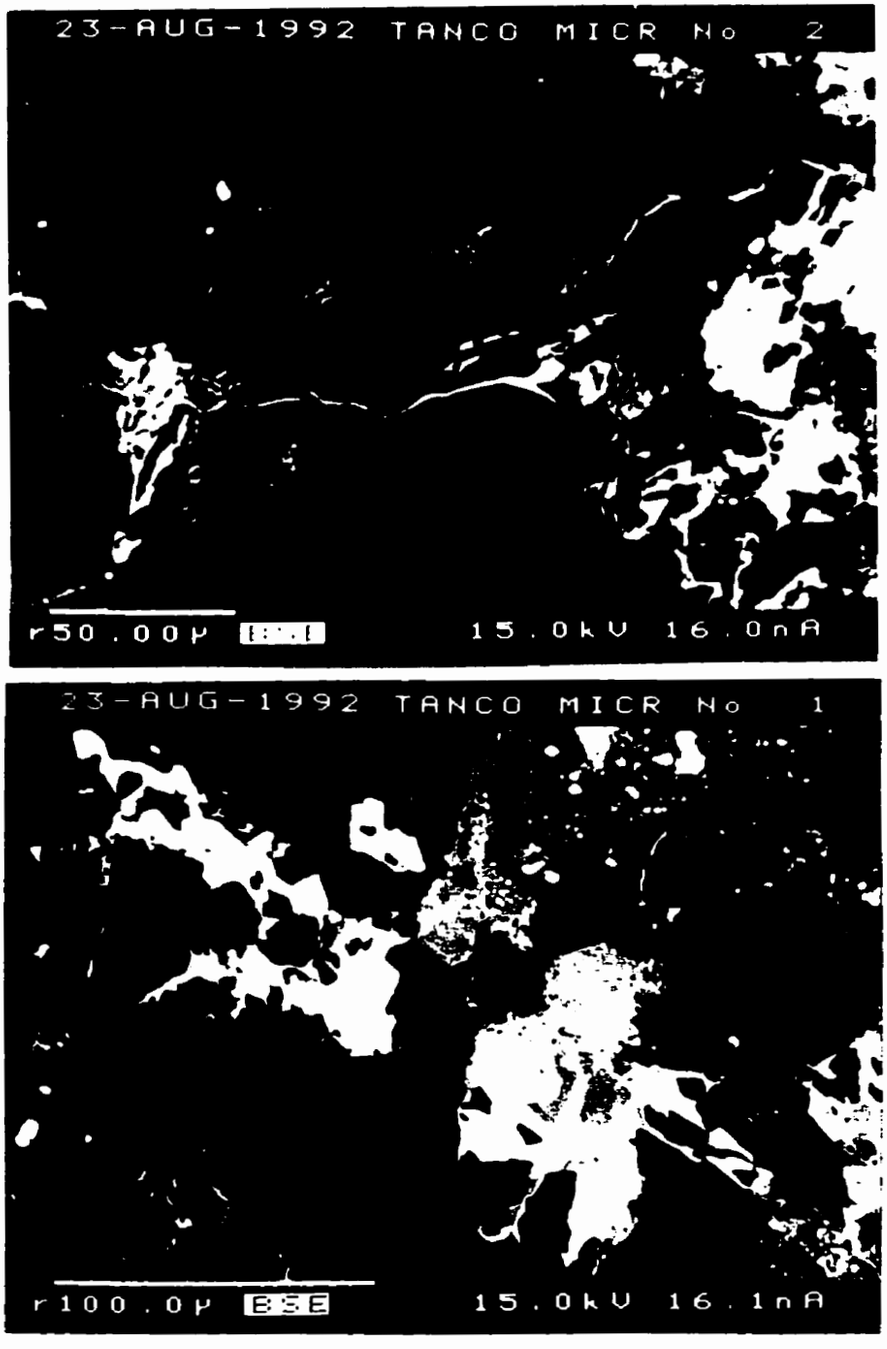

(A)

(B)

Fig. 4.20. BSE images of (K-Rb)-feldspar veining pollucite from the Tanco pegmatite: (A) Wispy veins of Rb-enriched feldspar in microcline (grey) associated with (Rb,K)-feldspar (white) + albite (black); (B) (Rb,K)-feldspar (white) + albite (black) in microcline (grey).

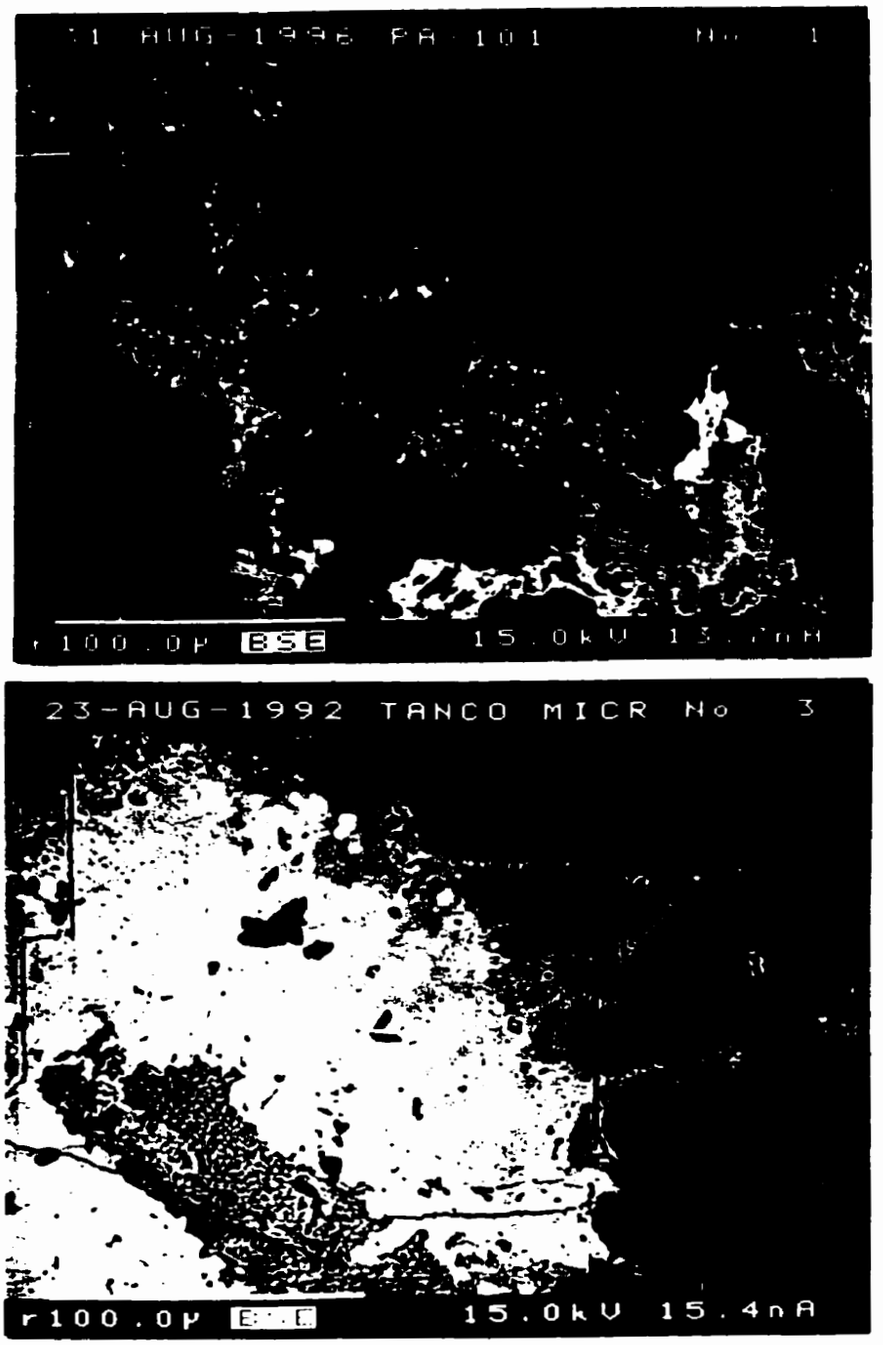

(C)

(D)

Fig. 4.20. BSE images of (K-Rb)-feldspar veining pollucite from Tanco: (C) Rb-enriched feldspar (grey to white) associated with mica (black) in microcline (patchy grey); (D) Rb-rich feldspar formed in association with alteration of microcline by muscovite. Note the cleavage of the early microcline (grey) continuous through the Rb-rich phase.

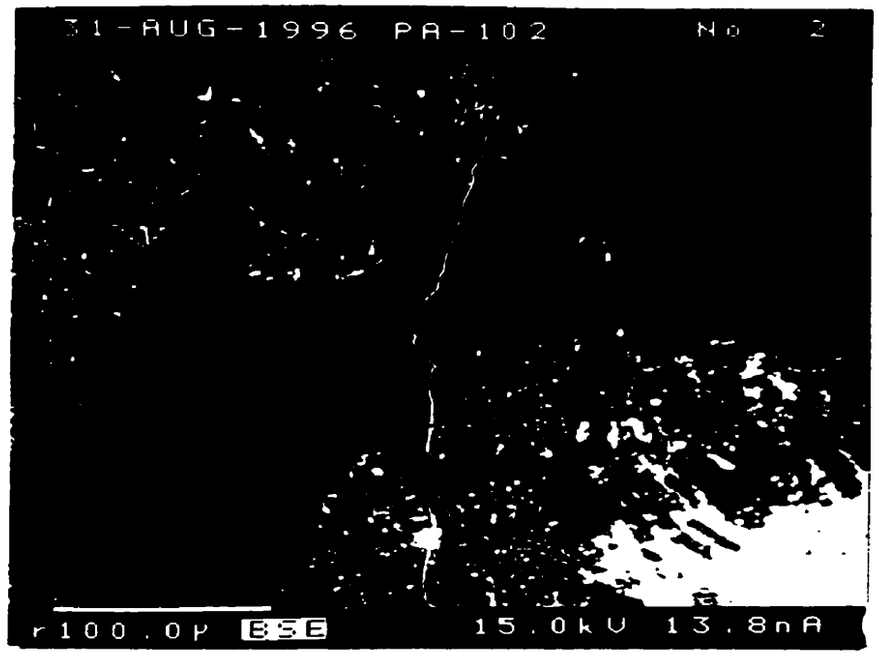

(E)

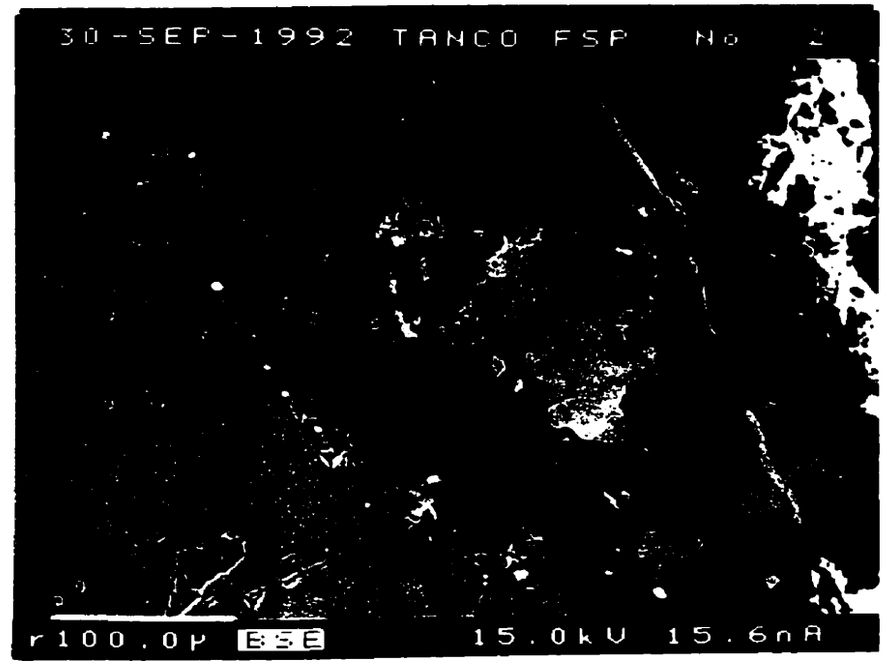

(F)

Fig. 4.20. BSE images of (K-Rb)-feldspar veining pollucite at Tanco: (E) Reaction of microcline (grey) to form porous, Rb-rich feldspar (pale grey) and (Rb,K)-feldspar (white) associated with cookeite (black); (F) Variable-Rb early microcline (grey), cut by a veinlet of Rb-richer feldspar (light grey), and replaced by Or_{100} adularia (dark grey) + Rb-rich feldspar (white).

Table 4.9: Representative compositions of (K-Rb)-feldspar veins in pollucite from Tanco, Manitoba.

oxide	1	2	3	4	5	6	7	8
SiO_2	63.61	63.73	62.54	59.10	56.53	64.37	57.98	56.82
Al_2O_3	18.40	18.07	17.39	16.20	16.06	18.24	16.17	16.05
P_2O_5	0.36	0.18	0.06	0.00	0.00	0.00	0.00	0.00
Na_2O	0.22	0.21	0.08	0.09	0.03	0.03	0.00	0.00
K_2O	14.88	14.38	12.41	5.54	1.79	16.83	4.00	2.68
Rb_2O	2.50	3.14	6.62	17.78	24.84	0.00	21.39	23.75
Cs_2O	0.27	0.33	0.16	0.82	1.43	0.03	0.81	0.56
SrO	0.09	0.05	0.06	0.10	0.18	0.07	0.02	0.10
BaO	0.10	0.00	0.00	0.00	0.00	0.08	0.00	0.00
sum	100.53	100.15	99.34	99.71	100.95	99.77	100.41	99.96
	Atomic contents based on 8 atoms of oxygen							
Si	2.972	2.994	3.011	3.023	2.994	2.996	3.008	3.000
Al	1.013	1.001	0.987	0.976	1.002	0.999	0.989	0.999
P	0.014	0.007	0.002	0.000	0.000	0.000	0.000	0.000
Na	0.020	0.019	0.007	0.009	0.003	0.002	0.000	0.000
K	0.887	0.862	0.762	0.362	0.121	0.995	0.265	0.181
Rb	0.075	0.095	0.205	0.584	0.846	0.000	0.713	0.806
Cs	0.005	0.007	0.003	0.018	0.032	0.001	0.018	0.013
Sr	0.002	0.001	0.002	0.003	0.006	0.001	0.002	0.003
Ba	0.002	0.000	0.000	0.000	0.000	0.001	0.000	0.000
ΣM	0.992	0.984	0.980	0.976	1.009	1.000	0.999	1.002
M^+	0.996	0.985	0.982	0.979	1.016	1.003	1.001	1.005
TO_2^-	1.000	0.994	0.984	0.976	1.002	1.002	0.989	0.999
ΣT	4.001	4.002	4.001	3.999	3.997	3.998	3.997	3.998
Si/Al	3.00	3.03	3.06	3.10	2.99	2.99	3.04	3.00

1-2. Typical composition of microcline veins in pollucite.
3-4. (Rb-K)-feldspar in microcline.
5. (Rb,K)-feldspar in microcline associated with albite.
6. Typical composition of late adularia replacing microcline.
7-8. (Rb,K)-feldspar associated with adularia.

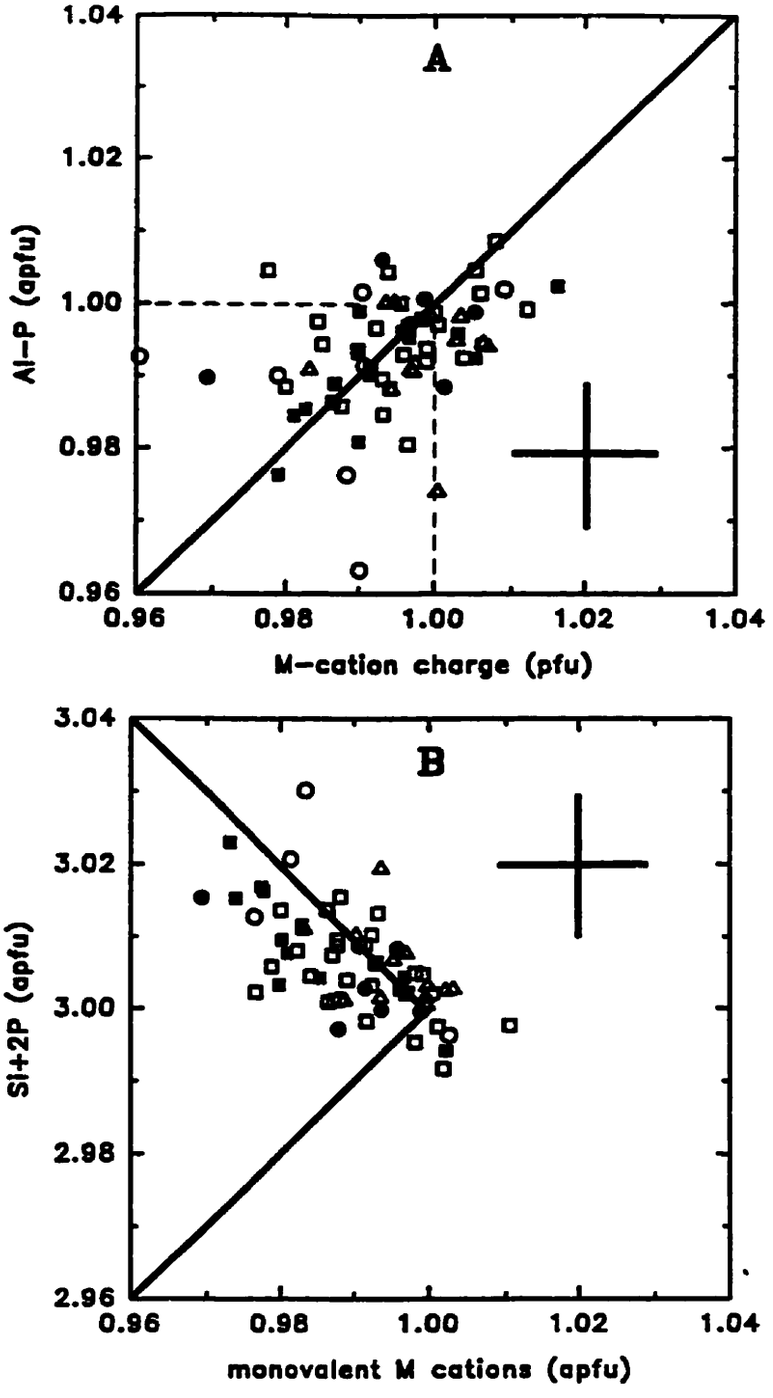

Fig. 4.21. Element variation in (K-Rb)-feldspar from Tanco: (A) (Al-P) *vs.* *M*-cation charge; (B) (Si+2P) *vs.* monovalent *M* cations. Symbols: Zone 5 feldspar (▵); vein microcline in pollucite (□) and associated (Rb,K)-feldspar (■); adularia (○) and associated (Rb,K)-feldspar (•) Error bars and substitutional lines as in Figure 4.3.

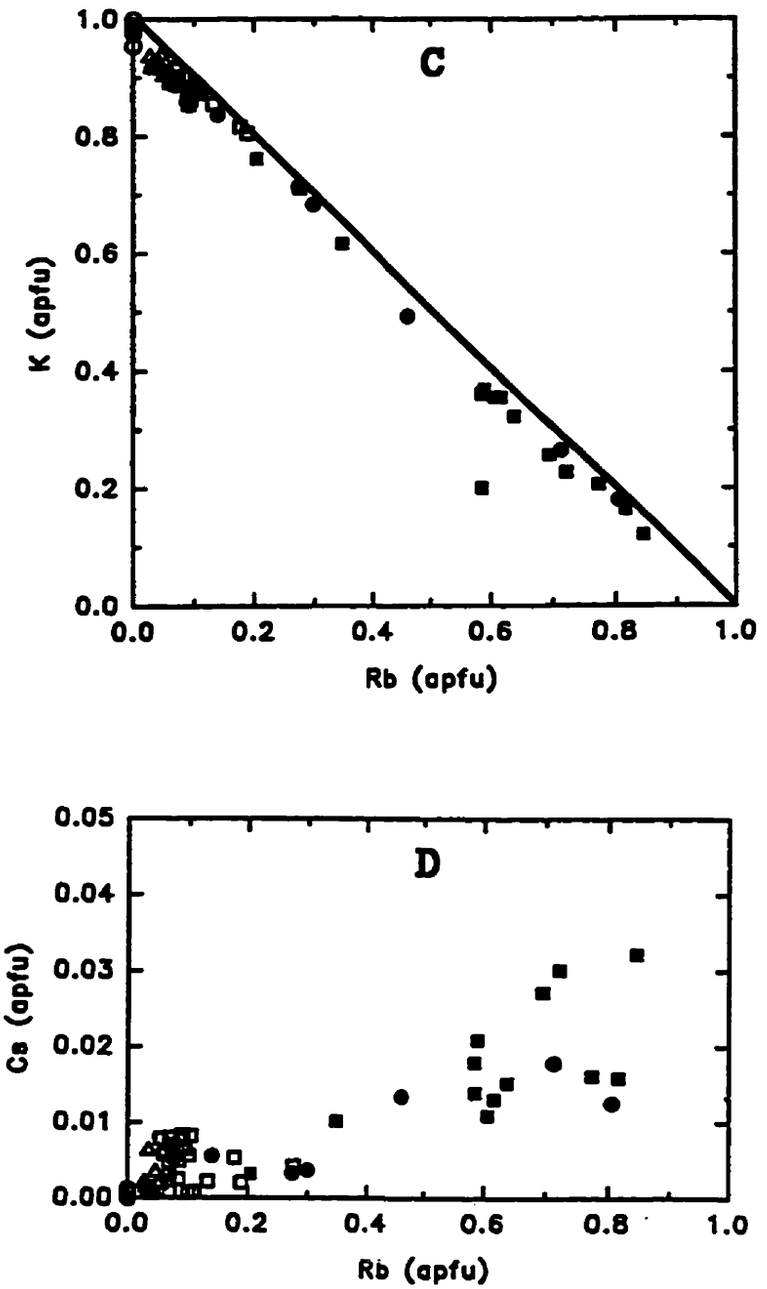

Fig. 4.21. Element variation in (K-Rb)-feldspar from Tanco: (C) K *vs.* Rb, with a line indicating $\Sigma M = 1$; (D) Cs *vs.* Rb.

4.6 *Breakdown reactions of (K,Rb)-feldspar from High Grade Dyke, SE Manitoba*

The High Grade Dyke pollucite-bearing granitic pegmatite is located near Donner Lake in SE Manitoba. It lies about 210 km E-NE of Winnipeg and is accessible on foot about 10 km from Highway 314. It is the most fractionated pegmatite of the Maskwa Lake group, which includes a petalite-bearing dyke, and is classified as a spodumene-subtype complex-type pegmatite. The host rocks are the tonalites of the Maskwa Lake batholith and pillow basalts of the Lamprey Falls formation. The Maskwa Lake group forms part of the Cat Lake - Maskwa Lake pegmatite district north of the Winnipeg River district and includes the Tanco pegmatite at Bernic Lake. The pegmatites occur in the westernmost exposed part of the English River subprovince of the Superior Province of the Canadian Shield (Černý *et al.* 1981).

The High Grade Dyke pegmatite has sharp contacts (strikes 170°, dip 65°W) with the host metabasalt along its exposed length of 18 m. Thickness is variable from 0.6 to 1.2 m. It is not systematically zoned, but contains primary assemblages of blocky K-feldspar + quartz, quartz + spodumene, and pollucite + lath spodumene. Later assemblages, in part metasomatic, include widespread albitic units that in part replace K-feldspar, and sporadic lepidolite + quartz (± spodumene). Patches of holmquistite occur locally at the wallrock contact. Minor minerals include apatite, beryl, microlite, columbite-tantalite, polychromatic (grey-pink) elbaite-liddicoatite and spessartine (Mn/(Mn+Fe) = 0.93).

Fifteen of the original samples available for study were provided by P. Černý and Mr. J. Donner, and 1 drill core sample was provided by Tanco. Twelve polished thin-sections were prepared and examined by optical microscopy and BSE imaging. There was a total of 32 analyses of feldspar. Compositional heterogeneity due to variable K/Rb was first noted in (K,Rb)-feldspar from High Grade Dyke. Sample PA-095G, in which adularia replaces pollucite, provided the first find of Rb-dominant feldspar, Nov. 5, 1990. Preliminary quantitative analysis (using 2ORTHO and RCL microcline) gave 0.00 Na_2O, 3.86 K_2O, 24.01 Rb_2O, 0.52 Cs_2O, 16.72 Al_2O_3, 55.81 SiO_2 sum 100.92 wt.%. The formula calculated on the basis of 8 atoms of oxygen is $(Rb_{0.82}K_{0.26}Cs_{0.01})_{\Sigma 1.09}(Al_{1.04}Si_{2.95})O_8$.

White-to-colourless blocky maximum microcline, locally microperthitic with 1-2 μm-wide albite lamellae, is closely associated with pollucite. White non-perthitic microcline forms veins in pollucite. Pollucite is also crosscut by 1-2 cm-wide veins of lepidolite + quartz, by later veinlets of fine-grained white mica and spodumene, and is replaced by abundant green untwinned adularia and minor clay minerals. Late Rb-rich feldspars are associated with all three of the above feldspar generations - blocky, vein and adularia.

Areas of the blocky microcline (~1-2 wt.% Rb_2O) adjacent to albite grains locally have Rb-poor zones parallel to the cleavage (Fig. 4.22A). Rb-rich feldspar occurs in the blocky microcline in association with irregular veins of albite and in microporous areas adjacent to the albite veins (Fig. 4.22B). However, the principal reaction generating (Rb,K)-feldspar is a breakdown of the non-perthitic vein microcline (~3-4 wt.% Rb_2O) to form an assemblage of porous Rb-poor adularia + (Rb,K)-feldspar (~10-24 wt.% Rb_2O) (Fig. 4.22C,D).

The porous cookeite-bearing adularia replacing pollucite is largely homogeneous with Or_{100} composition; its cell parameters (Ch. 5) are slightly greater than those of the end-member high sanidine reported by Ferguson *et al.* (1991). However, local areas rich in Rb with variable K/Rb occur with small < 1 μm-size inclusions of pollucite (Fig. 4.22E,F). The (Rb,K)-feldspar replacing pollucite has a similar compositional range as the (Rb,K)-feldspar occurring with Or_{100} adularia in the microcline veins in pollucite. Representative compositions are given in Table 4.10.

All generations of feldspar are P- and Fe-free. Most individual values of Al and *M*-cation charge are equal within standard deviations (Fig. 4.23A), as are the mean values of Al = 0.985(12) *apfu* and M^+ = 0.990(13) *pfu*. Individual values of Si extending to 3.04 *apfu* and sums of monovalent *M* cations as low as 0.96 *apfu* indicate up to 4 mol.% of the $\square Si_4O_8$ substitution (Fig. 4.23B). The mean Si value of 3.013(12) *apfu* corresponds well with the values of Al < 1, giving an average ΣT of 4.000(3) *apfu* and good agreement with the feldspar formula if substitution of $\square Si_4O_8$ is taken into account. Adularian (Rb,K)-feldspar has 50-81 mol.% Rbf (Fig. 4.23C) and up to 3 mol.% Csf (Fig. 4.23D). Substitution of $\square Si_4O_8$, indicated by *M*-cation sums of less than 1 *apfu*, is widespread among all generations of (K,Rb)-feldspar (Fig. 4.23E).

Late lepidolite associated with crystallization of adularia has up to 10.14 wt.% Rb_2O and 0.79 wt.% Cs_2O. Late clay with adularia has 1.0 wt.% Fe_2O_3, 4.5 wt.% MgO and 0.63 wt.% Cs_2O.

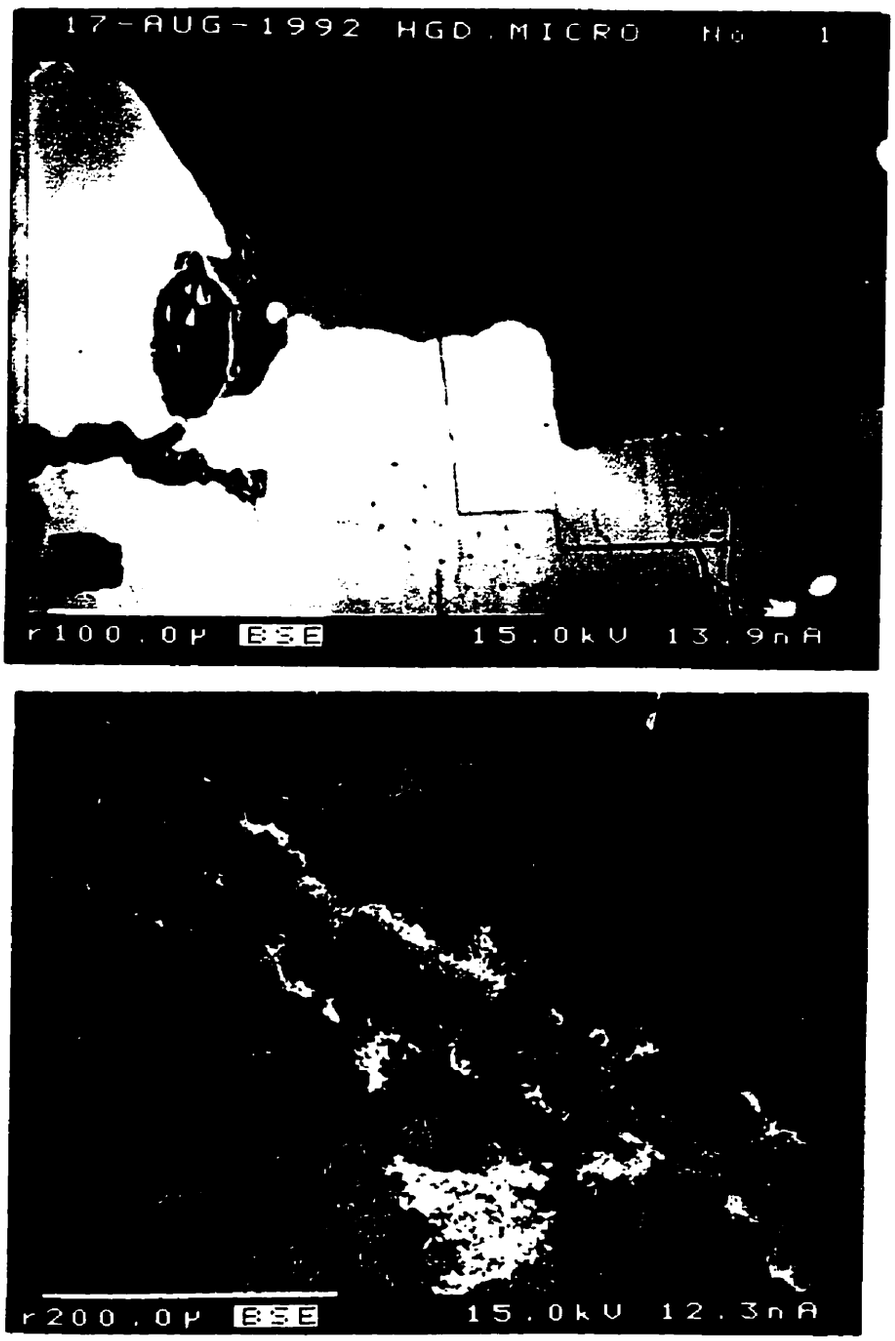

(A)

(B)

Fig. 4.22. BSE images of (K-Rb)-feldspar from High Grade Dyke: (A) Blocky (K,Rb)-feldspar depleted in Rb adjacent to albite (black) is zoned parallel to cleavage traces; (B) (K,Rb)-feldspar has enhanced porosity adjacent to veinlets of albite + (Rb-K)-feldspar (white).

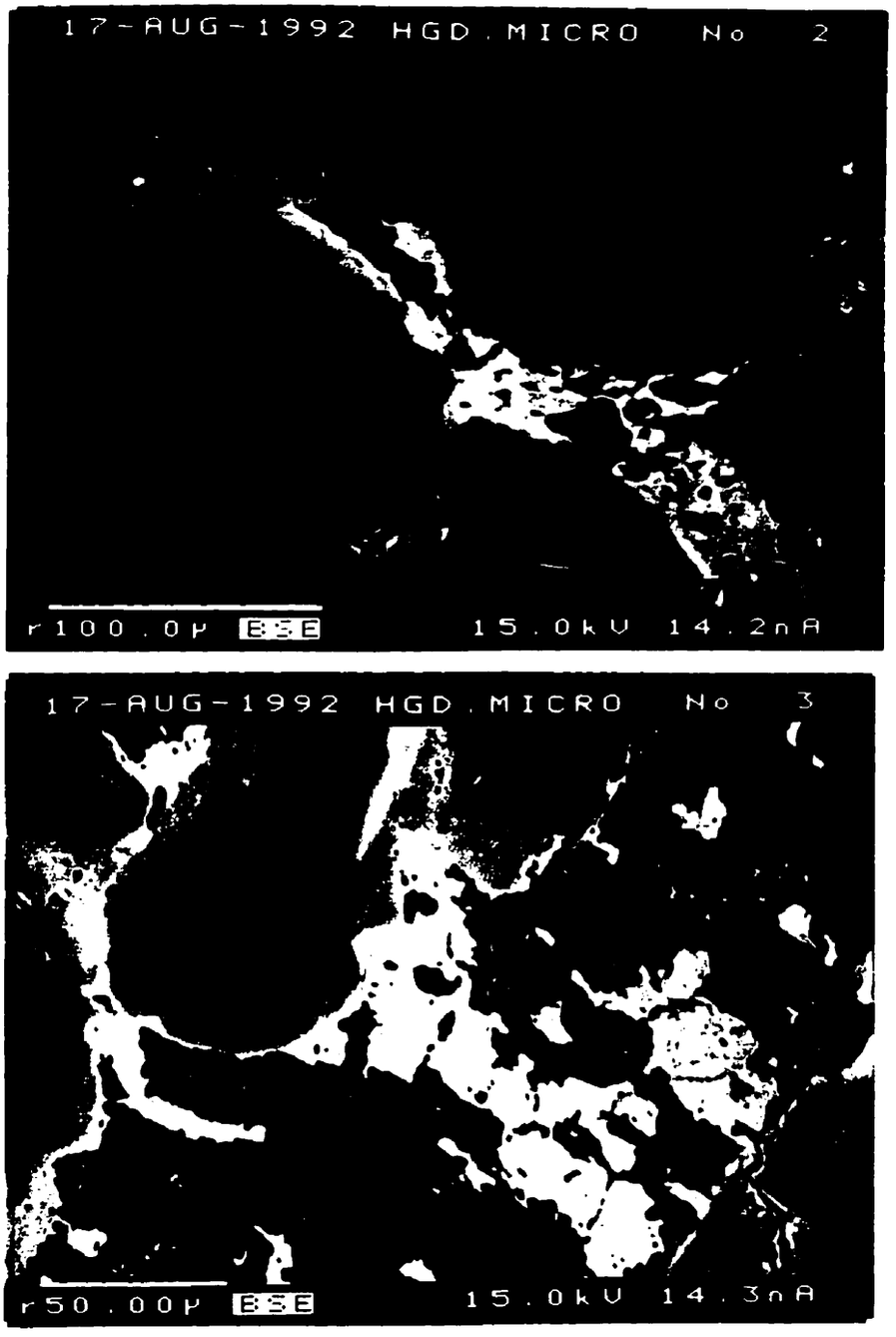

(C)

(D)

Fig. 4.22. BSE images of (K-Rb)-feldspar veining pollucite from High Grade Dyke: (C) and (D) Microcline with wispy veinlets of Rb-enriched feldspar, showing breakdown to porous adularia (dark grey) +(Rb,K)-feldspar (white).

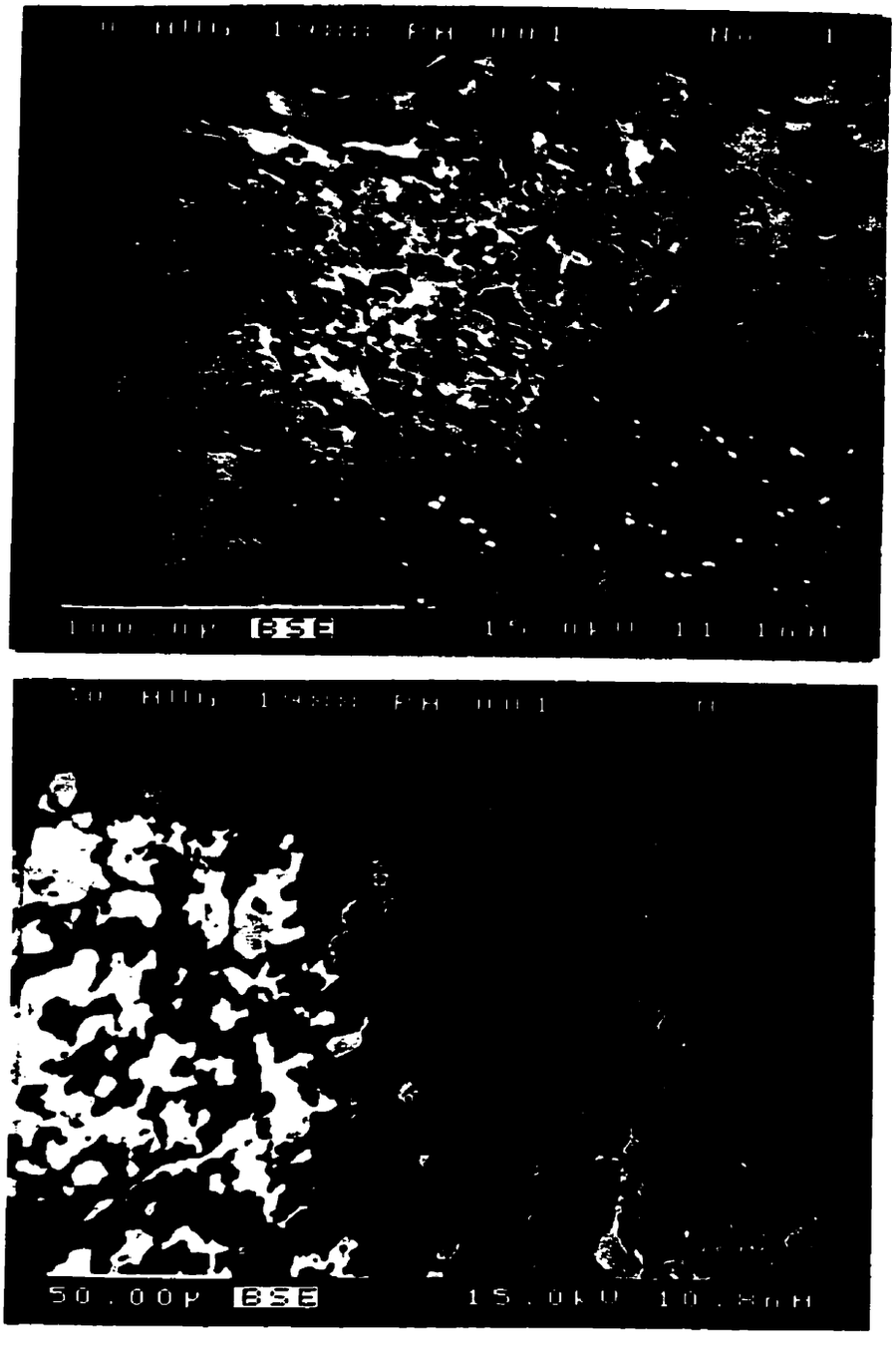

(E)

(F)

Fig. 4.22. BSE images of adularian (K-Rb)-feldspar from High Grade Dyke: (E) Fine-grained granular aggregates of variable-Rb adularia (grey) hosting cookeite (black) and pollucite spheres <2 μm in size (white); (F) (Rb,K)-feldspar (white) in adularia (dark grey) associated with cookeite (black) and Rb-enriched mica (grey).

Table 4.10: Representative compositions of (K-Rb)-feldspar from High Grade Dyke, Manitoba.

oxide	1	2	3	4	5	6	7	8
SiO_2	63.68	63.65	64.68	64.67	61.76	59.75	58.97	57.75
Al_2O_3	17.50	17.46	18.19	18.08	17.43	16.56	16.09	15.72
P_2O_5	0.02	0.02	0.04	0.00	0.02	0.00	0.00	0.01
Na_2O	0.15	0.10	0.01	0.00	0.01	0.00	0.00	0.00
K_2O	14.30	13.79	16.68	16.57	10.70	6.95	5.62	2.33
Rb_2O	2.93	3.95	0.00	0.00	9.95	16.76	18.25	24.07
Cs_2O	0.37	0.35	0.02	0.00	0.30	0.28	0.80	0.57
SrO	0.11	0.02	0.01	0.00	0.11	0.00	0.11	0.07
BaO	0.03	0.00	0.04	0.00	0.00	0.00	0.00	0.00
sum	99.09	99.44	99.96	99.35	100.34	100.35	100.02	100.66
	Atomic contents based on 8 atoms of oxygen							
Si	3.020	3.023	3.004	3.010	3.003	3.012	3.022	3.025
Al	0.978	0.977	0.996	0.992	0.999	0.984	0.974	0.973
P	0.001	0.001	0.000	0.000	0.001	0.001	0.000	0.000
Na	0.014	0.010	0.001	0.000	0.001	0.000	0.000	0.000
K	0.865	0.835	0.988	0.984	0.664	0.447	0.367	0.156
Rb	0.089	0.121	0.000	0.000	0.311	0.543	0.601	0.810
Cs	0.008	0.007	0.000	0.000	0.006	0.006	0.018	0.013
Sr	0.003	0.001	0.000	0.000	0.003	0.000	0.003	0.002
Ba	0.001	0.000	0.001	0.000	0.000	0.000	0.000	0.000
ΣM	0.979	0.973	0.991	0.984	0.985	0.996	0.989	0.981
M^+	0.983	0.974	0.992	0.984	0.988	0.996	0.993	0.983
TO_2^-	0.978	0.976	0.994	0.992	0.999	0.984	0.974	0.973
ΣT	3.999	4.001	4.001	4.002	4.002	3.997	3.995	3.997
Si/Al	3.09	3.10	3.02	3.04	3.01	3.06	3.10	3.11

1-2. Microcline veins in pollucite.
3-4. Adularia hosting Rb-feldspar.
5-8. Rb-feldspar in adularia.

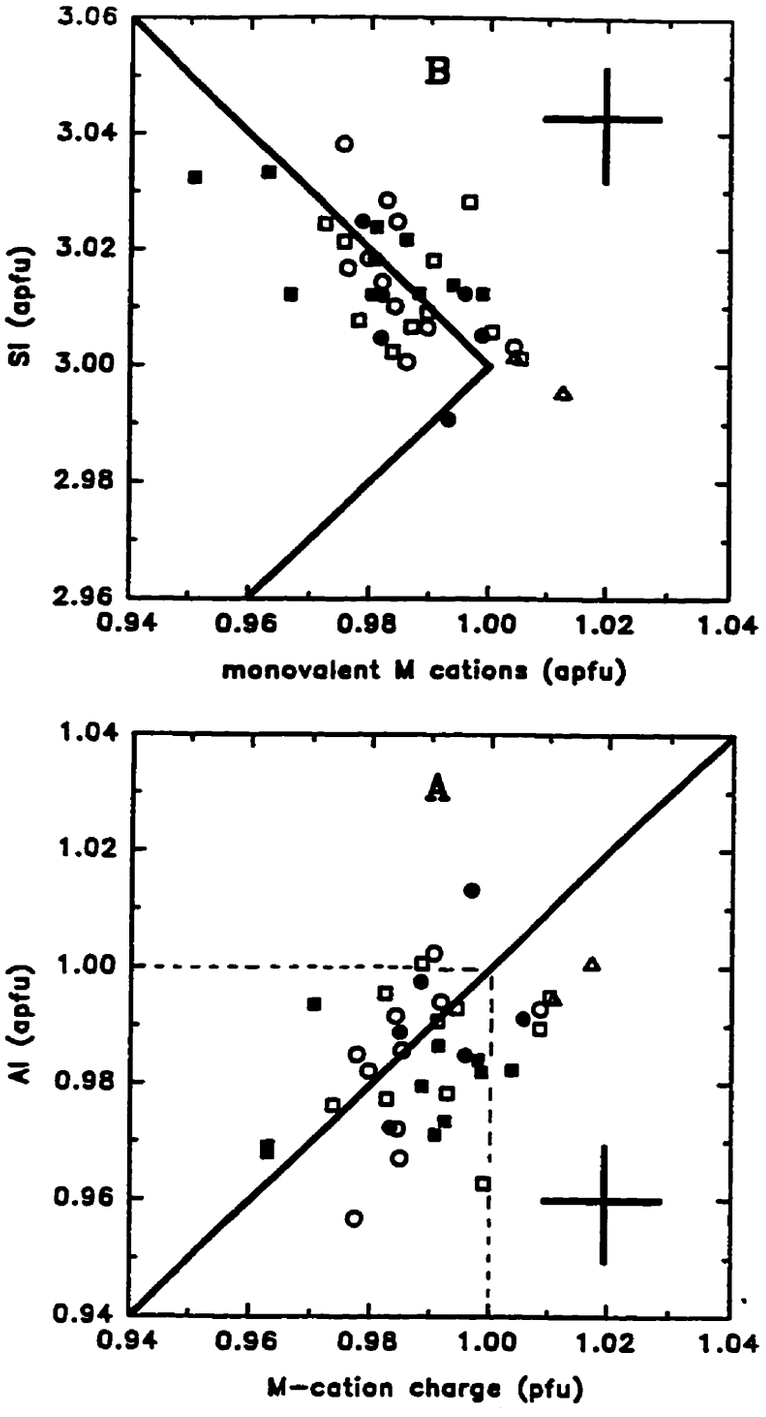

Fig. 4.23. Element variation in (K-Rb)-feldspar from High Grade Dyke: (A) Al *vs.* *M*-cation charge; (B) Si *vs.* monovalent *M* cations. Symbols: blocky microcline (▵); microcline veins in pollucite (□); and associated (Rb-K)-feldspar (■); late adularia (○) and associated (Rb-K)-feldspar (•). Error bars and substitutional lines as in Figure 4.3.

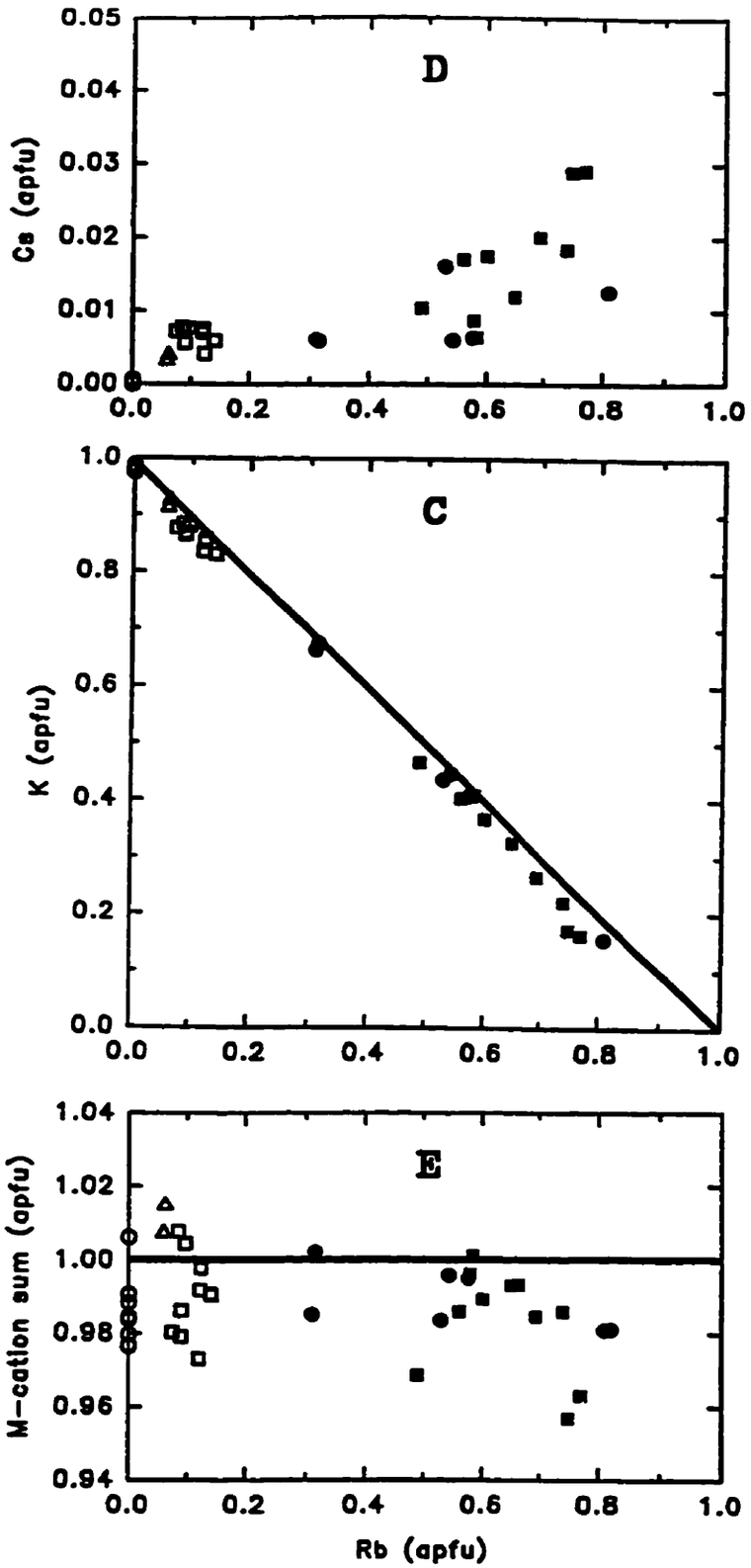

Fig. 4.23. Element variation in (K-Rb)-feldspar from High Grade Dyke: (C) K *vs.* Rb, with a line indicating $\Sigma M = 1$; (D) Cs *vs.* Rb; (E) ΣM *vs.* Rb.

4.7 *Extremes of Rb-enrichment: feldspar and mica from Kola Peninsula, Russia and Red Cross Lake, Manitoba*

The specific locality of our **Kola Peninsula** sample is essentially unknown. At least two pollucite-bearing pegmatites have been described from the Kola Peninsula (Kuzmenko 1976), but so far they have not been fully identified and discriminated in the literature (*e.g.*, Gordiyenko 1973, Voloshin *et al.* 1981). The high Rb content of our pollucite sample (up to 2.8 wt. % Rb_2O; Teertstra & Černý 1995) suggests that it may have come from the same locality as the pollucite analysed by Panasenko & Gorshchenko (1970; 2.13 wt. % Rb_2O). Gordiyenko & Kamentsev (1967) reported 4.1 wt. % Rb_2O and 0.5 wt. % Cs_2O in K-feldspar (bulk composition) from a pegmatite in the Kola Peninsula. Analysis of feldspar veins in pollucite have not been reported by any of the Kola investigators.

Our sample consists of translucent-to-cloudy white pollucite associated with apatite, spodumene, albite, quartz and amblygonite. It is cut by 1-2 mm-wide veins of quartz, colourless microcline and purple mica. Two generations of (K-Rb)-feldspar forming part of the alteration sequence of pollucite are evident on optical examination of polished thin-sections. Non-perthitic vein microcline (+lepidolite) with a faint cross-hatched twinning in cross-polarized light forms generation-1 feldspar. Late thin veinlets of fine-grained mica and spodumene locally crosscut recrystallized pollucite of end-member composition (Teertstra & Černý 1995). On the surface of these veins, and also embedded in the pollucite, are small (<0.5 mm) clusters of albite and untwinned adularian (K,Rb)-feldspar, constituting the second generation of feldspar. The clusters are interspersed with ~70 % pollucite. The Rb-richest grains occur at margins of the clusters,

surrounded by pollucite. Low abundance and a grain size of less than 15 μm preclude characterization of the Rb-richest feldspar by optical microscopy or X-ray diffraction.

BSE imaging indicates two populations of (K,Rb)-feldspar, each with a relatively homogeneous composition. Margins of the microcline vein contain pollucite, mica and minor albite, and grade into the surrounding pollucite (Fig. 4.28A). Grains are also scattered throughout the pollucite. Some of these are surrounded by small grains of Rb-rich feldspar, generally less than 15 μm in size, and constitute the second-generation feldspar (granular aggregates of adularia-type feldspar). Associated mica grains, identified by analysis as muscovite and lepidolite, have Rb-enriched rims (Fig. 4.28B).

Muscovite has 3.82-4.88 wt.% Rb_2O, 0.39-1.08 wt.% Cs_2O and 0.42-0.67 wt.% F, corresponding to 17-21 at.% interlayer Rb, 0.6-1.1 at.% interlayer Cs and 4.5-7.2 at.% anion-site F, respectively. The bulk of the zoned lepidolite has 5.51-6.53 wt.% Rb_2O, 1.08-3.23 wt.% Cs_2O and 1.89-8.54 wt.% F, corresponding to 27-29 at.% interlayer Rb, 3.2-9.4 at.% interlayer Cs and 22-99 at.% anion-site F, respectively. One analysis gave 10.51 wt.% Rb_2O, 1.59 wt.% Cs_2O and 7.30 wt.% F, corresponding to 51 at.% interlayer Rb, 5.1 at.% interlayer Cs and 86 at.% anion-site F, respectively. This represents the Rb analogue of lepidolite. Pollucite has the highest Rb content known for this mineral, with 2.8 wt.% Rb_2O, corresponding to 10 mol.% $RbAlSi_2O_6$ (Teertstra & Černý 1995).

In order to ensure accurate results, a small cluster of Rb-rich feldspar grains in the Kola sample were used as a standard for Rb, Al and Si. Preliminary analysis

indicated no elements present other than K, Rb, Cs, Al, Si and O. Curves for wt.% variations in Al_2O_3, SiO_2, K_2O and Rb_2O were prepared across the series $KAlSi_3O_8$ - $RbAlSi_3O_8$. Using the assumption that K_2O measurements (from 2ORTHO) were accurate, values for Al_2O_3, SiO_2 and Rb_2O were taken from the curves. The value for Rb_2O was corrected for minor Cs_2O (measured using a pollucite standard). This gave 2.29 K_2O, 24.44 Rb_2O, 0.56 Cs_2O, 16.00 Al_2O_3, 56.70 SiO_2, sum 100 wt.%. The results are comparable to those obtained using Eifel sanidine and $Rb_2ZnSi_5O_{12}$ glass. Both analytical approaches gave good agreement with the stoichiometric requirements of the general feldspar formula, although the latter approach seems to be somewhat more accurate, and only these results are reported in Figure 4.25 and Table 4.11.

The distribution of P in both generations of feldspar is patchy, but values reach 0.55 wt.% P_2O_5 in microcline. Values for the local charge generated by the framework were calculated as TO_2^- = (Al-P), for compensation with berlinite substitution $(AlP)Si_{-2}$. Values of (Al-P) of 0.987(8) and *M*-cation charge of 0.987(8) are equal within error (Fig. 4.25A; Table 4.11). Data are scattered about an average (Si+2P) value of 3.013(7) *apfu*, and the sum of the monovalent cations is slightly less than 1.0 *apfu* (Fig. 4.25B). Substitution of $\square Si_4O_8$ is negligible ($\leq$ 2 mol.%). Values for Rb are as high as 0.91 *apfu* (Fig. 4.25C). The two generations of feldspar have distinct composition (Table 4.11). The microcline has an average of 26 mol.% Rb-feldspar (range 22-28). The scattered Rb-rich grains have 82 mol.% Rb-feldspar (range 78-91). The Rb-richest feldspar, with K as low as 0.07 *apfu*, has Cs<0.021 *apfu* corresponding to 2.1 mol.% of a hypothetical Cs-feldspar end-member (Fig. 4.25D). The overall concentration of Cs in each generation is similar.

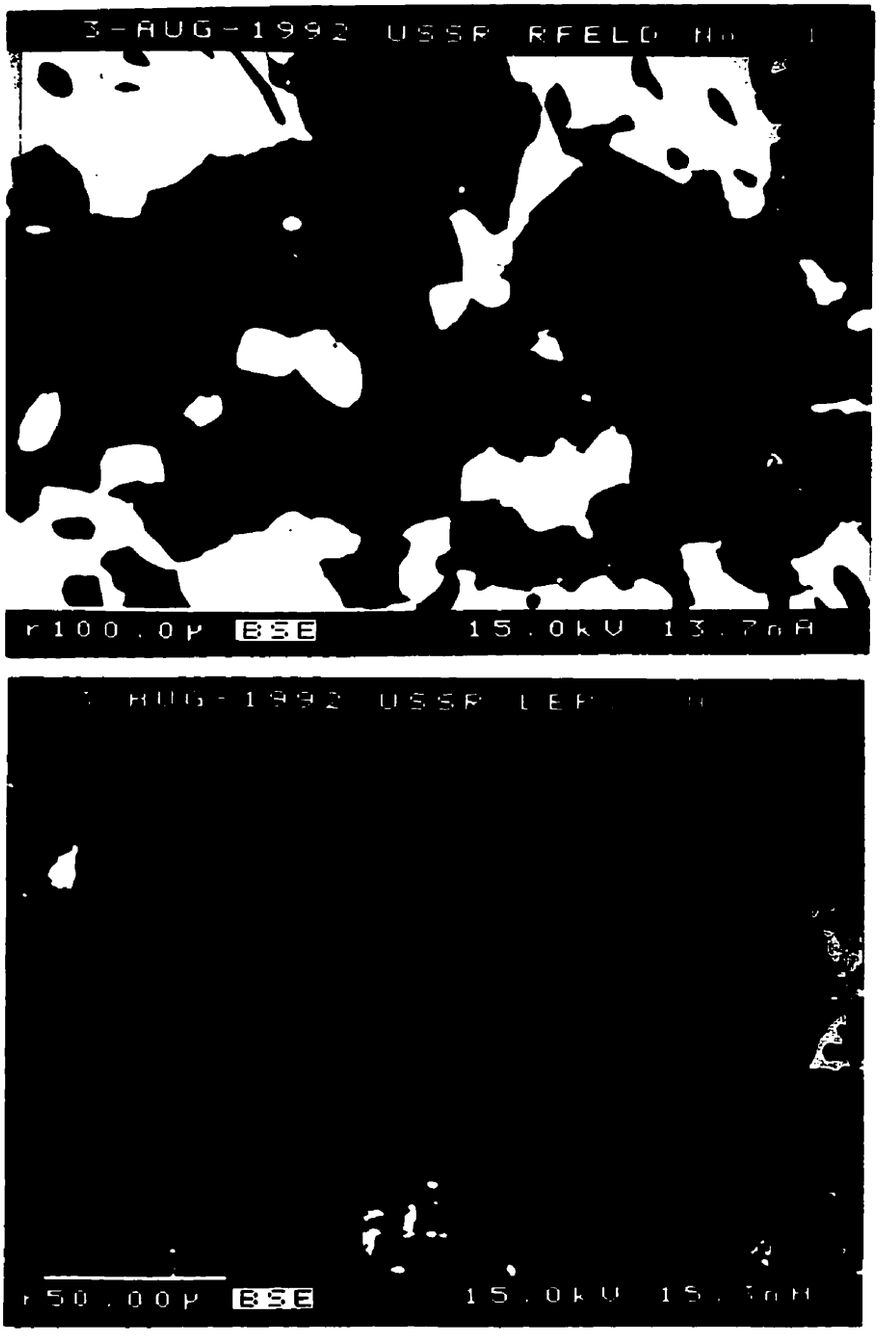

Fig. 4.24. BSE images of (K-Rb)-feldspar from Kola Peninsula: (A) ($K_{74}Rb_{26}$) microcline (grey) with pollucite (white) and albite (black); (B) Lepidolite with variable K/Rb ratio (grey to white) associated with albite (black).

Table 4.11: Representative compositions of (K-Rb)-feldspar from Kola Peninsula, Russia.

oxide	1	2	3	4	5	6
SiO_2	61.15	60.68	61.56(0.59)	57.37	55.73	56.73(0.68)
Al_2O_3	17.87	17.74	17.59(0.17)	16.14	15.67	15.86(0.17)
P_2O_5	0.32	0.31	0.37(0.16)	0.02	0.06	0.10(0.09)
Na_2O	0.31	0.31	0.23(0.09)	0.64	0.00	0.02
K_2O	11.40	11.07	11.26(0.40)	2.69	0.99	2.02(0.55)
Rb_2O	7.95	8.51	8.21(0.49)	22.44	26.12	24.39(1.03)
Cs_2O	0.73	1.00	0.68(0.17)	0.52	0.65	0.59(0.15)
SrO	0.07	0.05	0.02(0.01)	0.07	0.02	0.05
sum	99.84	99.86	99.90(0.74)	100.11	99.24	99.79(0.97)
	Atomic contents based on 8 atoms of oxygen					
Si	2.962	2.961	2.981(0.013)	2.994	3.003	3.006(0.011)
Al	1.026	1.026	1.004(0.007)	0.999	0.995	0.990(0.010)
P	0.013	0.013	0.015(0.006)	0.001	0.003	0.004(0.004)
Na	0.029	0.029	0.022(0.009)	0.065	0.000	0.001
K	0.709	0.693	0.696(0.022)	0.180	0.068	0.136(0.037)
Rb	0.249	0.269	0.256(0.017)	0.758	0.905	0.831(0.036)
Cs	0.015	0.021	0.014(0.003)	0.012	0.015	0.013(0.003)
Sr	0.002	0.001	0.001	0.002	0.001	0.000
ΣM	1.004	1.013	0.987(0.007)	1.018	0.988	0.983(0.010)
M^+	1.006	1.015	0.988(0.007)	1.021	0.989	0.986(0.010)
TO_2^-	1.013	1.014	0.988(0.005)	1.000	0.992	0.986(0.009)
ΣT	4.002	4.000	4.000(0.002)	3.995	4.001	4.000(0.003)

1 and 2. Microcline vein in pollucite.
3. Average composition of microcline (N = 8).
4 and 5. Adularian (Rb,K)-feldspar.
6. Average composition of (Rb,K)-feldspar (N = 9).

Table 4.11: Representative compositions of (K-Rb)-feldspar from Kola Peninsula, Russia.

oxide	1	2	3	4	5	6
SiO_2	61.15	60.68	60.92(0.65)	57.37	55.73	56.78(0.64)
Al_2O_3	17.87	17.74	17.69(0.16)	16.14	15.67	15.89(0.20)
P_2O_5	0.32	0.31	0.35(0.11)	0.02	0.06	0.09(0.09)
Na_2O	0.31	0.31	0.28(0.09)	0.64	0.00	0.06(0.20)
K_2O	11.40	11.07	11.20(0.27)	2.69	0.99	2.09(0.55)
Rb_2O	7.95	8.51	8.25(0.40)	22.44	26.12	24.20(1.03)
Cs_2O	0.73	1.00	0.72(0.13)	0.52	0.65	0.59(0.15)
SrO	0.07	0.05	0.04(0.01)	0.07	0.02	0.00
sum	99.84	99.86	99.44(0.74)	100.11	99.24	99.70(0.97)
	Atomic contents based on 8 atoms of oxygen					
Si	2.962	2.961	2.970(0.013)	2.994	3.003	3.004(0.011)
Al	1.026	1.026	1.016(0.013)	0.999	0.995	0.991(0.010)
P	0.013	0.013	0.014(0.004)	0.001	0.003	0.004(0.004)
Na	0.029	0.029	0.027(0.008)	0.065	0.000	0.007(0.020)
K	0.709	0.693	0.696(0.015)	0.180	0.068	0.141(0.037)
Rb	0.249	0.269	0.259(0.014)	0.758	0.905	0.823(0.041)
Cs	0.015	0.021	0.015(0.003)	0.012	0.015	0.013(0.003)
Sr	0.002	0.001	0.001	0.002	0.001	0.000
ΣM	1.004	1.013	0.999(0.011)	1.018	0.988	0.990(0.015)
M^+	1.006	1.015	1.001(0.011)	1.021	0.989	0.990(0.015)
TO_2^-	1.013	1.014	1.002(0.014)	1.000	0.992	1.000(0.010)
ΣT	4.002	4.000	4.000(0.003)	3.995	4.001	4.000(0.003)

1 and 2. Microcline vein in pollucite.
3. Average composition of microcline (N = 24).
4 and 5. Adularian (Rb,K)-feldspar.
6. Average composition of (Rb,K)-feldspar (N = 10).

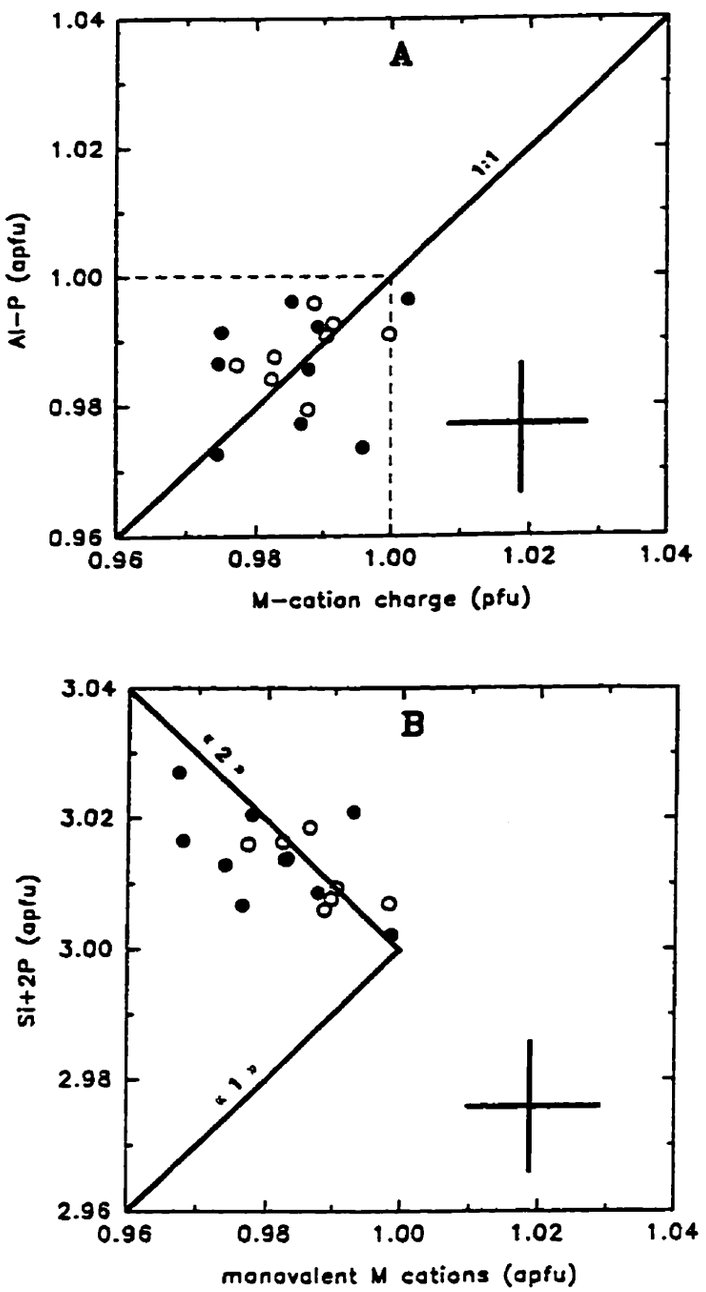

Fig. 4.25. Element variation in (K-Rb)-feldspar from the Kola pegmatite: (A) (Al-P) *vs.* *M*-cation charge; (B) (Si+2P) *vs.* monovalent *M* cations. Symbols: generation 1 (o) and generation 2 (•) feldspars (see text for details), and an average of all the data (■). Error bars and substitutional lines as in Figure 4.3.

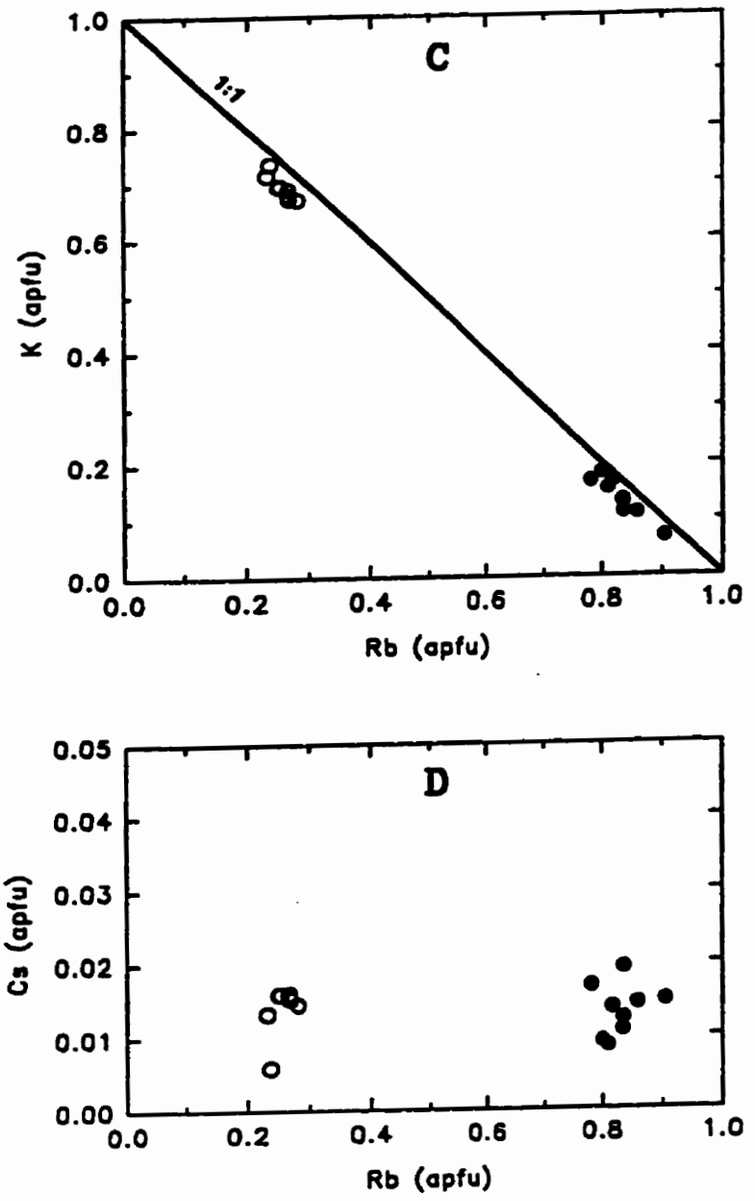

Fig. 4.25. Element variation in (K-Rb)-feldspar from the Kola pegmatite: (C) K *vs.* Rb, with a line indicating $\Sigma M = 1$; (D) Cs *vs.* Rb.

The Red Cross Lake pegmatite swarm is hosted by the Oxford Lake - Knee Lake greenstone belt exposed on the NE shore of Red Cross Lake, NE Manitoba. The area is surrounded by extensive granitic terrains. The highly fractionated pollucite-bearing lepidolite-subtype pegmatites are sheared to mylonitized. High deformation stress caused most primary grains to be reduced to a fine-grained mosaic of albite + mica ± spodumene or to a schistose quartz-mica aggregate. Rare primary albite has bent albite-twinning. The pegmatites contain spodumene + quartz pseudomorphs after primary petalite, along with schorl-elbaite, feruvite, almandine-spessartine, beryl, amblygonite and apatite. Accessory minerals include cassiterite, manganotantalite, microlite, wodginite and zircon (Černý *et al.* 1994). The micas are also extremely rich in Cs and Rb. Initial chemical analysis suggests that the Cs and Rb analogues of both biotite and lepidolite may have been found, as well as the Rb analogue of phlogopite. The K-feldspar is extremely rich in Rb (5.45 wt. % Rb_2O; Černý *et al.* 1985). Most of the K-feldspar is non-perthitic and coarsely Baveno-twinned microcline (with individual twins to 1 cm in size), but a slightly perthitic and grid-twinned microcline is also found locally (*cf.* Černý *et al.* 1985 for additional details).

The following observations are based on examination of numerous hand specimens and 54 thin-sections by optical microscopy, EMP analysis and BSE imaging. Coarse 1-3 cm-size grains of primary minerals, including K-feldspar, pollucite and less commonly amblygonite or beryl, occur locally as aggregates within the sheared rock. These grains are rotated, broken and smeared along shear planes. K-feldspar augen have bevelled edges and recrystallized tails. Grains of K-feldspar smaller than about 0.5 cm are rather rare, even in these tails. The (Rb,Cs)-rich micas (and the rare (Rb,K)-feldspar) tend to be associated with breakdown reactions of blocky rubidian feldspar, and the (Cs,Rb)-rich micas

tend to be associated with alteration of pollucite.

Considerable pollucite is present in the dikes. If there was originally a large pollucite body crosscut by cm-wide veins of coarse-grained feldspar, quartz or lepidolite (as at other localities of pollucite), evidence of this phenomena is not preserved. Augen of primary pollucite (2-3 cm in size) contain randomly-oriented veinlets of (Cs,Al)-rich pollucite + quartz (Fig. 4.26A). The veinlet-forming reequilibration might have taken place prior to shear, or it is possible that the veinlets may not be oriented regardless of the stress direction because pollucite is isotropic.

Micas buffered stress around the brittle pollucite grains. Thin veins of fine-grained mica and spodumene surround and cross-cut the lenses of pollucite and the (Cs,Al)-rich pollucite veinlets (Fig. 4.26A). The mica and spodumene grains within the veins are oriented, suggesting that they formed (or recrystallized) during shear (Fig. 4.26B). Small grains of near-end-member pollucite also occur throughout the pegmatite, particularly along the pollucite augen tails, with textures suggestive of late-stage recrystallization along with albite and spodumene (*i.e.*, during and probably also after shear deformation). Pollucite augen were locally replaced by hydrothermal assemblages of adularia (+ randomly-oriented cookeite), and by randomly-oriented calcite and quartz. The adularia-forming hydrothermal activity probably postdated the main phase of the shearing. Cs-rich lepidolite occurs in cookeite and adularia pseudomorphs after pollucite (Fig. 4.26C; Table 4.13), and adjacent to Cs-rich margins of beryl (Fig. 4.26D). The core of beryl crystals have 1.23 wt.% Na_2O and 1.93 wt.% Cs_2O, and margins have 0.23 wt.% Na_2O and 5.23 wt.% Cs_2O.

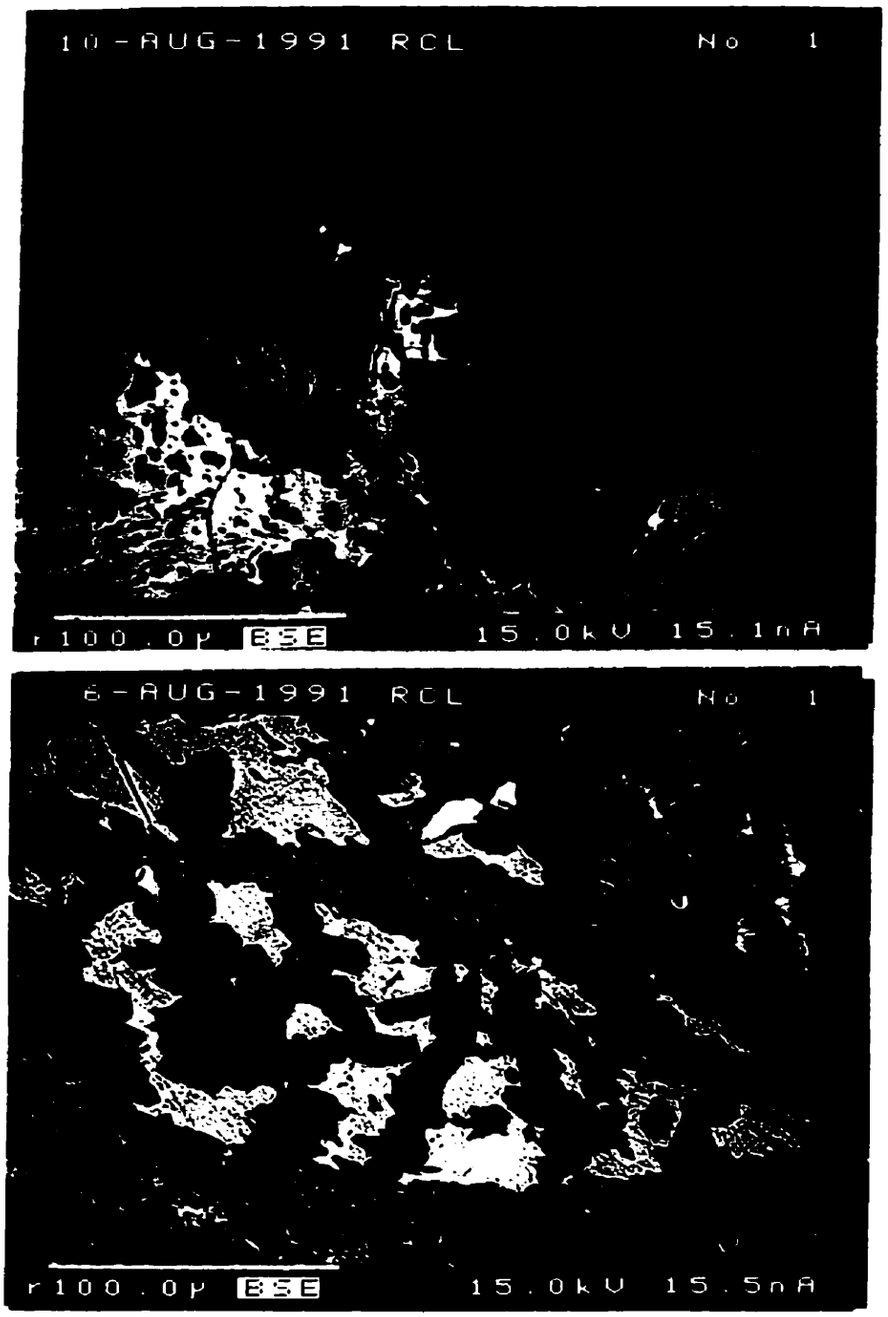

(A)

(B)

Fig. 4.26. BSE images of pollucite from Red Cross Lake: (A) Veinlets of (Cs,Al)-rich pollucite (white) + small grains of quartz (black) in primary pollucite (dark grey) crosscut by veins of fine-grained mica (black); (B) veins of fine-grained mica + spodumene outline eyelets of quartz (black) + calcite (white) pseudomorphs after pollucite.

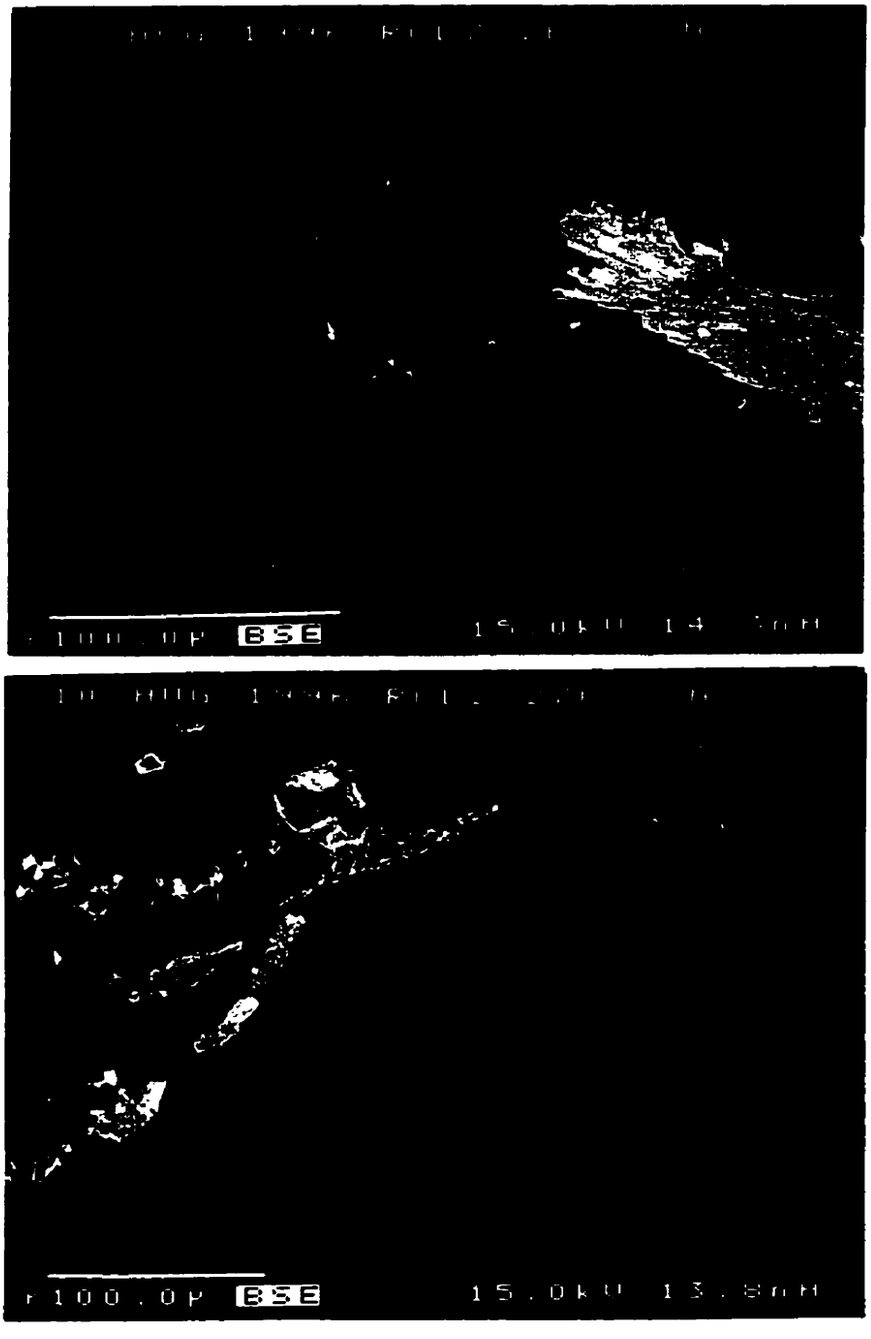

(C)

(D)

Fig. 4.26. BSE images of feldspar and mica from Red Cross Lake: (C) Cs-rich lepidolite (white) occurs with cookeite (dark grey) and adularia (grey) pseudomorphs after pollucite; (D) Cs-rich lepidolite (white) in quartz (grey, top) adjacent to the Cs-rich margins of beryl (light grey).

The Baveno-twinned K-feldspar (Baveno-feldspar) is grey in hand specimen, and is slightly translucent with minimal porosity. The microcline-twinned K-feldspar (microcline-feldspar) is mottled grey-white to pale red in hand specimen and is somewhat turbid and porous; albite micro-lamellae (up to 2 μm wide) are rare. K-feldspar with well-developed cross-hatched twinning is restricted to Rb-poor grains (No.1 in Table 4.12) found within a few cm of wallrock contacts.

BSE imaging shows that the Baveno-feldspar is compositionally homogeneous, whereas the microcline-feldspar is slightly heterogeneous. The two feldspars have similar Rb content, but the BSE grey-level of the Baveno feldspar is slightly higher than that of the microcline-feldspar. Analysis reveals compositional differences between the Baveno and microcline feldspars. The Baveno feldspar has higher contents of Na_2O (>0.2 wt.%), SiO_2 (>62 wt.%), P_2O_5 (>0.3 wt.%) and lower ΣM (average 0.990 *apfu*) than the microcline-feldspar (Fig. 4.27A-F). A smaller compositional range is found for the Baveno feldspar than for the microcline-feldspar, particularly for Na, Cs, Si and P. This may be due to fluid interaction during formation of microcline (and during albite exsolution) resulting in increased porosity. Values for Rb_2O, Al_2O_3 and K_2O are similar for both feldspars. *M*-cation sums for microcline are clustered near 1.000 *apfu*, and *M*-cation sums for the Baveno feldspar are clustered near 0.985 *apfu* (Fig. 4.27E; Table 4.12). This difference may be accounted for by the presence of an average of 0.015 *apfu* Li in the Baveno feldspar and no Li in the microcline feldspar. The current EMP-estimated Li contents are in close agreement with earlier estimates made using tugtupite, leucite and $Rb_2ZnSi_5O_{12}$ as standards to analyse RCL microcline (Table 3.8), and with values from bulk chemical analysis (Černý *et al.* 1985).

Overall, both varieties of blocky K-feldspar have a limited compositional range and negligible alteration. Fine-grained crushed K-feldspar is rare in all the samples examined, including augen tails. As a result of shear-related recrystallization reactions, the blocky K-feldspar is replaced along its margins by a schistose aggregate of mica + quartz + albite ± adularia. Margins of K-feldspar are typically replaced by assemblages of Or_{100} adularia, non-oriented cookeite and late (Rb,Cs)-rich mica (± quartz, albite, calcite, apatite) (Fig. 4.28A-D). By-and-large, these reactions generated (Rb,Cs)-rich mica (± adularia) rather than (Rb,K)-feldspar (+ adularia). Rare (Rb,K)-feldspar (+ cookeite) forms by reaction of microcline margins (Fig. 4.28B) and coprecipitation with adularia (Fig. 4.28C). (Rb,Cs)-rich micas formed by reaction of primary mica with late fluid (Fig. 4.28A,D), or by coprecipitation with cookeite and adularia (Fig. 4.28B). Textural observations suggest that the reaction $(K_{0.85}Rb_{0.15})AlSi_3O_8 \rightarrow KAlSi_3O_8$ (adularia) + (Rb,K)-mica + SiO_2 (quartz) was important.

Data for (Al-P) *apfu vs. M*-cation charge *pfu* (Fig. 4.29A) suggest substitution of 0.02-0.04 atoms of Li *apfu* in the Baveno-twinned feldspar, with average values (Table 4.12) similar to the amounts documented by bulk chemical analysis (Černý *et al.* 1985). Minor Sr and Ba was detected by EMP analysis (Table 4.12). A plot of (Si+2P) *vs.* the sum of monovalent *M*-cations suggests that the $\square Si_4O_8$ substitution, if present, is limited to less than 2 mol.% (Fig. 4.29B). Adularia has a wide range of (Si+2P) and may have up to 5 at.% light-element *M*-cation substitution. The primary feldspar has a rather limited compositional range (Fig. 4.28C); average values are given in Table 4.12. (Rb,K)-feldspar rims on microcline and coprecipitates with adularia have similar compositional ranges, with 55-85 mol.% $RbAlSi_3O_8$ (Fig. 4.29C). Cs concentrations increase with increasing Rb, but do not exceed 2 mol.% $CsAlSi_3O_8$ (Fig. 4.29D).

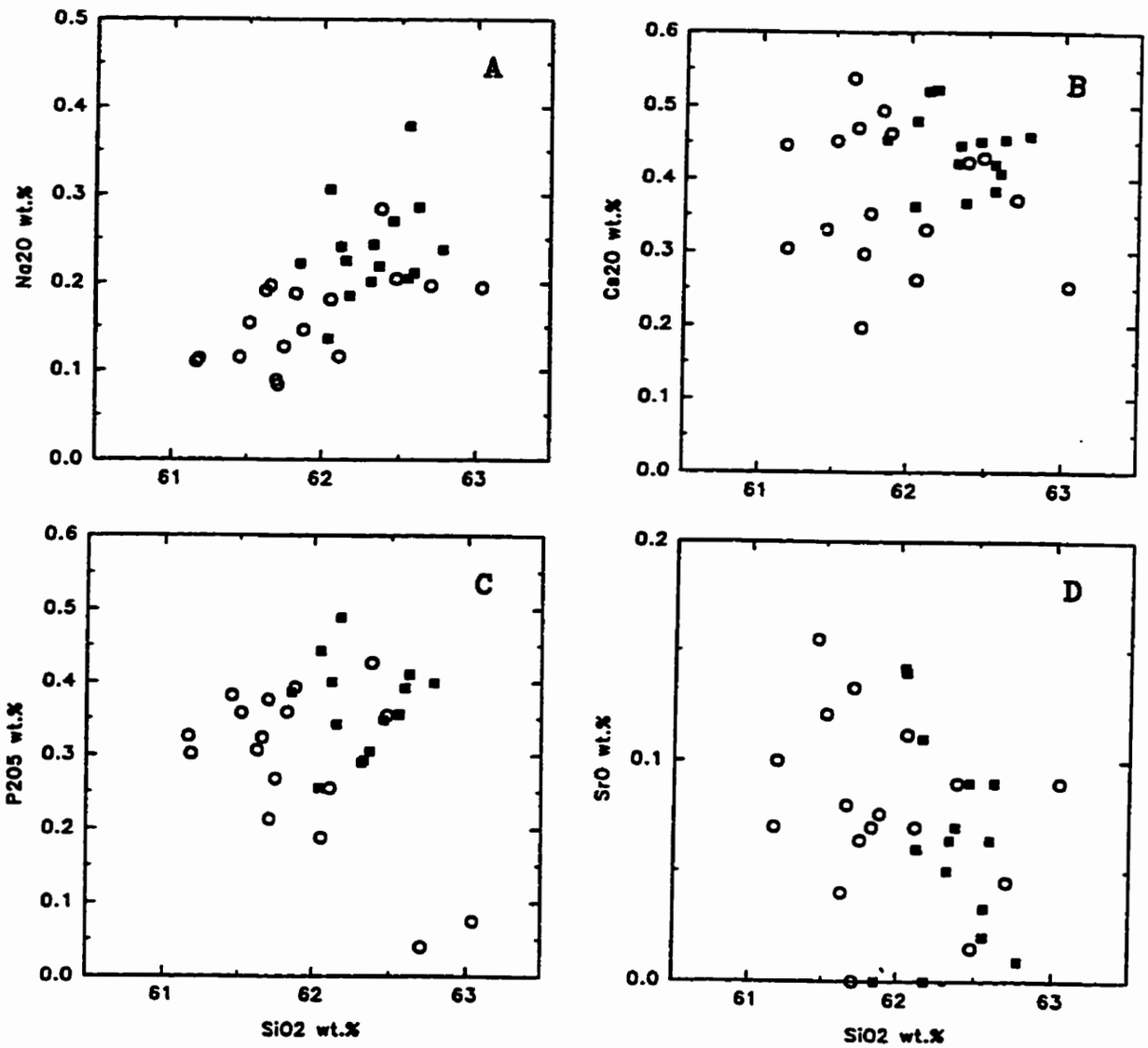

Fig. 4.27. Variation in chemical composition of Baveno-twinned (■) and microcline-twinned (○) blocky (K,Rb)-feldspar from Red Cross Lake: (A) Na_2O *vs.* SiO_2; (B) Cs_2O *vs.* SiO_2; (C) P_2O_5 *vs.* SiO_2; (D) SrO *vs.* SiO_2.

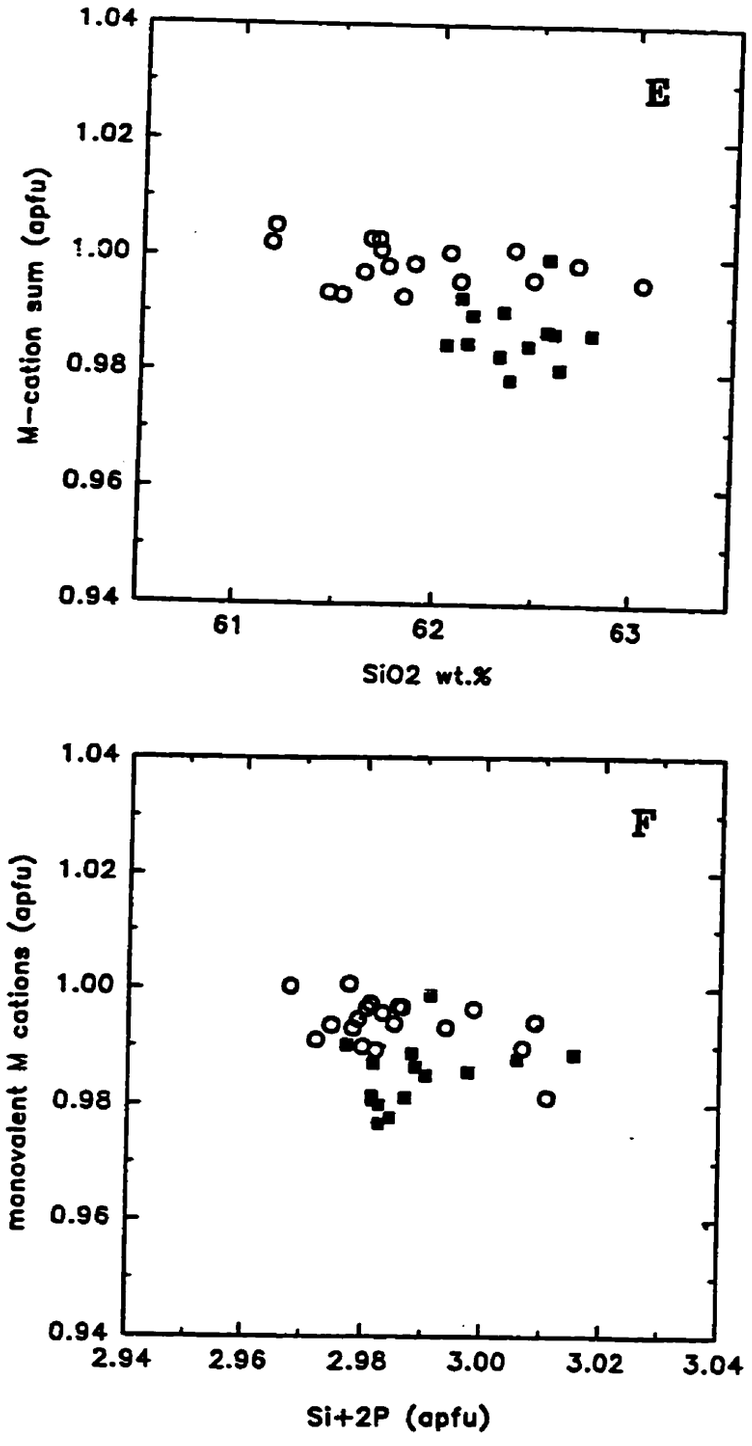

Fig. 4.27. Variation in chemical composition of Baveno-twinned (■) and microcline-twinned (○) blocky (K,Rb)-feldspar from Red Cross Lake: (E) Σ*M* *vs.* SiO_2; (F) monovalent *M* cations *vs.* (Si+2P).

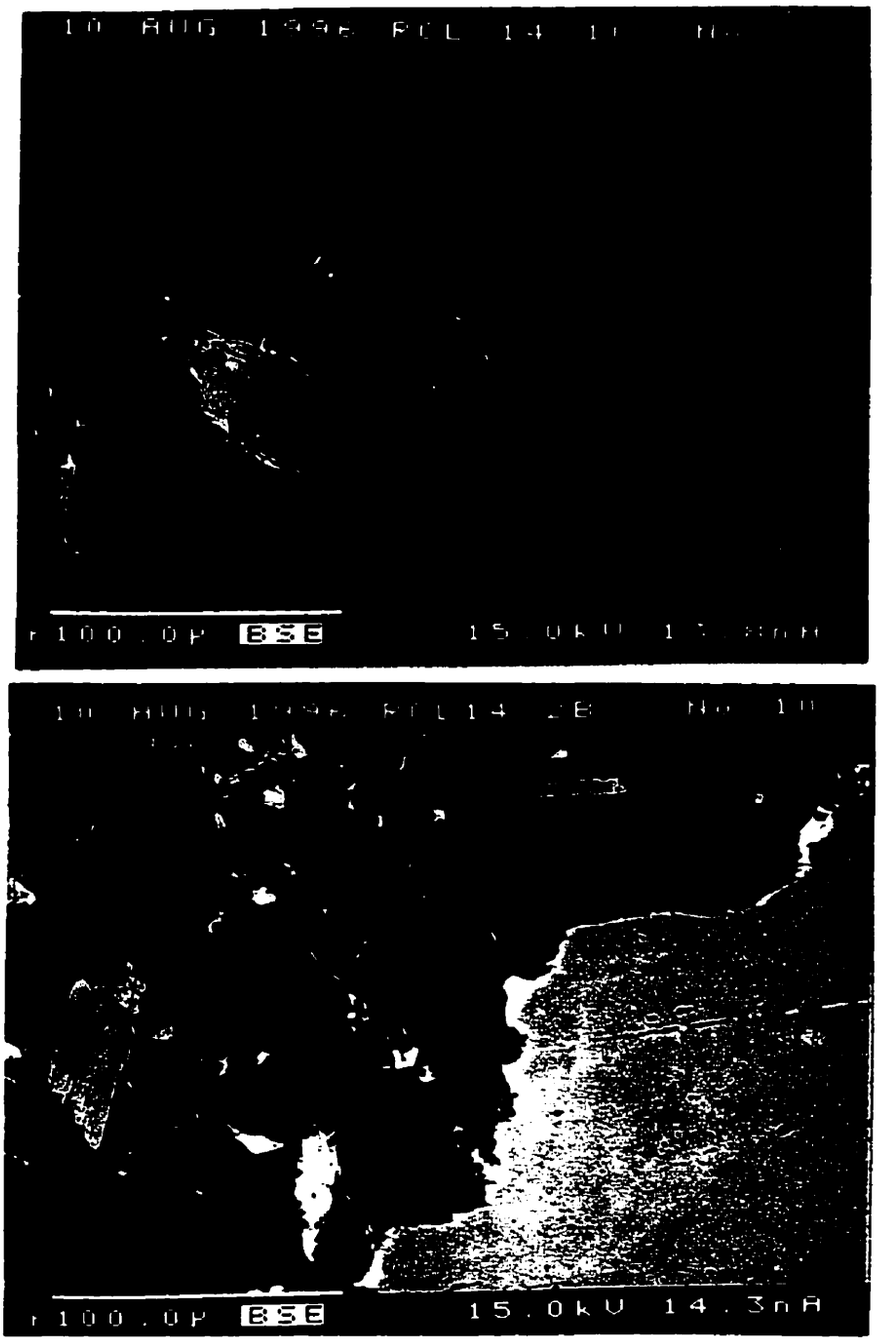

(A)

(B)

Fig. 4.28. BSE images of feldspar and mica from Red Cross Lake: (A) low-porosity Baveno-twinned (K,Rb)-feldspar (grey) replaced by albite (black) and adularia (dark grey). Exposed portions of primary, zoned muscovite (dark grey) - lepidolite (light grey) are enriched in Rb (white); (B) Rb-rich margins (white) of porous microcline-twinned (K,Rb)-feldspar (light grey) replaced by adularia (grey), cookeite (dark grey) and Rb-rich lepidolite (white).

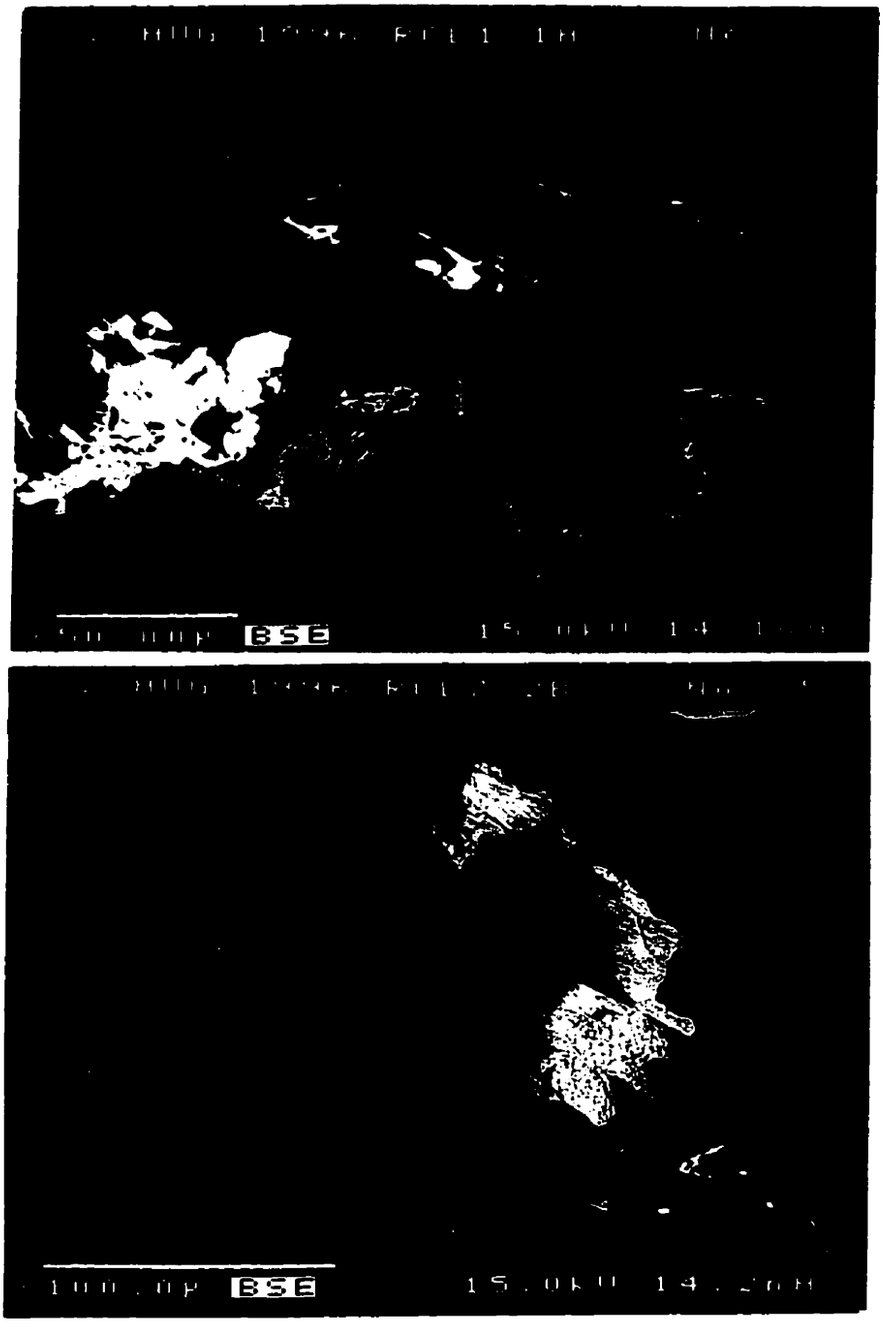

(C)

(D)

Fig. 4.28. BSE images of feldspar and mica from Red Cross Lake: (C) Rb-rich feldspar (white) hosted by Rb-free adularia (+ quartz and albite, black) is rare at Red Cross Lake, Rb-rich margins of muscovite-lepidolite grains are common; (D) Rb-rich margin (white) of lepidolite (grey) in adularia-albite matrix (grey-black).

Table 4.12: Representative compositions of (K-Rb)-feldspar from Red Cross Lake, Manitoba.

oxide	1	2	3	4	5	6
SiO_2	64.86	62.33(0.26)	61.90(0.51)	55.98	64.06	56.70
Al_2O_3	17.89	18.09(0.18)	18.03(0.16)	15.97	18.02	15.78
P_2O_5	0.01	0.36(0.06)	0.29(0.11)	0.00	0.17	0.00
Na_2O	0.28	0.25(0.06)	0.16(0.05)	0.00	0.09	0.00
K_2O	16.19	13.29(0.16)	13.37(0.16)	2.41	16.17	2.33
Rb_2O	0.64	4.86(0.41)	5.01(0.27)	23.47	0.00	24.37
Cs_2O	0.01	0.45(0.05)	0.38(0.10)	0.92	0.08	0.86
SrO	0.00	0.06(0.05)	0.08(0.04)	0.12	0.14	0.00
sum	99.89	99.72(0.34)	99.28(0.63)	99.17	99.05	100.05
Atomic contents based on 8 atoms of oxygen						
Si	3.013	2.971(0.007)	2.970(0.011)	2.991	2.995	3.008
Al	0.980	1.016(0.008)	1.019(0.009)	1.004	0.993	0.987
P	0.001	0.015(0.003)	0.012(0.004)	0.000	0.007	0.000
Na	0.025	0.022(0.005)	0.015(0.005)	0.000	0.008	0.000
K	0.959	0.808(0.011)	0.818(0.008)	0.165	0.964	0.158
Rb	0.019	0.149(0.013)	0.155(0.009)	0.806	0.000	0.831
Cs	0.000	0.009(0.001)	0.008(0.002)	0.021	0.002	0.019
Sr	0.000	0.002(0.001)	0.002(0.001)	0.004	0.004	0.000
ΣM	1.004	0.990(0.011)	0.999(0.004)	1.000	0.992	1.008
M^+	1.004	0.993(0.011)	1.002(0.005)	1.009	0.992	1.009
TO_2^-	0.980	1.002(0.008)	1.008(0.007)	1.009	0.986	0.987
ΣT	3.994	4.002(0.004)	4.002(0.002)	4.000	3.994	3.994

1. Microcline near wallrock contact.
2. Average composition of Baveno-twinned K-feldspar (N = 15).
3. Average composition of microcline-twinned Kfs (N = 17).
4. (Rb,K)-feldspar margins of microcline.
5. Late adularia.
6. (Rb,K)-feldspar associated with adularia + cookeite.

Table 4.13: Representative compositions of micas from Red Cross Lake, Manitoba.

oxide	1	2	3	4	5	6	7	8
SiO_2	47.15	55.75	52.09	49.99	48.60	54.95	50.64	48.83
Al_2O_3	30.72	16.02	19.89	23.50	17.31	16.83	19.59	17.27
Fe_2O_3	0.12	0.06	0.00	0.00	0.05	0.01	0.05	0.06
MnO	0.20	0.20	0.09	0.47	0.18	0.08	0.45	0.08
Na_2O	0.08	0.00	0.02	0.04	0.00	0.10	0.10	0.02
K_2O	8.45	6.42	3.68	7.00	2.65	5.74	5.16	1.31
Rb_2O	5.11	9.10	13.14	7.26	6.14	9.72	8.66	10.26
Cs_2O	0.59	1.03	1.69	1.36	12.96	1.27	3.94	10.66
F	2.26	6.83	4.97	4.59	5.12	6.15	5.83	4.83
H_2O	3.18	0.78	1.63	1.89	1.24	1.09	1.14	1.38
sum	96.91	93.67	95.12	94.16	92.09	93.35	93.11	92.68

1, 2 and 3. Muscovite, lepidolite and Rb-rich tip (Fig. 4.28A).
4 and 5. Lepidolite core and Cs-rich tip (Fig. 4.28D).
6. Rb-rich lepidolite in cookeite (Fig. 4.28B).
7. Cs-rich lepidolite near Cs-rich beryl (Fig. 4.26D).
8. (Cs,Rb)-rich lepidolite replacing pollucite (Fig. 4.26C).

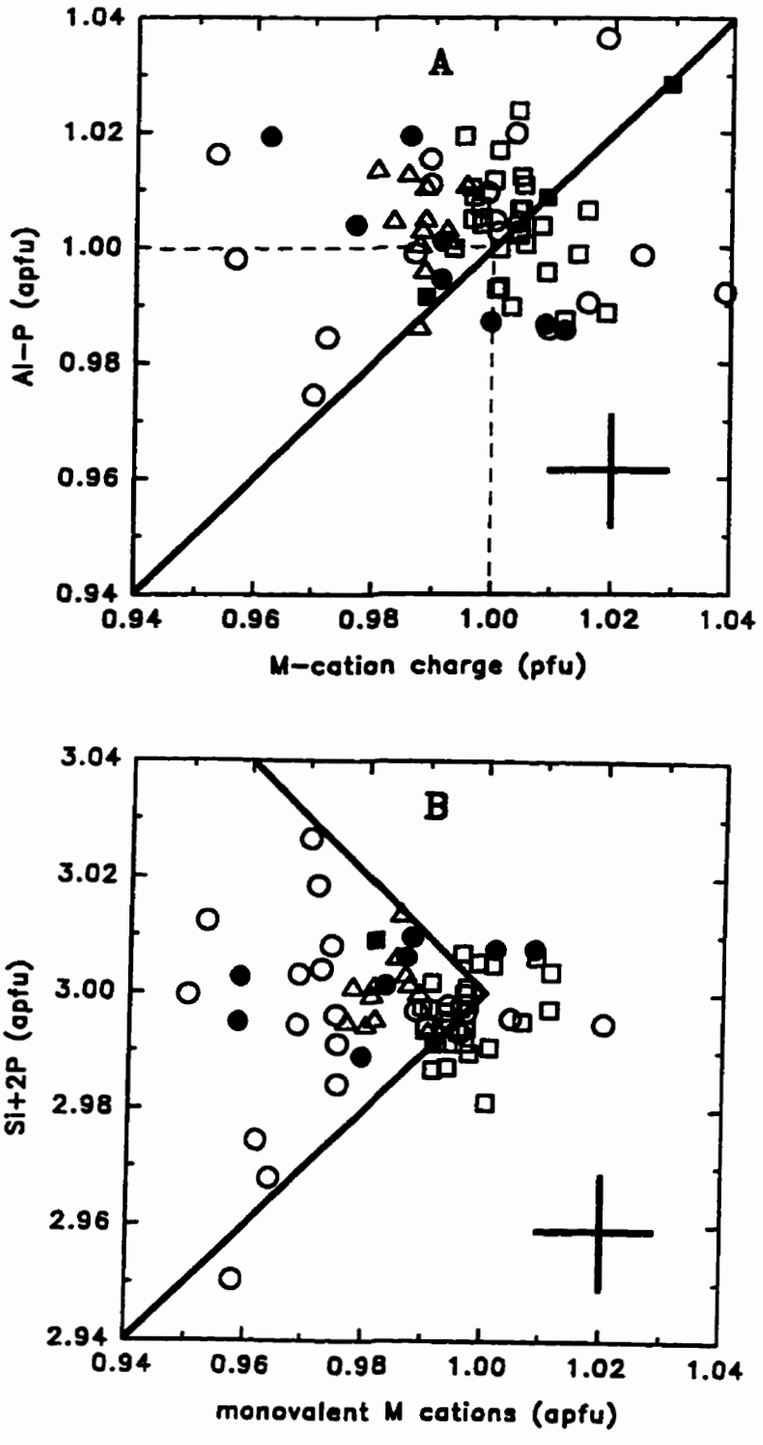

Fig. 4.29. Element variation in (K-Rb)-feldspar from Red Cross Lake: (A) (Al-P) *vs.* *M*-cation charge; (B) (Si+2P) *vs.* monovalent *M* cations. Symbols: microcline near wallrock (♦), blocky Baveno- (▵) and microcline- (□) twinned K-feldspar and associated (Rb,K)-feldspar (■), late adularia (○) and associated (Rb,K)-feldspar (•). Error bars, substitutional lines as in Figure 4.3.

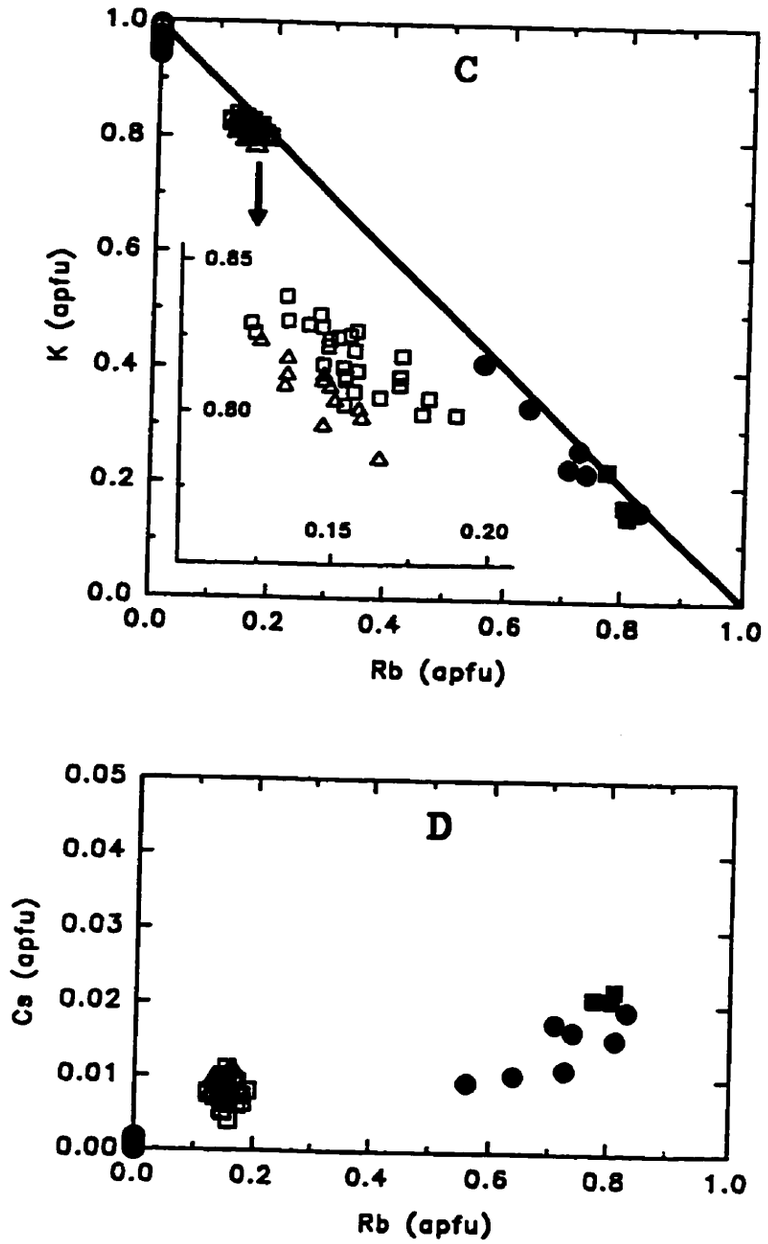

Fig. 4.29. Element variation in (K-Rb)-feldspar from Red Cross Lake: (C) K *vs.* Rb, with a line indicating $\Sigma M = 1$; (D) Cs *vs.* Rb.

4.8 *(K,Rb)-feldspar placed in the alteration sequence of pollucite: various localities*

(K,Rb)-feldspar occurs as a primary mineral which may crystallize at approximately the same time as pollucite (*i.e.*, a late, near-solidus regime). Veins of feldspar which crosscut pollucite most likely formed under subsolidus conditions. Low-temperature feldspar (adularia) which metasomatically replaces pollucite is associated with the formation of end-member pollucite at about 300-200°C (Teertstra & Černý 1995). At lower temperature (~ 150-100°C), pollucite adjacent to adularia undergoes cation-exchange to analcime, with subsequent leaching and replacement by clay minerals. As a guide to the following sections, correspondence of the chemical-textural reequilibration of pollucite with its sequence of alteration including K-feldspar is given in Figure 4.30. A discussion of the alteration sequence of pollucite as it relates to the reactions of (K,Rb)-feldspar is given in Ch. 6.4. Use of the term "adularia" is discussed in Ch. 6.5.

The following sections contain notes on feldspar associated with pollucite from a variety of localities. In many cases, insufficient sample is available to elucidate detailed relationships between various generations of feldspar and the alteration sequence of pollucite. Consequently, observations of the compositional variations of (K,Rb)-feldspar are usually limited, and a detailed examination (and a chapter subsection) is not warranted. The samples of pollucite from the United States are described in Teertstra (1991) and those from Africa are described in Teertstra & Černý (1997). Minor elements not referred to in the text were not detected in EMP analysis; others are given as wt.% oxides.

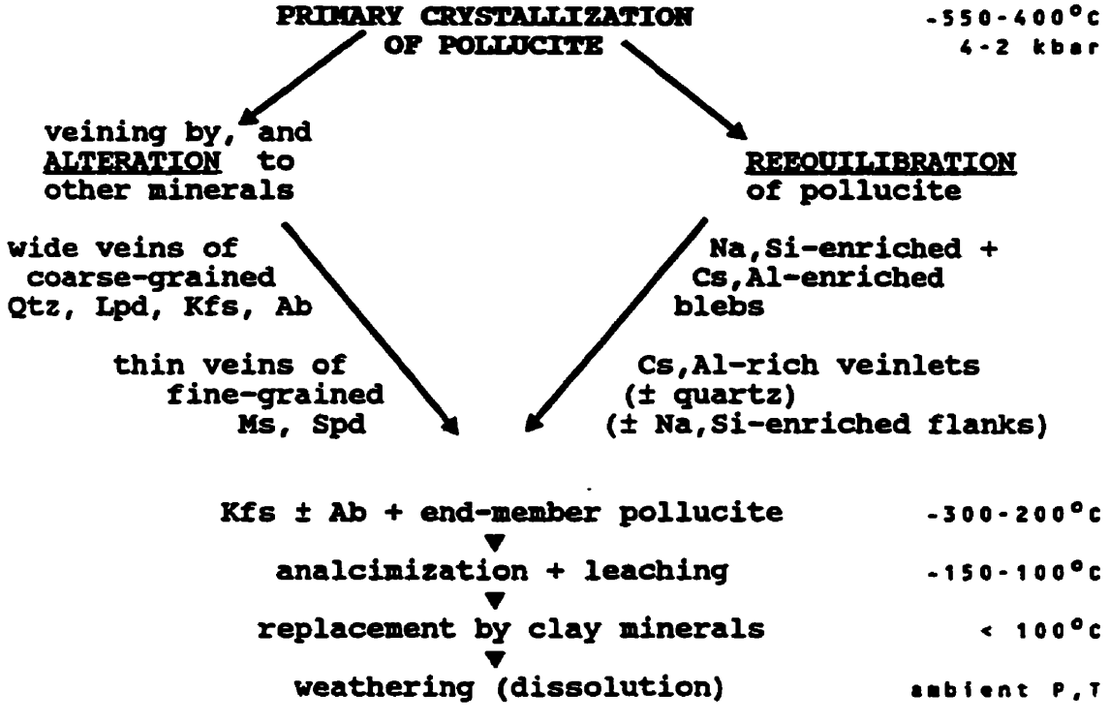

Fig. 4.30. Correlation of the alteration sequence of pollucite (left) with its chemical-textural reequilibration (right) and showing the association of late K-feldspar (Kfs) with end-member pollucite at about 300-200°C.

Pollucite (sample PA-005) from the **Tamminen Quarry**, Greenwood, Maine, is crosscut by a 1-2 mm-wide vein of microcline, and later veins of fine-grained mica + spodumene. The feldspar is homogeneous in BSE images. EMP analysis of the microcline gives compositional ranges of 0.14-0.91 wt.% Na_2O, 0.62-1.87 Rb_2O, 0.09-0.29 Cs_2O and 0.42-0.50 P_2O_5.

Pollucite (PA-078) from near **Norway**, Maine, contains clusters of adularia with 0.60-1.80 Rb_2O, 0.06-0.38 Cs_2O and 0.0-0.79 wt.% P_2O_5. The clusters contain about 30 vol.% inclusions of pollucite. The adularia is light brown in thin section (non-pleochroic) and grains are untwinned (0.5-1.0 mm grain size).

A second locality of pollucite (PA-031) from near **Norway**, Maine, contains a vein of microcline with 0.18-0.81 wt.% Na_2O, 0.51-0.80 Rb_2O, 0.25 Cs_2O and 0.60-0.64 P_2O_5, as well as late adularia containing up to 75% pollucite inclusions (most $< 2\mu m$ in size) with 1.23-2.29 wt.% Rb_2O and 0.12-0.22 Cs_2O.

Pollucite (PA-026) from the **BB #7** Mine, Norway, Maine, has thin veins of mica + spodumene, overgrown by Or_{100} adularia.

Pollucite (PA-139) from the **Walden Gem Mine**, Connecticut, contains 0.5 mm clusters of adularia with 50% pollucite inclusions (+ apatite) with 1.34-2.24 wt.% Rb_2O and 0.04-0.13 Cs_2O.

Pollucite (PA-020) from **Leominster**, Massachusetts, contains 0.5 mm-size granular overgrowths of adularia ($\pm$ mica and apatite) on albite. Adularia has 0.02-0.09 wt.% Na_2O, 0.42-0.47 Rb_2O, 0.10-0.18 Cs_2O and 0.03-0.13 P_2O_5.

Pollucite (PA-026) from **Old Tom Mt.**, Greenwood, Maine, contains clusters of adularia up to 2 mm in size, with abundant pollucite inclusions. Pollucite adjacent to the adularia has end-member composition (see Teertstra & Černý 1995 for details). The adularia is zoned: the main (core) area has 0.6-1.8 wt.% Rb_2O and 0.0-0.55 Cs_2O; the rim has 6-13 wt.% Rb_2O. Insufficient material was available for detailed analysis; the Rb-richest material occupies diminishingly small volume (< 5 μm area) compared to the main adularia.

Pollucite (PA-080) from **Brown Derby**, Colorado, has coarse grains of lepidolite and fine veins of mica, both overgrown by adularia. The composition of the adularia (0.19-0.38 wt.% BaO, 0.05-0.12 Na_2O and 0.0-0.42 Cs_2O) is very similar to the massive adularia analysed in Ch. 4.1 which probably replaces K-feldspar.

Adularia replacing pollucite at **Bikita**, Zimbabwe, has 2.87-9.57 wt.% Rb_2O and 0.19-0.36 Cs_2O, corresponding to 9-29 mol.% Rb-feldspar.

K-feldspar associated with pollucite at the **Benson #1** Zimbabwe, pegmatite has 0.12-0.16 wt.% Na_2O, 2.75-4.45 Rb_2O, 0.29 Cs_2O and 0.0-0.24 P_2O_5.

Microcline associated with pollucite from **Helikon**, Namibia, has 0.21 wt.% Na_2O, 1.12 Rb_2O, 0.30 Cs_2O and 0.41 P_2O_5. Altered margins of the microcline are Rb-enriched, with up to 8.55 Rb_2O and 0.28 Cs_2O, corresponding to 28 mol.% Rb-feldspar. Late adularia has 1.94-6.02 wt.% Rb_2O and 0.10-0.26 Cs_2O, corresponding to 6-19 mol.% Rb-feldspar.

Pollucite from the **Himalaya Dike**, California, contains a large (3 mm diameter) grain of Or_{100} adularia, but this locally contains Rb-richer areas with 3.45 Rb_2O and 0.19 Cs_2O.

Microcline veins in pollucite from **Viitaniemi**, Orivesi, Finland, have 0.14-0.20 wt.% Na_2O, 0.66-0.77 Rb_2O, 0.11-0.23 Cs_2O and 0.48-0.60 P_2O_5. Adularia is relatively homogeneous with 0.11 wt.% Na_2O, 2.08 Rb_2O, 0.23 Cs_2O and 0.62 P_2O_5; however, volumetrically minor late overgrowths have an Or_{100} composition.

Or_{100} adularia replacing pollucite from **Haapaluoma**, Peräseinäjöki, Finland, coprecipitated with albite and contains small grains of mica and apatite. Primary feldspar associated with the pollucite has 0.16 wt.% Na_2O, 0.06 Rb_2O, 0.23 Cs_2O and 0.05 P_2O_5. Details concerning pollucite and its alteration in Finnish pegmatites is given in Teertstra *et al.* (1993).

Adularia replacing pollucite from **Varuträsk**, Sweden, has trace Rb and Ba.

Analysis of amazonite from **Nyköpingsgruvan, Utö**, Sweden, by Sundius (1952) gave 2.54 wt.% Rb_2O. Adularia replacing pollucite from Utö varies in composition from Or_{100} to Ba-rich (0.10-1.06 BaO); individual grains have a variation in Rb_2O of 4-9 wt.% and Cs_2O of 0.0-0.38 wt.% (Fig. 4.31A,B). A large proportion of the adularia has 8-16 mol.% Rb_2O, with local extremes to 30 mol.% (about 10 wt.% Rb_2O). The alteration of pollucite from Swedish localities is given in Teertstra *et al.* (1996).

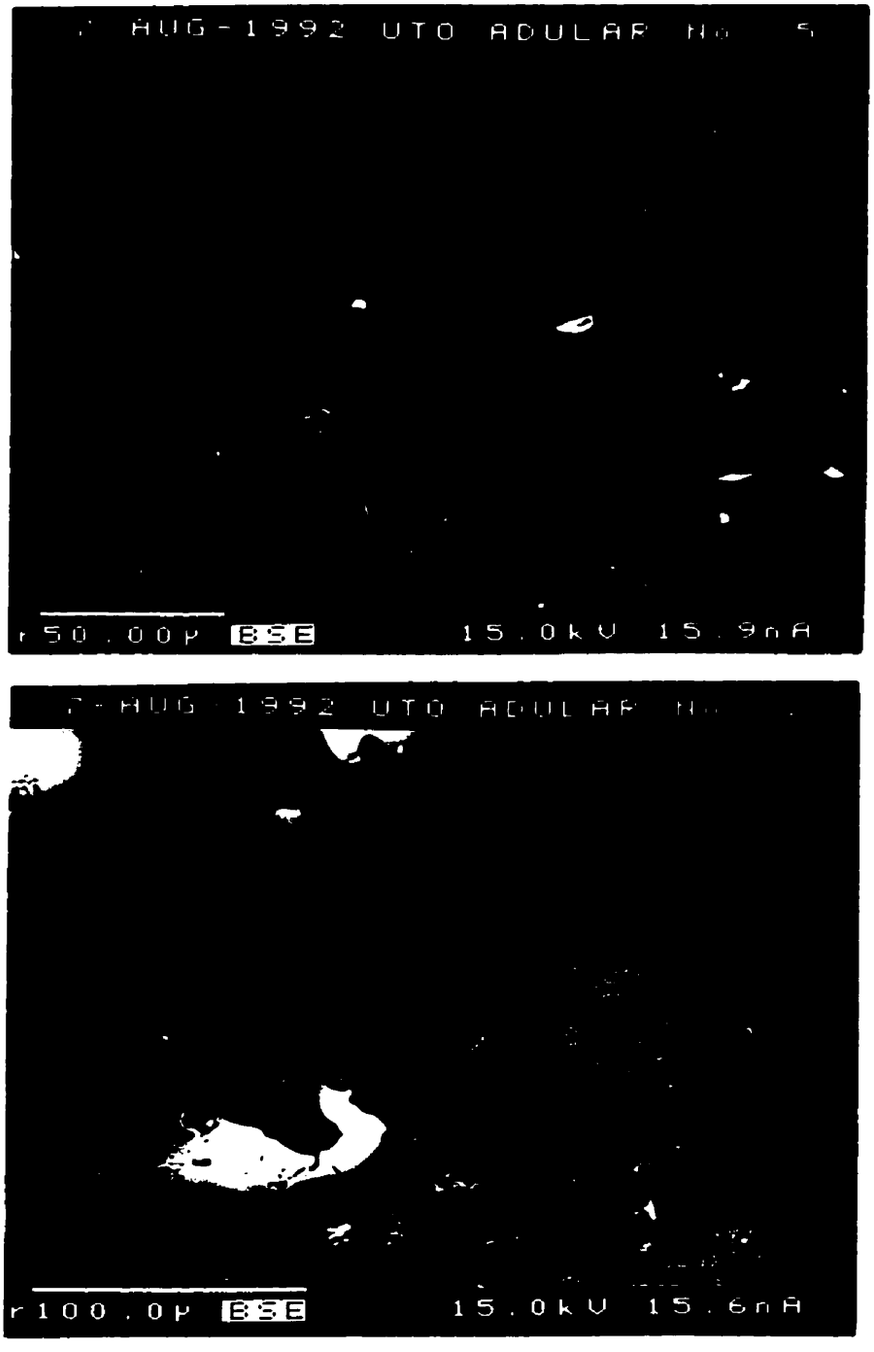

(A)

(B)

Fig. 4.31. BSE images of feldspar from Utö, Sweden: (A) highly porous Rb-variable adularia (dark to light grey); (B) Adularia (grey) with locally elevated Rb (white) in analcime-pollucite (grey to white gradation).

Pollucite from **Ambatonfinondrahana, Madagascar**, is cut by veins of microcline with 0.20 wt.% Na_2O, 0.77 Rb_2O and 0.25 Cs_2O. Adularia has variable Ba: crystal cores are Ba-free with 1.26 Rb_2O, but rims are Rb-free with up to 8 wt.% BaO (28 mol.% Cn). End-member pollucite occurs at this locality (Teertstra & Černý 1995).

Adularian K-feldspar replacing pollucite at a locality in **East Siberia** (sample PA-171) has 0.19 wt.% Na_2O, 2.37 Rb_2O, 0.30 Cs_2O and 0.57 P_2O_5.

Adularia replacing pollucite from **Sušice, Czech Republic**, has 0.10 wt.% Na_2O, 0.17-0.24 Rb_2O and 0.11 Cs_2O.

Microcline associated with pollucite from **Nová Ves u Českého Krumlova** has 0.40 wt.% Na_2O, 0.71 Rb_2O, 0.26 Cs_2O and 0.41 P_2O_5. Pollucite and its alteration has been described from several localities in the Czech Republic (Teertstra *et al.* 1995b).

A vein of microcline cutting pollucite from the **Mongolian Altai #1** pegmatite, China, has 0.11 wt.% Na_2O, 2.04 Rb_2O, 0.20 Cs_2O and 0.10 P_2O_5. Adularia (± cookeite) replacing pollucite from the **MA #3** pegmatite has 0.97-1.19 wt.% Rb_2O and 0.14-0.27 Cs_2O. Microcline adjacent to pollucite from the **MA #83** pegmatite has 0.13-0.15 wt.% Na_2O, 1.28-1.73 Rb_2O and 0.12-0.25 Cs_2O.

Adularia replacing pollucite from the surface of veins of mica and spodumene from the **Valor** pegmatite, Quebec, contains abundant microinclusions of pollucite and cookeite. Rb and Cs increase from core to rim, with 4.16-8.86 wt.% Rb_2O and 0.19-1.07 Cs_2O, corresponding to 12-27 mol.% Rb-feldspar. The geology and mineralogy of the pegmatites in the Preissac-Lacorne area, including the Valor prospect, has been described by Mulja *et al.* (1995, 1996).

The pollucite-bearing Tot Lake pegmatite is located in Webb township about 30 km NE of Dryden, Ontario, 5 km NE of Gullwing Lake and 1 km SW of Tot Lake (Taylor *et al.* 1992). The pegmatite is about 5 m thick at a depth of 20 m below the surface and it pinches out at a depth of 43 m (Ucakuwun 1981). It has poorly developed internal zonation with the exception of a quartz core, traceable along the 25 m length of pegmatite exposed at the surface. The shape is bilobate. Most of the pollucite occurs in the SW lobe associated with spodumene, quartz, albite, mica and beryl. Some is found in the central constricted zone, but pollucite is absent from the albite-rich NW lobe. Accessory minerals include columbite-tantalite, tourmaline, apatite, spessartine, calcite and sphalerite. Finely fibrous holmquistite occurs in the exocontact amphibolite (Ucakuwun 1981, Breaks 1989).

Microcline in contact with pollucite has 0.32-0.40 wt.% Na_2O, 1.75-2.72 Rb_2O, 0.30-0.36 Cs_2O and 0.03-0.27 P_2O_5. Areas of the microcline are clearly reequilibrated, as indicated by the development of porosity, alteration by mica, and locally elevated Rb contents (Fig. 4.32A). These Rb-richer areas have 0.05-0.09 wt.% Na_2O, 4.20-6.65 Rb_2O, 0.08-0.11 Cs_2O and 0.0-0.05 P_2O_5. Adularia replacing pollucite shows a sequence of crystallization similar to that observed at the Morrua Mine: (1) the core has variable K/Rb with 4.28-7.16 wt.% Rb_2O and 0.07-0.18 Cs_2O; (2) high Rb-enrichment marks the end of the core-zone crystallization with 12.34-16.32 wt.% Rb_2O and 0.14-0.39 Cs_2O; (3) Or_{100} adularia (with variable $BaO \leq 0.6$ wt.%) occurs adjacent to Na-exchanged pollucite (Fig. 4.32B). The highest Rb value corresponds to 54 mol.% Rb-feldspar. Insufficient microcline was found in association with the pollucite samples to warrant detailed investigation, but even these limited observations suggest that interesting results could be obtained on examination of additional material.

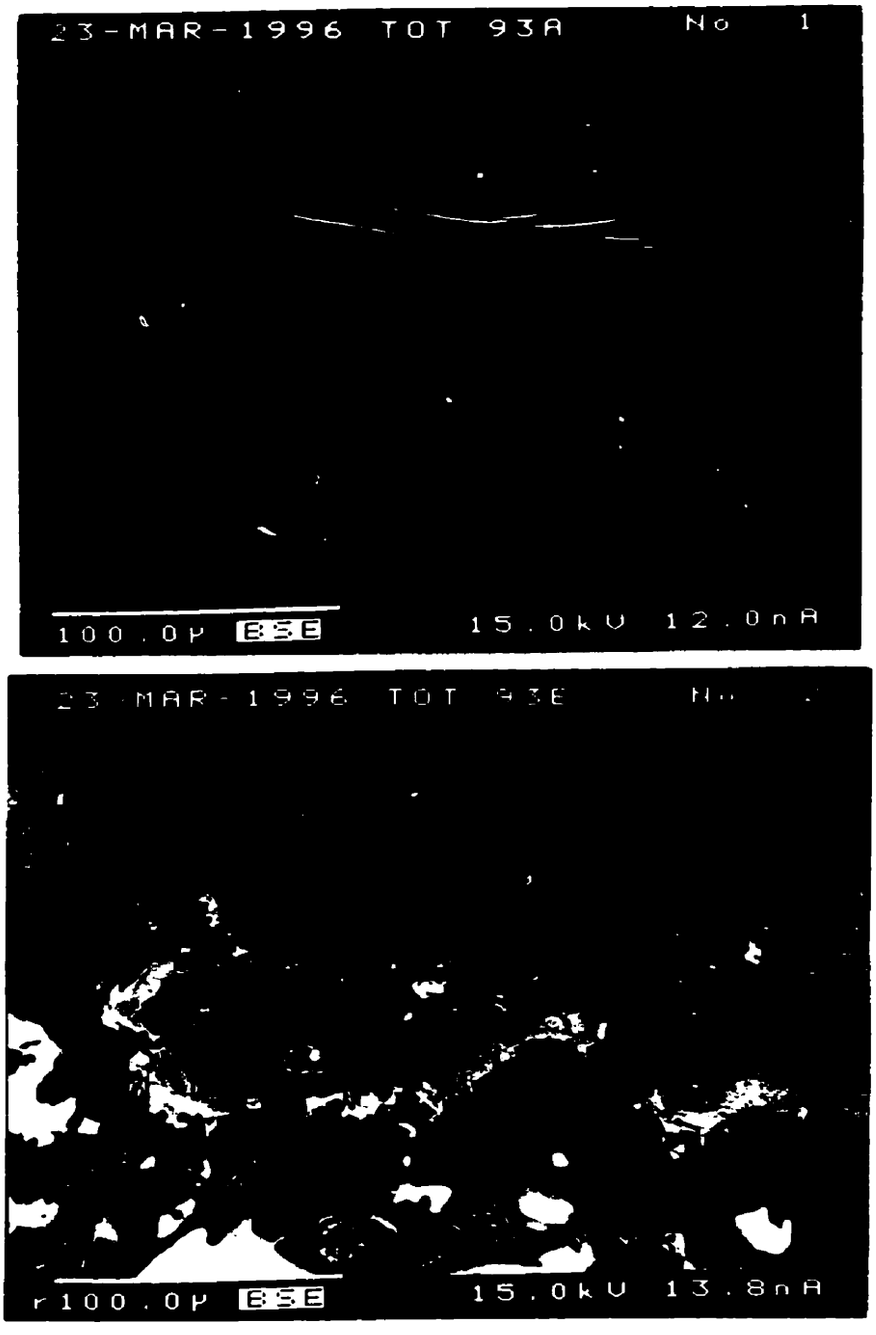

Fig. 4.32. BSE images of feldspar from Tot Lake, Ontario. (A) homogeneous (K,Rb)-feldspar (left) replaced with porous higher-Rb feldspar associated with mica (+ interlayer apatite); (B) Rb-variable adularia (grey to white) overgrowth on albite (top, black) with a late overgrowth of Rb-free adularia (dark grey) associated with analcimization of pollucite (bottom, grey to white).

4.9 *Late-subsolidus activity of Rb and Cs: cesian analcime, micas and clay minerals*

The reactions generating late (K-Rb)-feldspars and the reequilibration of pollucite indicate substantial late-hydrothermal activity of Rb and Cs. The intensity of alteration and reaction of K-feldspar, pollucite, micas and lithium aluminosilicates varies widely among pegmatites and within zones of individual pegmatites, and extends to low temperature. In this section, I document (1) the evolving Na/Cs ratio of late fluids as recorded in the fine-scale zoning of cesian analcime at Greenwood and Tanco; (2) the variable Rb and Cs activity of late fluids generating mica-group minerals at several localities; (3) an occurrence of Cs-rich clay minerals formed at $T<200°C$; (4) an occurrence of a Cs-rich zeolite-group(?) mineral associated with cesian analcime which replaces petalite at Luolamäki, Finland.

Patterns of zoning in **cesian analcime** are among the most complex in any mineral yet examined. Euhedral crystals of cesian analcime were first found and described from "alpine-vein" assemblages within the spodumene-rich zones from the Tanco pegmatite, SE Manitoba (Černý 1972). To date, however, cesian analcime has not been described from additional localities. However, because primary pollucite is consistently anhedral, any occurrences of euhedral Na-rich crystals are potentially those of cesian analcime (Smeds & Černý 1989, Teertstra & Černý 1992). This description is similar to that of Richmond & Gonyer (1938), who had described from Greenwood, Maine, an early generation of massive granular pollucite (with bulk CRK = 100(Cs + Rb + K)/Σ cations = 83), overgrown by euhedral "pollucite" crystals which are richer in sodium (with bulk CRK = 55; labelled cesian analcime in Table 4.14). This material was re-investigated and both primary pollucite (this study, No.3 in Table 4.14) and secondary cesian analcime (described below) were found.

Table 4.14: Reported bulk compositions of cesian analcime and pollucite from Greenwood, Maine and Tanco, Manitoba.

		1	2	3	4	5	6
SiO_2	wt.%	50.07	44.28	47.64(.34)	54.85	52.10	46.11
Al_2O_3		17.19	16.32	16.30(.16)	20.36	17.60	16.09
P_2O_5		----	----	0.34(.02)	----	----	0.32
Li_2O		0.09	----	----	----	----	0.27
Na_2O		4.34	1.59	1.99(.17)	10.30	6.46	1.52
K_2O		0.17	0.38	0.01	0.40	0.19	0.07
Rb_2O		----	----	0.10	0.01	0.06	0.95
Cs_2O		24.54	35.83	31.95(.52)	6.00	18.00	32.90
CaO		0.09	0.13	0.00	0.05	0.13	0.01
H_2O^+		3.81	1.62	----	7.51	4.45	1.69
H_2O-		----	----	----	0.41	0.14	0.01
sum		100.30	100.15	98.35	99.89	99.13	99.95
Si	*apfu*	2.142	2.092	2.140	2.093	2.146	2.116
Al		0.867	0.909	0.863	0.916	0.854	0.870
P		-----	-----	0.013	-----	-----	0.012
Li		0.016	-----	-----	-----	-----	0.050
Na		0.360	0.146	0.174	0.761	0.516	0.135
K		0.009	0.023	0.001	0.019	0.010	0.004
Rb		-----	-----	0.003	0.001	0.002	0.028
Cs		0.448	0.722	0.612	0.098	0.316	0.644
Ca		0.000	0.007	0.000	0.002	0.006	0.001
TO_2		0.867	0.909	0.863	0.916	0.854	0.870
M^+		0.833	0.904	0.789	0.887	0.856	0.813
Si/Al		2.47	2.30	2.48(.02)	2.28	2.51	2.43
CRK		54.9	83.0	78.0(1.8)	13.3	38.6	82.9

1. Cesian analcime (Greenwood B; Richmond & Gonyer 1938).
2. Pollucite Greenwood A: Richmond & Gonyer 1938).
3. Average (EMP,N=7) of Greenwood pollucite (this study).
4 and 5. Cesian analcime (Tanco #1 and #2 of Černý 1972).
6. Tanco pollucite (Bennington *et al.* (1983). Other compositions are similar: Si/Al 2.55 CRK 81.9 (Nickel 1961); Si/Al 2.51 CRK 79.3, 2.58 and 73.3, 2.38 and 73.8 (Černý & Simpson 1978).

Polished sections of generally-oriented crystals were prepared and analysed using a CAMECA SX-50 electron microprobe and using the *PAP* reduction procedure of Pouchou & Pichoir (1985). Back-scattered electron (BSE) imaging was used to select points for analysis. For compositions rich in Cs (CRK > 50), major elements were measured using 15 kV, 20 nA, a beam size of 5 μm and count times of 20 s (background 10 s). Standards used were pollucite (Al $K\alpha$, Si $K\alpha$, and Cs $L\alpha$) and albite (Na $K\alpha$). Minor elements were determined using 15 kV, 40 nA, a beam size of 5 μm and count times of 50 s (background 25 s). Standards used were rubidian microcline (Rb $L\alpha$), orthoclase (Fe $K\alpha$ and K $K\alpha$), anorthite (Ca $K\alpha$) and vanadium diphosphate (P $K\alpha$).

For compositions rich in Na (CRK < 50), major elements were measured using 15 kV, 10 nA, a beam size of 20 μm and count times of 20 s (background 10 s). Due to strong interactions of the electron beam with analcime, these conditions were necessary to reduce variation in X-ray counts. The main problem is loss of Na counts with time, probably due to diffusion of Na out of the analysed volume. Standards used were albite (Na $K\alpha$, Al $K\alpha$, and Si $K\alpha$) and pollucite (Cs $L\alpha$). Minor elements (Rb, Fe, K, Ca, and P) were determined using 15 kV, 10 nA, a beam size of 20 μm, count times of 50 s (background 25 s) and the same standards as above.

Results of the analysis were recalculated to atomic contents on the basis of six atoms of oxygen per anhydrous formula unit. The CRK index was calculated as 100(Cs + Rb + K)/Σ cations (Černý 1974), where Σ cations = (Li) + Na + Ca + Cs + Rb + K. The CRK index is based on assignment of the relatively large Cs^+, Rb^+, and K^+ cations to the 16*b* site which also hosts molecular H_2O, and assignment of the smaller Na^+ and Ca^+ cations to the 24*c* site (according to Beger's (1969) crystal-structure determination of pollucite).

The Greenwood, Maine, samples (one labelled Harvard #94791, and an aggregate of euhedral crystals labelled Harvard #94630 secondary) are from the Tamminen quarry, Noyes Mountain. The Harvard #94791 sample was identified as pollucite; it is isotropic, anhedral and mostly homogeneous in composition. Si/Al ranges from 2.46 to 2.51 and CRK from 75.8 to 80.6; an average composition is reported in Table 4.13 and the range is shown as a rectangle in Figure 4.34. Along fractures and adjacent to veins of fine-grained mica and spodumene, pollucite is locally Na-exchanged at constant Si/Al, with CRK decreasing to as low as 67. The textural relationships between pollucite and cesian analcime are not known: no cesian analcime was found within the sample of primary pollucite or vice-versa. The euhedral crystals were identified as cesian analcime, associated with fine-grained quartz and a light coating of white-to-buff clay minerals. As in Richmond & Gonyer's (1938) original description, the crystals are birefringent and replace petalite.

Zoning of cesian analcime is due to variation in Na/Cs and Si/Al. The bulk of the Greenwood crystals are homogeneous (with CRK $\approx$ 60) to modestly zoned (with Si/Al variable from 2.60 to 2.75; main grey areas in Figs. 4.33A, B). A minor volume of the crystals is occupied by CRK-high Si/Al-low zones with CRK variable from 62 to 66 and Si/Al variable from 2.35 to 2.55 (white areas in Figs. 4.33A, B; details of the lamellar-zoned structure is given in Figs. 4.33C, D). These zones seem to have crystallized at the same time as the bulk of the

homogeneous to modestly-zoned areas, and these form a linear compositional trend (Fig. 4.34).

A stage of high-CRK crystallization followed, generating compositions similar to that of the primary pollucite (Fig. 4.33E). However, compared to the primary pollucite, this material has a wider compositional range (Fig. 4.34) and lacks significant Rb or P (Table 4.15). The final phase of crystallization shows the classic features of oscillatory zoning (Fig. 4.33F). This is defined mainly by cyclic variation in CRK within a trend of broadly decreasing Cs concentration toward outer rims of analcime. There are relatively minor variations in Si/Al which contribute additional complexity to the zoning. The zone boundaries vary from sharp to gradational, and parts of the zonal sequence show oscillatory features.

All the above generations are locally overprinted by analcimization (decreasing CRK at constant Si/Al).

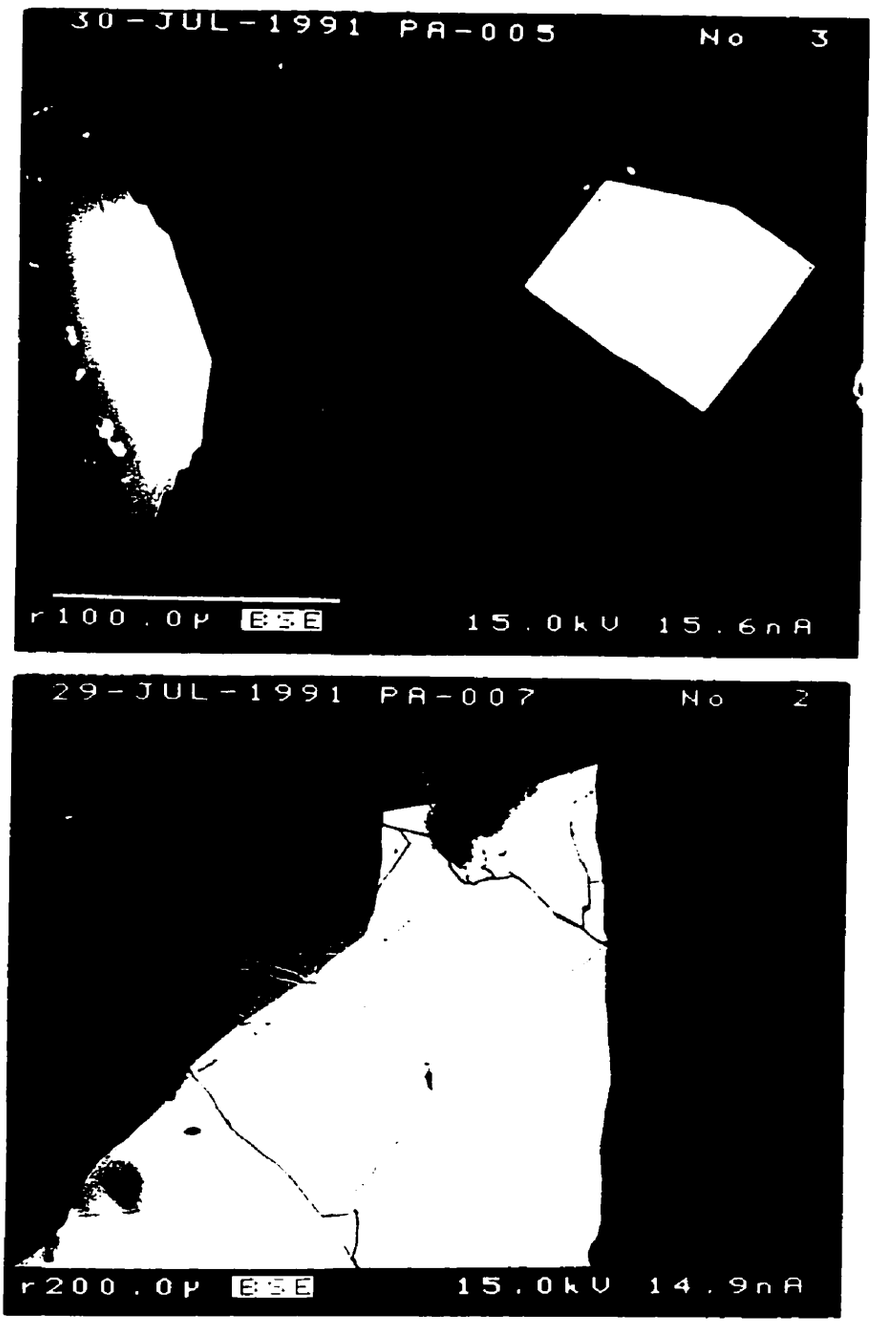

Fig. 4.33. BSE images of cesian analcime from Greenwood, Maine: (A) and (B) Zones of high-CRK low-Si/Al (white) occur in cesian analcime with slightly lower CRK and higher Si/Al ratio (variable grey); (B) Analcimization (black) affects all generations of cesian analcime.

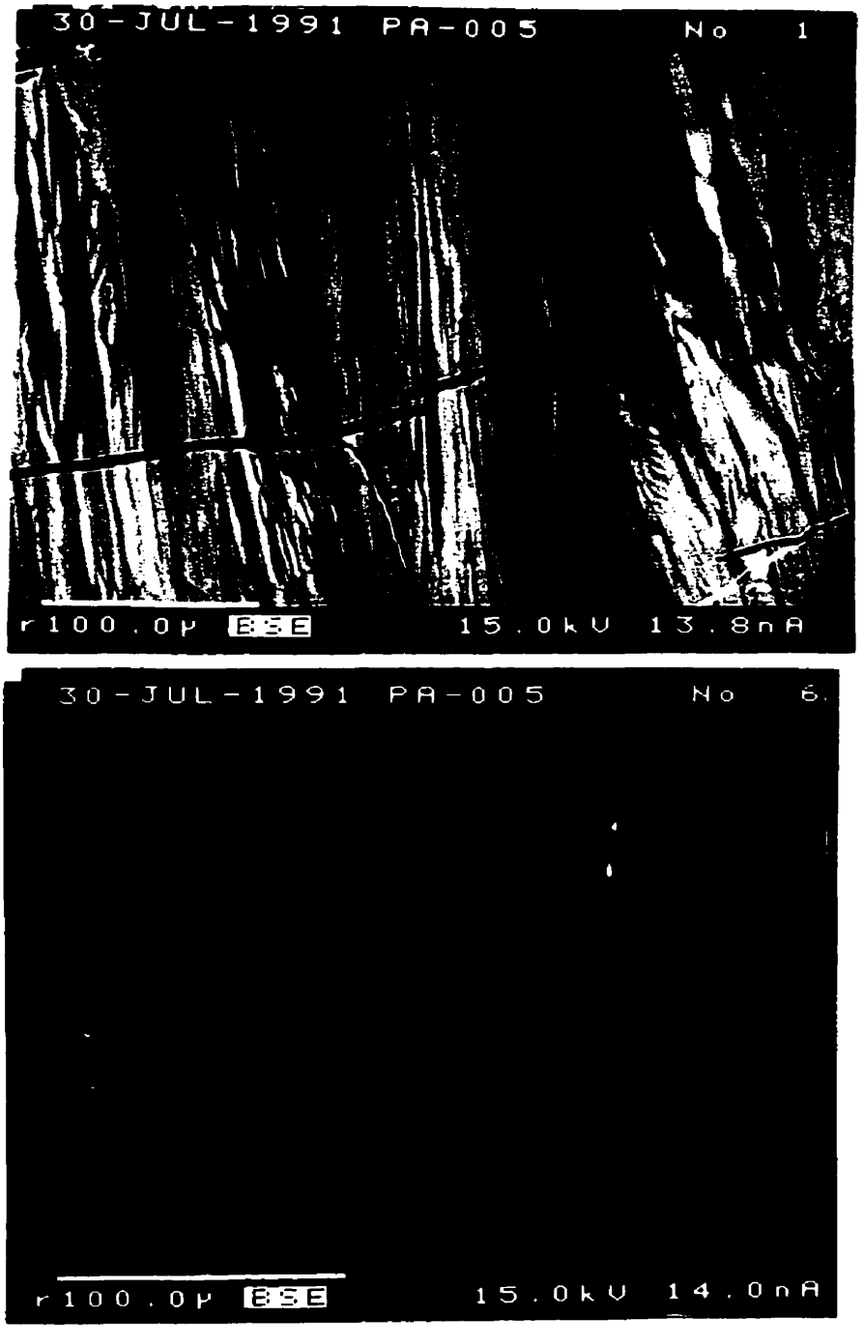

Fig. 4.33. BSE images of cesian analcime from Greenwood, Maine: (C) and (D) Complex zonation within the high-CRK low-Si/Al zones of cesian analcime. The zonation is primarily due to variation in Si/Al ratio.

Fig. 4.33. BSE images of cesian analcime from Greenwood, Maine: (E) An outer rim of pollucite (white, right) is developed on the main-phase cesian analcime; (F) Oscillatory zonation in the final stage of crystallization with variable Si/Al and a broad trend of decreasing Cs (decreasing grey levels from top right to lower left).

Table 4.15: Representative compositions of cesian analcime from Greenwood, Maine.

	50	53	49	67	87	101
SiO_2	52.32	55.16	49.11	46.54	57.67	50.98
Al_2O_3	17.13	17.10	17.20	16.17	20.49	16.50
Fe_2O_3	0.00	0.01	0.01	0.00	0.00	0.01
P_2O_5	0.00	0.00	0.00	0.00	0.03	0.00
Na_2O	3.39	3.48	3.13	1.84	11.66	5.93
K_2O	0.01	0.02	0.01	0.01	0.07	0.06
Rb_2O	0.00	0.00	0.00	0.00	0.00	0.00
Cs_2O	24.76	22.75	27.55	33.30	1.30	16.91
CaO	0.01	0.00	0.00	0.01	0.00	0.02
MgO	0.00	0.01	0.01	0.00	----	----
H_2O	----	----	----	----	----	----
sum	97.62	98.54	97.02	97.86	91.22	90.41
	Atomic contents based on 6 atoms of oxygen					
Si	2.188	2.225	2.142	2.139	2.119	2.176
Al	0.844	0.812	0.884	0.876	0.888	0.830
Na	0.274	0.272	0.265	0.163	0.830	0.492
K	0.000	0.001	0.001	0.000	0.003	0.003
Cs	0.442	0.391	0.513	0.653	0.021	0.308
TO_2^-	0.844	0.812	0.884	0.876	0.888	0.830
H^+	0.718	0.664	0.780	0.816	0.854	0.805
Si/Al	2.59	2.74	2.42	2.44	2.39	2.62
CRK	61.6	59.1	65.9	80.0	2.8	38.7

50. Main phase of crystallization; zone with low Si/Al.
53. Main phase of crystallization; zone with high Si/Al.
49. High-CRK low Si/Al zone in main phase.
67. High-CRK pollucite-like phase.
87. Final Na-rich overgrowth; zone with low Cs content.
101. Final Na-rich overgrowth; zone with high Cs content.

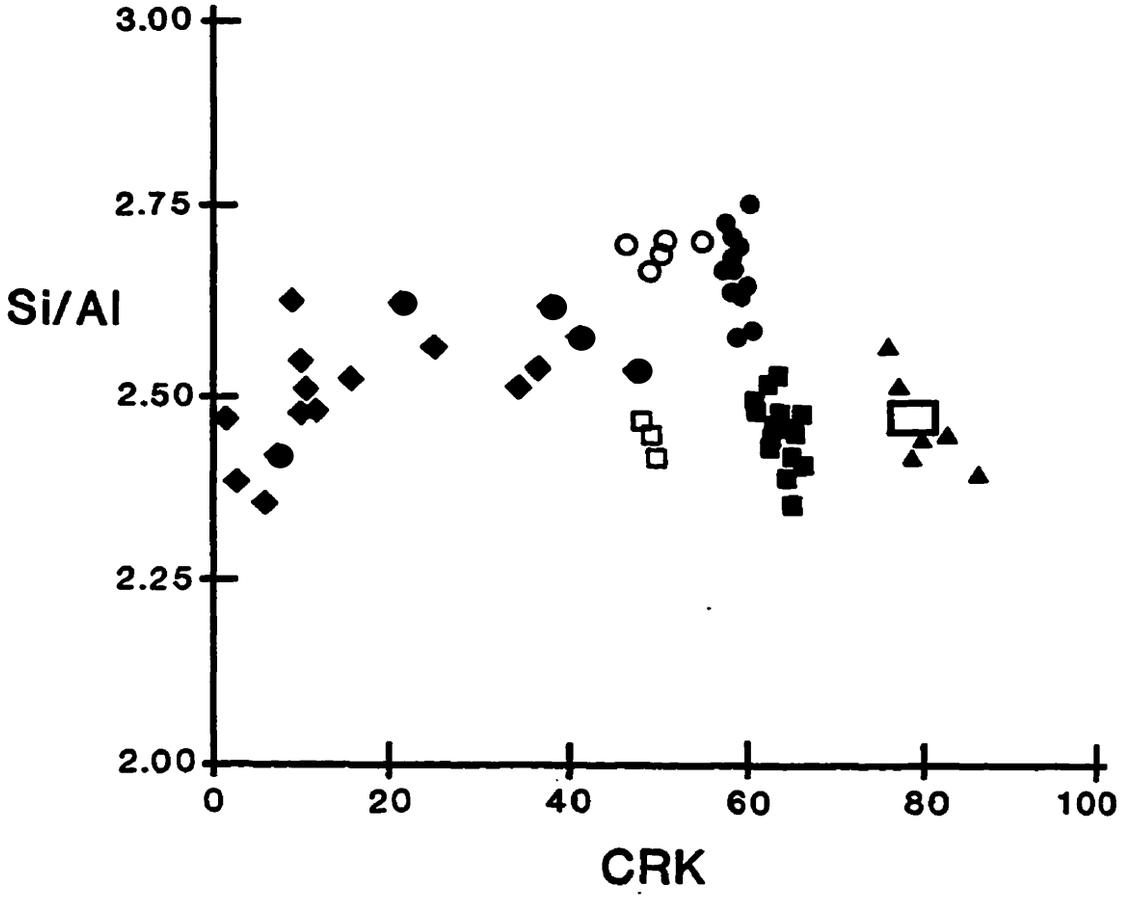

Fig. 4.34. Si/Al *vs.* CRK of cesian analcime from Greenwood, Maine. The open rectangle indicates the composition of primary pollucite from this locality. Symbols indicate the main phase (•, grey of Fig. 4.33A,B), the high-CRK low-Si/Al zones (■, white of Fig. 4.33A,B, main area of Fig. 4.33C,D), the pollucite-like compositions (▲), and the oscillatory zoning which exhibits variable Si/Al at decreasing CRK (◆, Fig. 4.33F). Open symbols indicate areas affected by late analcimization.

Euhedral single crystals of cesian analcime were examined from several locations within the pollucite-bearing Tanco pegmatite, mainly from the spodumene-rich zones. The birefringent crystals have trapezohedral {211} morphology, locally with subordinate cube {100} faces. Compositional zoning in individual crystals is indicated by distinct variations in refractive index. Associated minerals including adularia were described by Černý (1972) who also determined bulk compositions of some of the cesian analcime crystals (Table 4.14); compositional and structural properties of the adularia are given here (Ch. 4.1, Ch. 5.).

Compositional zoning recording sequential growth from core to rim is defined by major-element variation in Na/Cs and Si/Al. Time-equivalent concentric zones can usually be traced from sector to sector parallel to {211} faces using BSE images (Fig. 4.35A, B); however, complex optical properties also indicate differing structural properties between zones. Growth on {100} is not apparent by BSE imaging of cross-sections; rather, faces of high index (but near the dominant {211} growth direction) seem to be common. In addition to concentric and sectoral zoning, lateral variation in composition within a zone (termed intrasectoral zoning) is present. Differing composition at the junctions of growth sectors indicates the growth-sector boundaries (*e.g.*, Fig. 4.35B). Among zoned crystals of any mineral, intrasectoral zoning has been described only in calcite (Paquette & Reeder 1990). What makes the Tanco crystals unique is that a fine moiré pattern is present, overlaying the concentric zones and intrasectoral zoning (Fig. 4.35A, B) indicating compositionally anisotropic growth in three directions.

The core of most crystals (Fig. 4.35A-D) has CRK ≈ 40 with a compositionally-modest zoning pattern defined by variable Si/Al ratio (2.20 to 2.35; Fig. 4.36). Subsequent crystallization proceeded with an increase in CRK to 53 and Si/Al variable between 2.35 and 2.40. A minor period of crystallization generated a CRK ~70 composition along fractures (Fig. 4.35E). Following this, zonal crystallization proceeded with increasing Si/Al (as high as 2.50) and decreasing CRK (reduced to values as low as 40, dark of Fig. 4.35F). Final stages of crystallization (Fig. 4.35 A-D) proceeded with variable Si/Al and decreasing CRK. Outer rims saw a decrease of Si/Al to values as low as 2.05 while CRK decreased from 30 to nearly 0.0 (compositions closely approach the ideal-formula analcime composition).

All the above generations were subject to late local analcimization; however, the cation exchange was restricted to fracture surfaces. Features suggestive of recrystallization or replacement are absent or rare. A blebby structure is locally present and seems to crosscut zones (Fig. 4.35C). The features could represent change from a linear to an irregular growth-sector boundary rather than replacement. Whereas the zoning patterns of individual crystals from the same leaching cavity seem identical, crystals from different vug locations have different patterns. Nevertheless, all compositional trends fall on some part of the general evolutionary path (Fig. 4.36). Additional information could be gained on examination of specifically-oriented crystals.

The evolution of Cs/Na and Si/Al ratios in fluid of the leaching cavity is recorded in the detailed concentric, sectoral and intrasectoral zoning of cesian analcime crystals. It is remarkable that the two localities examined have such a similar evolutionary path. This similarity may indicate a typical low-temperature evolution of pegmatitic fluids. The source of cesium in these late fluids (and the development of Cs/Na ratios in time) may be related to sequences of reequilibration and alteration of pollucite. The crystals probably formed over a long period of time, well after consolidation of primary units. For analcime to form (rather than albite), pressures of less than 3-4 kbar at $T<200°C$ are required (Campbell & Fyfe 1965).

Concentric zoning in {211} growth sectors records the main evolutionary features of crystallization (at both localities): (i) the initial stage and bulk of the growth occurred with CRK of 55-65 and Si/Al of 2.3-2.7; (ii) during a brief period, pollucite-like compositions formed with CRK of 78-82 and Si/Al of 2.4-2.5; (iii) CRK continually decreased at a constant Si/Al of 2.4 to 2.5; (iv) during final growth, compositions with CRK < 20 developed to end-member analcime with Si/Al nearing 2.0. This general pattern of evolution is observed at both localities; however, zoning in individual crystals has additional complexity. CRK and Si/Al differ between {211} and other higher-index forms. Within one form, there are lateral variations in the composition of a zone: this is only the second documented case of "intrasectoral zoning". In addition, a fine-scale moiré pattern is superimposed across the concentric zoning and over the intrasectoral zoning. This indicates compositional variation in three directions during anisotropic crystal growth.

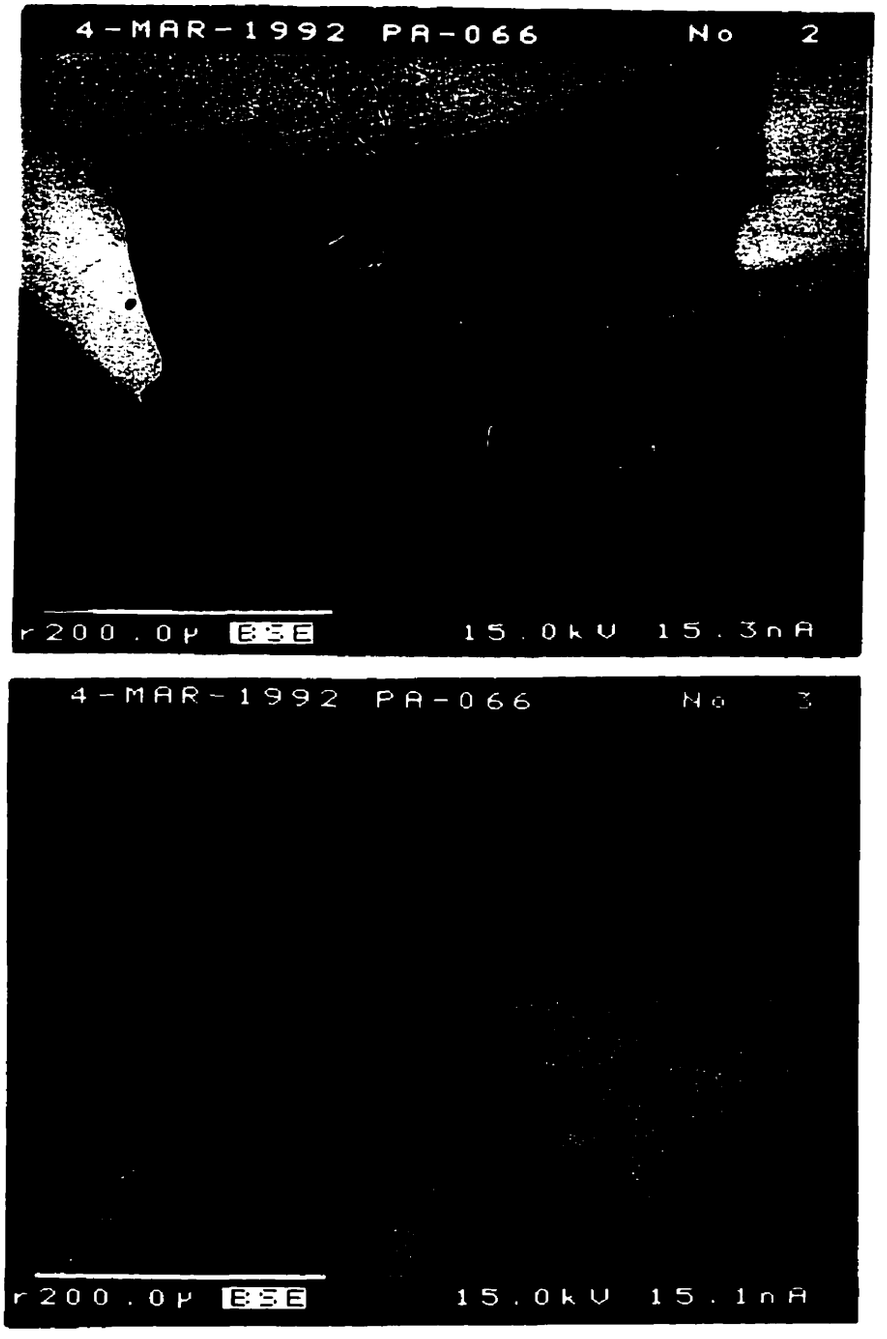

(A)

(B)

Fig. 4.35. BSE images of cesian analcime from Tanco, Manitoba: (A) and (B) The outer zone of most crystals has concentric zoning parallel to crystal faces. Because of lateral variation in Na/Cs and Si/Al, growth-sector boundaries are well-defined some cases and hidden in others. Lateral variations in composition within individual zones of a sector indicate intrasectoral zoning.

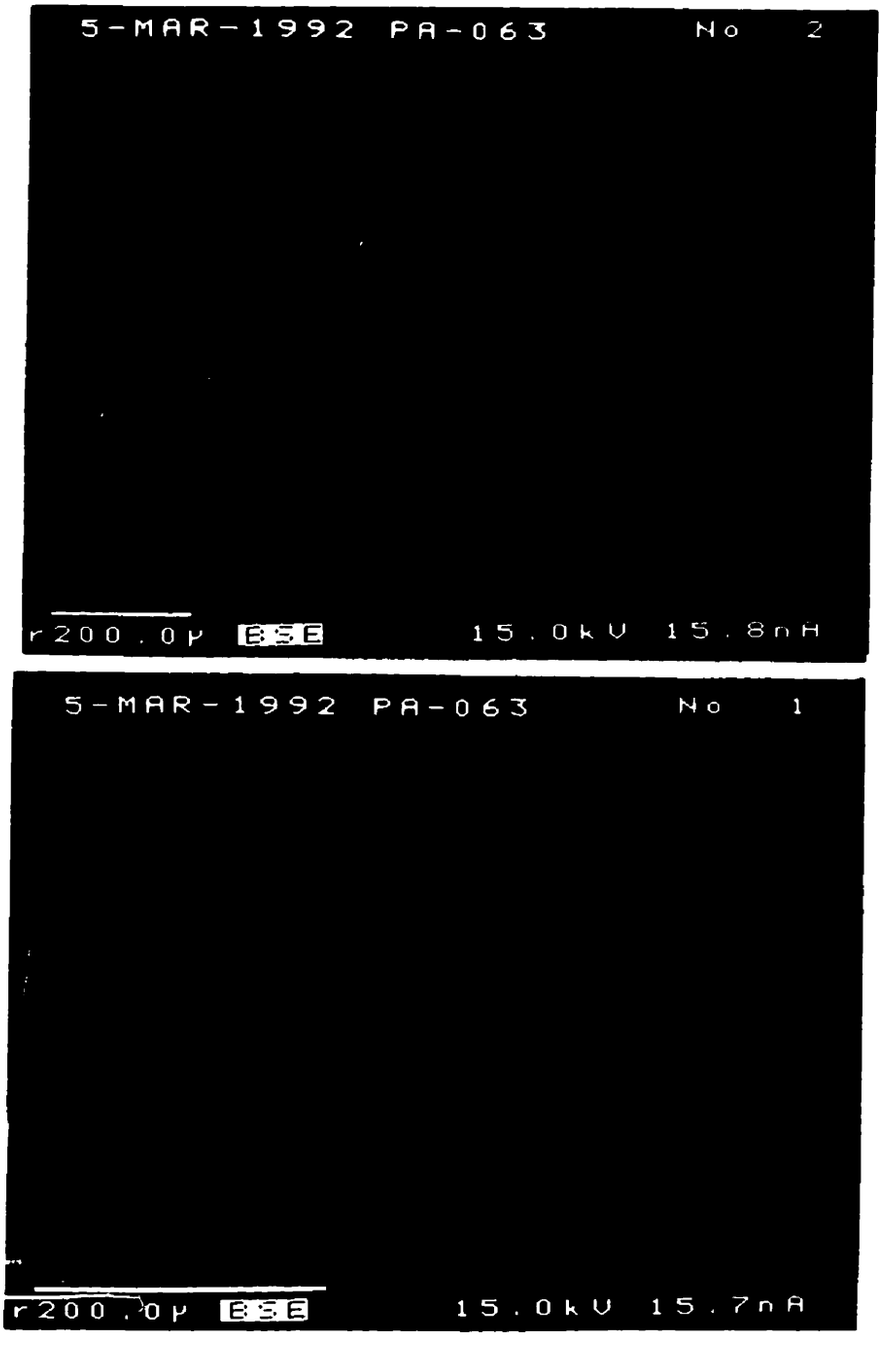

(C)

(D)

Fig. 4.35. BSE images of cesian analcime from Tanco, Manitoba: (C) Complex zoning with irregular boundaries (patchy, dark grey) preceded crystallization of outer {211} zones; (D) Extremely complex compositional variation of core zones, with clearly-defined growth-sector boundaries in outer zones.

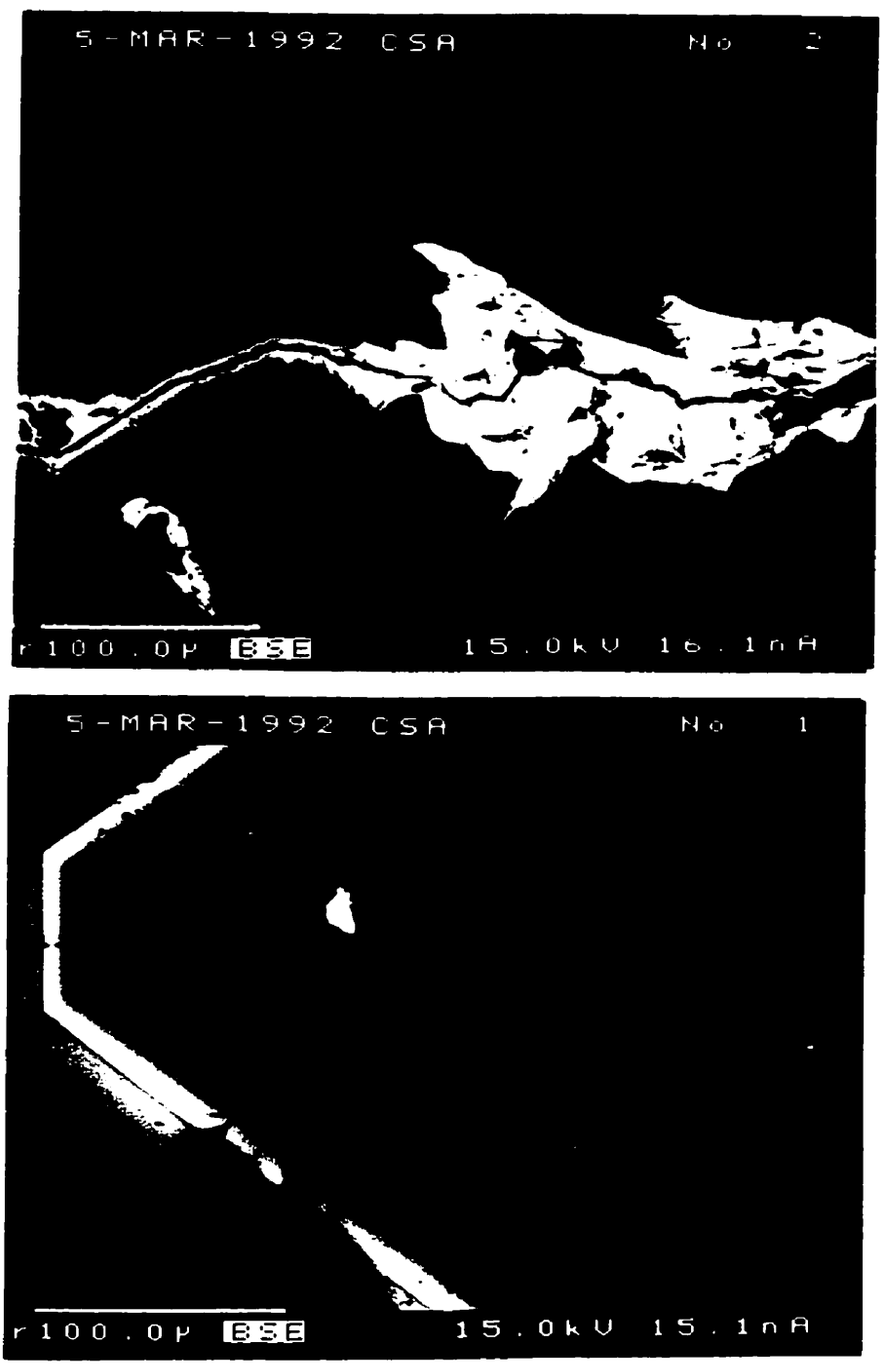

(E)

(F)

Fig. 4.35. BSE images of cesian analcime from Tanco, Manitoba: (E) Cesium-exchange along a fracture in cesian analcime, generating pollucite-like compositions; (F) The Cs-rich core of sample CsA, with minor analcimization along fractures.

Table 4.16: Representative compositions of cesian analcime from Tanco, Manitoba.

	37	39	49	67	87	101
SiO_2	46.69	46.07	49.11	46.54	57.67	50.98
Al_2O_3	17.94	17.17	17.20	16.17	20.49	16.50
Fe_2O_3	0.00	0.00	0.01	0.00	0.00	0.01
P_2O_5	0.00	0.00	0.00	0.00	0.03	0.00
Na_2O	6.14	4.97	3.13	1.84	11.66	5.93
K_2O	0.01	0.00	0.01	0.01	0.07	0.06
Rb_2O	0.00	0.00	0.00	0.00	0.00	0.00
Cs_2O	19.67	23.36	27.55	33.30	1.30	16.91
CaO	0.03	0.02	0.00	0.01	0.00	0.02
H_2O	----	----	----	----	----	----
sum	90.47	91.60	97.02	97.86	91.22	90.41
	Atomic contents based on 6 atoms of oxygen					
Si	2.071	2.089	2.142	2.139	2.119	2.176
Al	0.938	0.917	0.884	0.876	0.888	0.830
Na	0.528	0.437	272	0.265	0.163	0.830
Cs	0.372	0.451	0.513	0.653	0.021	0.308
M^+	0.902	0.891	0.780	0.816	0.854	0.805
Si/Al	2.209	2.277	2.42	2.44	2.39	2.62
CRK	41.3	50.7	65.9	80.0	2.8	38.7

37. Core of crystal CSA (Fig. 4.35F).
39 and 49. Cs-richer zone (Fig. 4.35F).
67. Pollucite-like composition (Fig. 4.35E).
87 and 101. Outer Na-rich zones, with low and high Cs content, respectively.

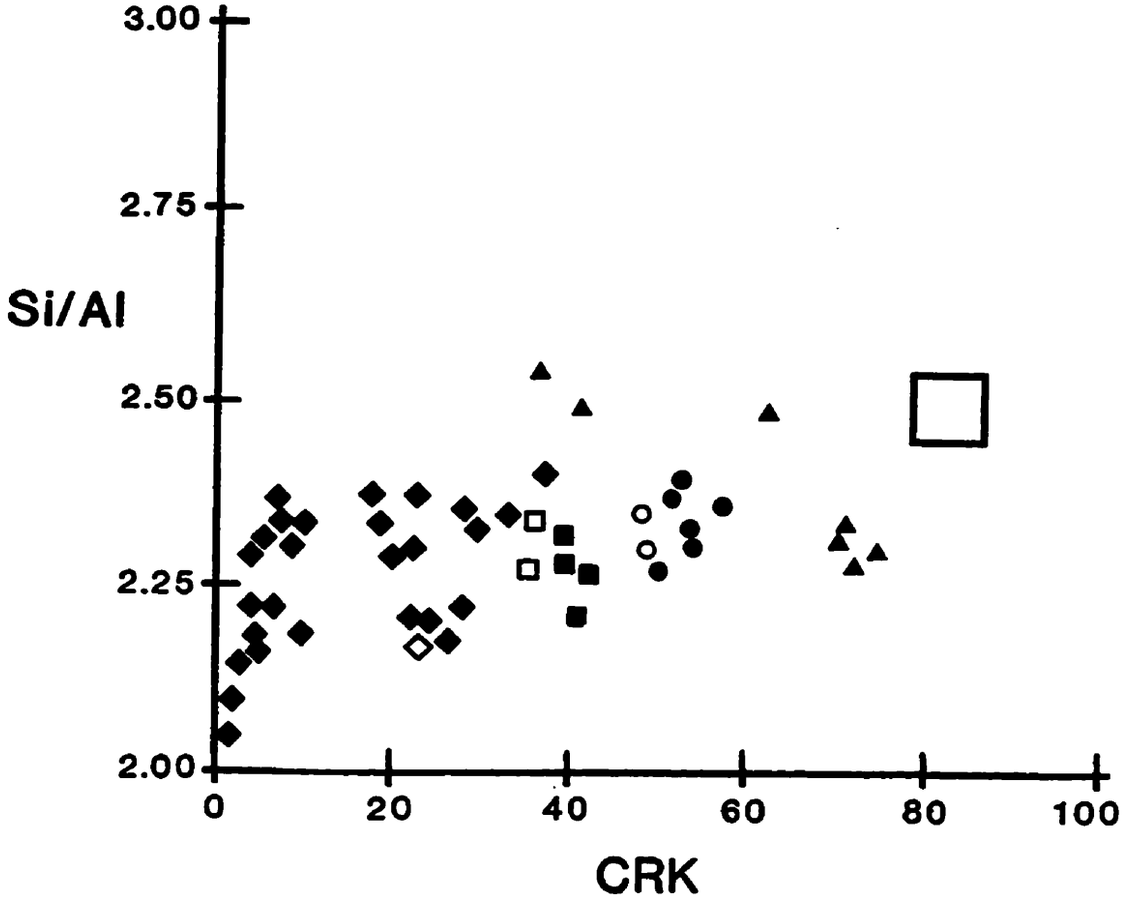

Fig. 4.36. Si/Al *vs.* CRK of cesian analcime from Tanco, Manitoba. The open rectangle indicates the composition of primary pollucite from this locality. Symbols indicate the initially-crystallizing phase (■, core of Fig. 4.35F), its high-CRK zone (•, bright rim in Fig. 4.35F), the pollucite-like compositions (▲ zoned with decreasing CRK), and the final stage of crystallization trending to CRK 0 and Si/Al 2.0 (●, Fig. 35A-D). Open symbols: analcimization.

Rb and Cs-rich micas are associated with the low-temperature reaction products of pollucite and (K,Rb)-feldspar (*e.g.*, some of the micas from Red Cross Lake, Ch. 4.7). Insufficient data were collected to fully characterize the micas and their late rims as primary or secondary, or to fully identify processes of growth, and this was not the aim of the thesis. I also investigated the mica and clay minerals associated with pollucite from about 60 localities; most are muscovite and lepidolite, and are not particularly enriched in Rb or Cs, having less than 1 wt.% Rb_2O or Cs_2O. The sheet silicates reported below are of interest for their high-to-extreme Rb and/or Cs values.

Micas were analysed using a CAMECA SX-50 electron microprobe operating at 15 kV, 20 nA with a beam diameter of 5 μm. Standards used were albite (Na *K*α), fayalite (Fe *K*α), diopside (Ca *K*α, Si *K*α), kyanite (Al *K*α), spessartine (Mn *K*α), sanidine (Na *K*α), zinnwaldite 1B (F *K*α), pollucite (Cs *L*α), $Rb_2ZnSi_5O_{12}$ (Rb *L*α), $SrTiO_3$ (Sr *L*α, Ti *K*α), gahnite (Zn *K*α), barite (Ba *L*α), $NaScSi_2O_6$ (Sc *K*α), apatite (P *K*α), and tugtupite (Cl *K*α). Data were reduced using the PAP routine of Pouchou & Pichoir (1985). Li and H_2O were not determined. Formulae were calculated on the basis of 12 anions, including 2(OH+F+Cl) using calculated OH values. This calculation is incorrect because it ignores substantial cation-charge due to the presence of Li; therefore, the atomic contents reported below represent only relative proportions and not absolute values.

At the Věžná beryl-columbite subtype pegmatite, Czech Republic, rims of micas associated with analcimized pollucite and harmotome are strongly enriched in Cs (Fig. 4.37A,B; Teertstra *et al.* 1995). Minor quantities of muscovite, with negligible Rb and Cs, are intergrown with lepidolite. Cores of lepidolite grains have 0.41-0.59 wt.% Rb_2O, 0.30-1.05 wt.% Cs_2O and 6.13-7.60 wt.% F, corresponding to 2-3 at.% interlayer Rb, 1-3 at.% interlayer Cs, and 67-85 at.% anion-site F. Outer rims of the lepidolite grains are enriched in Cs, with 0.13-0.55 wt.% Rb_2O, 9.31-17.97 wt.% Cs_2O and 4.53-6.13 wt.% F, corresponding to 1-3 at.% interlayer Rb, 29-61 at.% interlayer Cs, and 46-71 at.% anion-site F. Outer rims of the mica grains are also enriched in Cs, with up to 10.2 wt.% Cs_2O, corresponding to 33 at.% interlayer Cs. The rims may be formed as part of final-stage primary growth, or by cation exchange or recrystallization. Interaction with late fluids, possibly derived by wallrock interaction, is suggested by introduction of up to 1.18 wt.% MgO in the late rims. Rims are lower in F than the cores, suggesting interaction with F-poor aqueous fluids. A mechanism of Cs-exchange is proposed for the curved boundaries of Cs-rich mica with the Cs-poor cores. For lepidolite, values of Si (apfu) are constant between core and rim, and values of Al are constant (or tend to decrease slightly) as Mg is introduced (Table 4.17). For muscovite, values of Si increase and values of Al decrease as Mg (and F, Cs) are introduced (Table 4.17). The Cs-rich fluids are derived from the Na-Cs cation exchange of pollucite and its replacement by Cs- and Rb-free harmotome.

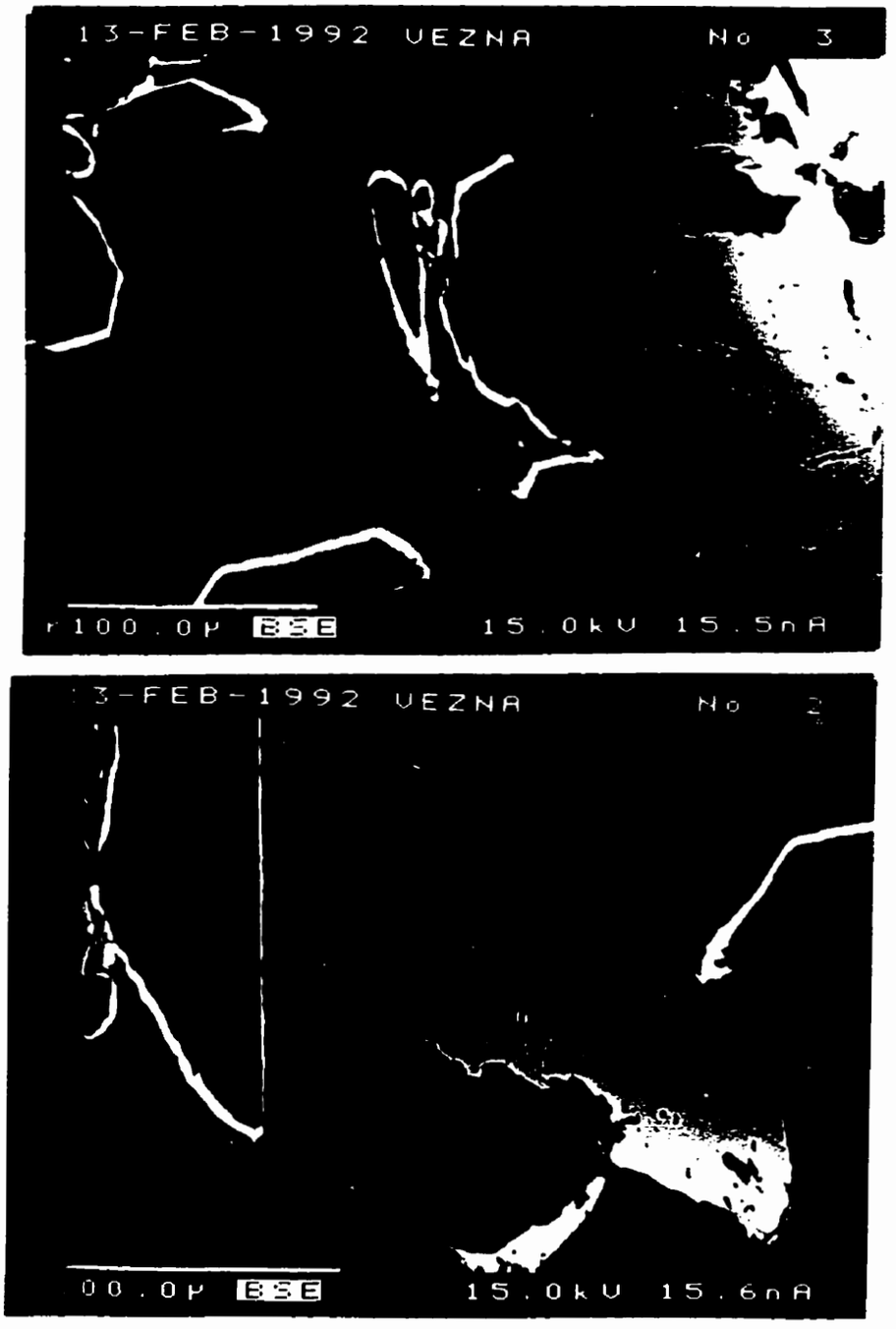

Fig. 4.37. BSE images of mica minerals with late alteration: (A) and (B) Cs-rich rims of lepidolite from Věžná, Czech Republic associated with analcime-pollucite (grey-white) and harmotome (dark grey).

Table 4.17: Representative compositions of micas from Věžná, Czech Republic.

oxide	1c	1r	2c	2r	3c	3r	4c	4r
SiO_2	56.10	50.57	55.49	52.80	47.38	49.51	56.91	51.03
Al_2O_3	19.89	18.92	20.81	18.11	33.80	21.11	20.62	15.97
Fe_2O_3	0.02	0.00	0.01	0.01	0.01	0.05	0.00	0.03
MnO	0.55	0.28	0.22	0.23	0.00	0.27	0.17	0.36
MgO	0.00	0.10	0.02	0.03	0.02	1.18	0.00	0.06
Na_2O	0.10	0.01	0.04	0.01	0.17	0.03	0.03	0.00
K_2O	11.27	5.55	11.23	7.20	10.94	5.71	11.55	4.58
Rb_2O	0.49	0.37	0.59	0.42	0.17	0.23	0.48	0.30
Cs_2O	0.49	14.69	1.05	10.47	0.06	10.23	0.37	17.09
F	7.60	4.72	7.13	5.03	0.91	4.53	7.29	5.76
H_2O	0.63	1.62	0.86	1.56	3.98	1.79	0.85	1.01
sum	93.95	94.76	94.42	93.72	97.03	92.73	95.20	93.72

1 and 2. Lepidolite core (c) - rim (r) pairs.
3. muscovite core (c) - rim (r) pair.
4. Lepidolite core and Cs-dominant rim.

The occurrence of Rb- and Cs-rich mica at Red Cross Lake was described in Ch. 4.7. Exocontact biotite has Cs-rich to Cs-dominant rims (Fig. 4.37C).

Lithian muscovite to lepidolite associated with analcimized pollucite at Haapaluoma, Peräseinäjoki, Finland, has textural and compositional features suggestive of cation exchange or other late reaction with Cs-rich fluids (Fig. 4.37D, Table 4.19). At Viitaniemi, Orivesi, Finland, analcimization of pollucite seems to be associated with accumulation of Cs adjacent to mica veins (Fig. 4.38A) (Teertstra *et al.* 1993). Similar features occur in altered analcimized pollucite from Åkerberg, Sweden (Fig. 4.38B) (Teertstra *et al.* 1996), and from Tin Mountain, South Dakota (Fig. 4.38C). It is possible that Cs accumulates adjacent to micas prior to their late exchange, and that the reaction occurs once Cs becomes highly concentrated. The micas may form by more than one mechanism, however, and some parameter of the reaction may vary with changing conditions.

Clay minerals form an important part of the alteration sequence of pollucite at $T<200°C$ (Fig. 4.30). Residual concentrations of Cs in clay-pod pseudomorphs after pollucite were first noted by Černý (1978). The most common products are illite, kaolinite, chlorite, smectites and mixed-layer clays. Analysis of Mg- and Cs-rich clay replacing pollucite at the Dunton Quarry, Newry, Maine, gave up to 6.54 wt.% Cs_2O (Fig. 4.38D; Table 4.18). Fine-grained Cs-rich lepidolite occurs in association with the clay minerals (Table 4.18).

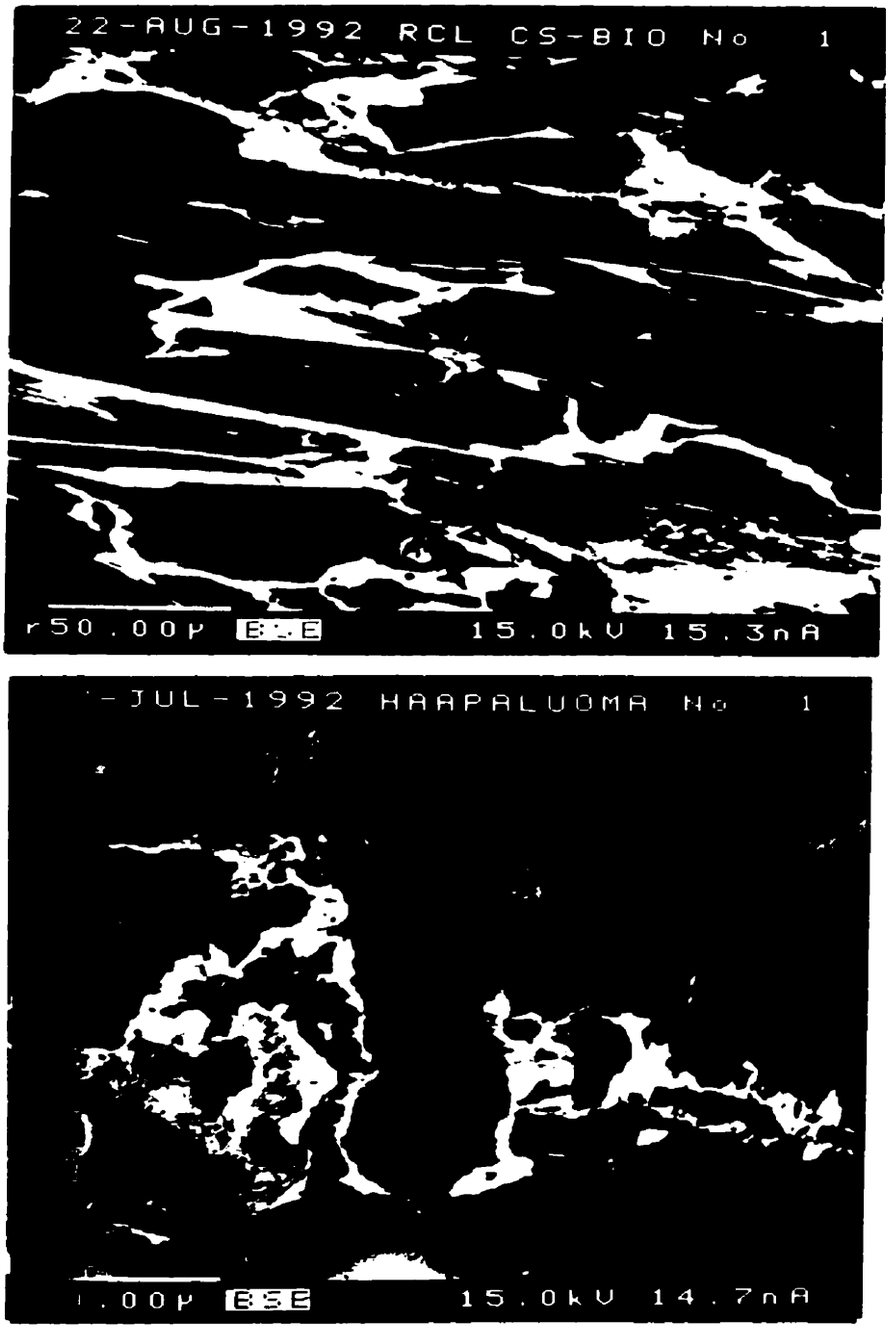

Fig. 4.37. BSE images of mica minerals with late alteration: (C) Cs-rich rims of exocontact biotite from Red Cross Lake, Manitoba, associated with albite; (D) Cs-rich rims of lepidolite from Haapaluoma, Finland, associated with quartz (black) and analcime-pollucite (lower left, grey-white).

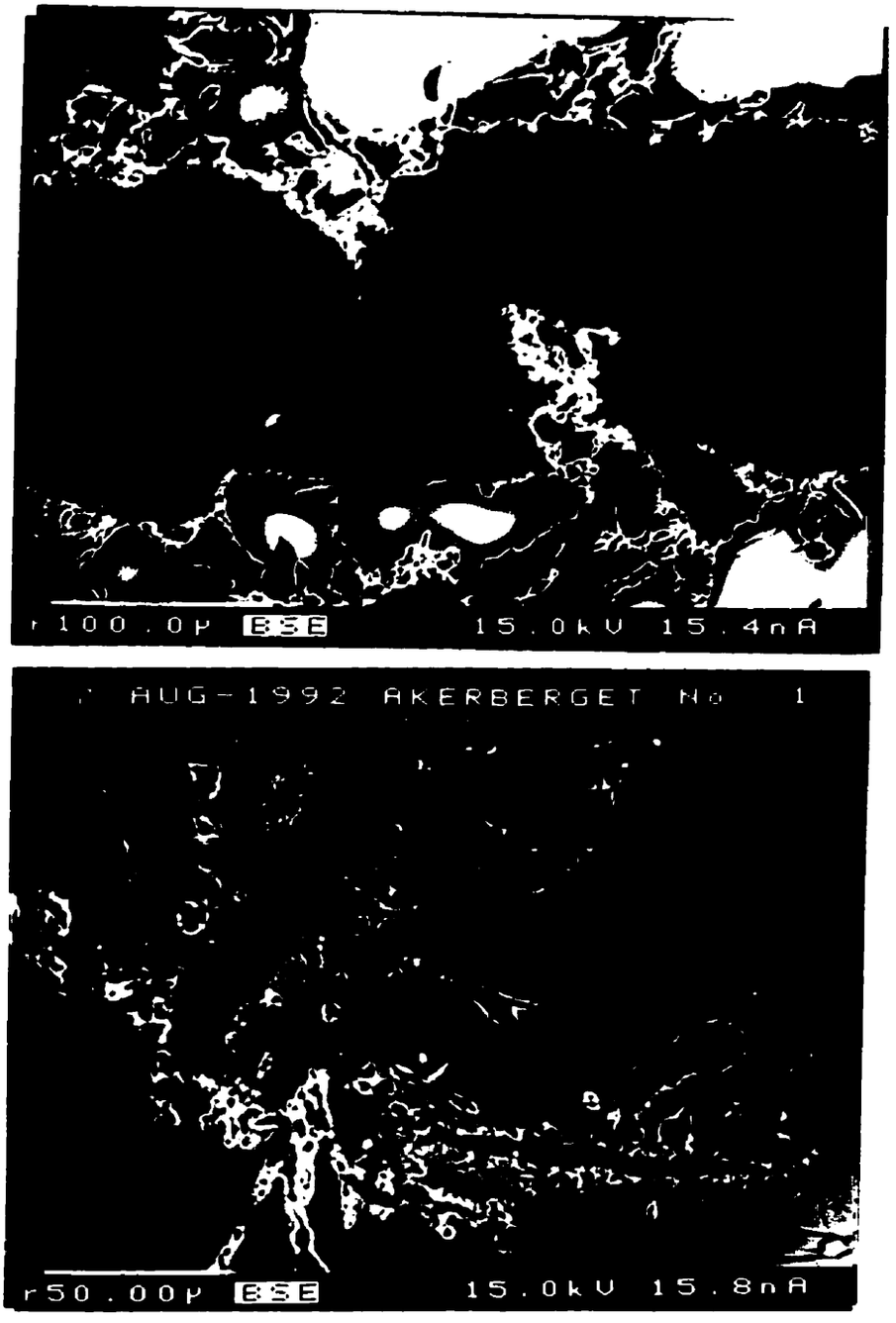

(A)

(B)

Fig. 4.38. BSE images of mica minerals associated with analcimization of pollucite: (A) Enrichment of Cs in analcime-pollucite (grey-white) adjacent to coarse-grained lepidolite vein, Viitaniemi, Finland; (B) Enrichment of Cs in analcime-pollucite (grey-white) adjacent to vein of fine-grained mica, Åkerberg, Sweden.

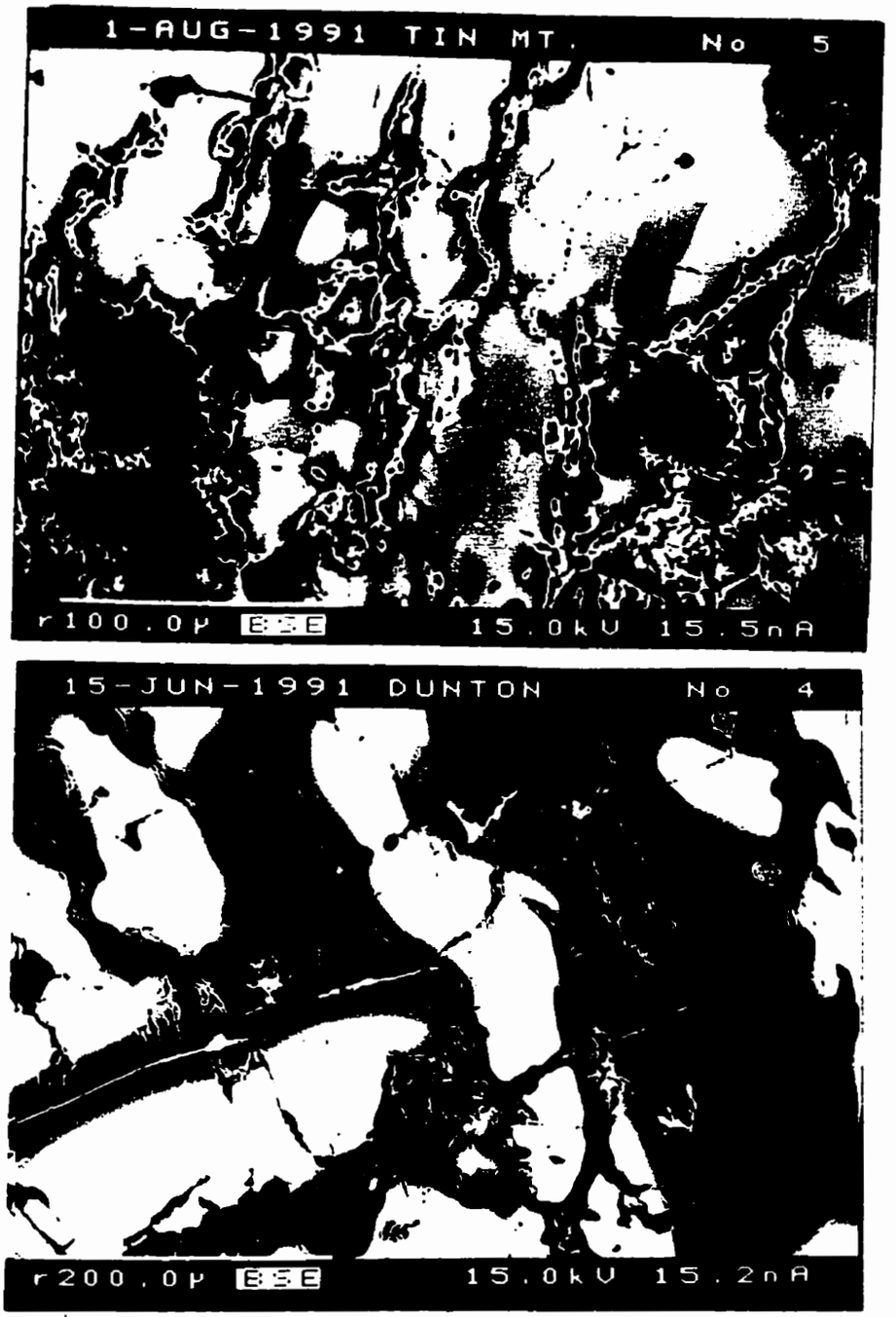

(C)

(D)

Fig. 4.38. BSE images of mica minerals associated with analcimization of pollucite: (C) Enrichment of Cs in analcime-pollucite (grey-white) adjacent to fine-grained quartz and mica, Tin Mountain; (D) Cs-rich clay mineral (+ apatite veinlets) in analcimized pollucite, Dunton Quarry, Newry, Maine.

Table 4.18: Representative compositions of mica and clay minerals, Dunton Quarry, Maine.

oxide	1	2	3	4	5	6
SiO_2	54.24	54.85	55.84	43.01	56.08	57.88
Al_2O_3	20.75	20.36	19.26	22.04	19.34	19.56
Fe_2O_3	0.60	0.26	0.67	0.49	0.40	0.16
MnO	0.17	0.07	0.00	0.00	0.01	0.00
MgO	0.00	0.08	2.98	4.18	3.43	4.34
Na_2O	0.04	4.21	0.02	0.08	0.00	0.02
K_2O	9.64	3.00	0.55	0.42	0.64	0.71
Rb_2O	3.26	0.66	0.00	0.00	0.00	0.00
Cs_2O	1.00	8.56	4.16	5.02	6.25	6.54
F	7.02	2.44	0.13	0.34	0.17	0.29
H_2O	0.85	3.05	4.09	3.47	4.11	4.19
sum	94.62	96.50	87.64	78.91	90.36	93.56

1. Lepidolite.
2. Cs-bearing mica with paragonite-like composition.
3-6. Cs-bearing clay mineral, possibly montmorillonite.

Table 4.19: Representative compositions of micas from Haapaluoma, Finland.

oxide	1c	1r	2c	2r	3c	3r	3r	3r
SiO_2	48.47	54.20	52.26	53.68	54.74	49.97	50.50	49.99
Al_2O_3	27.86	13.03	26.38	13.34	22.87	11.55	13.71	11.28
Fe_2O_3	0.00	0.00	0.01	0.03	0.00	0.03	0.02	0.02
MnO	0.08	0.14	0.09	0.14	0.08	0.38	0.35	0.26
MgO	0.01	0.04	0.03	0.06	0.00	0.30	0.08	0.12
Na_2O	0.12	0.00	0.07	0.05	0.12	0.11	0.01	0.03
K_2O	10.41	6.22	10.86	5.39	10.11	1.84	2.84	1.42
Rb_2O	0.56	0.70	0.66	0.87	0.97	0.20	0.46	0.42
Cs_2O	0.55	12.63	0.39	11.83	2.02	13.72	16.62	17.91
F	4.91	7.87	3.86	7.67	6.85	7.08	6.79	7.25
H_2O	1.85	0.04	2.49	0.11	1.04	0.06	0.36	0.00
sum	92.75	91.51	95.47	89.94	95.81	82.26	88.88	85.62

1. Lepidolite core (c) - rim (r) from coarse vein.
2. Lepidolite core (c) - rim (r) from fine vein.
3. Lepidolite core (c) and Cs-dominant rims (r) from scattered grains in analcime-pollucite.

The sequence of alteration of pollucite from Haapaluoma, Peräseinäjoki, Finland, was investigated in some detail, particularly with regard to the evolution of mica composition. Margins of the pollucite are crosscut by 5 mm-wide veins containing a spodumene-quartz intergrowth. Veins of coarse-flaked lepidolite (+ quartz ± apatite) 1-2 mm wide also transect the pollucite, but pinch out near the margins of the pollucite aggregates. Sinuous veins of cookeite are followed (in time) by thin veinlets of fine-grained mica (Fig 4.39C). Compositionally homogeneous Or_{100} adularia replaces pollucite from the surfaces of the mica veins, and also occurs as spherical granular aggregates up to 1 mm in diameter, fully embedded in the pollucite. Analcimization of pollucite, associated with enrichment of margins of mica grains in Cs, is widespread at Haapaluoma (Fig. 4.39A,B; Teertstra *et al.* 1993).

The coarse-flaked Haapaluoma lepidolite has an average of 0.56 wt.% Rb_2O, 0.59 wt.% Cs_2O, and 4.9-6.2 wt.% F, corresponding to 3 at.% interlayer Rb, 2 at.% interlayer Cs, and 55-71 at.% anion-site F. Its rims have up to 10 wt.% Cs_2O (35 at.% interlayer Cs) and are also enriched in F up to 7.9 wt.% (100 at.% anion-site F). The thin veinlets of fine-grained mica have 0.65 wt.% Rb_2O, 0.68 wt.% Cs_2O, and 3.9-4.7 wt.% F, corresponding to 3 at.% interlayer Rb, 2 at.% interlayer Cs, and 42-51 at.% anion-site F (lithian muscovite). Its rims have up to 11.8 wt.% Cs_2O (40 at.% interlayer Cs) and are also enriched in F up to 7.7 wt.% (87 at.% anion-site F). Scattered grains of lepidolite, embedded in analcime and adjacent to the thin veinlets of fine-grained mica, have Cs-enriched tips and margins (Fig.4.39B). These grains have up to 1 wt.% Rb_2O, 2 wt.% Cs_2O and 6.6-7.4 wt.% F, corresponding to 5 at.% interlayer Rb, 6 at.% interlayer Cs and 75-83 at.% anion-site F. The Cs-rich rims have have similar Rb and F contents as the cores, but up to 17.9 wt.% Cs_2O (67 at.% interlayer Cs, Table 4.19).

(A)

(B)

Fig. 4.39. BSE images of mica minerals with associated with analcimization of pollucite (grey to white): (A) and (B) Cs-rich rims of micas, Haapaluoma, Finland.

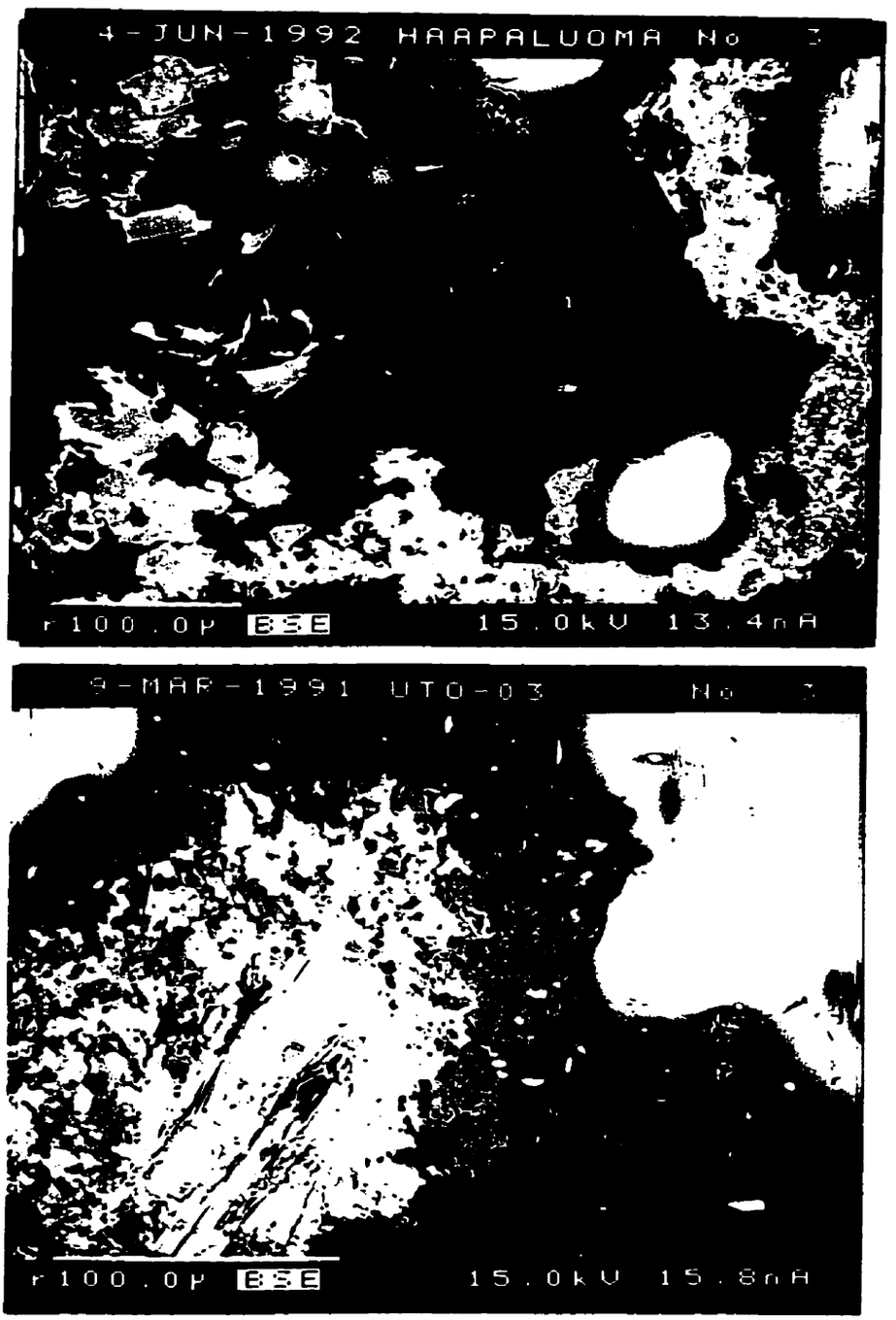

(C)

(D)

Fig. 4.39. BSE images of mica minerals with associated with analcimization of pollucite (grey to white): (C) Cs-rich micas associated with veins of cookeite, Haapaluoma, Finland; (D) mica and Rb-rich feldspar (white), hosted by Rb-poor adularia (grey).

At Utö, Sweden, Cs- and Rb-rich micas occur in association with (K,Rb)-rich adularia (Fig. 4.45D).

The final note is reserved for a Cs- and Ca-rich aluminosilicate mineral which is associated with cesian analcime and Or_{100} adularia replacing petalite at Luolamäki, Finland. The mineral has 5.9-11.2 Cs_2O, 0.09-0.6 Na_2O, 1.0-2.9 K_2O, 2.7-4.0 CaO, 11.5-12.7 Al_2O_3 and 66.5-67.9 SiO_2, sum 90.6-93.3 wt.%. No other elements were detected by EDS analysis or by analysis using the feldspar analytical program. The low total suggests that the mineral is hydrous. It has one good cleavage (Fig. 4.40A). It is colourless in thin section and white in hand specimen. The Cs-richest material has atomic proportions of Cs>Ca. The composition is similar to that of laumontite (Table 4.20). Laumontite was identified at Luolamäki by Neuvonen & Vesasalo (1960).

A similar but Ca-rich mineral, containing significant Ba and Sr, was found replacing petalite from Utö, Sweden (Fig. 4.40B). Its composition is similar to that of clinoptilolite (Table 4.20).

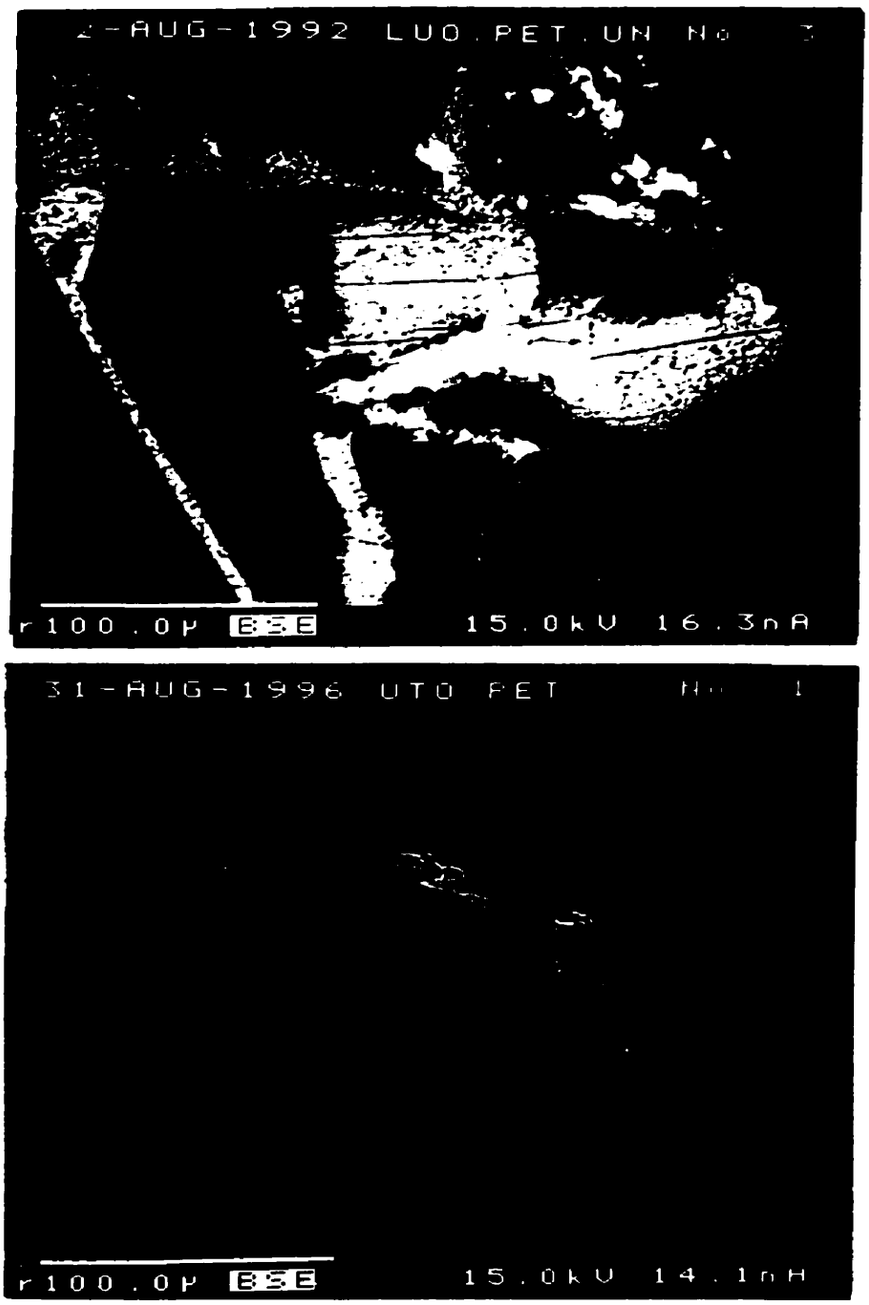

(A)

(B)

Fig. 4.40. BSE images of: (A) unknown Cs-rich mineral (white, one good cleavage) replacing petalite from Luolamäki, Finland; (B) a similar mineral (Cs-poor) replacing petalite from Utö, Sweden.

Table 4.20: Representative compositions of zeolite-like minerals replacing petalite from Luolamäki, Finland and Utö, Sweden.

	Luolamäki				Utö			
oxide	1	2	3	4	1	2	3	4
SiO_2	66.54	66.68	67.91	66.54	65.37	59.60	59.55	54.16
Al_2O_3	12.66	12.65	12.39	11.49	13.50	14.90	14.30	17.28
Fe_2O_3	0.00	0.00	0.00	0.00	0.00	0.10	0.09	0.41
MgO	0.00	0.00	0.00	0.00	0.24	0.34	0.33	0.24
Na_2O	0.09	0.58	0.16	0.22	0.22	0.12	0.07	0.37
K_2O	1.04	2.82	1.14	0.96	2.18	1.90	1.69	1.98
Cs_2O	6.44	5.88	7.74	11.21	0.00	0.00	0.00	0.00
CaO	3.89	2.93	3.98	2.68	3.48	3.82	4.01	3.11
SrO	0.00	0.00	0.00	0.00	1.12	1.38	1.17	1.86
BaO	0.00	0.00	0.00	0.00	2.55	4.35	4.62	7.41
sum	90.66	91.54	93.32	93.10	88.66	86.51	85.83	86.82
	Atomic contents *per formula unit*							
Si	19.746	19.699	19.813	20.027	29.063	27.849	28.041	26.237
Al	4.428	4.404	4.260	4.076	7.074	8.206	7.936	9.866
Fe	0.000	0.000	0.000	0.000	0.000	0.035	0.032	0.149
Mg	0.000	0.000	0.000	0.000	0.159	0.237	0.232	0.173
Na	0.052	0.332	0.091	0.128	0.190	0.109	0.064	0.348
K	0.394	1.063	0.424	0.369	1.236	1.133	1.015	1.224
Cs	0.815	0.741	0.963	1.439	0.000	0.000	0.000	0.000
Ca	1.237	0.927	1.244	0.864	1.658	1.912	2.023	1.614
Sr	0.000	0.000	0.000	0.000	0.289	0.374	0.319	0.522
Ba	0.000	0.000	0.000	0.000	0.444	0.797	0.852	1.407
ΣM	2.50	3.06	2.72	2.80	3.97	4.60	4.53	5.44
M^+	3.74	3.99	3.97	3.66	2.55	7.96	7.99	9.31
Si+Al	24.2	24.1	24.1	24.1	36.1	36.1	36.0	36.1

Luolamäki 1-4. Formula normalized on the basis of 48 atoms of oxygen. This may be cesian laumontite.
Utö 1-4. Formula normalized on the basis of 72 atoms of oxygen. This may be strontian barian clinoptilolite.

CHAPTER 5

STRUCTURAL ASPECTS OF THE (K-Rb)-FELDSPAR SERIES

A brief review of the structure of (K-Rb)-feldspar was given in Chapter 2.2. Variable (Al,Si) order is found in both the monoclinic (sanidine to orthoclase) and triclinic (high- to low-microcline) series according to X-ray measurements. The monoclinic → triclinic phase-transformation is often irregularly distributed on a μm-scale, and many bulk samples examined by XRD contain a mixture of structural states, usually orthoclase + microcline.

In this thesis, I use Rietveld refinement as a routine method for refinement of accurate cell-parameters of feldspars. Structural information may be obtained with minimal additional effort. Some of the samples are twinned and fine-grained, and thus in need of Rietveld refinement; even in the case of coarse crystals being available, results are obtained more rapidly by Rietveld refinement than by single-crystal methods. In some cases, twinning was absent in thin section and these samples required identification by XRD. My focus is on disordered end-member K-feldspar (adularia) and on (K,Rb)-feldspar, particularly if it hosts Rb-rich feldspar. Numerous attempts to physically separate Rb-dominant feldspar from intergrown K-feldspar, albite, mica and quartz failed due to low abundance, very fine grain-size, lack of distinguishing optical characteristics, and structural coherency with the host. Nevertheless, X-ray powder diffraction of a microcline + (Rb,K)-feldspar ±quartz mixture (Ch. 4.4, Elba) did not reveal the presence of any potential non-feldspathic structure which could be attributed to a $(Rb,K)AlSi_3O_8$ compound.

5.1 *Rietveld refinement of (K,Rb)-feldspar cell parameters*

Shim *et al.* (1996) reported successful modal analysis of microcline + albite and microcline + quartz mixtures using multi-phase Rietveld refinement (without refinement of structural parameters). As far as I am aware, there are no Rietveld refinements of the feldspar structure in the literature, and there has been no structural work involving natural Rb-bearing feldspar.

X-ray powder diffraction is a standard method for quantitative structural and chemical characterization of feldspars. With careful indexing of reflections, refined unit-cell parameters are relatively accurate indicators of (Al,Si) order and T1 and T2 site occupancies (Hovis 1989). However, routine powder XRD methods are not suitable for crystal-structure analysis because of the difficulty of measuring accurate Bragg intensites as a result of extensive peak overlap. In this approach, a large proportion of the pattern information is discarded. This problem is overcome by Rietveld structure refinement which uses the intensity information of the entire diffraction pattern. In the Rietveld method, a best fit is obtained (by least-squares methods) between the observed pattern and a pattern calculated from a structure model. For low-symmetry minerals with complex diffraction patterns, the Rietveld method is probably better than standard powder-diffraction methods for refining precise and accurate cell parameters because it does not require measurement of individual peak positions. Peak positions are located very precisely with the Rietveld method because each data point that defines a peak profile is used in the refinement of peak-modelling parameters. The positions are relatively insensitive to errors in the peak-shape function or in the structure model (Post and Bish 1989); however, corrections for peak asymmetry may shift the

apparent peak positions. The refinement includes background modelling, peak fitting, and cell-parameter calculation, after which the structure model may be refined. In principle, Rietveld-refined cell parameters may be as accurate as those obtained by conventional powder + internal standard methods, provided the refinement includes realistic zero-point, sample displacement and transparency corrections (Post and Bish 1989). In practice, Rietveld-refined cell parameters often tend to be slightly larger than those obtained by single-crystal methods (*e.g.*, Liang & Hawthorne 1994). Refined cell parameters may vary to fit the observed pattern, rather than the zero-point correction refining to an appropriate value. This correlation is significant if high accuracy is required, as in determination of structural state of feldspar.

Single fragments of phase-pure feldspar, approximately 25 mg in weight, were selected from off-cuts of thin sections which had been examined for optical homogeneity by optical microscopy and analysed for chemical homogeneity by electron microprobe. Samples were finely ground and spread onto 4 μm-thick XRF Prolene film using L'Oréal hairspray as a mounting medium. Data were collected using a Siemens D5000 automated X-ray powder-diffractometer operating in transmission geometry; the resulting pattern is nearly identical to the pattern obtained with reflection-geometry. A Huebner incident-beam monochromator was used to obtain Cu$K\alpha_1$ X-radiation generated using 40 kV and 35 mA with a fine-focus X-ray tube. A 2 mm antiscatter slit, a 0.6 mm receiving slit and a KEVEX solid-state detector were used. For the first set of samples examined, a scan range of $7° < 2\theta < 77°$ was chosen to avoid essentially featureless parts of the feldspar XRD pattern. The sample was rotated at 60 rpm during a 60 s per step, 0.10° 2θ step-width data collection. A smaller step-width

gives reasonably accurate results, but values for precision are unrealistic due to serial correlation (Hill & Flack 1987). For a feldspar pattern collected using the above conditions, the full peak-width at half-maximum height (FWHM) of the narrowest resolved peak is $\sim 0.3°$ 2θ and the peak shoulders cover $\sim 1.0°$ 2θ, so that each peak is characterized by 10 data points. Hill & Madsen (1986) recommended stepwidths of 1/5 to 1/2 the FWHM, and count-times such that the strongest peak has ~ 1000 counts.

A second set of data was collected for some of the samples using Si as an internal standard, a scan range of $8° < 2\theta < 88°$, a $0.04°$ 2θ step-width and a count rate of 30 s per step.

The refinement was done using the Siemens WIN-RIETVELD set of programs. Four starting models were used, with the appropriate atom parameters for high sanidine (Ferguson *et al.* 1991), orthoclase (Prince *et al.* 1973), intermediate microcline (Bailey & Taylor 1955) and low microcline (Brown & Bailey 1964). Isotropic-displacement parameters and site occupancies were fixed throughout the refinements at the values reported in the starting models. Ionized scattering factors were used. The first variables refined were the 2θ zero-point and scale factor. For samples with an internal standard, fitting of the Si pattern was used to refine the zero-point correction. The background was fitted with a polynomial function using five refined variables and an origin at $77°$ or $88°$ 2θ. After this stage, each variable was refined to convergence (with parameter-shifts $< 1\%$) before additional variables were added. Variables which did not improve the fit between the observed and calculated patterns were usually discarded. Diffraction peaks were modeled using a pseudo-Voigt profile function, refining the peak

FWHM parameters W and V as well as Gaussian-Lorentzian mixing parameters. Intensity due to diffracted peaks was constrained to decay within five times the FWHM from each peak shoulder. For best fit of patterns, refinement of the peak asymmetry function P was restricted to $2\theta < 45°$; however, for refinement of cell parameters, P was given a value of 0.0: this constrains the calculated pattern to symmetric peaks and optimizes the precision of peak location. Atom coordinates were then refined. In most cases, the fit was not improved significantly by refinement of transparency and displacement parameters, or with use of the Dollase-March function with [0 0 1] as the preferred-orientation vector. This latter feature is as expected, as the transmission- and reflection-geometry patterns are nearly identical.

The best agreement between observed and calculated patterns occurs with unconstrained refinement of the zero-point, cell parameters and the peak asymmetry function (P). However, unconstrained refinement gave values of *b*, *c* and *V* larger than expected from the chemical composition (Fig. 5.1). A correlation was found between large values of P and anomalous values for the cell parameters. In most of the refinements, however, values of P are close to zero, indicating that the peaks are highly symmetric. The relation between varying zero-point and cell parameters is explicit in a *b*-*c* plot (Fig. 5.2). The cell parameters increase with increasingly positive zero-point values with a trend approximately perpendicular to the ideal MM-HS line (*i.e.*, even with incorrect values of zero-point, the degree of (Al,Si)-order can be estimated). The poorest overall fit occurs if the zero-point is constrained by the calculated positions of the Si peaks, but this gives reasonable and accurate cell-parameters (Fig. 5.3). Final values for cell parameters are given in Table 5.1.

The strongest peaks in the residual K-feldspar patterns had less than 4 counts, with most refinements having less than 2 counts. For samples with $\square Si_4O_8$ substitution, it is significant that no peak of quartz was found in the observed or residual patterns, as this substitution can be chemically mimicked by overlap of the EMP-analysed volume of feldspar with quartz.

All the microcline samples have residual peaks of albite, even though care was taken to choose samples which were phase-pure by optical microscopy and BSE imaging (Fig. 5.4). The microcline samples have less than 0.5 wt.% Na_2O (<3 mol.% Ab) according to EMP analysis, and this must be distributed as grains of albite much less than 1 μm in size. No albite peaks were noted in the orthoclase or in adularian high-sanidine. Strain indices measured from a plot of *a vs. bc* (Kroll & Ribbe 1987) range from -6 to -10 for the albite-bearing microcline. Strain indices should increase between albite and microcline if the microcline is rich in Rb, because of the increased cell parameters of Rb-rich microcline compared to Rb-poor microcline. However, the substitution of Rb might change the strain contours on a plot of *a vs. bc*, and the strain indices reported in Table 5.1 might not be accurate for the Rb-rich samples (8Lily, HGD096, RCL2011, APB3).The albite-free but Na-bearing orthoclase (Table 3.19) has a strain index of -8. The two samples of Na-free microcline (5Lily and BrownD in Table 5.1) both have a strain index of -3, but the Or_{100} high-sanidine samples are strain-free (S.I. = 0). The cause of strain indices as high as -10 and the anomalous cell-parameters reported for Na-free adularia (Woodard 1972, Sibley 1978, Ali & Turner 1982, Martin 1982, Černý & Chapman 1984, 1986, Martin & Falster 1986, Marshall *et al.* 1986, Dong & Morrison 1985) remain to be determined.

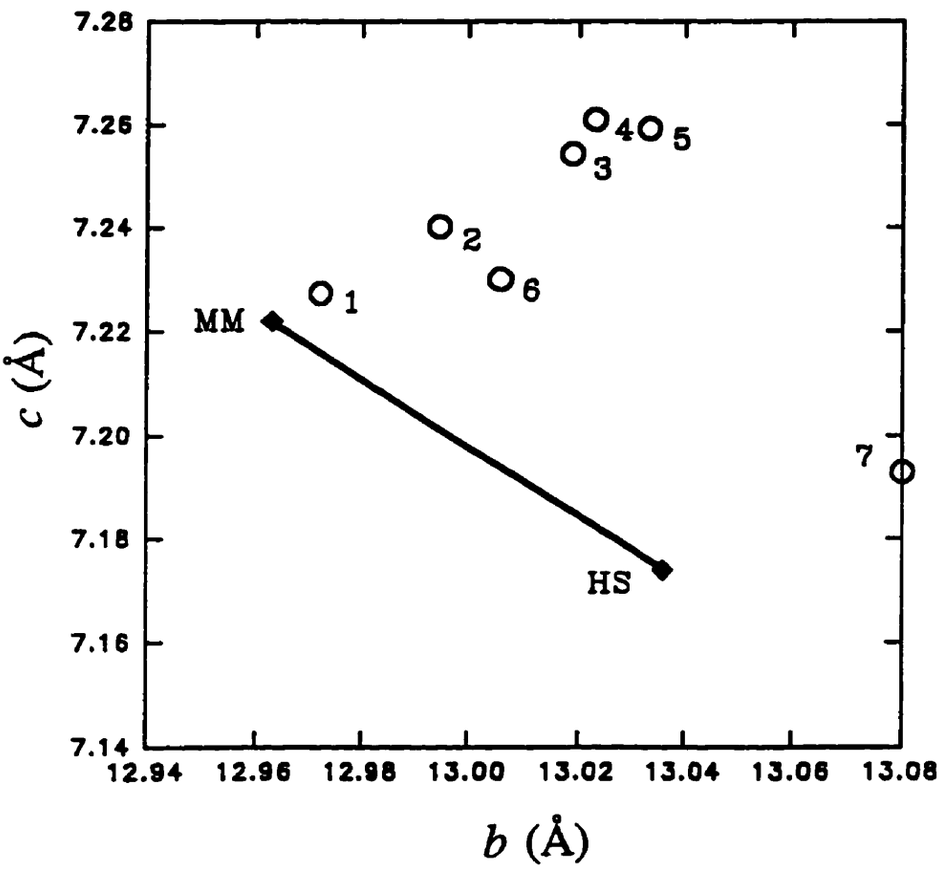

Fig. 5.1. Cell parameter *b*-*c* (Å) plot for (K-Rb)-feldspars showing values refined without an internal standard. The ideal MM-HS line is indicated using filled symbols. The numbers refer to samples in Table 5.1.

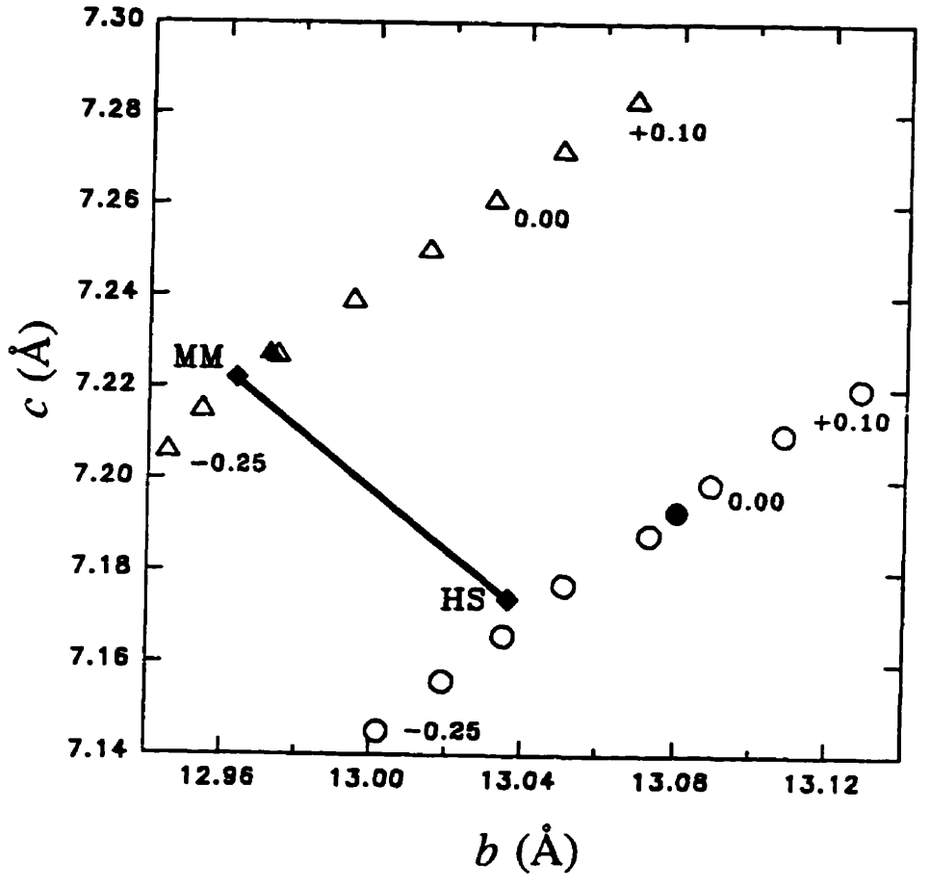

Fig. 5.2. Cell parameter *b*-*c* (Å) plot for the late salmon-coloured microcline from the Rubellite pegmatite (triangles) and green sanidine from High Grade Dyke (circles) showing values refined with no internal standard and refining the zero-point (filled symbols with high *b* and *c* values relative to the ideal MM-HS line), and refined using zero-point values from +0.10° to -0.25°, variable in steps of 0.05°2θ.

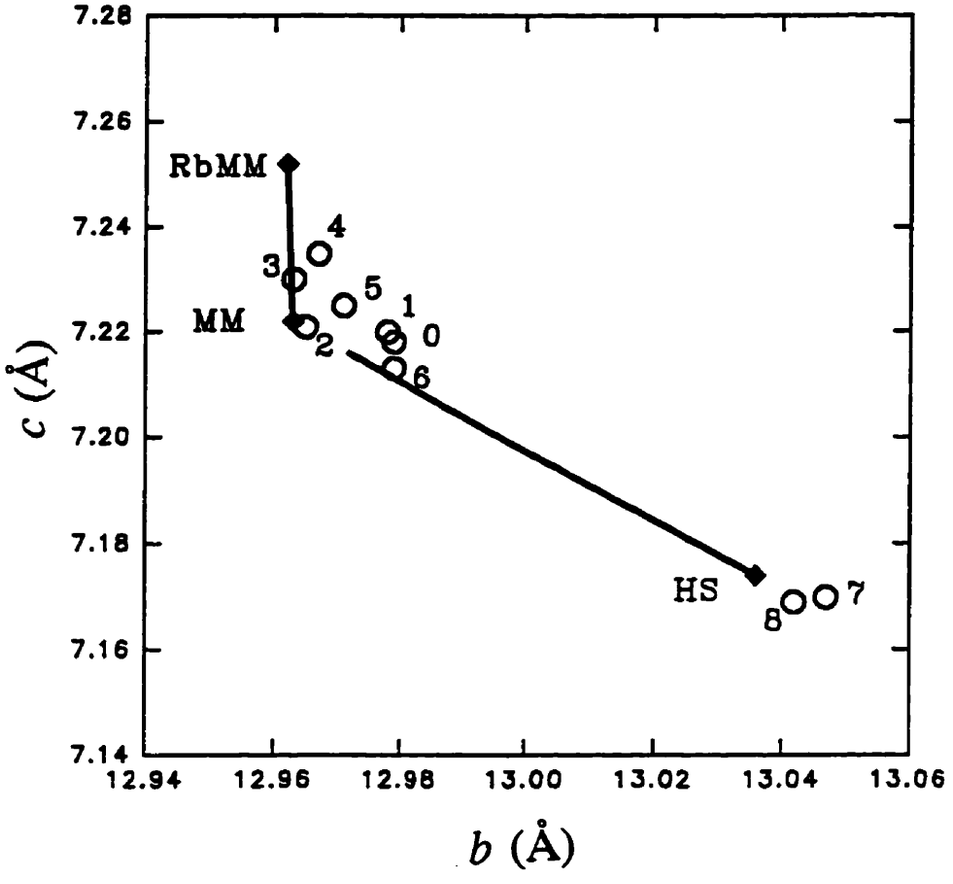

Fig. 5.3. Cell parameter *b*-*c* (Å) plot for (K-Rb)-feldspars showing final values for samples 0-9 (Table 5.1) and ideal values for HS, MM and RbMM end-members (filled symbols).

Table 5.1: Cell parameters of (K,Rb)-feldspars.

	a (Å)	*b* (Å)	*c* (Å)	$\alpha°$	$\beta°$	$\gamma°$	S.I.
0.	8.567(2)	12.979(3)	7.218(1)	90	116.04(2)	90	-8
1.	8.623(1)	12.978(1)	7.220(1)	90.45(1)	115.98(1)	88.40(1)	-6
2.	8.599(2)	12.965(2)	7.221(2)	90.54(2)	115.92(2)	87.95(1)	-3
3.	8.602(1)	12.963(2)	7.230(1)	90.60(2)	115.92(1)	87.78(1)	-7
4.	8.598(1)	12.967(2)	7.235(1)	90.58(2)	115.96(1)	87.73(1)	-10
5.	8.609(2)	12.971(3)	7.225(2)	90.62(3)	115.98(2)	87.79(2)	-7
6.	8.592(2)	12.979(3)	7.213(2)	90.28(4)	115.93(3)	88.85(3)	-3
7.	8.591(1)	13.042(2)	7.169(1)	90	115.99(1)	90	0
8.	8.591(1)	13.047(2)	7.170(1)	90	115.97(1)	90	0

0. Ortho gem orthoclase, White Queen Mine.
1. 8Lily black microcline, Rubellite pegmatite, Lilypad Lakes.
2. 5Lily salmon-coloured microcline, Rubellite pegmatite.
3. HGD096 white microcline, High Grade Dyke.
4. RCL2011 blocky microcline, Red Cross Lake.
5. APB3 vein microcline in pollucite, Tanco pegmatite.
6. BrownD massive pink adularia, Brown Derby, Colorado.
7. Tanco adularian high-sanidine, PA-057, Tanco pegmatite.
8. HGD green adularia, veins in pollucite, High Grade Dyke.

S.I. strain index from *a vs. bc* plot of Kroll & Ribbe (1987).

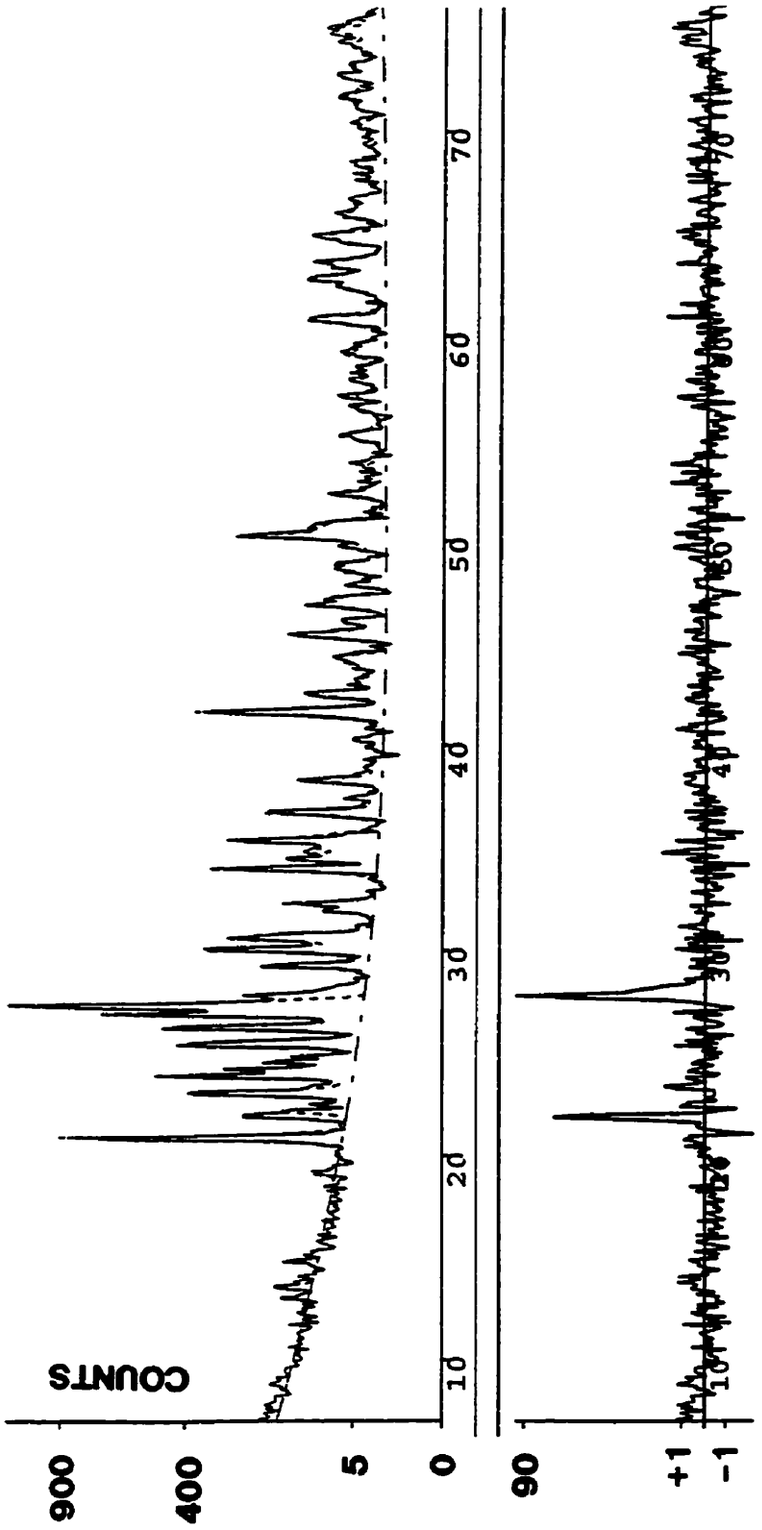

Fig. 5.4. Observed (solid line) and calculated (dashed line) log-scale diffraction patterns for blocky microcline (RCL2011) from Red Cross Lake, with residual peaks attributed to finely-dispersed albite (lower pattern).

5.2 *Cell parameters of end-member high-sanidine*

As noted in Chapter 2.2, there are uncertainties concerning the cell parameters of end-member high-sanidine (and RbHS). Černý & Chapman (1984, 1986) report cell parameters for Or_{100} adularian high-sanidine which are larger than those reported by Ferguson *et al.* (1991) for a sample with equal values of $<T_1\text{-}O>$ and $<T_2\text{-}O>$. End-member HS should have completely random occupancy of all T-sites by Al and Si, generating a maximum number of Al-O-Al bonds and equal values of $<T_1\text{-}O>$ and $<T_2\text{-}O>$ in structure refinement (Ferguson *et al.* 1991). However, there may be significant short-range order which minimizes the number of Al-O-Al bonds but maintains long-range disorder. Such variation in order is suggested by ordering experiments in which the NMR parameters continue to change even after XRD parameters become constant (Xiao *et al.* 1995). The data of Ferguson *et al.* (1991) indicate that the samples with the most disorder in terms of cell parameters are, unexpectedly, the least disordered in terms of $<T\text{-}O>$ distances. This could be ascribed to inaccuracy, as the crystals examined had irregular optical characteristics and the structure refined to somewhat high R-indices. It is possible that more than 25% of the T_2 site is occupied by Al, giving values of $<T_2\text{-}O>$ greater than $<T_1\text{-}O>$, but the driving force for such an ordering scheme is uncertain. A conventional explanation would be that samples with the largest cell parameters are the most disordered, with no more than 25% Al occupying any T-site, but if this is the case, then the cell parameters for end-member high-sanidine need to be revised to the higher values

reported by Černý & Chapman (1984, 1986).

In the series from LA to MM and from HA to HS, the cell-parameter trends are parallel to one another due to near-identical mechanisms of substitution. In the series from MM to HS and LA to HA, cell parameter trends are also parallel, due to near-identical mechanisms of (Al,Si)-disorder. According to Stewart & Ribbe (1969), the increases in b, β and γ and the decreases in c and α (at near-constant a and V) which occur with (Al,Si)-disordering of MM result largely from a shift of Al to the T2 sites because there are a greater number of T2 sites along b than along c. Trends for the substitution series from MM to RbMM and from HS to RbHS, and for the (Al,Si) order-disorder series from MM to HS and from RbMM to RbHS, might also be expected to be parallel. The (K-Rb)-feldspar series most well-characterized is from MM to RbMM, in which V increases at constant b. If accurate values for HS and RbHS are determined, plots of V *vs.* b or c *vs.* b should form a parallelogram with MM, RbMM, HS and RbHS at the corners. This is not observed for the present values of HS and RbHS (Fig. 2.1). Either these values are inaccurate or a structural explanation which is different from that of Stewart & Ribbe (1969) is required for the difference in substitution of Rb in MM *vs.* Rb in HS, and for the difference in (Al,Si) disordering from MM to HS *vs.* RbMM to RbHS.

I examined samples of disordered adularian high-sanidine from High Grade Dyke (HGD) and from Tanco, both in SE Manitoba (Černý & Chapman 1984, 1986). Rietveld-refined cell-parameters using Si as an internal standard are given in Table 5.1 and plotted in Fig. 5.3. EMP-measured compositions are reported in Table 5.2. The composition of the High Grade Dyke sanidine is close to that of end-member $KAlSi_3O_8$, but with local patchy substitution of up to 4 mol.% $\square Si_4O_8$. The average composition has only 1.5 mol.% $\square Si_4O_8$. The composition of the Tanco sample varies between that of end-member $KAlSi_3O_8$ and $K_{0.97}Al_{0.97}Si_{3.03}O_8$ (*i.e.*, local substitution of up to 3 mol.% $\square Si_4O_8$); however, the average composition has only 1.2 mol.% $\square Si_4O_8$. With such minor $\square Si_4O_8$ substitution, the cell parameters should be only slightly smaller than those of ideal $KAlSi_3O_8$ disordered end-member, as Si-O bonds are shorter than Al-O bonds. The Rietveld-refined cell parameters (Table 5.2) are virtually identical for both localities, but are larger than the values suggested by Ferguson *et al.* (1991) for end-member high-sanidine, and are in close agreement with the values reported by Černý & Chapman (1984, 1986). The unit-cell dimensions reported here should be closely representative of the structure and composition of end-member high-sanidine.

Table 5.2: Average composition of adularia from High Grade Dyke and Tanco.

High Grade Dyke				
oxide	(N=10)	formula (*apfu*)		range
SiO_2	64.97(21)	Si	3.015(13)	2.998-3.038
Al_2O_3	17.98(34)	Al	0.983(14)	1.004-0.957
K_2O	16.62(20)	K	0.984(8)	1.004-0.975
sum	99.58	ΣT	4.000	

Tanco				
oxide	(N=12)	formula (*apfu*)		range
SiO_2	65.03(41)	Si	3.012(11)	2.993-3.032
Al_2O_3	18.10(19)	Al	0.988(12)	1.010-0.967
K_2O	16.72(17)	K	0.988(12)	1.009-0.972
sum	99.88	ΣT	3.999	

Elements sought but not detected:
Na, Rb, Cs, Ca, Sr, Ba, Pb, Mg, Mn, F, Ga, Fe, Ti, P.

CHAPTER 6

DISCUSSION

This thesis examines the compositional and structural characteristics of the (K-Rb)-feldspar series as it occurs in complex-type rare-element granitic pegmatites. The discussion begins with examination of the P-T conditions of pegmatite emplacement and consolidation, as far as it concerns (K-Rb)-feldspar in association with pollucite (Ch. 6.1). Next, the K/Rb ratio of K-feldspar is discussed as a feature which records advancing fractionation among related pegmatites, and among internal zones of individual pegmatites (Ch. 6.2). The sequences of reaction and alteration of the (K,Rb)-feldspars are constrained by their occurrences as part of the alteration sequence of pollucite, bounded by the crystallization of late primary phases and the lowest-temperature alteration at near-ambient conditions. The reactions and alteration shown by (K,Rb)-feldspar and pollucite are related to the compositional features of late cesian analcime and micas, and their description provides additional evidence for widespread subsolidus activity of Rb and Cs (Ch. 6.3). Low-temperature end-member K-feldspar (variety name adularia) is an important member of the sequence of alteration of both pollucite and early K-feldspar, and a model of crystallization is presented (Ch. 6.4). The crystal chemistry of (K-Rb)-feldspar is then discussed, particularly as it relates to the accuracy and precision of the analytical method (Ch. 6.5). The paragenesis of Rb-dominant feldspars is then traced from textural evidence for exsolution of Rb-rich feldspar from the higher-temperature precursor to the low-temperature co-precipitation of K-feldspar + Rb-feldspar (Ch. 6.6). Examination of pegmatitic (K,Rb)-feldspar, using Rietveld refinement of X-ray data as a method of obtaining accurate cell-parameters, has provided new insight into the monoclinic → triclinic, sanidine → microcline phase transformation and exsolution processes (Ch. 6.7). Finally, evidence pertinent to the characterization of new Rb-dominant feldspar species is presented (Ch. 6.8).

6.1 *Pressure-temperature conditions*

Geochemically primitive pegmatitic magmas, equivalent to "wet" haplogranite systems, probably crystallize at temperatures between 700 and 600°C (Černý 1991). In somewhat more-evolved pegmatites, the presence of the lithium aluminosilicate minerals petalite or spodumene constrains the temperature to less than 700°C at any pressure (London 1990). The temperature range of consolidation of highly fractionated peraluminous melts of granitic bulk composition, rich in H_2O, B, F, Li, Rb and Cs, is estimated to be about 650-450°C at 4-2 kbar (London 1986, Chakamoukos & Lumpkin, 1990). In complex-type granitic pegmatites, the most Rb-enriched feldspars associated with hydrous sodian pollucite crystallized near the lower end of this temperature range, so it is important to discuss the timing of pollucite crystallization.

The upper temperature limits of pollucite crystallization are constrained by the following observations. Field evidence has long suggested that pollucite is a late-forming phase. Historically, many authors considered pollucite to be of replacement origin; however, more recent investigations suggest that pollucite is of late primary igneous origin (Černý & Simpson 1978). In cases where the sequence of crystallization is clear, it seems to be rather consistent. At the ≤ 100 localities that are currently known, primary pollucite generally occurs interstitial to spodumene, quartz and albite or microcline, and is less frequently in direct contact with lepidolite, petalite or amblygonite. For the localities examined in this study, large and euhedral crystals of primary minerals formed first, and pollucite is anhedral and interstitial to these. Textural observations concerning sequences of crystallization tend to be ambiguous, because for each mineral, there is a range of stability, and coprecipitation is common. Three examples from Finnish pegmatites demonstrate this feature. At Oriselkä, a crystallization sequence of spodumene + quartz → pollucite → albite + lepidolite is observed, with later units infilling (but not replacing) spaces between earlier crystals. At Haapaluoma,

the sequence is K-feldspar + quartz ± schorl → quartz + beryl + rubellite → pollucite → albite → lepidolite. At Viitaniemi, laths of montebrasite "float" in pollucite and also occur in the quartz, albite and lepidolite units marginal to the pollucite (Teertstra *et al.* 1993). In most cases where evidence is available, it seems that fine-grained albite and lepidolite crystallized after pollucite.

The occurrence of petalite also constrains the P-T conditions. Close associations of pollucite with primary petalite are rare (*e.g.*, Elba, Italy; Utö, Sweden; Tanco, Manitoba), but pollucite is known from many petalite-subtype or petalite-bearing rare-element pegmatites (*e.g.*, Karibib, Namibia; Bikita, Zimbabwe; Varutträsk, Sweden; Dunton Quarry, Maine; Jeclov, Czech Republic; Himalaya, California; Brown Derby, Colorado; Smeds & Černý 1989). Pollucite from Luolamäki, Finland, is cut by coarse veins of petalite (Teertstra *et al.* 1993). Pollucite from Nová Ves u Českého Krumlova, Czech Republic, contains a three-dimensional rectangular grid of acicular petalite (Teertstra *et al.* 1995). The field of stability of petalite lies below 680°C at $P \leq 4$ kbar (London 1984). The observation that within a pegmatite group or field, pollucite-bearing dykes tend to intrude shallow low-pressure areas is also significant (Smeds & Černý 1989).

An approximate lower-temperature limit of pollucite crystallization is indicated by features of its occurrence near margins of gem-bearing zeolite- and clay-filled pockets at the Himalaya Mine, California (Foord *et al.* 1986), and by similar observations at Elba, Italy (unpublished data of DKT). At these localities, pollucite is largely enclosed by primary phases. There is, however, some evidence for minor overlap of the crystallization field of primary pollucite with that of late secondary cesian analcime. At Elba, a small proportion of the pollucite is found in cavities, in association with petalite and rare cesian analcime. Most of the pollucite is waterclear, anhedral and partially dissolved (to heavily

etched) by late fluids and compositionally homogeneous; however, rare euhedral crystals occur, and exhibit internal zonation with variable Na/Cs and Si/Al ratio (unpublished data of DKT). The zonation indicates lack of buffering of Na due to loss of equilibrium with albite which occurs at low temperature (Sebastian & Lagache 1990).

The change of form from anhedral to euhedral is also significant: it is more typical for late hydrothermal cesian analcime to have a well-developed morphology than pollucite (Černý 1972, Teertstra & Černý 1992). Waterclear euhedral pollucite is also known from miarolitic cavities from pegmatites in the Gilgit area, Pakistan (Teertstra & Černý 1992). At Kulam, Afghanistan, secondary euhedral pollucite (possibly cesian analcime) has recrystallized from massive white pollucite (Teertstra & Černý 1992). Crystallization of pollucite ends just before pocket formation, prior to the onset of vapour phase separation and the formation of gem-bearing pockets.

In summary, the evidence strongly suggests that, among the primary phases, hydrous sodian pollucite is among the last to crystallize in the absence of a separate vapour phase, in near-equilibrium with albite and probably at about 550-400°C and 3-2 kbar. Blocky K-feldspar forms at equal to higher temperature and pressure than coexisting pollucite, possibly in the stability field of low microcline; feldspar veining pollucite formed at lower P-T conditions, distinctly in the stability field of low microcline; adularian (K-Rb)-feldspar formed at very low temperature, late in the alteration sequence of pollucite. The distribution of Rb between K-feldspar and pollucite is discussed next (Ch. 6.2); the significance of feldspar in the alteration sequence of pollucite is discussed in Ch. 6.3.

6.2 *Evolution of K/Rb ratios*

Plots of K/Rb ratio and Cs content of K-feldspar are widely used as an indicators of progressive fractionation among related pegmatites and granites, and to indicate sequences of crystallization within zoned pegmatites (a recent example is provided by Shearer *et al.* 1992). Smooth and continuously decreasing K/Rb ratios indicate geochemical links between parental granites and associated aureoles of evolved pegmatites (*e.g.*, Černý *et al.* 1981). High concentrations of Rb and Cs in the first- and second-intermediate zones of upper parts of the Tin Mountain pegmatite, South Dakota (rather than in lower potentially later-crystallizing zones) prompted Walker *et al.* (1989b) to suggest that Rb and Cs were transported upward by an aqueous fluid-film operative along crystallization fronts. Such a mechanism involving early separation of a fluid phase is central to the Jahns & Burnham (1969) model of internal evolution, and has been proposed to explain the zonal separation of Na- and K-rich components as well as the concentration of Rb in feldspar near pollucite zones (Walker *et al.* 1989b).

Values of K/Rb from 20 to 5 and of Cs from 500 to 5000 ppm are typical of feldspar from the interior zones of pollucite-bearing pegmatites (Smeds & Černý 1989). However, the geochemical criteria for recognizing pollucite-bearing pegmatites from the feldspar composition given by Gordiyenko (1976) and Trueman & Černý (1982) should be applied with caution. In certain pollucite-bearing pegmatites, blocky K-feldspar crystals adjacent to pollucite have rather low contents of Rb and Cs (Teertstra *et al.* 1993). Feldspar highly enriched in Rb has been found in pegmatites in which no pollucite has been found (3.39 wt.% Rb_2O, 500-1400 ppm Cs; Lagache & Quéméneur 1997).

I collected data on coexisting feldspar-pollucite pairs which seemed to be in textural equilibrium. For the Rb-rich localities, multiple analyses were done on both the feldspar and the pollucite. The K-feldspar adjacent to pollucite typically has a wide range of Rb values, but pollucite may also occur adjacent to Rb-poor K-feldspar (Table 6.1). There is a positive correlation of $Rb_2O_{feldspar}$ with $Rb_2O_{pollucite}$; on average, Rb prefers K-feldspar over pollucite by a factor of ~5:1 (Fig. 6.1). The distribution of Rb_2O between the two phases gives an approximately linear trend, supports the assumption of near-equilibrium based on textural features.

If erratic variations appear in geochemical trends of K/Rb *vs.* Cs, these may be (in part) due to (1) microscopic inclusions of pollucite in feldspar which are relatively common and must affect bulk-chemical measurements, and to (2) post-crystallization chemical reequilibration of feldspar. The H_2O-catalysed microcline-forming phase transformation is largely isochemical as it involves only (Al,Si)-ordering not changes in Si/Al ratio, but minor- and trace-element abundances are potentially to likely disturbed because the reconstructive transformation occurs in the presence of fluids (*e.g.* Clark 1982). The patchy composition of Rb-bearing microcline has a greater range of K/Rb ratio in highly-porous altered feldspar than in low-porosity less-altered feldspar; this is attributed to low-temperature reequilibration rather than to primary crystallization. The variable Rb of pollucite is also attributed to low-temperature reequilibration (Fig. 6.1).

The K/Rb *vs.* Cs (ppm) geochemical indicator should remain useful for overall estimates of alkali metal fractionation in granites and pegmatites, but cannot be used in all cases to indicate the presence of pollucite (unless pollucite inclusions

give high Cs values!). If the pegmatite happens to be Rb-rich, then the highest contents of Rb occur specifically in K-feldspar closely associated with (Rb-bearing) pollucite and generally in the latest-crystallizing primary units near the core of a pegmatite (*e.g.*, Tanco, Černý *et al.* 1996). Although Rb and Cs have similar geochemical behaviour, Figure 6.1 shows that these elements may be decoupled, and Rb-poor pollucite becomes associated with Rb-poor K-feldspar, particularly in pegmatites where only small volumes of pollucite are found. This might be due to an initial Rb- and Cs-poor pegmatitic melt, or to incorporation of Rb in early pegmatitic mica. The principal sink for Rb, both in a pegmatite and in its source region, is mica, particularly lepidolite in the pegmatite. Depending upon the amount of earlier-formed muscovite and lepidolite, a melt may be Cs-rich but Rb-poor at the time of pollucite crystallization.

The geochemical fractionation of Rb and Cs is a function of partitioning between melt and K-feldspar, quartz, albite and mica. Rb has a slight preference for K-feldspar over melt ($D(\mathrm{Rb})^{\mathrm{Kf/melt}} \approx 1.0$), and a stronger preference for biotite ($D(\mathrm{Rb})^{\mathrm{Bi/melt}} \approx 2.0$) and muscovite ($D(\mathrm{Rb})^{\mathrm{Ms/melt}} \approx 1.6$), whereas Cs is strongly incompatible in K-feldspar ($D(\mathrm{Cs})^{\mathrm{Kf/melt}} \approx 0.13$), biotite ($D(\mathrm{Cs})^{\mathrm{Bi/melt}} \approx 0.4$) and muscovite ($D(\mathrm{Cs})^{\mathrm{Ms/melt}} \approx 0.3$) (Icenhower & London 1996). A fractionating assemblage would have to be made up largely of lepidolite (>50 vol.%) for Rb to prefer solid phases over a residual melt. The K-feldspar partition coefficient for Rb of ~ 1 indicates that the Rb concentration in magmatic K-feldspar provides a record of the evolving Rb concentration of the coexisting melt. In summary, both the experimental evidence and the compositional measurements verify the observation that concentrations of Rb are usually highest in the latest-formed units, in association with (Rb-bearing) pollucite.

Table 6.1: Rb_2O concentrations in coexisting pairs of primary pollucite and K-feldspar.

Locality	Pollucite	K-feldspar	
	wt.% Rb_2O mean (range)	wt.% Rb_2O mean (range)	K/Rb (at.) mean (range)
Kola Peninsula	2.45 (2.4-2.5)	*8.25 (6.5-9.2)*	*2.58 (3.9-2.3)*
Red Cross Lake	0.90 (0.8-1.1)	4.94 (4.0-6.0)	5.83 (6.7-4.2)
Benson #1	0.87 (0.8-1.0)	3.60 (2.8-4.5)	8.90 (10-7.6)
Lilypad Lakes	0.60 (0.1-1.0)	3.44 (2.8-4.9)	7.65 (9.8-5.3)
Luolamäki	0.67 (0.5-0.9)	3.33 (1.5-5.9)	10.7 (18-4.6)
High Grade Dyke	1.48 (0.9-1.7)	3.21 (2.0-4.0)	9.62 (15-7.0)
Tanco	0.83 (0.3-1.3)	2.68 (2.0-3.5)	11.5 (16-8.2)
Elba	0.78 (0.6-0.8)	*1.98 (0.9-3.4)*	*19.6 (30-9.1)*
Mongolian Altai:			
Dike #1	0.32	*2.04*	*16*
Dike #83	0.18	1.51	23
Tot Lake	0.55	2.09	14
Tin Mountain	0.25	1.22	25
Helikon	0.00	1.12	31
Viitaniemi	0.04	*0.72*	*46*
Madagascar	0.32	*0.77*	*43*
Nová Ves	0.19	0.71	46
Norway, Maine	0.26	*0.66*	*51*
Haapaluoma	0.00	0.06	80

In most of the samples blocky K-feldspar was examined; feldspar *veins* in pollucite are indicated by *italics*. Full locality names and descriptions of the material are given in the text (Ch. 4).

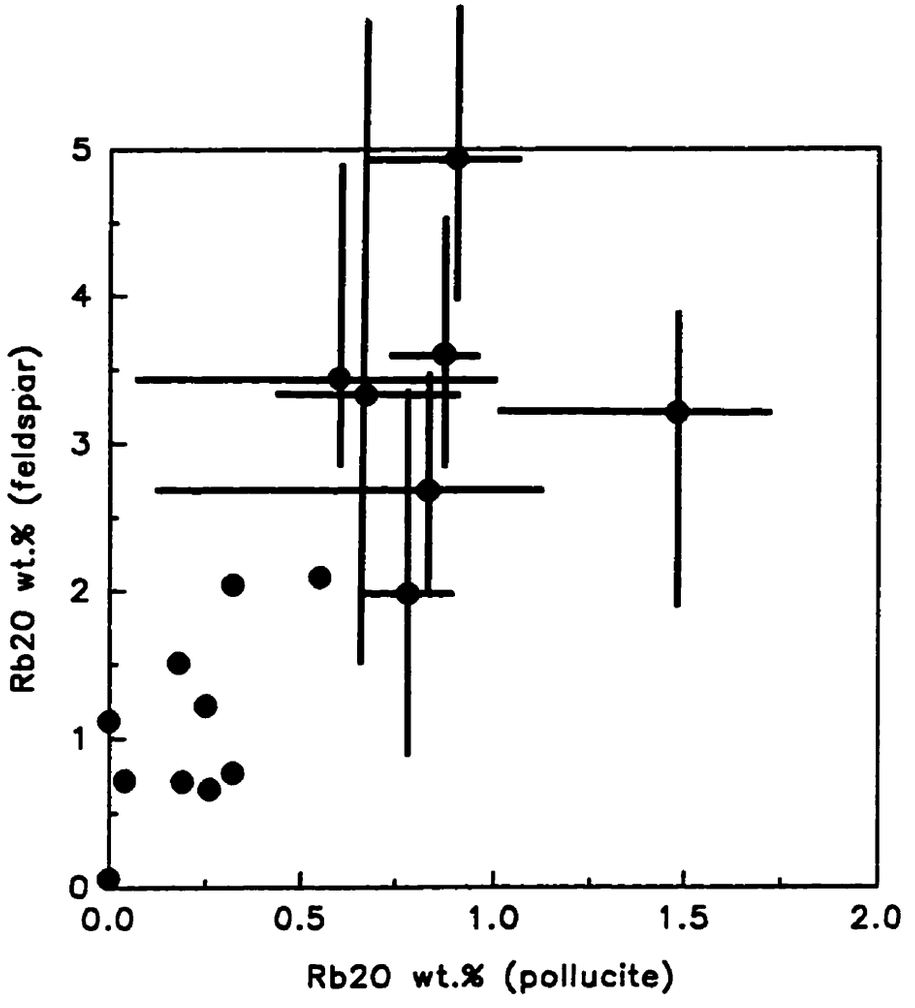

Fig. 6.1. Rb_2O concentrations in coexisting pairs of primary pollucite and K-feldspar showing average values (•) and ranges for the Rb-rich material.

6.3 *Subsolidus alteration*

Study of late-stage subsolidus alteration has provided new information which requires amendment of the Morgan & London (1987) model concerning the correlations of pegmatite subsolidus events and exomorphic sequences of wallrock alteration. (K-Rb)-feldspars, cesian analcime and Rb- and Cs-rich micas occur as part of a sequence of subsolidus alteration which affects several minerals, including pollucite, and indicates widespread subsolidus activity of Rb and Cs. The alteration sequence of pollucite is examined in detail because it constrains the P-T conditions of formation of each type of feldspar (blocky, vein and adularian) and provides a framework in which detailed observations of adularia (Ch. 6.4) and (K-Rb)-feldspar (Ch. 6.6) can be placed.

Three stages of exomorphic alteration of host lithologies have been connected with stages of pegmatite consolidation at Tanco (Morgan & London 1987; on this topic also see Shearer *et al.* 1986):

(1) B ($\pm$Li) metasomatism, generating tourmalinization of host rock at 550-500°C is closely followed by precipitation of fine-grained albite units in the pegmatite;

(2) K-Rb-Cs-F ($\pm$Li) metasomatism, generating exomorphic biotite at 450°C, is related to the crystallization of fine-grained albite which generates acidic F-rich fluids within the pegmatite, closely followed by precipitation of mica units;

(3) H_2O-CO_2 ($\pm$Li) propylitic alteration of (Hbl + Pl) → (Ep + Chl + Tn + Cc + smectite-rich clay) at T<450°C is related to sericitization of microcline and

pollucite by F-rich vapour liberated from the latest stage albitic units.

Two principal modifications to the model of Morgan & London (1987) are required, concerning point (3) above.

(I) Morgan & London (1987) use the term "sericitization" to indicate large-scale replacement of K-feldspar by late-mica (lepidolite) units, rather than to indicate the development of turbidity. The turbidity of feldspars, previously thought to be caused by alteration by fine-grained mica, is now known to be related mainly to the development of microporosity (Lalonde & Martin 1983, Walker *et al.* 1995. Lee *et al.* 1995).

The term "magmatic-hydrothermal transition" has been used to indicate the replacement of primary minerals by late units and the alteration of primary minerals under subsolidus conditions. For example, London (1990) emphasized the reactive nature of late fluids which are exsolved during the course of pegmatite consolidation, and suggested that the sporadic and variable nature of metasomatic replacement is due to fluids migrating between largely consolidated mineralogical zones which are always grossly out of equilibrium with their new local environment. This argument applies to clear-cut cases of metasomatic replacement due to reaction of primary minerals with migrating hydrothermal fluid. However, the argument must not be extended to include the case of enhanced reactivity of early-formed phases which is a result of phase instability on change of P-T conditions. An example of the latter case is the isochemical

conversion of petalite to aggregates of spodumene + quartz (SQUI) as the P-T path intersects the stability field of spodumene (London 1984). In the case of pollucite, the hydrous Na-rich primary phase is stable with high Si/Al ratios under the conditions of crystallization. However, with decreasing temperature reequilibration generates a Cs-rich phase with a lower Si/Al ratio (Teertstra & Černý 1995, Lagache 1995, Lagache *et al.* 1995). These largely isochemical reactions are aided by a high activity of aqueous fluid and may be considered to be the result of deuteric alteration. The best example is provided by high sanidine or orthoclase, and by cryptoperthite. The H_2O-catalysed monoclinic → triclinic orthoclase → microcline transformation, coupled with exsolution of albite, goes to near-completion in most rare-element (and simple barren) granitic pegmatites. Microcline-perthite, and coarse aggregates of microcline + albite are the dominant low-temperature phases, formed as a pseudomorphic assemblage differing significantly from the structure and composition of the original feldspars (as crystallized from the pegmatite melt) (Ch. 6.8).

(II) The present evidence suggests that pollucite is not replaced by mica. Coarse veins of lepidolite, which occur in a polygonal pattern throughout large blocks of pollucite, probably formed from fluids excluded during the crystallization of pollucite. Fine-scale sericitization probably represents a continuation of this process at low temperature. The alteration of pollucite (discussed in detail below), spodumene and petalite occurs in a distinct sequence which is characteristic of the sequential compositional evolution of late pegmatitic fluids (Černý *et al.* 1981,

Teertstra *et al.* 1993), and could not have been consistently derived by hydrothermal fluids infiltrating from the different host lithologies. The assemblages of minerals in these alteration sequences and the order of crystallization (Fig. 6.2) are similar to the crystallization sequences of late hydrothermal leaching cavities at Tanco (Černý 1972) and gem-bearing clay-filled cavities (*e.g.* California, Foord *et al.* 1986). Only toward very low temperature is there evidence for influx of externally-derived non-pegmatitic fluid (*e.g.*, the incorporation of Ba in adularia). The H_2O-CO_2 ($\pm$Li) propylitic alteration of (Hbl + Pl) wallrock (stage (3) of the model of Morgan & London 1987) may result solely from the exsolution of excess fluids which were not consumed by the crystallization of late-mica units.

Widespread subsolidus activity of Rb and Cs is indicated by the low-temperature formation of cesian analcime and the occurrence of Rb- and Cs-rich-to-dominant micas and clay minerals. Zoning in cesian analcime records a complex evolution of $Cs^+_{(aq.)}$ activity, with a broad decrease a_{Cs} in latest stages of growth. Outermost rims of lepidolite, muscovite and exomorphic biotite record a distinct, late increase in Cs and Rb activity. Fine-flaked lepidolite associated with analcimization of pollucite also indicates locally high activities of F at low-temperature. Rare occurrences of Cs-rich clay minerals indicate rare-alkali activity extending to very low-temperature conditions. Compositions of these late minerals indicate that hydrothermal wallrock-derived fluids have negligible influence on the internal evolution of pegmatite fluid, except at low temperature.

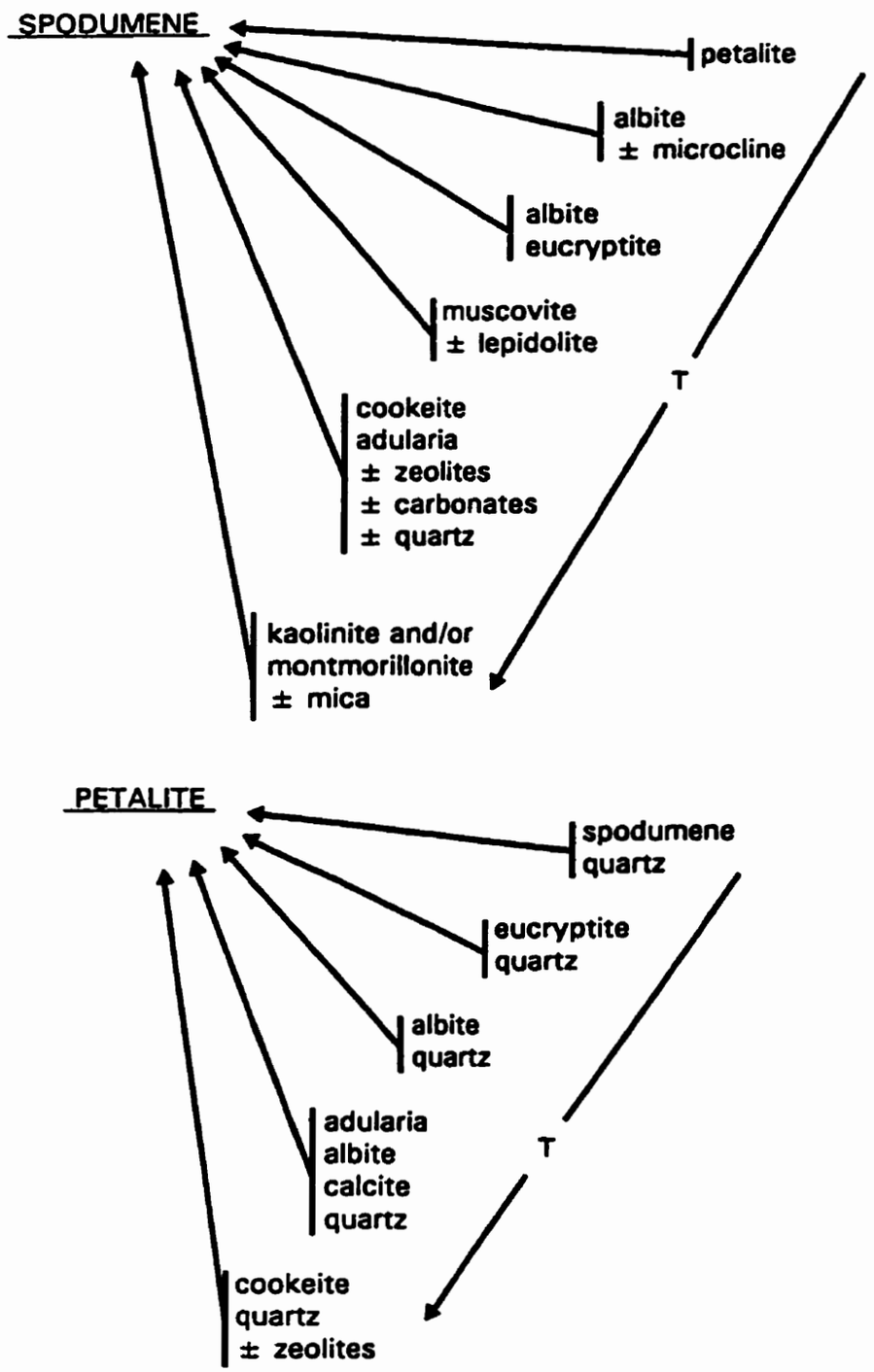

Fig. 6.2. Characteristic alteration sequences of spodumene and petalite from some pegmatites in SE Manitoba (from Černý *et al.* 1981). The arrow indicates alteration products appearing with decreasing temperature (T).

Three consecutive stages of alteration of pollucite, first described in pollucite from the Tanco pegmatite by Černý & Simpson (1978), are now recognized to be rather consistent in pegmatites worldwide (Teertstra *et al.* 1993). In the present work, representative sequences of alteration are given in Figures 4.6 and 4.14 for pollucite from Morrua (Mozambique) and Luolamäki (Finland), respectively. The stages include (i) coarse polygonal veining by lepidolite, quartz, albite and non-perthitic microcline, (ii) fine subparallel to braided veining of muscovite (± quartz) and spodumene, and (iii) replacement assemblages of adularian K-feldspar, quartz, muscovite, albite and cookeite ± apatite. The alteration is typically followed by cation exchange of pollucite and leaching and replacement by clay minerals.

(K,Rb)-feldspar is an important and typical part of the sequence from the crystallization of primary pollucite to its veining and late replacement. The crystallization temperature of adularian K-feldspar (+ cookeite), formed prior to analcimization and associated with end-member pollucite, is constrained by its relative placement in the sequence of alteration minerals to approximately 300-200°C (Teertstra & Černý 1995). Feldspar formed during analcimization of pollucite may have formed at a somewhat lower temperature range of about 250-150°C. The sequences of phase transformation, reequilibration and alteration of alkali feldspar and pollucite, approximately correlated with decreasing temperature, are summarized in Fig. 6.3.

Stage (i). Coarse (cm-wide) veining by quartz, albite, microcline (+ mica) and lepidolite (+ quartz), and rarely petalite, fills fractures in large pollucite bodies. This assemblage occurs at the margins of smaller segregations of pollucite. The mineralogy of the coarse veining is variable, and resembles that of late-crystallizing assemblages in the surrounding pegmatite, but genetically distinctive. The only mineral consistently present as coarse veining is lepidolite (+ quartz ± apatite). Lepidolite is never physically connected to lepidolite units, and pinches out within the pollucite. Rather than having a source external to the pollucite bodies, lepidolite seems to have formed by crystallization of residual fluids excluded during crystallization of pollucite. The same conclusion may apply to veins of microcline which seem to be restricted to the interiors of pollucite bodies. The abundance of lepidolite and microcline veins decrease toward the margins of pollucite bodies. In contrast, albite units cutting across margins of pollucite bodies may often be traced in outcrop to nearby albite units.

Stage (ii). Fine veining (mm-wide) of muscovite (± quartz) and later spodumene is characteristic of most localities where pollucite has segregated into masses larger than about 1 cm in size. The veins are pervasive throughout the pollucite and do not necessarily become more abundant near the margins of pollucite; this suggests that the vein-forming fluids were not derived from a source external to the pollucite bodies. They are a probably a finer-grained lower-temperature continuation of earlier micaceous veining.

Stage (iii). Adularian K-feldspar metasomatically replaces pollucite, crystallizing along surfaces of the earlier veins. Spherical aggregates fully embedded in pollucite usually lie along fracture planes. Aggregates are generally 0.5-1.0 mm in size, but clusters 2-3 mm in diameter are not uncommon. Many of the aggregates also contain albite, but virtually all include cookeite and finely-dispersed apatite and pollucite. At many localities, margins of the pollucite bodies tend to be more highly altered than the interiors, and there are wide variations in local abundances of metasomatic feldspar. Massive K-feldspar, in hand specimen usually porous, opaque and brown, green or salmon in colour, replaces pollucite at several localities. Optical-microscopic examination of thin sections of the feldspar shows that individual grains tend to be untwinned. Optical properties are typically obscured by extreme porosity and high inclusion density. Most grains are brown (non-pleochroic) in thin section. In virtually all cases, late K-feldspar aggregates can be distinguished from earlier generations by visual inspection of hand specimens or thin section (by optical microscopy) and by EMP analysis. EMP analysis shows that, in contrast to earlier K-feldspar, the late aggregates have no detectable Na or P but may contain minor Sr and Ba (suggestive of influx of host-rock fluid). The principal substitution corresponds to the (K-Rb)-feldspar series. The feldspars also replace, react with, and represent breakdown products of, earlier generations of (K,Rb)-feldspar (see discussion, Ch. 6.6). Because of the widespread occurrences of low-temperature end-member K-feldspar, it is necessary to discuss its characteristics and the application of the term "adularia".

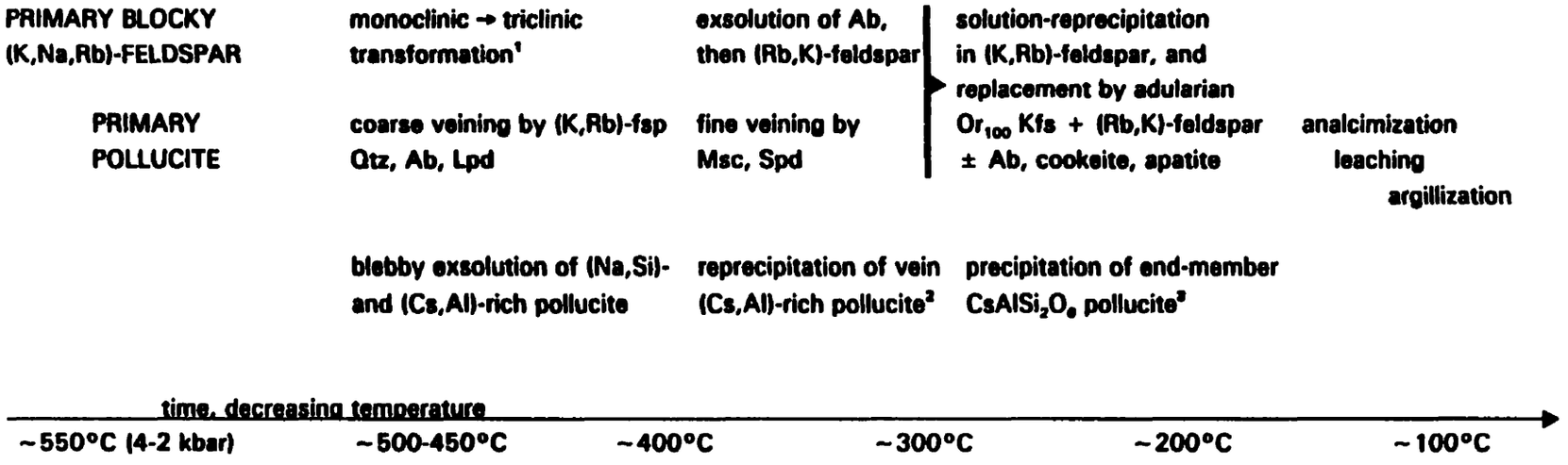

Fig. 6.3. Sequences of phase transformation, reequilibration and alteration of alkali feldspar and pollucite, approximately correlated with decreasing temperature. Additional information may be found in (1) Brown & Parsons (1989), (2) Teertstra *et al.* (1996) and (3) Teertstra & Černý (1995).

6.4 *A model for the crystallization of adularia*

Adularia belongs to the category of long-established varietal names permitted by the International Mineralogical Association. It is widely used to describe the non-perthitic morphologically distinct variety of K-feldspar typical of low-temperature environments. From high- to low- temperature among a broad range of geological environments, the morphology of K-feldspar varies from the Carlsbad (prominent {010}, *c*-axis elongation) to the Baveno (prominent {010} and {001}, *a*-axis elongation) to the Adularia (near-rhombohedral {110} and {10$\bar{1}$}) habits (*cf.* Černý & Chapman 1986 for additional information). In contrast to some of the pre-1980 literature, the term adularia currently has no connotations with regard to structural state. The term is fully embedded in the literature, however, and is used to define and distinguish at least two types of epithermal-vein ore deposits (*e.g.*, adularia-sericite and acid-sulphate types; Heald *et al.* 1987).

In addition to its distinct morphology, a prominent and defining feature of adularia from the majority of geological environments is its chemical composition, closely approaching to attaining end-member $KAlSi_3O_8$. The Or_{100} composition is expected,based on extrapolation of experimentally-derived solvus curves at T<300°C (Bachinski & Müller 1971, Smith & Parsons 1974) and from synthesis at T<80°C (Flehmig 1977). Except for minor substitution of Ba at some localities, the principal stoichiometric deviation from $KAlSi_3O_8$ is due to the newly-discovered $\square Si_4O_8$ substitution (Ch. 4.1).

In this thesis, non-perthitic K-feldspar which has end-member composition, a low-temperature paragenesis and optical features resulting from primary growth rather than transformation from a higher-symmetry precurser,are termed "adularian", regardless of whether open space was available for the development of a distinct crystal habit and crystal-form hierarchy.

The unit-cell parameters of feldspars correlate very precisely with composition and state of order (Kroll & Ribbe 1987). However, cell parameters for the majority of samples of adularia deviate significantly from the values expected from the Or_{100} composition: (1) cell parameters lie outside the standard *b-c* plot for alkali feldspars; (2) individual diffracted lines have anomalous positions; (3) calculated strain-indices have strongly negative values even though the samples are non-perthitic and should not be strained (Woodard 1972; Sibley 1978; Ali & Turner 1982; Martin 1982; Černý & Chapman 1984, 1986; Martin & Falster 1986; Marshall *et al.* 1986; Dong & Morrison 1995). The relations between anomalous chemical composition and anomalous cell parameters need to be established because of the significance of adularia in the characterization of Or_{100} end-member high sanidine (Ch. 5.2).

Of the low-temperature sanidine samples examined in this thesis, the Or_{100} adularia from Tanco is of particular structural interest. Because its average structure corresponds to that of end-member high-sanidine, its complex optical features must result from processes of primary growth. Twinning in low-

temperature K-feldspar is usually a feature of primary growth, rather than a result of transformation twinning from a higher-symmetry precurser (Akizuki & Sunagawa 1978). In samples with less disorder, locally variable optics (Černý & Chapman 1984) and linear structural features observable by TEM (Worden & Rushton 1992) might also be attributed to variation in structural state. In the case of the end-member high-sanidine, variable optics may also result from simultaneous growth of adjacent areas which are slightly misaligned (Worden & Rushton 1992).

The precipitation of largely monoclinic and (Al,Si)-disordered adularia under low-temperature conditions in granitic pegmatites has been previously thought to occur rapidly as a result of a pressure-release event (Foord & Martin 1979; Martin & Falster 1986; Černý & Chapman 1984, 1986). In the pressure-release hypothesis, vapour-saturated miarolitic cavities rupture, and the drastic reduction in water pressure induces rapid nucleation and growth of precipitates on cavity surfaces. The hypothesis is consistent with the observation that adularia with the finest grain-size and a sheaf-like radiating growth structure tends to have the highest degree of (Al,Si) disorder (Černý & Chapman 1986; Dong & Morrison 1995). Such a feldspar crystallizing in the stability field of low microcline may have a higher degree of disorder than K-feldspar phenocrysts from volcanic rocks (*e.g.*, adularian end-member Or_{100} high sanidine; Ferguson *et al.* 1991). In order to preserve the structural state, it has been proposed that the feldspar must be shielded from order-promoting agents such as H_2O or alkaline fluids.

These special conditions, one to generate disordered K-feldspar, the other to preserve its structure, are probably necessary if the feldspar crystallized at a high enough temperature such that post-crystallization (Al,Si)-ordering was possible. On the other hand, feldspar grows readily in diagenesis, and is one of the first minerals to form in clastic sediments during burial at 25-60°C and 5-100 bar (Ali & Turner 1982). Diagenetic K-feldspar usually crystallizes as the disordered monoclinic polymorph, and rarely as triclinic intermediate-to-high microcline, because disordered crystals have a simpler growth mechanism than ordered crystals (Worden & Rushton 1992). The growth of ordered phases is necessarily a more complex process than the growth of disordered phases. At low temperature, an additional controlling factor for (Al,Si) order is the atomic arrangement exposed on the growth surface, so that certain zones may be more ordered than others (Akizuki & Sunagawa 1978). At conditions far from equilibrium, the interactions at a mineral surface are controlled by crystallization kinetics. The distinct low-temperature morphology of K-feldspar results from a mechanism of growth which differs from that at high temperature.

The suggestion that a high growth rate is responsible for (Al,Si)-disorder in adularia is somewhat misleading. Under conditions of metastable growth, equilibrium will not be attained if the rate of species attachment (crystal growth) greatly exceeds the rate of detachment (dissolution). On the surface of a growing crystal, the attachment energy of an incoming species depends on its interactions with the surface structure (*cf.* review of Smith 1994). If the attachment energy is

low, the probability of detachment increases and the residence time for species such as Na, Ca or Cl at the surface is low. If the growth rate is high, the probability of permanent attachment of an unfavourable arrangement with a slightly lower attachment energy than ideal is increased. The growth rate is not an absolute value, but must be expressed relative to the attachment/detachment rate: as such, it is strongly dependent on temperature, surface structure and speciation. At very low temperature, virtually any growth rate is too high relative to the energy barrier of surface-structural rearrangement, and hydrated molecular complexes of Al^{3+} and Si^{4+} will require a catalyst for structural reorganization so that Al attaches to an exposed T_1 site in preference to Si.

Aluminate and silicate solutions have been well studied, and at a given pH, one can predict what species will be present. At high pH, aluminate solutions have only one type of ion, the $Al(OH)_4^-$ monomer. Toward neutral pH, polymeric ions appear, and then ultimately give way to $Al(H_2O)_6^{3+}$ in acid conditions. In contrast, silicate monomers form in acid to neutral conditions, but at higher pH, polymeric ions form readily. Chains larger than the trimer are rare, whereas rings and cages are the preferred form of the polymerized silicate species; 4-membered rings are particularly common. In aluminosilicate solutions, aluminum preferentially complexes with the largest silicate polymers. Rearrangement in response to dilution or increased alkalinity occurs by breaking Si-O-Si bonds in preference to Al-O-Si bonds which are not normally cleaved in alkaline solution. The rate of polymer rearrangement depends primarily on pH, but also on the

identity of the alkaline cation; the rate decreases from Na to Cs (Harvey & Glasser 1989).

Low-temperature synthesis of K-feldspar from solutions and gels indicates that the feldspar inherits the fully disordered (Al,Si) arrangement of the aluminosilicate complexes (Flehmig 1977). (Al,Si) order of K-feldspar increases slightly with increased total alkalinity (proton-accepting capacity) and with increased pH (Martin 1974). Among the nucleophiles which catalyse aluminosilicate polymer rearrangement, the most geologically-important are the hydroxide, fluoride and carbonate anions. Authigenic K-feldspar is always disordered, with the exception of untwinned microcline which forms by diagenesis of carbonate rocks (*e.g.*, Kastner 1971). Altered K-feldspar is usually more-ordered than clear K-feldspar, and feldspar associated with calcite or fluorite tends to be highly ordered (Černý & Chapman 1986, Dong & Morrison 1995). These results are confirmed here: the salmon-coloured adularia associated with fluorite (± calcite) at the Rubellite pegmatite (Ch. 4.3) is highly ordered, whereas high-sanidine at other localities (*e.g.*, High Grade Dyke) is not accompanied by F^- or CO_3^{2-} phases. It is common that the original disordered state of adularian K-feldspar is preserved because temperatures are too low for (Al,Si)-ordering, even on a geological time-scale and in the presence of abundant H_2O (Černý & Chapman 1984, Martin & Falster 1986).

6.5 *Crystal chemistry*

A key feature of accurate mineral analysis is the use of accurate standards with well-defined precision. An excellent check on accuracy is the formula of the standard, which must agree with the stoichiometry indicated by the crystal structure. In turn, this requires that the crystal chemistry of that structure type be properly understood. If this is the case, we may require that the standard composition give the exact stoichiometry of the structure on calculation of the mineral formula of the standard. Analysis of well-characterized minerals of similar composition provides a further check on the composition of this standard: this should provide average mineral formulae of correct stoichiometry, varying only in a random fashion within the precision of the analysis. If this is the case for a specific standard, then subsequent analysis of similar minerals that show significant deviation from ideal stoichiometry indicates a crystal-chemical feature of the structure that is not currently incorporated in the structural model of that mineral. Examination of the deviation(s) of the mineral from ideal stoichiometry may allow identification of the relevant substitution mechanism(s).

If the composition of a mineral is well constrained by chemical analysis, then minor deviations from the ideal formula which are due to analytical error may be eliminated. If the mineral has suitable characteristics of homogeneity, adequate grain size and freedom from inclusions, it may be used as a standard. The accuracy of this well-established standard may then be checked by analysis of

other well-characterized minerals, if they have a similar matrix. In this thesis, I have demonstrated the utility of this approach and have prepared an internally consistent set of alkali aluminosilicate standards of $Z<22$ including leucite, jadeite, diopside, kyanite, tugtupite, $Rb_2ZnSi_5O_{12}$ and members of the scapolite and feldspar groups. As far as K-feldspar is concerned, Eifel sanidine shows excellent characteristics as a standard, with ideal compositional homogeneity indicated by the lack of correlations between elements determined from multiple analysis. Subsequent analysis of unknown feldspars (Ch.4) reveals the following features of crystal chemistry:

(1). The overall conformation of the analytical results (Ch. 4) to the feldspar formula indicates that the composition of the standard is accurate. Multiple analysis of gem orthoclase from the White Queen Mine (Ch. 3.7, Table 3.19) gives similar compositional ranges and standard deviations as the Eifel sanidine. However, larger ranges are found in the compositions of the Ch. 4 feldspars (largely microcline), particularly for the *M*, *T* and oxide sums, and even for samples in which mean values of M^+ and TO_2^- are equal. Average oxide sums tend to be less than 100. Increased scatter of results which occurs independently of any particular substitutional mechanism is attributed to overlap of the analysed volume with microinclusions. Microporosity is negligible in gem feldspar, but fluid-filled micropores occupy up to 4 vol.% (but typically 1.5%) of turbid feldspar and have a population density of up to 10^9 mm^{-3} (Walker *et al.* 1995).

The presence of micro-inclusions of a non-feldspar mineral within the analysed volume may be recognized by non-stoichiometric deviations from the ideal formula. Analysis of red adularia from the Tanco pegmatite gave locally anomalous results attributed to the presence of micro-inclusions of an Fe-rich phase. Whereas the analytical total was near 100 wt.%, Si contents do not agree with the expected sum of monovalent cations, and ΣT values range up to 4.1 *apfu* (Ch. 4.1).

(2) The difficulties encountered during characterization of K-feldspar standards were in part due to variable and widespread substitution of up to 5 mol.% $\square Si_4O_8$. This substitution was unknown in microcline prior to this work.

Substitution of up to 8 mol.% $\square Si_4O_8$ has been recorded in natural and synthetic plagioclase (Muramaki *et al.* 1992, Beaty & Albee 1980). Grew *et al.* (1993) reported Si-excess compositions for reedmergnerite: decrease in Na+B is coupled with increase in Si, giving a range of Si from 2.91 to 3.06 *apfu*; this was suggested to be due to either a systematic error or a real but undefined compositional trend, and is unconvincing as a proof of $\square Si_4O_8$ substitution. Up to 3.10 Si *apfu* has been found in Fe- and Mg-rich sanidine (Smith & Franks 1986). Potential $\square Si_4O_8$ substitution of 4-5 mol.% has been suggested in ferrian high sanidine (Linthout & Lustenhouwer 1993, Kuehner & Joswiak 1996), but because the formulae of these samples are complicated by substitution of Fe, Mg and Ti, other substitutional mechanisms are possible (*e.g.*, $\square MgSi_3O_8$). However,

if the overall composition is constrained to near-end-member K-feldspar, free from Fe and divalent cations, the viability of the $\square Si_4O_8$ substitution is more convincingly demonstrated.

Distinct compositional trends for the $\square Si_4O_8$ substitution were found in most generations of feldspar from Morrua, Luolamāki, Elba, High Grade Dyke and Tanco. The substitution seems to be widespread in feldspar from complex granitic pegmatites. It also occurs in low-temperature disordered monoclinic adularia which formed as a metastable species. It is possible that primary magmatic feldspar also had far more vacancy + excess-Si than is currently found in microcline, but that SiO_2 was lost with decreasing temperature or during the reconstructive microcline-forming phase-transformation. If Si-excessive compositions allow occupancy of the *M*-site by a few mol.% H_2O, this could internally catalyse the sanidine → microcline transition and explain the tendency toward complete conversion of sanidine to microcline in most granitic pegmatites. This substitution provides a mechanism for the suggestion of Waldron *et al.* (1993) that the transformation might be aided by water exsolved from the feldspar structure and not entirely externally introduced.

(3). The $(AlP)Si_{-2}$ (berlinite) substitution has been suggested as the principal mechanism of P incorporation in alkali feldspar. Departures of P/(Al-1) from values of unity might imply non-stoichiometry related to vacancy-generating defects (London 1992b), but the data available to date have been of insufficient

accuracy for verification. In this thesis, K-feldspar with up to 2.0 wt.% P_2O_5 was analysed corresponding to 0.08 P *apfu* and verifying the berlinite mechanism (Ch. 3.7). Phosphorus has a patchy distribution in K-feldspar. London (1992b) suggested that this is due to local heterogeneity of P in the melt in which the feldspar grew. A more viable explanation is that the heterogeneity results from the fluid-catalysed reconstructive nature of the feldspar phase-transitions. In contrast to the work of London (1992b), I found abundant fine-grained apatite in association with albite and microporous areas, suggesting influx of Ca. The porous blocky feldspar also had a patchy distribution of Ba and Sr, increasing in the later generations; this can also be taken as evidence for the influx of wall-rock-derived fluids. Compositional trends for P-rich feldspars indicate no significant deviation from the berlinite substitution. The principal deviation from stoichiometry is the possible incorporation of light-element *M*-cations in P-rich K-feldspar.

(4). The presence of light-element substitution can be recognized at values greater than 1 at.% (the EMP "detection limit"). I found no evidence for substitution of B in any of the feldspars I examined. EMP analysis of Na-, H- and Li-exchanged samples of Eifel sanidine, previously characterized by EMP and bulk-chemical analysis, infrared spectroscopy and crystal-structure refinement (Behrens & Müller 1995, Deubener *et al.* 1991, Paulus & Müller 1988, Müller 1988), suggests that calculated values of light-elements may be accurate to within 5 at.% relative (Ch. 4.1, Table 4.3). In most samples of feldspar, light-element

substitution does not exceed 0.01 *apfu*; however, up to 4 at.% *M*-cation deficiency was recorded in P-bearing feldspar and later generations derived therefrom. Analysis of intermediate microcline from Red Cross Lake gives good agreement with a measured value of Li of only 0.02 *apfu* (Table 3.2, Table 3.8, Table 4.10, Fig. 4.35). Compositions of adularia from the Tanco pegmatite indicate up to ~16 at.% light-element substitution (Fig. 4.3 and Table 4.2).

(5). The data presented in this thesis populate most of the series from $KAlSi_3O_8$ to $RbAlSi_3O_8$ and show that compositions in the range 50 to 70 mol.% Rb-feldspar are rather common (a summary is given in Table 6.2). Without exception, the Rb-enriched part of the series (with greater than ~10 mol.% Rbf) is Ca-free with negligible to undetectable contents of Na, Sr, Ba, Fe or P at all localities and for all types of (Rb,K)-feldspar - blocky, vein and adularian. The only persistent minor element is Cs, in almost all cases positively correlated with Rb, present to a maximum of 0.03 *apfu* (~1.5 wt.% Cs_2O, the highest recorded for a feldspar). The Rb-poor part of the series is Ca- and Fe-free but has minor Na_2O or P_2O_5 (both $\leq$ ~0.5 wt.%), and SrO or BaO (both $\leq$ ~0.2 wt.%). K-feldspar with high values of Na (or P) is thought to represent compositions closer to that of the original primary phase than feldspar with lower Na values. Nevertheless, exsolution of albite is largely complete, and Rietveld refinement indicates the presence of albite even though EMP analysis indicates <0.5 wt.% Na_2O, so that the Na values represent "bulk" analysis including fine-grained albite, potentially cryptoperthite (Ch. 5).

Table 6.2: Rb_2O content of the K-phase of microcline precursors and of the late (K-Rb)-feldspars from pollucite-bearing pegmatites.

Locality	wt.% Rb_2O in blocky and vein microcline: mean (range)	maximum Rb of late feldspars: Rb_2O wt.%	Rbf mol.%
Tanco, Manitoba	2.68 (2.0-3.2)	3.52	11
	3.25 (1.8-8.3)	*24.84*	*84*
Red Cross Lake, Manitoba	4.94 (4.0-6.0)	6.13	19
		24.37	83
High Grade Dyke, Manitoba	*3.21 (2.0-4.0)*	*23.46*	*78*
		24.07	82
Tot Lake, Ontario	2.77 (1.8-4.3)	6.65	20
		16.32	53
Rubellite Dyke, Ontario	3.44 (2.8-4.9)	13.44	43
		22.00	74
Valor, Quebec		8.86	27
Tamminen quarry, Greenwood, Maine	*1.24 (0.6-1.8)*	*1.87*	*7*
Old Tom quarry, Greenwood, Maine		13.33	42
Norway 1, Maine	0.66 (0.5-0.8)	0.80	2
		2.29	7
Norway 2, Maine	*1.24 (0.6-1.8)*	*1.78*	*6*
		2.29	8
Walden, Connecticut		2.24	8
Leominster, Massachusetts		0.47	2
Tin Mountain, South Dakota		19.24	64
Himalaya Mine, California		3.45	11
Viitaniemi, Finland	*0.68 (0.6-0.7)*	*0.77*	*3*
		2.08	6
Luolamäki, Finland	*3.33 (1.5-5.9)*	*26.02*	*89*
		20.95	70
Nyköpingsgruvan, Utö, Sweden		10.09	31
Susice, Czech Republic (CR)		0.24	1
Nová Ves u Českého Krumlova (CR)	0.71	0.71	3
La Speranza, Elba, Italy	*1.98 (0.9-3.4)*	*25.48*	*87*
		22.70	75
Kola Peninsula, Russia	*8.25 (6.5-9.2)*	*9.80*	*31*
		26.12	87
Eastern Siberia, Russia	2.37	2.37	7
Mongolian Altai #1, China	*2.04*	*2.04*	*7*
Mongolian Altai #3, China		1.19	4
Mongolian Altai #83, China	1.51 (1.3-1.7)	1.73	6
Morrua Mine, Mozambique		19.81	66
Bikita, Zimbabwe		9.57	28
Benson #1, Zimbabwe	3.60 (2.8-4.4)	4.45	15
Helikon, Namibia	1.12 (1.1-8.5)	8.55	27
		6.02	19
Ambatofinondrahana, Madagascar	*0.77*	*0.77*	*3*
		1.26	4

The K-phase of blocky and *vein* microcline and their Rb-enriched derivatives are indicated by normal type and *italics*, respectively; adularian (K-Rb)-feldspar is indicated by boldface.

6.6 *Reactions of (K-Rb)-feldspar*

Primary blocky (K,Na,Rb)-feldspar from the interior zones of highly fractionated pegmatites originally had more Na and a lower K/Rb ratio than is currently observed in the microcline phase of perthite. In the samples analysed in this study, the separation of albite from its host is largely complete, and perthite lamellae are commonly replaced by K-feldspar or coarsened into irregular trains of granular albite. In general, albite may even migrate beyond the confines of the present K-feldspar crystals. The principal reaction involving Rb (noted in blocky K-feldspar which has less than about 2 wt.% Rb_2O) is a patchy compositional heterogeneity on a scale of a few μm. The patchy composition could result from local solution-redeposition during the H_2O-catalysed reconstructive transformation from sanidine or orthoclase to microcline, rather than to exsolution, because P_2O_5 also has a patchy distribution on this scale. However, in slightly Rb-richer microcline ($\geq \sim$2-4 wt.% Rb_2O), local formation of diffuse veins of Rb-enriched feldspar, parallel to the cleavage of the host and in association with albite, are attributed to processes of exsolution of Rb-rich feldspar (Fig. 4.13A, B, C, Lilypad Lakes; Fig. 4.22B, High Grade Dyke). Diffuse compositional gradients suggest structural coherency of the Rb-enriched feldspar and its host (typically microcline). Well-developed microporosity and the formation of Rb-depleted K-feldspar near grains of albite provide ample evidence for interaction with fluid. Textural coarsening of albite and (Rb,K)-feldspar was probably fluid-assisted.

Veins of non-perthitic (K,Rb)-feldspar in pollucite, largely Na-poor but typically with up to ~5 wt.% Rb_2O, probably formed in the stability field of microcline. However, most veins exhibit tartan twinning, indicating transformation from a monoclinic precurser rather than direct precipitation of microcline. They must have transformed and exsolved Rb-enriched feldspar shortly after crystallization of the (Al,Si)-disordered primary phase. Textural evidence suggests that the nucleation, exsolution and coarsening of potassian Rb-feldspar followed that of albite. (Rb,K)-feldspar locally shows compositional gradients with its host (Fig. 4.16A, Luolamäki; 4.22C, High Grade Dyke), suggesting structural coherency. However, in most cases the textural evidence at the scale of BSE imaging (*i.e.*, sharp phase boundaries) suggests that Rb-feldspar forms a distinct phase (Fig. 4.16B, C, D, Luolamäki). TEM analysis shows that the Rb-rich feldspar at Elba is structurally coherent with host microcline, even though BSE imaging shows a sharp phase boundary (Fig. 4.18).

An exsolution origin for (Rb,K)-feldspar grains in microcline is suggested by its typical occurrence near grains of mica, quartz or albite. The thin veinlets of Rb-feldspar which occur in pollucite-veining microcline from Tanco and Luolamäki probably also exsolved from the host (K,Rb)-feldspar. Zones of structural weakness may provide suitable sites for nucleation of Rb-feldspar. Deuteric alteration is likely responsible for subsequent coarsening of exsolution textures.

Reaction of early K-feldspar with late fluids is locally intense and should probably

be considered hydrothermal rather than deuteric (as defined by Brown & Parsons 1994). Textural evidence suggests that the breakdown of (K,Rb)-feldspar to an assemblage of highly porous K-feldspar + Rb-feldspar occurs by solution-reprecipitation from early (K,Rb)-feldspar at low temperature in the presence of fluids. Such reactions are abundant in High Grade Dyke microcline, but also occur locally at Tanco (Fig. 4.20F) and Red Cross Lake (Fig. 4.27C). The proportions of K-feldspar and (Rb,K)-feldspar suggest local derivation from a Rb-bearing host; there is no particular evidence for widespread long-range migration of a Rb-rich aqueous fluid.

End-member K-feldspar, zoned sequences of (K-Rb)-feldspar solid-solution compositions and an assemblage of coprecipitated K-feldspar + Rb-feldspar were also generated in a period of hydrothermal alteration which affected both microcline and pollucite. The association of late feldspar with cookeite (± apatite, quartz, calcite, fluorite, clay minerals) indicates a low-temperature origin. K-feldspar replaces other minerals as well (*e.g.*, lithium aluminosilicates); however, in these cases, Rb-rich feldspar is not generated, indicating that the hydrothermal solutions were not a source of Rb. Reaction of hydrothermal fluid with Rb-bearing phases was responsible for generation of the assemblages. In some cases, veining by (Rb,K)-feldspar indicates that exsolution processes were operative (or the (Rb,K)-feldspar precipitated along fractures), but the typical preservation of K/Rb zoning in adularian (K-Rb)-feldspar indicates that, in these cases, the temperature was too low for extensive solid-state alkali diffusion. In

the final stages of reaction, only end-member K-feldspar was precipitated.

6.7 *Ordering and exsolution processes*

Primary monoclinic (K,Na,Rb)-feldspar presumably inherited a highly disordered (Al,Si) distribution from the pegmatitic melt, which by definition has long-range disorder. The monoclinic → triclinic change of symmetry is due to rapid (Al,Si)-ordering at ~450°C rather than to framework collapse (*i.e.*, maximum microcline and high sanidine have near-identical cell volumes), and in Or-rich feldspar, the (Al,Si)-ordering precedes exsolution (Brown & Parsons 1989). The subsolidus transformation stage of feldspar evolution in igneous rocks, characterized by formation of the orthoclase tweed texture and coherent albite microlamellae (Brown & Parsons 1994), must occur immediately upon consolidation of the late interior zones of complex rare-element pegmatites. The low-temperature deuteric alteration stage, characterized by "unzipping" of coherent microstructures and formation of microcline, then leads to essentially isochemical coarsening of twin domains and extensive strain-free phase separation of exsolved feldspars (Brown & Parsons 1994). In an H_2O-rich environment, the symmetry transformation might not be energetically stranded at the orthoclase stage; continued coarsening of the adjacent ordered and anti-ordered unit-cell-size triclinic domains could lead directly to microcline (Brown & Parsons 1989). The microcline-forming phase transformations occur dominantly by solution-reprecipitation at $T < 500°C$ (Waldron *et al.* 1993). The transformation generates

turbid permeable K-feldspar with abundant fluid-filled micropores with the adularia form (Walker *et al.* 1995).

The emplacement of a small body of granitic-pegmatite magma into a relatively cool host rock leads to rapid crystallization and subsequently to a time-compressed subsolidus-transformation stage. High activity of H_2O leads to an intense deuteric-alteration stage with large-scale phase separation, making it difficult to establish the original feldspar textures and composition. In granitic pegmatites, not only are the microcline-forming phase transformations commonly driven to near-completion, but coarsening of twin domains occurs to the extent that microcline appears untwinned, segregation of albite progresses far beyond recognizable perthitic textures, and "micro"pores are visible by routine microscopy or even in hand specimen. In many cases, the isochemical nature of the deuteric-alteration stage is highly questionable (isotopic compositions and trace element abundances are extensively disturbed, *e.g.*, Walker *et al.* (1989b), and the deuteric alteration may be transitional into hydrothermal alteration (as defined by Brown & Parsons 1994).

The occurrence of near-maximum microcline with 16 mol.% Rbf at Red Cross Lake and low-to-intermediate microcline with 26 mol.% Rbf at Kola Peninsula indicates that ordering proceeds in Rb-rich K-feldspar to the same extent as in Rb-poor K-feldspar (Černý *et al.* 1985). It is possible that the large Rb^+ ion sterically hinders (Al,Si)-ordering, but this would only reduce the rate of

ordering. It is significant that the feldspar from these two Rb-rich localities shows minimal evidence for subsolvus reequilibration, whereas at all other (Rb-poorer) localities, the widespread occurrence of Rb-feldspar in microcline and the two-phase assemblage of Rb-feldspar + K-feldspar suggest a compositional gap at low temperature. If exsolution generated the Rb-feldspar, the primary composition must have been higher in Rb than the present composition of the microcline. The Red Cross Lake and Kola Peninsula feldspars differ from the feldspar at most of the other localities investigated in that significant $\square Si_4O_8$ substitution is not detected. It is reasonable to propose that rates of alkali diffusion are greater in feldspar with a few per-cent vacancy than in vacancy-free feldspar, due to vacancy migration.

Substitution of $\square Si_4O_8$ is probably responsible, in part, for the extensive phase separation of albite from K-feldspar in granitic pegmatites. As far as the rather complete conversion of disordered primary phases to microcline is concerned, it is proposed that the vacant fraction of the *M*-site may be occupied by molecular H_2O. It has been long established that the presence of H_2O is necessary for the orthoclase → microcline transition. H_2O in the feldspar structure would have a profound effect on the rate of (Al,Si)-ordering and lead to a rather complete conversion to microcline, as found in granitic pegmatites. In the reconstructive process, "excess" Si is not exsolved in the form of quartz from the feldspar and evidence for $\square Si_4O_8$ is preserved in microcline. No diffraction peaks of quartz were found in XRD-patterns of feldspar with $\square Si_4O_8$ substitution.

Experimental measurement of partition coefficients for Rb between feldspar and peraluminous melt gives values near 1.0 (Icenhower & London 1996) and agree with values measured for natural sanidine in Rb-rich rhyolitic melt (0.8, Congdon & Nash 1991). Values are lower in aqueous solution at lower temperature (0.26 at 400°C/1kbar, Volfinger (1976); 0.28 at 180°C/1kbar, Pauwels *et al.* (1989)). At very low temperature, our observations indicate that Rb is excluded from Or_{100} sanidine and forms separate (Rb,K)-feldspar phase (*e.g.*, at High Grade Dyke). The possibility of a solvus is indicated by positive values for the Gibbs free energy of mixing of (K-Rb)-feldspar determined experimentally by Lagache & Sabatier (1973). End-member K-feldspar coprecipitates in equilibrium (presumably strain-free) textures with ~80 mol.% Rb-feldspar at ~250-150°C. Compositions in the range 50-70 mol.% Rbf are rather common and show zoning and/or patchy K/Rb distributions indicative of disequilibrium crystallization. The solvus must crest at $T < 400°C$ because experimental evidence shows continuous solid solution at and above this temperature (Volfinger 1976, Lagache 1984, Ghelis & Gasperin 1972). Data are not available at lower temperature because of the extreme sluggishness of reactions (M. Lagache, pers. comm. 1994). The low temperature of the process is in agreement with the typical low-temperature hydrothermal character of associated minerals such as cookeite, calcite, fluorite, cesian analcime and bavenite, and is constrained by its placement in the alteration sequence of pollucite extending to $T < 100°C$ (Teertstra & Černý 1995).

6.8 *New members of the feldspar group*

As noted in the introduction and documented throughout Ch. 4, two new species should be added to the feldspar group: rubicline, the rubidium analog of microcline, and rubidine, the proposed rubidium analogue of sanidine. Rubicline is the first mineral with Rb as an essential constituent. Both species occur as small blebs and veinlets in K-feldspar and have a similar compositional range along the series $KAlSi_3O_8$ - $RbAlSi_3O_8$. Both are widespread minerals occurring in the interior zones of complex-type rare-element pegmatites, associated with pollucite and Rb- and Cs-rich micas, albite, quartz, cookeite and apatite. A typical grain-size of less than 20 μm, extending to $\leq$50 μm, precludes meaningful characterization of most physical and optical properties by routine methods, including streak, hardness, fracture, density, refractive indices, 2V or dispersion. Its small grain-size and similarity to microcline in thin section and in X-ray powder diffraction probably hindered its earlier identification. By electron microprobe, the EDS Rb $L\alpha$ peak is hidden under Si $K\alpha$, leaving only WDS analysis and BSE imaging as methods of detection.

For Rb-feldspar occurring in microcline, diffuse compositional gradients suggest structural coherency of the (Rb,K)-feldspar and imply structural coherency with the host microcline (Fig. 4.13C, 4.16A, 4.20D). In thin and polished sections, cleavage passes through both the host microcline and the exsolved rubicline. Thus

by analogy with microcline the cleavage is {001} perfect, {010} good. Structural coherency hinders manual separation of phases. Rubicline is colourless. From the grains positively identified in thin section, the relief is higher than that of the adjacent microcline, the birefringence is low (first-order grey interference colours) and the crystals are apparently untwinned. Refractive indices are slightly higher than those of the host microcline, as determined by Becke-line tests in thin section.

For rubidium feldspar occurring in untwinned adularian sanidine, optical continuity of the zoned (K-Rb)-feldspars suggests structural coherency resulting from parallel to subparallel growth (Fig. 4.7A, B, 4.10D, 4.16F). Rb-feldspar also occurs as fine-grained clustered aggregates in Or_{100} adularia associated with cookeite and apatite ($\pm$ albite, quartz) (Fig. 4.22D, E, F). The Rb-feldspar is probably as disordered as its host, which extends compositionally to end-member adularian high sanidine (*e.g.*, High Grade Dyke).

CHAPTER 7

CONCLUSIONS

(1) Late low-temperature fine-grained Rb-feldspars were found in 12 highly fractionated pollucite-bearing pegmatites, and K-dominant but Rb-rich feldspars were studied from an additional 21 localities. These represent the first mineral(s) with Rb as an essential constituent. Paragenetic considerations indicate that (Rb,K)-feldspars may be present at a much greater number of rare-element pegmatites worldwide, particularly in association with pollucite.

(2) Compositions of the feldspars lie close to the join $KAlSi_3O_8$ - $RbAlSi_3O_8$, with up to 26 wt.% Rb_2O (91 mol.% Rbf) and 1.5 wt.% Cs_2O (3 mol.% of a hypothetical Csf component). Na and Ca contents are negligible, and the main deviation from ideal stoichiometry is due to a few per cent $\square Si_4O_8$ and light-element *M*-cation substitutions. Mineral compositions are constrained to within 2% accuracy by using internally consistent standards with stoichiometry compatible with their structural formulae.

(3) Although verified as feldspar phases, the structural state of most samples of Rb-dominant feldspar cannot be measured due to small grain-size. Approved mineral names will become available for the Rb-analogs of monoclinic sanidine and triclinic microcline for a few localities. However, samples can be generally

named on the basis of chemical composition: K-feldspar as commonly used for alkali feldspars containing mainly K in the *M*-site; rubidian K-feldspar for Rb-bearing to Rb-rich K-feldspar with Rb < K; (potassic) Rb-feldspar for (Rb,K)-feldspar with Rb ≥ K.

(4) Rubidium feldspars occur in three associations: (1) in blocky microcline (-perthite) of internal pegmatite zones commonly adjacent to pollucite bodies; (2) in late veins of non-perthitic microcline crosscutting pollucite; (3) in adularian feldspar metasomatic after microcline and pollucite. Rubidium feldspars are formed by three genetic mechanisms: (1) exsolution from Rb-bearing K-feldspar precursors; (2) reequilibration by local solution-reprecipitation of (K,Rb)-precursors; (3) direct crystallization of adularian (K-Rb)-feldspar.

(5) The occurrence of Rb- and Cs-rich-to-dominant micas and clay minerals, and a complex internal zoning history of cesian analcime, indicate widespread chemical activity of Rb and Cs under subsolidus conditions. Characteristic sequences of alteration of pollucite, petalite and spodumene, of leaching cavities, and sequences of crystallization in gem- and zeolite-bearing clay-filled pockets, all indicate that hydrothermal wallrock-derived fluids have negligible influence on the internal evolution of late pegmatite fluid except at very low temperature. The micas need additional characterization as new mineral species. The clays need TEM-scale identification as they are significant to the containment of nuclear

waste and its fate in contaminated soils.

(6) Exsolution typically operates in early (K,Rb)-feldspars which display $\square Si_4O_8$ substitution, followed by coarsening assisted by deuteric processes. Structural coherency of the exsolved Rb-dominant phases with the triclinic host is definite in one case and strongly suggested in others. The exsolution is promoted by migration of *M*-site vacancies, and (Al,Si)-ordering is possibly catalysed by partial occupancy of $\square$ by molecular H_2O.

(7) Late-precipitating $Rbf_{\sim 80}$ adularian feldspars are probably as (Al,Si)-disordered as their Or_{100} disordered host. These occur as distinct phases due to the presence of a strain-free solvus in the Kf-Rbf system cresting at $T < 400°C$. Compositionally zoned feldspars in the range Rbf_{50} to Rbf_{70} are not infrequent, but are probably metastable because of slow Rb diffusion at low temperature. The mechanism of feldspar growth at low-temperature does not allow significant (Al,Si)-ordering except in the presence of a catalyst.

(8) Substitution of light elements, particularly in association with P substitution, needs to be verified by chemical analysis. For feldspar with substitution of $\square Si_4O_8$, potential occupancy of the *M*-site by H_2O needs to be verified. Rates of alkali-cation diffusion need to be measured for this feldspar and compared with those of ideal stoichiometric feldspar. There may be differences in composition

between orthoclase and microcline in typical granitic rocks if substitution of $\square Si_4O_8$ is related to the H_2O-catalysed reconstructive phase-transformation.

(9) Rietveld refinement of X-ray powder-diffraction data gives accurate cell parameters for feldspars. However, study by TEM is necessary to provide structural information on a local scale. The cell parameters *a* 8.591(1), *b* 13.047(2), *c* 7.170(1) , ß 115.97(1)° are closely representative of the structure and composition of Or_{100} end-member high-sanidine.

(10) The precision of EMP measurements at a 4-sigma level of confidence is about 1%. By using internally consistent standards with compositions compatible with stoichiometries of the structural formulae, minerals with a generally similar matrix may be analysed with $\leq 2\%$ accuracy. Systematic analytical error of a standard may be greatly reduced by examination of the results of analysis of closely-related minerals. If a standard is compositionally and structurally well-characterized, the accuracy of analysis of samples of near-identical composition may then approach 1% absolute. The bulk of the results, which give the expected stoichiometry of the structure, may be classified as normal, and anomalous measurements which do not conform to ideal feldspar stoichiometry may be identified.

REFERENCES

ABAD-ORTEGA, M. D. M., HACH-ALI, P.F., MARTIN-RAMOS, J.D. & ORTEGA-HUERTAS, M. (1993): The feldspars of the Sierra Albarrana granitic pegmatites, Cordoba, Spain. *Can. Mineral.* **31**, 185-202.

AKIZUKI, M. & SUNAGAWA, I. (1978): Study of the sector structure in adularia by means of optical microscopy, infra-red absorption, and electron microscopy. *Mineral. Mag.* **42**, 453-462.

ALI, A.D. & TURNER, P. (1982): A study of authigenic feldspars. *J. Geol.* **64**, 132-155.

BACHINSKI, S.W. & MÜLLER, G. (1971): Experimental determinations of the microcline - low albite solvus. *J. Petrol.* **12**, 329-356.

BAILEY, S.W. & TAYLOR, W.H. (1955): The structure of a triclinic potassium feldspar. *Acta Cryst.* **8**, 621-632.

BAMBAUER, H.U., KRAUSE, C. & KROLL, H. (1989): TEM investigation of the sanidine/microcline transition across metamorphic zones: The K-feldspar varieties. *Eur. J. Mineral.* **1**, 47-58.

BAMBAUER, H.U., KROLL, H., NAGER, H.E. & PENTINHAUS, H. (1974): Feldspar-mischkristalle - Eine übersicht. *Bull. Soc. fr. Minéral. Cristallogr.* **97**, 313-345.

BARKER, D.S. (1964): Ammonium in alkali feldspars. *Am. Mineral.* **49**, 851-858.

BARRER, R.M. & McCALLUM, N. (1953): Hydrothermal chemistry of silicates. Part IV. Rubidium and cesium aluminosilicates. *J. Chem. Soc.*

(London), 4029-4053.

BEATY, D.W. & ALBEE, A.L. (1980): Silica solid solution and zoning in natural plagioclase. *Am. Mineral.* **65**, 63-74.

BEGER, R.M. (1969): The crystal structure and chemical composition of pollucite. *Z. Krystallogr.* **129**, 280-302.

BEHRENS, H. & MÜLLER, G. (1995): An infrared spectroscopic study of hydrogen feldspar ($HAlSi_3O_8$). *Mineral. Mag.* **59**, 15-24.

BENNINGTON, K.O., BEYER, R.P. & JOHNSON, G.K. (1983): Thermodynamic properties of pollucite (a cesium-aluminum-silicate). *U.S. Bureau Mines Report of Investigations* **RI 8779**, 1-18.

BERAN, A. (1986): A model of water allocation in alkali feldspar, derived from infrared-spectroscopic investigations. *Phys. Chem. Minerals* **13**, 306-310.

BERNOTAT-WULF, H., BERTELMANN, D. & WONDRATSCHEK, H. (1988): The annealing behaviour of Eifel (Volkesfeld) sanidine III. The influence of sample surface and sample size on the order-disorder transformation rate. *Neues Jahrb. Mineral. Mh.* **11**, 503-515.

BLASI, A. & BLASI, C. DE POL (1994): Aspects of alkali feldspar characterization: Prospects and relevance to problems outstanding. *In* "Feldspars and Their Reactions" (I. Parsons, ed.) NATO-ASI series C, Mathematical and Physical Sciences, Reidel Publishing Company, 51-102.

BORUTSKAYA, V.L. (1975): Synthesis of various rubidium and cesium feldspars. *Dokl. Akad. Nauk SSSR* **222**, 924-927.

BREAKS, F.W. (1989): Origin and evolution of peraluminous granite and

rare-element pegmatites in the Dryden area, Superior Province of northwestern Ontario. Volumes 1 and 2. Unpublished Ph.D. thesis, Department of Earth Sciences, Carleton University, 1-594.

BRIETHAUPT, J.F.A. (1846): X. Neue Mineralien. 4 and 5. Kastor und Pollux. *Pogg. Ann.* **99**, 439.

BROWN, B.E. & BAILEY, S.W. (1964): The structure of maximum microcline. *Acta. Cryst.* **17**, 1391-1400.

BROWN, W.L., OPENSHAW, R.E., McMILLAN, P.F. & HENDERSON, C.M.B. (1984): A review of the expansion behaviour of alkali feldspars: Coupled variations in cell parameters and possible phase transitions. *Am. Mineral.* **69**, 1058-1071.

BROWN, W.L. & PARSONS, I. (1989): Alkali feldspars: Ordering rates, phase transformations and behaviour diagrams for igneous rocks. *Mineral. Mag.* **53**, 25-42.

BROWN, W.L. & PARSONS, I. (1994): Feldspars in igneous rocks. *In* "Feldspars and Their Reactions" (I. Parsons, ed.) NATO-ASI series C, Mathematical and Physical Sciences, Reidel Publishing Company, 449-499.

BRUNO, E. & PENTINGHAUS, H. (1974): Substitution of cations in natural and synthetic feldspars. *In* "The Feldspars" (W.S. Mackenzie & J. Zussman, eds.) University Press, Manchester, England, 574-609.

CAMPBELL, A.S. & FYFE, W.S. (1965): Analcime-albite equilibria. *Am. J. Sci.* **263**, 807-816.

ČERNÝ, P. (1972): The Tanco pegmatite at Bernic Lake, Manitoba. VIII. Secondary minerals from the spodumene-rich zones. *Can. Mineral.* **11**, 714-

726.

ČERNÝ, P. (1974): The present status of the analcime-pollucite series. *Can. Mineral.* **12**, 334-341.

ČERNÝ, P. (1978): Alteration of pollucite in some pegmatites of southeastern Manitoba. *Can. Mineral.* **16**, 89-95.

ČERNÝ, P. (1982): Mineralogy of rubidium and cesium. *In* Granitic Pegmatites in Science and Industry (P. Černý, ed.). *Mineral. Assoc. Can., Short Course Handbook* **8**, 149-161.

ČERNÝ, P. (1991): Rare-element granitic pegmatites. Part I: Anatomy and internal evolution of pegmatite deposits. *Geoscience Canada* **18**, 49-67.

ČERNÝ, P. (1994): Evolution of feldspars in granitic pegmatites. *In* "Feldspars and Their Reactions" (I. Parsons, ed.), NATO-ASI series C, Mathematical and Physical Sciences, Reidel Publishing Company, 501-540.

ČERNÝ, P. & CHAPMAN, R. (1984): Paragenesis, chemistry and structural state of adularia from granitic pegmatites. *Bull. Minéral.* **107**, 369-384.

ČERNÝ, P. & CHAPMAN, R. (1986): Adularia from hydrothermal vein deposits: Extremes in structural state. *Can. Mineral.* **24**, 717-728.

ČERNÝ, P., ERCIT, T.S. & VANSTONE, P.T. (1996): Petrology and mineralization of the Tanco rare-element pegmatite, southeastern Manitoba. Field Trip Guidebook A4, Geol. Assoc. Can., Mineral. Assoc. Can. Annual Meeting, Winnipeg, Manitoba, 1-63.

ČERNÝ, P. & MACEK, J. (1972): The Tanco pegmatite at Bernic Lake. V. Coloured potassium feldspars. *Can. Mineral.* **11**, 679-689.

ČERNÝ, P. & MACEK, J. (1974): Petrology of potassium feldspars in two lithium-bearing pegmatites. *In* The Feldspars (W.S. Mackenzie & J. Zussman, eds.). *Proc. NATO Adv. Study Inst.* (Manchester 1972). Manchester University Press, England 615-628.

ČERNÝ, P., PENTINGHAUS, H. & MACEK, J.J. (1985): Rubidian microcline from Red Cross Lake, northeastern Manitoba. *Bull. Geol. Soc. Finland* **57**, 217-230.

ČERNÝ, P. & SIMPSON, F.M. (1978): The Tanco pegmatite at Bernic Lake, Manitoba. X. Pollucite. *Can. Mineral.* **16**, 325-333.

ČERNÝ, P. , STANĚK, J., NOVÁK, M., BAADSGAARD, H., RIEDER, M., OTTOLINI, L., KAVALOVÁ, M. & CHAPMAN, R. (1995): Geochemical and structural evolution of micas in the Rožná and Dobrá Voda pegmatites, Czech Republic. *Mineral. Petrol.* **55**, 177-201.

ČERNÝ, P. , TEERTSTRA, D.K., CHAPMAN, R., FRYER, B.J., LONGSTAFF, F.J., WANG, X.-J., CHACKOWSKY, L.E. & MEINTZER, R.E. (1994): Mineralogy of extreme fractionation in rare-element granitic pegmatites at Red Cross Lake, Manitoba, Canada. *Int. Mineral. Assoc., 16th General Meeting, Pisa.* Abstracts, 406.

ČERNÝ, P., TRUEMAN, D.L., ZIEHLKE, D.V., GOAD, B.E. & PAUL, B.J. (1981): The Cat Lake - Winnipeg River and the Wekusko Lake pegmatite fields, Manitoba. *Man. Mineral. Res. Div. Econ. Geol. Rept.* **ER80-1** 1-240.

CHAKOUMAKOS, B.C. & LUMPKIN, G.R. (1990): Pressure-temperature constraints on the crystallization of the Harding pegmatite, Taos County, New Mexico. *Can. Mineral.* **28**, 287-297.

CLARK, G.S. (1982): Rubidium-strontium isotope systematics of complex

granitic pegmatites. *In* Granitic Pegmatites in Science and Industry (P. Černý, ed.). *Mineral. Assoc. Can., Short Course Handbook* **8**, 347-372.

CONGDON, R.D. & NASH, W.P. (1991): Eruptive pegmatite lava: rhyolite of the Honeycomb Hills, Utah. *Am. Mineral.* **76**, 1261-1278.

CORREIA NEVES, J.M. (1981): Pegmatitos Graniticos. Morphologia, Mineralogia, Geoquimica, Gênese, Metalogênese. Unpublished Ph.D. Thesis, Institute Geosciênces, Universidade Federal de Minas Gerais, A1-R23.

DANØ, M. (1966): The crystal structure of tugtupite - a new mineral, $Na_8Al_2Be_2Si_8O_{24}(Cl,S)_2$. *Acta Cryst.* **20**, 812-816.

DEUBENER, J., STERNITZKE, K. & MÜLLER, G. (1991): Feldspars $MAlSi_3O_8$ (M=H,Li,Ag) synthesized by low-temperature ion exchange. *Am. Mineral.* **76**, 1620-1627.

DINGWELL, D.B. (1989): The structures and properties of fluorine-rich magmas: A review of experimental studies. *In* Recent Advances in the Geology of Granite-Related Mineral Deposits, CIM Special Volume **39**, 1-12.

DOLLASE, W.A. & NEWMAN, W.I. (1984): Statistically most probable stoichiometric formulae. *Am. Mineral.* **69**, 553-556.

DONG, G. & MORRISON, G.W. (1995): Adularia in epithermal veins, Queensland: morphology, structural state and origin. *Mineral. Deposita* **30**, 11-19.

DUNN, P.J., NELEN, J.E. & NORBERG, J. (1978): On the composition of gem scapolites. *J. Gemmol.* **16**, 4-10.

EGGLETON, R.A. & BUSECK, P.R. (1980): The orthoclase-microcline

inversion: A high-resolution transmission electron microscope study and strain analysis. *Contrib. Mineral. Petrol.* **74**, 123-133.

EUGSTER, H.P. & McIVER, N.L. (1959): Boron analogues of alkali feldspars and related silicates. *Geol. Soc. Am. Bull.* **70**, 1598-1599.

FAUST, G.T. (1936): The fusion relations of iron-orthoclase, with a discussion of the evidence of the existance of an iron-orthoclase molecule in feldspars. *Am. Mineral.* **21**, 753-763.

FERGUSON, R.B., BALL, N.A. & ČERNÝ, P. (1991): Structure refinement of an adularian end-member high sanidine from the Buck Claim pegmatite, Bernic Lake, Manitoba. *Can. Mineral.* **29**, 543-552.

FLEET, M.E. (1992): Tetrahedral-site occupancies in reedmergnerite and synthetic boron albite ($NaBSi_3O_8$). *Am. Mineral.* **77**, 76-84.

FLEHMIG, W. (1977): The synthesis of feldspars at temperatures between 0°-80°C, their ordering behaviour and twinning. *Contrib. Mineral. Petrol.* **65**, 1-9.

FOORD, E.E. & MARTIN, R.F. (1979): Amazonite from the Pikes Peak batholith. *Mineral Rec.* **10**, 373-384.

FOORD, E.E., STARKEY, H.C. & TAGGART, J.E.Jr. (1986): Mineralogy and paragenesis of "pocket" clays and associated minerals in complex granitic pegmatites, San Diego County, California. *Am. Mineral.* **71**, 428-439.

FOWLER, A.D. (1990): Self-organized mineral textures of igneous rocks: The fractal approach. *Earth-Science Reviews* **29**, 47-55.

FRÝDA, J. & BREITER, K. (1995): Alkali feldspars as a main phosphorus

reservoirs in rare-metal granites: Three examples from the Bohemian Massif (Czech Republic). *Terra Nova* **7**, 315-320.

GASPERIN, M. (1971): Structure crystalline de $RbAlSi_3O_8$. *Acta Crystallogr.* **B27**, 854-855.

GHELIS, M. & GASPERIN, M. (1970): Evolution des paramètres dans le système $KAlSi_3O_8$ - $RbAlSi_3O_8$. *Compt. Rend. Acad. Sci.* **271**, 1928-1929.

GHELIS, M. & LAGACHE, M. (1972): Étude de l'equilibre entre les solutions hydrothermales et les feldspaths de la série $KAlSi_3O_8$ - $RbAlSi_3O_8$ à 600°C sous une pression de 1 kb. *Bull. Soc. fr. Minér. Crystallogr.* **95**, 157-158

GINSBURG, A.I. (1960): Specific geochemical features of the pegmatitic process. Int. Geol. Congress, 21st session Norden, Rep. **17**, 111-121.

GORDIYENKO, V.V. (1973): Cesium in lepidolite as an indicator of the cesium content in granitic pegmatites. *Dokl. Acad. Sci. USSR* **209**, 193-196.

GORDIYENKO, V.V. & KAMENTSEV, I.E. (1967): On the nature of the rubidium admixture in potassic feldspar. *Geokhimiya* **1967**, 478-481 (in Russian).

GORDIYENKO, V.V. (1976): Diagrams for prognostic evaluation of rare-element mineralization in granitic pegmatites utilizing compositional variations in potassium feldspar. *Dokl. Acad. Sci. U.S.S.R., Earth Sci. Sect.*, **228**, 442-444.

GREW, E.S., BELAKOVSKIY, D.I., FLEET, M.E., YATES, M.G., McGEE, J.J. & MARQUEZ, N. (1993): Reedmergnerite and associated minerals from peralkaline pegmatite, Dara-i-Pioz, southern Tien Shan,

Tajikistan. *Eur. J. Mineral.* **5**, 971-984.

HALLUM, M. & EUGSTER, H.P. (1976): Ammonium silicate stability relations. *Contrib. Mineral. Petrol.* **57**, 227-244.

HARLOW, G.E. & BROWN, G.E. Jr. (1980): Low albite: An X-ray and neutron diffraction study. *Am. Mineral.* **65**, 986-995.

HARVEY, G. & GLASSER, L.S.D. (1989): Structure and properties of aluminosilicate gels and solutions. *ACS Symp. Ser.* **398**, 49-65.

HASSAN, I. & GRUNDY, H.D. (1991): The crystal structure and thermal expansion of tugtupite, $Na_8[Al_2Be_2Si_8O_{24}]Cl_2$. *Can. Mineral.* **29**, 385-390.

HAUTEFEUILLE, P. & PERREY, A. (1888): Sur la préparation et les propriétés d'orthose ferrique. *Compt. Rend. Acad. Sci. Paris* **107**, 1150-1152.

HEALD, P., FOLEY, N.K. & HAYBA, D.O. (1987): Comparative anatomy of volcanic-hosted epithermal deposits: acid-sulphate and adularia-sericite deposits. *Econ. Geol.* **82**, 1-26.

HENDERSON, C.M.B. (1978): Thermal expansion of alkali-feldspars. II. Rb-sanidine and maximum microcline. *NERC Progress in Experimental Petrol. 4th report No.11*, 53-57.

HILL, R.J. & MADSEN, I.C. (1986): The effect of profile step width on the determination of crystal structure parameters by X-ray Rietveld analysis. *J. Applied Crystallogr.* **17**, 297-306.

HILL, R.J. & FLACK, H.D. (1987): The use of the Durbin-Watson *d*-statistic in Rietveld analysis. *J. Appl. Crystallogr.* **20**, 356-361.

HORSKY, S.J. & MARTIN, R.F. (1977): The anomalous ion-exchange behaviour of "ordered" orthoclase. *Am. Mineral.* **62**, 1191-1198.

HOVIS, G.L. (1988): Enthalpies and volumes related to K-Na mixing and Al-Si order/disorder in alkali feldspars. *J. Petrol.* **29**, 389-397.

HOVIS, G.L. (1989): Effect of Al-Si distribution on the powder-diffraction maxima of alkali feldspars and an easy method to determine *T*1 and *T*2 site occupancies. *Can. Mineral.* **27**, 107-118.

ICENHOWER, J. & LONDON, D. (1996): Experimental partitioning of Rb, Cs, Sr, and Ba between alkali feldspar and peraluminous melt. *Am. Mineral.* **81**, 719-734.

JAHNS, R.H. & BURNHAM, C.W. (1969): Experimental studies of pegmatite genesis; 1, A model for the derivation and crystallization of granitic pegmatites. *Econ. Geol.* **64**, 843-864.

JAHNS, R.H. & WRIGHT, L.A. (1951): Gem- and lithium-bearing pegmatites of the Pala District, San Diego County, California. *Calif. Div. Mines Spec. Rep.* **7A**, 1-72.

JAROSEWICH, E., NELEN, J.A. & NORBERG, J.A. (1979): Electron microprobe reference samples for mineral analyses. *Smithsonian Contrib. Earth Sci.* **22**, 68-72.

JOLLIFF, B.J., PAPIKE, J.J. & SHEARER, C.K. (1986): Tourmaline as a recorder of pegmatite evolution: Bob Ingersoll pegmatite, Black Hills, South Dakota. *Am. Mineral.* **71**, 472-500.

KASTNER, M. (1971): Authigenic feldspars in carbonate rocks. *Am. Mineral.* **56**, 1403-1442.

KENNEDY, J.J. (1938): The alkali metal cesium and some of its salts. *Chem. Revs.* **23**, 157-163.

KIMATA, M. (1977): Synthesis and properties of reedmergnerite. *J. Japanese Assoc. Mineral., Petrol. Econ. Geol.* **72**, 162-172.

KNEIP, H.-J. & LIEBAU, F. (1994): Feldspars with trivalent non-tetrahedral cations: Experimental studies in the system $NaAlSi_3O_8$ - $CaAl_2Si_2O_8$ - $LaAlSi_3O_8$. *Eur. J. Mineral.* **6**, 87-98.

KOHN, S.C., HENDERSON, C.M.B. & DUPREE, R. (1994): NMR studies of the leucite analogues $X_2YSi_5O_{12}$, where X=K,Cs,Rb; Y=Mg,Zn,Cd. *Phys. Chem. Minerals* **21**, 176-190.

KONTAK, D.J., MARTIN, R.F. & RICHARD, L. (1996): Patterns of phosphorus enrichment in alkali feldspar, South Mountain Batholith, Nova Scotia, Canada. *Eur. J. Mineral.* **8**, 805-824.

KROLL, H. & RIBBE, P.H. (1987): Determining (Al,Si) distribution and strain in alkali feldspars using lattice parameters and diffraction-peak positions. A review. *Am. Mineral.* **72**, 491-506.

KUEHNER, S.M. & JOSWIAK, D.J. (1996): Naturally occurring ferric iron sanidine from the Leucite Hills lamproite. *Am. Mineral.* **81**, 229-237.

KUZMENKO, M.V. (ed.) (1976): Rare-element granitic pegmatite fields (geochemical specialization and distribution). Nauka Moscow 1-332 (in Russian).

LAGACHE, M. (1984): The exchange equilibrium distributions of alkali and alkaline-earth elements between feldspars and hydrothermal solutions. *In* Feldspars and Feldspathoids (Wm. Brown, ed.). Reidel Publishing Company,

Dordrecht, 247-279.

LAGACHE, M. (1995): New experimental data on the stability of the pollucite-analcime series: Application to natural assemblages. *Eur. J. Mineral.* **7**, 319-323.

LAGACHE, M., DUJON, S.-C. & SEBASTIAN, A. (1995): Li-Cs pegmatite mineral assemblages in equilibrium with a fluid from their primary crystallization to their hydrothermal alteration: An experimental study. *Mineral. Petrol.* **55**, 281-290.

LAGACHE, M. & SABATIER, G. (1973): Distribution des éléments Na, K, Rb et Cs à l'état de trace entre feldspaths alcalins et solutions hydrothermales à 650°C, 1 kbar: données expéimentales et interpretation thermodynamique. *Geochim. Cosmochim. Acta.* **37**, 2617-2640.

LAGACHE, M. & QUÉMÉNEUR , J. (1997): The Volta Grande pegmatites, Minas Gerais, Brazil: An example of rare-element pegmatites exceptionally enriched in lithium and rubidium. *Can. Mineral.* **35**, 153-165.

LALONDE, A.E. & MARTIN, R.F. (1983): The Baie-des-Moutons syenite complex, La Tabatière, Quebec. I. Petrography and feldspar mineralogy. *Can. Mineral.* **21**, 65-79.

LEE, M.R., WALDRON, K.A. & PARSONS, I. (1995): Exsolution and alteration microtextures in alkali feldspar phenocrysts from the Shap granite. *Mineral. Mag.* **59**, 63-78.

LENTZ, D.R. & FOWLER, A.D. (1992): A dynamic model for graphic quartz-feldspar intergrowths in granitic pegmatites in the southwestern Grenville province. *Can. Mineral.* **30**, 571-585.

LIANG, J.-J. & HAWTHORNE, F.C. (1994): Characterization of fine-grained mixtures of rock-forming minerals by Rietveld structure refinement: Olivine + pyroxene. *Can. Mineral* **32**, 541-552.

LINDQVIST, B. (1966): Hydrothermal synthesis studies of potash-bearing sesquioxide-silica systems. *Geol. Fören. i Stockholm Förhr.* **88**, 133-178.

LINTHOUT, K. & LUSTENHOUWER, W.J. (1993): Ferrian high sanidine in a lamproite from Cancarix, Spain. *Mineral. Mag.* **57**, 289-299.

LONDON, D. (1984): Experimental phase equilibria in the system $LiAlSiO_4$ - SiO_2 - H_2O: A petrogenetic grid for lithium-rich pegmatites. *Am. Mineral.* **69**, 995-1004.

LONDON, D. (1986): Magmatic-hydrothermal transition in the Tanco rare-element pegmatite: Evidence from fluid inclusions and phase-equilibria experiments. *Am. Mineral.* **71**, 376-395.

LONDON, D. (1990): Internal differentiation of rare-element granitic pegmatites: A synthesis of recent research. *Geol. Soc. Am. Special Paper* **246**, 35-50.

LONDON, D. (1992a): Application of experimental petrology to the genesis and crystallization of granitic pegmatites. *Can. Mineral.* **30**, 499-540.

LONDON, D. (1992b): Phosphorus in S-type magmas: The P_2O_5 content of feldspars from peraluminous granites, pegmatites and rhyolites. *Am. Mineral.* **77**, 126-145.

LONDON, D. & BURT, D.M. (1982): Alteration of spodumene, montebrasite, and lithiophilite in pegmatites of the White Picacho District, Arizona. *Am. Mineral.* **67**, 97-113.

LONDON, D., ČERNÝ, P., LOOMIS, J. & PAN, J.J. (1990): Phosphorus in alkali feldspars of rare-element granitic pegmatites. *Can. Mineral.* **28,** 771-786.

LONDON, D., MORGAN, G.B.VII & HERVIG, R.L. (1989): Vapor-undersaturated experiments with Macusani glass + H_2O at 200 MPa, and the internal differentiation of granitic pegmatites. *Contrib. Mineral. Petrol.* **102,** 1-17.

MARSHALL, B.D., WOODARD, H.H. & DePAOLO, D.J. (1986): K-Ca-Ar systematics of authigenic sanidine from Waukau, Wisconsin, and the diffusivity of argon. *Geology* **14,** 936-938.

MARTIN, R.F. (1971): Disordered authigenic feldspars of the series $KAlSi_3O_8$ - $KBSi_3O_8$ from southern California. *Am. Mineral.* **56,** 281-291.

MARTIN, R.F. (1974): Controls of ordering and subsolidus phase relations in the alkali feldspars. *In* Proc. Adv. Study Inst. (W.S. Mackenzie and J. Zussman, eds.), Manchester Univ. Press, Manchester, England 313-336.

MARTIN, R.F. (1982): Quartz and the feldspars. *In* Granitic Pegmatites in Science and Industry (P. Černý, ed.). *Mineral. Assoc. Can., Short Course Handbook* **8,** 41-57.

MARTIN, R.F. (1988): The K-feldspar mineralogy of granites and rhyolites: A generalized case of pseudomorphism of the magmatic phase. *Rendiconti della Soc. Ital. Mineral. Petrol.* **43,** 343-354.

MARTIN, R.F. & FALSTER, A.U. (1986): Proterozoic sanidine and microcline in pegmatite, Wausau Complex, Wisconsin. *Can. Mineral.* **24,** 709-716.

MARTIN, R.F. & LAGACHE, M. (1970): L'effet du remplacement du potassium par le rubidium sur les paramètres de la maille de la sanidine et la leucite. *Bull. Soc. fr. Minéral. Crystallogr.* **93**, 581-582.

MASON R.A. (1980a): Changes in the crystal morphology of synthetic reedmergnerite ($NaBSi_3O_8$) during ordering experiments. *Mineral. Mag.* **43**, 905-908.

MASON, R.A. (1980b): The ordering behaviour of reedmergnerite, $NaBSi_3O_8$. *Contrib. Mineral. Petrol.* **72**, 329-333.

McMILLAN, P.F., BROWN, W.F. & OPENSHAW, R.E. (1980): The unit-cell parameters of an ordered K - Rb alkali feldspar series. *Am. Mineral.* **65**, 458-464.

MERTZ, D.F., LIPPOLT, H.J. & SCHNORRER-KöLLER, G. (1989): Early Cretaceous mineralizing activity in the St Andreasberg ore district (southwest Harz, FRG). *Mineral. Deposita* **24**, 9-13.

MILTON, C., CHAO, E.C.T., AXELROD, J.M. & GRIMALDI, F.S. (1960): Reedmergnerite, $NaBSi_3O_8$, the boron analogue of albite, from the Green River Formation, Utah. *Am. Mineral.* **45**, 188-199.

MORGAN, G.B. VI & LONDON, D. (1987): Alteration of amphibolitic wallrocks around the Tanco rare-element pegmatite, Bernic Lake, Manitoba. *Am. Mineral.* **72**, 1097-1121.

MULJA, T., WILLIAMS-JONES, A.E., WOOD, S.A. & BOILY, M. (1995): The rare-element-enriched monzogranite - pegmatite - quartz vein system in the Preissac-Lacorne batholith, Quebec. I. Geology and Mineralogy. *Can. Mineral.* **33**, 793-815.

MULJA, T., WILLIAMS-JONES, A.E., MARTIN, R.F. & WOOD, S.A. (1996): Compositional variation and structural state of columbite-tantalite in rare-element granitic pegmatites of the Preissac-Lacorne batholith, Quebec, Canada. *Am. Mineral.* **81**, 146-157.

MÜLLER, G. (1988): Preparation of hydrogen and lithium feldspars by ion exchange. *Nature* **332**, 435-436.

MURAMAKI, H., KIMATA, M., SHIMODA, S., ITO, E. & SASAKI, S. (1992): Solubility of $CaMgSi_3O_8$ and $\square Si_4O_8$ endmembers in anorthite. *J. Mineral. Petr. Econ. Geol.* **87**, 491-509.

NEUVONEN, K.J. & VESASALO, A. (1960): Pollucite from Luolamäki, Somero, Finland. *Bull. Comm. géol. Finlande* **188**, 133-146.

NICKEL, E.H. (1961): The mineralogy of the Bernic Lake pegmatite, southeastern Manitoba. *Dept. Mines Branch Tech. Bull.* **TB 20**, 1-38.

ORLANDI, P. & SCORTECCI, P.B. (1985): Minerals of the Elba pegmatites. *Mineral. Rec.* **16**, 353-363.

PAN, J.J.Y. (1988): The Geochemistry and Mode of Occurrence of Phosphorus in Pegmatite Feldspars. Unpublished B.Sc. thesis, University of Manitoba, Winnipeg, Manitoba, 1-71.

PANASENKO, E.B. & GOROSHCHENKO, Ya.G. (1970): Reaction of pollucite with limewater solutions at 220°C. *Zhurnal Prikladnoi Khimii* (Leningrad) **43**, 1470-1474 (in Russian).

PAQUETTE, J. & REEDER, R.J. (1990): New type of compositional zoning in calcite: Insights into crystal-growth mechanisms. *Geology* **18**, 1244-1247.

PAULUS, H. & MÜLLER, G. (1988): The crystal structure of a hydrogen-feldspar. *N. Jb. Miner. Mh.* **11**, 481-490.

PAUWELS, H., ZUDDAS, P. & MICHARD, G. (1989): Behavior of trace elements during feldspar dissolution in near-equilibrium conditions: Preliminary investigations. *Chem. Geol.* **78**, 255-267.

PEARCE, T.H. (1994): Recent work on oscillatory zoning in plagioclase. *In* "Feldspars and Their Reactions" (I. Parsons, ed.), NATO-ASI series C, Mathematical and Physical Sciences, Reidel Publishing Company, 313-350.

PENTINGHAUS, H. & HENDERSON, C.M.B. (1979): Rubidium-aluminosilikat-Feldspat ($RbAlSi_3O_8$): Stabilität, strukturelle Zustande und Schmelzverhalten: Chemische und thermische Ausdehnung des ($AlSi_3O_8$)-Gerüstes. *Fortschr. Mineral.* **57**, 119-120.

PEZZOTTA, F., HAWTHORNE, F.C., COOPER, M.A. & TEERTSTRA, D.K. (1996): Fibrous foitite from San Piero in Campo, Elba, Italy. *Can. Mineral.* **34**, 741-744.

PHILLIPS, B.L. & KIRKPATRICK, R.J. (1994): Short-range Si-Al order in leucite and analcime: Determination of the configurational entropy from ^{27}Al and variable-temperature ^{29}Si NMR spectroscopy of leucite, its Cs- and Rb-exchanged derivatives, and analcime. *Am. Mineral.* **79**, 1025-1031.

POST, J.E. & BISH, D.L. (1989): Rietveld refinement of crystal structures using powder X-ray diffraction data. *In* Reviews in Mineralogy **20**, Modern Powder Diffraction (Bish, D.L. and Post, J.E., eds.), 277-308.

POUCHOU, J.L. & PICHOIR, F. (1985): "PAP" (phi-rho-Z) procedure for improved quantitative microanalysis. *In* "Microbeam Analysis", J.T. Armstrong (ed.). San Francisco Press, 104-106.

PRINCE, E., DONNAY, G. & MARTIN, R.F. (1973): Neutron-diffraction refinement of an ordered orthoclase structure. *Am. Mineral.* **58**, 500-507.

QUADRADO, R. (1963): Ocurrência de gahnite e polucite nos pegmatitos do Alto Ligonha (Moçambique). *Bol. Soc. Geol. Portugal* **14**, 179-190.

RIBBE, P.H. (1994): The crystal structures of the aluminum-silicate feldspars. *In* "Feldspars and Their Reactions" (I. Parsons, ed.), NATO-ASI series C, Mathematical and Physical Sciences, Reidel Publishing Company, 1-50.

RICHMOND, W.E. & GONYER, F.A. (1938): On pollucite. *Am. Mineral.* **23**, 783-789.

SCARFE C.M. (1986): Viscosity and density of silicate melts. *In* Silicate Melts (C.M. Scarfe, ed.). *Mineral. Assoc. Can., Short Course Handbook* **12**, 36-56.

SEBASTIAN, A. & LAGACHE, M. (1990): Experimental study of the equilibrium between pollucite, albite and hydrothermal fluid in pegmatitic systems. *Mineral. Mag.* **54**, 447-454.

SHEARER, C.K., PAPIKE, J.J. & JOLLIFF, B.L. (1992): Petrogenetic links among granites and pegmatites in the Harney Peak rare-element granite-pegmatite system, Black Hills, South Dakota. *Can. Mineral.* **30**, 785-809.

SHEARER, C.K., PAPIKE, J.J., SIMON, S.B. & LAUL, J.C. (1986): Pegmatite - wallrock interactions, Black Hills, South Dakota: Interaction between pegmatite-derived fluids and quartz-mica schist wallrock. *Am. Mineral.* **71**, 518-539.

SHERRIFF, B.L. & HARTMAN, J.S. (1985): Solid-state high-resolution ^{29}Si NMR of feldspars: Al-Si disorder and the effects of paramagnetic centres.

Can. Mineral. **23**, 205-212.

SHIM, S.-H., KIM, S.J. & AHN, J.H. (1996): Quantitative analysis of alkali feldspar minerals using Rietveld refinement of X-ray diffraction data. *Am. Mineral.* **81**, 1133-1140.

SIBLEY, D.F. (1978): K-feldspar cement in the Jacobsville Sandstone. *J. Sed. Petrol.* **48**, 983-986.

SIMPSON, D.R. (1977): Aluminum phosphate variants of feldspars. *Am. Mineral.* **62**, 351-355.

SINKAKAS, J. (1968): Classic mineral occurrences: I. Geology and mineralogy of the Rutherford pegmatites, Amelia, Virginia. *Am. Mineral.* **53**, 373-405.

SMEDS, S.-A. & ČERNÝ, P. (1989): Pollucite from the Proterozoic petalite-bearing pegmatites of Utö, Stockholm archipelago, Sweden. *GFF* **111**, 361-371.

SMITH, J.V. (1974): Feldspar minerals. I. Crystal Structure and Physical Properties. Springer-Verlag, New York.

SMITH, J.V. (1994): Surface chemistry of feldspars. *In* "Feldspars and Their Reactions" (I. Parsons, ed.), NATO-ASI series C, Mathematical and Physical Sciences, Reidel Publishing Company, 541-594.

SMITH, M.P. & FRANKS, P.C. (1986): Mg-rich hollow sanidine in partially melted granite xenoliths in a mica peridotite at Rose dome, Woodson County, Kansas. *Am. Mineral.* **71**, 60-67.

SMITH, P. & PARSONS, I. (1974): The alkali feldspar solvus at 1 kilobar

water-vapour pressure. *Mineral. Mag.* **39**, 747-767.

STEWART, D.B. & RIBBE, P.H. (1969): Structural explanation for variations in cell parameters of alkali feldspars with Al/Si ordering. *Am. J. Sci.* **267A**, 444-462.

STEWART, D.B. & WRIGHT, T.L. (1974): Al/Si order and symmetry of natural potassic feldspars, and the relationship of strained cell parameters to bulk composition. *Bull. Soc. franç. Minéral. Cryst.* **97**, 356-377.

SUNDIUS, N. (1952): Quartz, feldspar and mica, and their deposits in Sweden. *Sveriges Geol. Underskökning, Ser. C Avhandl. och Uppsat. 520; Arsok* **45**, 1-231.

SWANSON, S.E. & FENN, P.M. (1992): The effect of F and Cl on the kinetics of albite crystallization: A model for granitic pegmatites? *Can. Mineral.* **30**, 549-559.

TAYLOR, R.P., FALLICK, A.E. & BREAKS, F.W. (1992): Volatile evolution in Archean rare-element granitic pegmatites: Evidence from the hydrogen isotopic composition of channel H_2O in beryl. *Can. Mineral.* **30**, 877-894.

TEERTSTRA, D.K. (1991): Compositional Heterogeneity and Alteration of Pollucite. M.Sc. Thesis, University of Manitoba, Winnipeg, Manitoba 1-225.

TEERTSTRA, D.K. & ČERNÝ, P. (1992): Controls on morphology of analcime-pollucite in natural minerals, synthetic phases, and nuclear waste products. *Cryst. Res. Technol.* **27**, 931-939.

TEERTSTRA, D.K. & ČERNÝ, P. (1995): First natural occurrences of end-member pollucite: A product of low-temperature reequilibration. *Eur. J.*

Mineral. **7,** 1137-1148.

TEERTSTRA, D.K. & ČERNÝ, P. (1997): The compositional evolution of pollucite from African granitic pegmatites. *J. African Earth Sci.* **21,** (in press).

TEERTSTRA, D.K., ČERNÝ, P. & CHAPMAN, R. (1992): Compositional heterogeneity of pollucite from High Grade Dyke, Maskwa Lake, southeastern Manitoba. *Can. Mineral.* **30,** 687-697.

TEERTSTRA, D.K., ČERNÝ, P., LANGHOF, J., SMEDS, S.-A. & GRENSMAN, F. (1996): Pollucite in Sweden: Occurrences, crystal chemistry, petrology and subsolidus history. *GFF* **118,** 141-149.

TEERTSTRA, D.K., ČERNÝ, P. & NOVÁK, M. (1995): Compositional and textural evolution of pollucite in pegmatites of the Moldanubicum. *Mineral. Petrol.* **55,** 37-51.

TEERTSTRA, D.K., LAHTI, S.I., ALVIOLA, R. & ČERNÝ, P. (1993): Pollucite and its alteration in Finnish pegmatites. *Geological Survey of Finland, Bulletin* **368,** 1-39.

TEERTSTRA, D.K. & SHERRIFF, B.L. (1996): Scapolite cell-parameter trends along the solid-solution series. *Am. Mineral.* **81,** 169-180.

TEERTSTRA, D.K. & SHERRIFF, B.L. (1997): Substitutional mechanisms, compositional trends and the end-member formulae of scapolite. *Chemical Geology* **111,** 745-756.

TEERTSTRA, D.K., SHERRIFF, B.L., ZHI XU & ČERNÝ, P. (1994): MAS and DOR NMR study of Al-Si order in the analcime-pollucite series. *Can. Mineral.* **32,** 69-80.

TOMASCAK, B.P. (1991): Granites and Rare-element Pegmatites of the Aylmer Lake Pegmatite Field, Slave Structural Province, N.W.T.: Petrochemistry, Mineralogy and Exploration Guidelines. Unpublished M.Sc. Thesis, University of Manitoba, Winnipeg, MB.

TRUEMAN, D.L. & ČERNÝ, P. (1982): Exploration for rare-element granitic pegmatites. *In* Granitic Pegmatites in Science and Industry (P. Černý, ed.). *Mineral. Assoc. Can., Short Course Handbook* **8**, 463-493.

UCAKUWUN E.K. (1981): The pegmatites and granitoid rocks of the Dryden area, northwestern Ontario. M.Sc. thesis, University of Manitoba, Winnipeg, MB.

VIDAL, O. & GOFFÉ, B. (1991): Cookeite $LiAl_4(Si_3Al)O_{10}(OH)_8$: Experimental study and thermodynamic analysis of its compatibility relations in the Li_2O - Al_2O_3 - SiO_2 -H_2O system. *Contrib. Mineral. Petrol.* **108**, 72-81.

VOLFINGER, M. (1976): Effet de la température sur les distributions de Na, Rb et Cs entre la sanidine, la muscovite, la phlogopite et une solution hydrothermale sous une pression de 1 kbar. *Geochim. Cosmochim. Acta* **40**, 267-282.

VOLOSHIN, A.V., MENSHIKOV, Yu.P., PAKHOMOVSKYI, Ya.A. & POLEZHAYEVA, L.I. (1981): Cesstibtantite $(Cs,Na)SbTa_4O_{12}$ a new mineral from granitic pegmatites. *Zapiski Vses. Mineral. Obschtsch.* **110**, 245-351 (in Russian).

VONCKEN, J.H.L., KONINGS, R.J.M., JANSEN, J.B.H. & WOENSDREGT, C.F. (1993a): Hydrothermally grown buddingtonite, an anhydrous ammonium feldspar ($NH_4AlSi_3O_8$). *Phys. Chem. Minerals* **15**, 323-328.

VONCKEN, J.H.L., KONINGS, R.J.M., VAN DER EERDEN, A.M.J., JANSEN, J.B.H., SCHUILING, R.D. & WOENSDREGT, C.F. (1993b): Crystal morphology and X-ray powder diffraction of the Rb-analogue of high sanidine, $RbAlSi_3O_8$. *N. Jb. Miner. Mh.* **1993**, 10-16.

WALDRON, K., PARSONS, I. & BROWN, W.I. (1993): Solution-redeposition and the orthoclase-microcline transformation: Evidence from granulites and relevance to ^{18}O exchange. *Mineral. Mag.* **57**, 687-695.

WALKER, F.D.L., LEE, M.R. & PARSONS, I. (1995): Micropores and micropermeable texture in alkali feldspars: Geochemical and geophysical implications. *Mineral. Mag.* **59**, 505-534.

WALKER, R.J., HANSON, G.N. & PAPIKE, J.J. (1989a): Trace element constraints on pegmatite genesis: Tin Mountain pegmatite, Black Hills, South Dakota. *Contrib. Mineral. Petrol.* **101**, 290-300.

WALKER, R.J., HANSON, G.N., PAPIKE, J.J., O'NEIL, J.R. & LAUL, J.C. (1989b): Internal evolution of the Tin Mountain pegmatite, Black Hills, South Dakota. *Am. Mineral.* **71**, 440-459.

WALLACE, H. (1978): Geology of the Opikeigen Lake area, District of Kenora (Patricia Portion). *Ontario Geol. Survey Rep.* **185**, 1-58.

WEITZE, R. & VISWANATHAN, K. (1971): Rubidium Plagioclase durch Kation enaustausch. *Fortschr. Mineral.* **49**, 63.

WHITE, J.C. & BARNETT, R.L. (1990): Microstructural signatures and glide twins in microcline, Hemlo, Ontario. *Can. Mineral.* **28**, 757-769.

WONES, D.R. & APPLEMAN, D.E. (1963): Properties of synthetic triclinic $KFeSi_3O_8$, iron-microcline, with some observations on the iron-microcline ⇄

iron-sanidine transition. *J. Petrol.* **4**, 131-137.

WOODARD, H.H. (1972): Syngenetic sanidine beds from Middle Ordovician Saint Peter Sandstone, Wisconsin. *J. Geol.* **80**, 323-332.

WORDEN, R.H. & RUSHTON, J.C. (1992): Diagenetic K-feldspar textures: A TEM study and model for diagenetic feldspar growth. *J. Sed. Petrol.* **62**, 779-789.

XIAO, Y., KIRKPATRICK, R.J., HAY, R.L., KIM, Y.J. & PHILLIPS, B.L. (1995): Investigation of Al,Si order in K-feldspars using ^{27}Al and ^{29}Si MAS NMR. *Mineral. Mag.* **59**, 47-61.

XU, ZHI & SHERRIFF, B.L. (1994): ^{23}Na ^{27}Al ^{9}Be ^{29}Si solid state NMR study of tugtupite. *Can. Mineral.* **32**, 935-943.

APPENDIX 1

List of Samples

Luolamäki, Finland: PA-003 (Poll-45, P. Černý); PA-004 (Poll-18A, K.J. Neuvonen); PA-009 (Poll-44S, P. Černý); PA-010 (Poll-4, C. Guillemin, Ecole des Mines, Paris); PA-014 (Poll-16, R. Kristiansen); PA-017 (Poll-38, O. von Knorring); PA-019 (Poll-18B,2, K.J. Neuvonen); PA-073 (Poll-42, P. Černý).

Viitaniemi, Orivesi, Finland: PA-002 (Poll-43, P. Černý); PA-011 (Poll-34, O. von Knorring); PA-013 (Poll-14, R. Kristiansen); PA-131 (S.I. Lahti).

Haapaluoma, Peräseinäjoki, Finland: PA-132 (P. Černý).

Varuträsk, Sweden: PA-016 (Poll-28, J.S. White, U.S.N.M. #R11884); PA-072 (Poll-40, O. von Knorring); PA-090 (VAR-38, P. Černý); PA-091 (VAR-4, P. Černý).

Nykõpingsgruvan, **Utö**, Sweden: Utõ-02; Utõ-03 (P. Černý).

Åkerberg, Sweden: PA-179, PA-180, PA-181 (Pollucite Type I, II and III, respectively, F. Grensman).

Nová Ves u Českého Krumlova, Czech Republic: PA-157, PA-166 (M. Novák).

Věžná, Czech Republic: PA-161, PA-162, PA-163 (M. Novák).

Mongolian Altai, **MA#1**, China: PA-142 (Zhou Tianren).

Mongolian Altai, **MA#3**, China: PA-144 (Zhou Tianren); PA-153 (Qui Yuzhuo).

Mongolian Altai, **MA#83**, China: PA-146 (Zhou Tianren); PA-156 (Qui Yuzhuo).

Kola Peninsula, NW USSR: PA-039 (Poll-2, C. Guillemin, Ecole des Mines, Paris).
East Siberia, USSR: PA-171 (M. Novák).

San Piero in Campo, Elba: PA-024 (Poll-3, C. Guillemin, Ecole des Mines, Paris).

Tamminen Quarry, Greenwood, Maine: PA-135 (M.A. Wise, U.S.N.M. # 126627); PA-005 (C. Frondel, Harvard #94630); PA-006 (C. Frondel, Harvard #92864 primary); PA-006 (C. Frondel, Harvard #94791 secondary).
Locality 1, near Norway, Maine: PA-031 (Poll-7, University of Manitoba M-47); Locality 2, near Norway, Maine: PA-078 (Poll-12, Univ. MB).
BB#7 Mine, Norway, Maine: PA-026 (Poll-26, V.T. King).
Walden Gem Mine, Portland, Connecticut: PA-139 (M.A. Wise, U.S.N.M. # R16708).
Leominster, Massachusetts: PA-020 (Poll-30, J.S. White, U.S.N.M. # 103386).
Old Tom Mt., Greenwood, Maine: PA-134 (M.A. Wise, U.S.N.M. # 126152).
Dunton Quarry, Newry, Maine: PA-038 (Poll-24, V.T. King).
Brown Derby, Colorado: PA-080 (P. Černý).
Himalaya Dike, California: PA-216 (S.I. Lahti).
Tin Mountain, near Custer, South Dakota: PA-008 (Poll-6, D.H. Garske); PA-022 and PA-025 (Poll-20, D.H. Garske); PA-034 (Poll-21, D.H. Garske); PA-127 (TM-20, J. Farrar); PA-128 (P. Černý); PA-136 (M.A. Wise, U.S.N.M. # 97634-5); PA-137 (M.A. Wise, U.S.N.M. # 95890); PA-133 (M.A. Wise, U.S.N.M. # 133855).

Benson #1, Zimbabwe: PA-023 (Poll-27, V.T. King); PA-079 (Poll-35, O.

von Knorring).

Bikita, Zimbabwe: PA-018 (A.J. Anderson); PA-021 (Poll-22, D.H. Garske); PA-028 (Poll-10, C. Guillemin, Ecole Des Mines, Paris).

Helikon, Namibia: PA-029 (Poll-31, J.S. White, U.S.N.M. #R8270); PA-077 (Poll-36, O. von Knorring); PA-125 (G. Friedrich); PA-167 (M. Novák).

Morrua, Mozambique: PA-032 (Poll-39, O. von Knorring).

Ambatonfinondrahana, Madagascar: PA-037 (Poll-1, C. Guillemin, Ecole des Mines, Paris).

Valor prospect, Lacorne Twp., Quebec: PA-036 (Poll-9, M. Latulippe).

Tot Lake, Dryden, Ontario: PA-093A-H.

Rubellite pegmatite, Lilypad Lake, Ontario: PA-097A-E, Lily1-12.

Red Cross Lake, Manitoba: RCL-series; multiple specimens.

Tanco pegmatite, SE Manitoba: PA-series; CsA-series and Poll-series; multiple specimens of P. Černý. P. Vanstone, D.K. Teertstra. Samples EMP-analysed: PA-043, 051, 101, 105, 112, 117, 119; 85u32, C53-201', 203', 204', 207'.

Lower Tanco: PA-158, PA-159, PA-160 (P. Vanstone).